A STUDY OF CELL GROWTH, DIVISION AND PROGRAMMED DIFFERENTIATION BY SIMULATION AND EXPERIMENTS.

A Dissertation

Presented to the Faculty of the Graduate School

of Cornell University

in Partial Fulfillment of the Requirements for the Degree of

Doctor of Philosophy

by

Satyaprakash Nayak

May 2010

A STUDY OF CELL GROWTH, DIVISION AND PROGRAMMED DIFFERENTIATION BY SIMULATION AND EXPERIMENTS.

Satyaprakash Nayak, Ph.D.

Cornell University 2010

Deregulation of cellular mechanisms responsible for cell growth, reproduction and differentiation is one of the hallmarks of all cancers. This study aims to elucidate the mechanisms underlying cell growth and differentiation using innovative computational and experimental tools. In the current study, we first review the basic cell cycle mechanisms in a typical eukaryotic cell (Chapter 1). In chapter 2, we analyze three published cell-cycle models and test our hypothesis that cell-cycle control architecture follow the "robust yet fragile" or the Highly Optimized Tolerance (HOT) paradigm. A very important fragile sub-system in the cell-cycle, revealed in our analysis of the cell-cycle models is protein translation. In chapter 3, we study the process of protein translation in detail, especially protein translation initiation. We formulate a detailed, mechanistic model of translation initiation from interactions validated in the literature. Novel systems-biology tools such as coupling analysis are developed and employed to gain insight into critical components of translation initiation. This study reveals the importance of the Akt and mTOR proteins in the presence of growth factors and that of negative regulators such as PTEN and 4E-BP1 in their absence. Differentiation is the process by which a less specialized cell becomes more committed in its lineage, in response to the external environment. Chapter 4 presents an experimental study of Arsenic Trioxide on Human Leukemia (HL-60) myeloblastic cells. Our results show that Arsenic Trioxide enhances All Trans Retinoic

Acid (ATRA) induced differentiation of HL-60 cells. This increase in differentiation is associated with an increase in the sustained Mitogen Activate Protein Kinase (MAPK) response. Chapter 5 presents an ensemble approach to model the response of HL-60 cells to ATRA and the role of sustained MAPK in differentiation. The model and its analysis present a systematic method to understand mechanisms involved in programmed cell differentiation in adult stem cells. In Chapter 6, we present a model combining hormone growth factor receptor signaling and prostate specific antigen (PSA) in LNCaP prostate adenocarcinoma cells. Finally, the concluding chapter discusses future directions of the current study.

BIOGRAPHICAL SKETCH

Satyaprakash Nayak was born in India. He received his education at the Indian Institute of Technology Roorkee (IIT Roorkee) in Chemical Engineering. After graduation he worked at Dr. Reddy's Laboratory, Hyderabad and at Oil and Natural Gas Corporation (ONGC), Mumbai, India. He was offered the McMullen Fellowship to join the MS/PhD program in the School of Chemical and Biomolecular Engineering at Cornell University, Ithaca, NY in August 2005. His PhD research focused on understanding the mechanisms behind cell-cycle, protein translation and cellular differentiation by mathematical modeling, simulation and experimentation in adult stem cells.

Dedicated to baba, ma and didi.

ACKNOWLEDGEMENTS

I would like to express my heart-felt gratitude to Prof. Jeffrey D. Varner, my doctoral advisor for his continuous support, guidance and encouragement throughout my PhD. He has always been very understanding has always encouraged me to perform to the best of my abilities. I am thankful to him for the patience he has shown with me all these years and the independence he gave me to explore my research horizons which has greatly contributed to my evolution as a researcher. His passion and commitment for research and science will always be a source of inspiration to me.

I am very grateful to Prof. Andrew Yen for providing me the opportunity to work in his laboratory. Working in his lab has been a wonderful learning experience for me and I have thoroughly enjoyed my experience there. He is a very open-minded, diligent and earnest researcher whose vast knowledge I have always found fascinating . The many insightful discussions I've had with him have gone a long way to shape my thesis in its present form.

I am sincerely thankful Prof. Matthew DeLisa for his stimulating questions and intelligent suggestions, which have greatly contributed to improving the quality of my research.

A special thanks to the members of Varner group and Yen group, especially Dr. Sang Ok Song, Dr. Deyan Luan, Thomas J. Mansell, Ryan A. Tasseff, Anirikh Chakrabarty and Dr. Miaoqing Shen, Dr. Rodica P. Bunaciu and Johanna Congleton for their timely help and constructive suggestions and criticisms. It was a joy to work with all of you. I would also like to thank all the undergraduates

who worked with me, especially Saniya Salim, Sarah Villarreal, Jalal K. Siddiqui and Emilda Gomez for the efforts they put in all my projects. Lastly, thanks to Shelby Clark-Shevaliar and Carol Casler for their support.

I am highly indebted to my parents and my sister for their unwavering moral support and encouragement all these years. I am thankful to them for instilling in me a love of science and the desire to pursue it to the highest levels. I could not have completed my PhD without your support and encouragement.

Finally, I would like to acknowledge Cornell University, Weill Cornell Medical College and the various funding agencies for the research assistant scholarships awarded to me.

TABLE OF CONTENTS

LIST OF TABLES

LIST OF FIGURES

CHAPTER 1

INTRODUCTION

According to statistics from the American Cancer Society ~1,500,000 new cases of cancer are estimated to be diagnosed in the U.S. and ~560,000 patients are expected to die, i.e. more that 1500 deaths per day in 2009 alone [1]. Worldwide, an estimated 12 million new cases were seen in 2007, with around 7.6 million deaths, i.e., approximately 20,000 deaths per day. [2]. Cancer is the second leading cause of death in developed countries (after heart diseases) whereas globally it is responsible for more deaths than HIV, tuberculosis and malaria combined [2].

Cancer is characterized by the uncontrolled growth and division of cells. In general, the cellular processes controlling the passage of a cell through its various life stages are tightly controlled. However, deregulation of these processes, referred to as cell-cycle, is one of the hallmarks of all cancers. Another cellular process often found to be dysfunctional in cancer cells is cell differentiation. Differentiation is the process by which a less committed cell moves ahead in its lineage, in response to environmental cues, leading to formation of more specialized cells. An inability of precursor cells from the bone marrow to terminally differentiate leads to a deficiency of healthy blood cells and an accumulation of immature cells in the body, giving rise to leukemia.

Cellular networks controlling proliferation as well as differentiation are large, immensely complex systems composed of a huge number of specialized proteins and protein complexes. We use latest tools from systems biology and

develop new computational analysis tools to find potential novel targets whose manipulation could be of therapeutic value. The following section gives a brief overview of computational biology, its tools and its role in understanding cellular processes controlling critical functions. A good predictive mathematical model requires that the underlying biology must by thoroughly understood. Although mathematical methods of biological systems are never complete, it is imperative that an exhaustive search of underlying biological relationships is performed and incorporated in the model to make its predictions reliable. Our research started with the study of cell-cycle, and led us to investigate in detail, some of its critical sub-systems such as protein translation and cell differentiation mechanisms. To acquaint the reader with biological basis of our models, an overview of biology behind the cell-cycle presented in the subsequent sections of this chapter. The other systems are explained in their respective chapters.

1.1 Computational Biology approaches to modeling of biological systems

Biological systems are often complex, highly interconnected networks of a huge number of components. Usually, they are also composed of a number of smaller sub-systems. The use of computational methods to understand biological systems is borne out of a desire to understand the complex relationships between interacting components and predict non-obvious, emergent properties as a result of these interactions. As observed by Kitano, [3] computational biology has two distinct roles to play, first it can be used to perform a large number of *in-silico* experiments faithfully, which would have otherwise been very time

consuming and expensive to perform in a lab. Secondly, using tools of knowledge discovery and data-mining it can be used to guide experiments better as well as to gain valuable insight into biological systems. It can therefore be used to produce experimentally testable hypotheses as well as provides us with a reliable way to test many of those hypotheses rapidly.

Since, biological systems come in a range of sizes and variety, a large number of computational approaches have been developed to deal with the diversity of such systems. A popular approach to model cellular systems such as cell-cycle is the boolean approach [4, 5]. Such an approach is based on the fact that some molecular systems are very robustly designed and that timing of events is not of critical importance. The main aim of this modeling approach is to predict the sequence of dynamical states confidently in cases where intricate machinery of the system is not well-known. On the other end of the spectrum is the stochastic simulation of models to accurately predict time-dependent behavior of systems in which interactions are well established [6, 7]. In between, there are a plethora of modeling approaches, prominent amongst them being reverse engineering genetic networks [8, 9] and bayesian approaches [10, 11]. One of the most well established and popular approach is the use of differential equations to model such systems [12, 13, 14, 13, 15]. This modeling approach produces the most faithful replica of the chemical processes in the cell and is perhaps, the most accurate representation of the cellular events. Modeling cellular systems in the form of differential equation though requires a very detailed and mechanistic knowledge of the underlying biological interactions, and is thus most demanding in terms of biological input. Although, this approach is also computationally intensive, due to advances in modern computing technology this

obstacle has largely been overcome, except for some extremely huge systems.

As diverse as the modeling approaches, a large variety of analysis tools have also been developed to better understand these models. The tools most often used in differential equation models of biological systems are dynamical analysis and sensitivity analysis. Dynamical analysis of models reveals the information about the different dynamical states of the whole system, e.g. hysteresis and bistability in the system, reversibility and oscillatory behavior etc. [13, 16, 14, 12, 17, 18] Although mathematically elegant and insightful, such an analysis fails to produce an experimentally testable hypothesis and a valid target for treatment approaches. For this reason, amongst others, we chose sensitivity analysis as our preferred tool for analysis of kinetic models.

Sensitivity analysis is an enabling tool for the investigation of robustness and fragility in networks relevant to human health and more generally for model-based knowledge discovery. Sensitivity analysis is an elegant method to computationally discover critical components of a large and complex system. It aims to answer the question, which part of the system affects it the most and thus is most important. It provides a clean, experimentally testable output. The validity of using such approach is evident in its popularity, as seen from a literature review.

1.1.1 Sensitivity Analysis in Literature

Leibler computationally predicted and later experimentally verified robust features of chemotaxis control networks [19, 20]. Cho *et al.*, used sensitivity analysis to study TNF-α-mediated NK-κB signalling where parametric uncertainty was addressed using a monte-carlo parameter sampling protocol; a family of random parameter sets, generated from the best parameter guess, was used to calculate the sensitivity profile in a region of parameter space [21]. Bullinger and coworkers explored the robustness of models of programmed cell death or apoptosis [22] while Stelling *et al.*, computationally identified points of robustness and fragility, using monte-carlo sensitivity analysis and Overall State Sensitivity Coefficients (OSSCs), in models of circadian rhythm [23]. Mahdavi *et al.*, employed sensitivity analysis, in conjunction with a mechanistic model of transcription-3 (Stat3) pathway kinetics, to better understand stem cell differentiation [24], while Luan *et al.*, used an uncertain mechanistic model of the coagulation cascade in combination with monte-carlo sensitivity analysis, to show that computationally derived sensitive mechanisms were consistent with anticoagulation therapeutic strategies [25]. Sensitivity analysis has also been used to integrate model identification and discrimination with optimal experimental design. Kremling *et al.*, investigated the benchmark problem of growth of a microorganism in a continuous bioreactor subject to feed shifts using sensitivity based model identification and discrimination strategies; they determined optimal experimental design and perturbation strategies to identify and discriminate between rival model formulations [26]. Gadkar *et al.*, identified signal transduction models from time-course measurements using a nonlinear scheme to estimate missing protein measurements from measured values, proposed strategies to calculate D-optimal experimental designs that maximized

the experimental information for model identification and proposed an iterative strategy to explore the space of model structures [27, 28]. Other optimal experimental design and model identification studies are resident in the literature [29, 30, 31] along with many techniques to estimate sensitivity coefficients for models composed of ordinary differential equations, differential algebraic and stochastic equations [32, 33, 34, 35, 36, 37, 38, 39, 40, 41].

The main advantage of using kinetic modeling coupled with sensitivity analysis is that such a framework gives results which are directly relatable to the underlying biology of the system.

1.2 An overview of cell cycle

The process by which cells grow and divide is called the cell cycle. The lifetime of a cell is divided into G1 (Gap 1), S (Synthesis of DNA), G2 (Gap 2) and M (Mitosis) phases, and an additional G0, or the resting phase. The cell receives signals from the extra-cellular environment, e.g. growth hormones as well as from intracellular checkpoints which determine the rate of growth of the cell and the appropriate time for cellular division. Three main checkpoints have been identified at which the cell checks to see whether the previous stages have been completed satisfactorily and whether it is in a good enough physiological state to continue to the next stage. These checkpoints occur in the late G1 phase (Restriction point), late G2 phase and in the latter stage of M phase. Once the cell gets past the Restriction point, it is committed to go through the cell cycle [42, 43, 44, 45, 46, 16].

The cell cycle is regulated by a family of proteins called Cdks (Cyclin dependent kinases) and Cyclins, which bind to them. The programmed synthesis and degradation of different cyclins is responsible for the progression of cell through the various cell cycle stages [43, 42]. Passage through the Restriction point and into the S phase is regulated by Cdk4 and Cdk6, which complex with CycD and Cdk2 which complexes with CycE. D-type Cyclins (D1, D2, D3) act as growth factor sensors and get induced in their presence. CycD2/D3 induce the formation of Cdk2 [42, 43]. The Cyclin-Cdk complexes are inhibited by special polypeptide inhibitors, called the Cyclin Dependent Kinase Inhibitors (CDKIs or CKIs). The INK4 family of CKIs consisting of $p16^{INK4a}$,$p15^{INK4b}$,$p18^{INK4c}$,$p19^{INK4d}$ interacts with CycD-Cdk4/6 complex. Thus, CycD-Cdk4/6 complex titrates away the CKIs, leading to an increase in the concentration of CycE-Cdk2 complex. CycE-Cdk2 is formed in an inactive state with phosphorylated Cdk2 and has to be dephosphorylated at Thr^{14} and Tyr^{15} to become active. Dephosphorylation is catalyzed by a phosphatase known as CDC25A. Active Cdk2-CycE complex can also interact with CKIs $p27^{KIP1}$ and $p21^{CIP1,WAF1,SDI1}$to form an inactive trimer. Aguda *et al.* [47] have correctly simulated the Restriction Point to lie somewhere in late G1 phase, originally derived for NIH 3T3 cells to lie about 2 hrs before the S phase. A central feature of their model is positive feedback loop between CDC25A and active CycE-Cdk2, CycE-Cdk2 is activated from its inactive state by dephosphorylation catalyzed by CDC25A and CycE-Cdk2 catalyzes phosphorylation of CDC25A to make it active. Another feedforward loop involves E2F and CycE, E2F catalyzes formation of CycE, and CycE interacts with Cdk2 to form an active complex which catalyzes formation of free E2F by phosphorylating pRb in the pRb-E2F com-

plex. The primary role of active CycE-Cdk2 complex is to inactivate Rb famliy of proteins by phosphorylating them. The main component of this family is the Retinoblastoma protein or pRb. pRb in its active hypophosphorylated state is bound with the E2F family of transcription factors [42, 43, 48, 49]. Thus, pRb on getting hyperphosphorylated by the CycE-Cdk2 complex releases E2F bound to itself. Release of E2F marks the beginning of S phase as it is a transcription factor for RNA polymerases, essential for duplication of DNA.The model of G1/S stage by Hatzimanikatis and Lee [50] is able to predict oscillatory nature of concentration of Cyclins with time. They were also able to simulate activation of cell from quiescence and vice-versa depending on E2F and CycE concentration by Bifurcation Analysis. Qu *et al.*[49] have modeled G1/S phase taking into account multiphosphorylation of sites at CDC25A, pRb and CKIs $p27^{KIP1}$ and $p21^{CIP1}$, and studied the dynamics of the system. They showed that multisite phosphorylation is critical for instability, and positive feedback between CDC25A and CycE-Cdk2 is responsible for limit cycle and bistability of the system. More importantly, they showed that the same system shows a range of dynamical behaviors, depending upon the values of kinetic parameters chosen. Thus, underscoring the need for accurate values of kinetic rate parameter for each reaction.

In the G2 phase, cell checks its readiness to enter M Phase and DNA damage, if any, is corrected. The main molecular entity driving the cell past the second checkpoint (G2/M) is called Maturation Promoting Factor (MPF). The components of MPF are CycB and Cdc2(also called Cdk1 or p34)[51]. Accumulation of CycB actually starts during the S phase and it starts to complex with Cdc2 (Cdk1) to form an inactive dimer called pre-MPF. Activation of MPF

requires Cdk1 to be dephosphorylated at Thr^{14} and Tyr^{15} residues. This reaction is catalyzed by CDC25C, whereas the reverse reaction requires Wee1/Myt kinase[52, 42]. Also, the activated CycB-Cdk1 complex can interact with the CKI $p21^{CIP1}$ to form an inactivating complex. There exist mechanisms in this phase to check DNA damage and accordingly halt cell cycle till the damage has been repaired. The central molecular entity for sensing DNA damage and taking corrective action is p53. Not surprisingly, p53 is the most frequently mutated gene in cancer and has been implicated in more than 50% of all cancers [43]. Upon sensing DNA damage, it up-regulates the synthesis of CKIs p21 and p27, amongst others. Thus, p53 induced up-regulation of CKIs is responsible for arresting cells at the G1/S transition (in case of stress) as well as at G2/M (in case of DNA damage). Also, in case of irreparable DNA damage to the cell, chemotherapeutic agents etc. p53 guides the cell towards apoptosis (programmed cell death) by either activating death genes like BAX or down-regulating survival genes like BCL-2. Aguda [52] has presented a detailed model of G2/M phase and simulated cell cycle arrest in case of DNA damage. The main components of the G2/M phase are MPF, CDC25C and the DNA damage pathway. There exists an antagonistic behavior between Wee1 and MPF as MPF also catalyzes phosphorylation of Wee into inactive Wee1P. The DNA damage pathways consist of Rad3/ATM pathways and p53 pathways. Upon sensing DNA damage, Rad/ATM pathway catalyzes phosphorylation of Chk1 to Chk1P, Chk1P in turn, phosphorylates CDC25C at Ser^{216} residue making it susceptible to combination with 14-3-3σ protein and thus, sequestration. p53 on the other hand, affects a number of molecular entities, it down-regulates formation of preMPF and up-regulates formation of CKI p27 and 14-3-3σ protein. The author showed that p53 pathway is essential to arrest cell cycle in G2 phase,

reinforcing experimental reports that p53 is a central character in enforcing G2 cell arrest [53].

Important feature of the full cell cycle model by Tyson *et al.*[48] is antagonistic behavior between CycB/Cdk1 and Cdh1/APC, i.e. APC dependent degradation of CycB is mediated by adapters Cdc20 and Cdh1. Cdc20 is activated by CycB-Cdk1 complex, whereas Cdh1 is inhibited by the same. This creates two antagonistic states, G1 having active Cdh1 and low CycB and S-G2-M having high CycB and inactive Cdh1. Their model accurately predicts oscillatory behavior for Cyclins A, E as well as CycE-Cdk2 and CycB-Cdk1 complex. Also, it shows rapid decrease in the concentration of tumor suppressors $p27^{KIP1}$ and pRb as CycE and CycB concentration begin to rise.

The degradation of Cyclins is done by the Ubiquitin-Mediated-Proteolysis System (UPS). The UPS has two main steps, first the peptide ubiquitin attaches itself to a protein, marking it for degradation and then poly-ubiquitinated proteins are degraded by the 26S proteosome complex. Ubiquitination of a protein involves co-ordinated action of three families of proteins. APC/C is one of the largest class of ligases involved in the proteolysis of core components of cell cycle [54, 55]. It consists of three core protein subunits and a variable sub-unit consisting of Cdc20 and Cdh1 which confer substrate specificity [56].

CHAPTER 2

A TEST OF HIGHLY OPTIMIZED TOLERANCE REVEALS FRAGILE CELL-CYCLE MECHANISMS ARE MOLECULAR TARGETS IN CLINICAL CANCER TRIALS

2.1 Abstract

Robustness, a long-recognized property of living systems, allows function in the face of uncertainty while fragility, i.e., extreme sensitivity, can potentially lead to catastrophic failure following seemingly innocuous perturbations. Carlson and Doyle hypothesized that highly-evolved networks, e.g., those involved in cell-cycle regulation, can be resistant to some perturbations while highly sensitive to others. The "robust yet fragile" duality of networks has been termed Highly Optimized Tolerance (HOT) and has been the basis of new lines of inquiry in computational and experimental biology. In this study, we tested the working hypothesis that cell-cycle control architectures obey the HOT paradigm. Three cell-cycle models were analyzed using monte-carlo sensitivity analysis. Overall state sensitivity coefficients, which quantify the robustness or fragility of a given mechanism, were calculated using a monte-carlo strategy with three different numerical techniques along with multiple parameter perturbation strategies to control for possible numerical and sampling artifacts. Approximately 65% of the mechanisms in the G1/S restriction point were responsible for 95% of the sensitivity, conversely, the G2-DNA damage checkpoint showed a much stronger dependence on a few mechanisms; 32% or 13 of 40 mechanisms accounted for 95% of the sensitivity. Our analysis predicted that CDC25 and cyclin E mechanisms were strongly implicated in G1/S malfunctions, while fragility

in the G2/M checkpoint was predicted to be associated with the regulation of the cyclin B-CDK1 complex. Analysis of a third model containing both G1/S and G2/M checkpoint logic, predicted in addition to mechanisms already mentioned, that translation and programmed proteolysis were also key fragile subsystems. Comparison of the predicted fragile mechanisms with literature and current preclinical and clinical trials suggested a strong correlation between efficacy and fragility. Thus, when taken together, these results support the working hypothesis that cell-cycle control architectures are HOT networks and establish the mathematical estimation and subsequent therapeutic exploitation of fragile mechanisms as a novel strategy for anti-cancer lead generation.

2.2 Introduction

Robustness, a system level property that allows function in the face of uncertainty and perturbation, is a long-recognized characteristic of living systems [57, 58, 59, 60]. Conversely, fragility, i.e., extreme sensitivity to small perturbations, is very undesirable, potentially leading to catastrophic system failure following seemingly innocuous perturbations [61]. Biological reaction networks and cellular systems operate in a dynamic context, hence, they must balance robustness against evolvability, performance and resource limitations. Venkatasubramaian and coworkers demonstrated the structure of complex networks can result from a trade-off between efficiency and robustness [62] while You and Yin explored how the environment has shaped the robust properties of bacteriophage T7 [63]. Stelling *et al.,* reviewed several examples of robust biological networks [60]; perhaps no better example of robustness can be found than cell division. Cell division, sometimes referred to as the cell-cycle, is one of the

most fundamental and highly regulated processes in biology. The decision to divide is tightly regulated integrating extracellular signals, such as growth factors and hormones, with intracellular cues that coordinate events leading to division [64]. Despite extensive control and surveillance subsystems guiding the progression of cells through the division cycle, malfunctions do occur as evidenced by the uncontrolled proliferation underlying many cancers [65]. Indeed, leading researchers have hypothesized that the networks underlying cancer progression and the phenotypic variation observed in solid tumors make cancer a robust and challenging disease [66, 67]. Carlson and Doyle have hypothesized that highly-evolved networks, e.g., those involved in cell-cycle regulation, can be resistant to some perturbations while extremely sensitive to others. The "robust yet fragile" duality of networks and systems has been termed Highly Optimized Tolerance (HOT) and has been the basis of new lines of inquiry in computational and experimental biology [61].

In this study, we employ tools from systems biology, namely mathematical modeling and monte-carlo sensitivity analysis, to explore the working hypothesis that cell-cycle control architectures obey the HOT paradigm. If our working hypothesis is true, then fragile cell-cycle mechanisms should be overrepresented among experimentally observed malfunctions underlying solid and hematological cancers. Moreover, the manipulation of fragile mechanisms in a therapeutic context, which has been suggested by Kitano [68] to be more likely to elicit an efficacious response from a network or system, should also be prevalent in the treatment literature. We test our working hypothesis by computationally screening three overlapping qualitative models of cell-cycle control architectures; we employ monte-carlo sensitivity analysis and k-means clustering

to rank-order mechanisms in cell-cycle and then contrast the predicted fragile and robust mechanisms with literature. If our working hypothesis is true, then the classification and therapeutic exploitation of fragile mechanisms could be a novel strategy for anti-cancer lead generation. Moreover, while the current development is restricted to cell-cycle control, the broader strategy of computationally probing and exploiting network weakness could be applied to arbitrary networks relevant to human health.

2.3 Materials and Methods

2.3.1 Model formulation and validation

The whole-cycle model of Novak and Tyson (Fig. 2.1), the G1-S model of Qu *et al.*, (Fig. 2.2A) and the G2-DNA damage model of Aguda (Fig. 2.2B) were implemented from literature and screened for fragile mechanisms using monte-carlo sensitivity analysis [52, 49, 48]. In each case, the model equations were represented as a system of Differential Algebraic Equations (DAEs) of the form:

$$\mathbf{f}(\mathbf{x}, \mathbf{p}) - \mathbf{\Theta}\frac{d\mathbf{x}}{dt} = \mathbf{0} \qquad \mathbf{x}(t_o) = \mathbf{x}_o \tag{2.1}$$

where $\mathbf{x} \in \mathbf{R}^m$ denotes the concentration vector, $\mathbf{f}(\mathbf{x}, \mathbf{p}) \in \mathbf{R}^m$ denotes the mass balance equation vector describing the kinetics and connectivity of the cell cycle network and $\mathbf{p} \in \mathbf{R}^p$ denotes the parameter vector. The diagonal $m \times m$ matrix $\mathbf{\Theta}$ contains 1's for those elements of the concentration vector that are dynamic (governed by a differential equation), 0 otherwise. We assume the mass balance vector $\mathbf{f}(\mathbf{x}, \mathbf{p})$ is at least once differentiable with respect to its arguments. The Novak and Tyson model, which employed complex kinetics to describe the

G1/S and G2/M checkpoints, programmed protein expression and degradation, was composed of 18 dynamic species, 4 species constraints and 74 parameters. On the other hand, the G1/S and G2-DNA damage models described only the specific molecular logic in their respective checkpoints and were mechanism based; the G1/S model was composed of 16 dynamic protein balances, 2 species constraints and 44 parameters while the G2-DNA damage model was composed of composed of 15 dynamic protein balances,1 constraint and 40 parameters.

2.3.2 Computation of Overall State Sensitivity Coefficients (OSSC)

The sensitive or fragile elements of the cell-cycle networks were determined by computing Overall State Sensitivity Coefficients (OSSC) [23]. OSSC values were calculated by first calculating the first-order sensitivity coefficients:

$$\sigma_{ij}(t_k) = \left.\frac{\partial x_i}{\partial p_j}\right|_{t_k} \tag{2.2}$$

which are solutions of the differential equation:

$$\frac{d\mathbf{s}_j}{dt} = \mathbf{A}(t)\,\mathbf{s}_j + \mathbf{b}_j(t) \qquad j = 1, 2, \ldots, P \tag{2.3}$$

subject to the initial condition $\mathbf{s}_j(t_0) = \mathbf{0}$ where j denotes the parameter index and P denotes the number of parameters. The Jacobian matrix ($\mathbf{A}$) and the matrix of first-derivatives of the mass balances w.r.t the parameter values ($\mathbf{B}$) are given by:

$$\mathbf{A} = \left.\frac{\partial \mathbf{f}}{\partial \mathbf{x}}\right|_{(\mathbf{x}^*, \mathbf{p}^*)} \qquad \mathbf{B} = \left.\frac{\partial \mathbf{f}}{\partial \mathbf{p}}\right|_{(\mathbf{x}^*, \mathbf{p}^*)} \tag{2.4}$$

where $(\mathbf{x}^*, \mathbf{p}^*)$ denotes a point along the *nominal* or *unperturbed* system solution. We solved the sensitivity equations for each parameter using three different numerical methods to control for possible artifacts; a 3-order fixed step size Backward Difference (BDF3) method was compared with forward Finite Difference (FD), and the fifth-order variable step-size ODE15s routine of Matlab (The Mathworks, Natick MA). The matrices **A** and **B** were estimated numerically at each time step using a generalized gradient algorithm [69]. Overall State Sensitivity Coefficients (OSSC), first used by Stelling *et al.*, to characterize mechanisms in circadian rhythm as fragile or robust [23], were calculated for each parameter j:

$$S_{o_j}(t) = \frac{p_j^*}{N_s}\left(\sum_{k=1}^{N_T}\sum_{i=1}^{N_s}\left[\frac{1}{x_i^*}\frac{\partial x_i}{\partial p_j}\bigg|_{t_k}\right]^2\right)^{1/2} \tag{2.5}$$

The quantity N_T denotes the number of time points used in the simulation while N_s denotes the number of proteins/protein complexes in the model. To account for parametric uncertainty, the OSSC values (S_{o_j}) were calculated over a *family* of random parameter sets; we randomly perturbed each nominal parameter by up to ±1-order of magnitude then solved the sensitivity balances for *each* family member. To control for perturbation effects, two other random parameter families were also tested (±50% and ±2-orders of magnitude, N=500 each).

2.3.3 Statistical analysis and clustering of overall state sensitivity coefficients

Three different statistical tests were performed to identify large statistically significant shifts in the OSSC values with qualitative significance between different numerical solution algorithms and random parameter families. A Welch t-test [70] was used to find all statistically significant shifts resulting from the different

treatments and then a secondary test on the $z-$score of each shift was preformed to find only the most prominent significant shifts. The OSSC values calculated over the family of parameter sets were assumed to follow normal distributions in each treatment case. The statistical significance of shifts in OSSC values for each treatment case relative to the control were determined by performing a Welch t-test with the null hypothesis that the means of the OSSC values were equal at a 1% significance level. The Welch t-test is similar to the student t-test with the exception that the two distributions being compared are not required to have equal variances. The list of significant OSSC values was further restricted to only those shifts with a magnitude larger than a specified z-score (0.1) away from the squared mean displacement over the significant OSSC values. We defined the displacement of an OSSC value relative to the control as:

$$d_{j,q} = \left(\bar{S}^{q}_{o_j} - \bar{S}^{c}_{o_j}\right)^2, \qquad j = 1, 2, \ldots, P \tag{2.6}$$

where $\bar{S}^{c}_{o_j}$ denotes the mean OSSC value over the family of parameter sets for parameter j in the control while $\bar{S}^{q}_{o_j}$ denotes the same quantity for treatment case q. A significant shift in OSSC value was *accepted* if:

$$d_{j,q} > z\sigma_{d_q} + \mu_{d_q} \tag{2.7}$$

where z denotes a desired z-score, σ_{d_j} denotes the standard deviation of the total displacement over all significant OSSC values for the *qth* treatment case and μ_{d_q} denotes the mean of the significant displacements for treatment case q. Large statistically significant shifts in OSSC values, while perhaps indicative of the shifting importance of mechanisms, do not guarantee that mechanisms are qualitatively different between treatment cases. The Spearman rank correlation denoted by ρ and defined as:

$$\rho = 1 - \frac{6\sum_{i=1}^{P} d_i^2}{N\left(N^2 - 1\right)} \tag{2.8}$$

measures the difference in qualitative ranking between mechanisms by quantifying the difference in the ordinal ranking of OSSC values. The quantity d_i denotes the difference in the ordinal rank of mechanism i between treatment cases, N denotes the number of pairs of values and P denotes the number of parameters considered. The Spearman rank is bounded by $-1 \leq \rho \leq 1$; a Spearman rank of one indicates that two ranked lists are identical, a Spearman rank equal to negative one indicates that two ranked lists are perfectly negatively correlated, while a Spearman rank of zero indicates that two ranked lists are uncorrelated.

Lastly, the distributions of OSSC values obtained from monte-carlo sampling were clustered using a standard k-means algorithm [71]. The mean and standard deviation obtained from the monte-carlo sensitivity analysis was used to estimate the underlying OSSC distribution (N=500 points) where the OSSC values were assumed to be normally distributed. One-hundred different clustering attempts were run for each model to control for clustering artifacts. The most probable configuration was reported.

2.4 Results

2.4.1 An implementation of cell cycle models shows results qualitatively consistent with the published literature

The whole-cycle model of Novak and Tyson (Fig. 2.1), the G1-S model of Qu *et al.,* (Fig. 2.2A) and the G2/M-DNA damage model of Aguda (Fig. 2.2B) were implemented from literature and screened for fragile mechanisms using monte-

carlo sensitivity analysis [52, 49, 48]. The Novak and Tyson model, which employed complex kinetics to describe both the G1/S and G2/M checkpoints and programmed protein expression and degradation, was composed of 18 dynamic species, 4 species constraints and 74 parameters. The G1/S and G2/M-DNA damage models described only the specific molecular logic in their respective checkpoints and were mechanism based; the G1/S model was composed of 16 dynamic protein balances, 2 species constraints and 44 parameters while the G2/M-DNA damage model was composed of composed of 15 dynamic protein balances,1 constraint and 40 parameters. Parameter values for each model were taken from literature. Unreported initial conditions were adjusted so that simulated model trajectories were qualitatively consistent with published values (Fig. 2.3). Unreported initial conditions were adjusted so that simulated model trajectories were qualitatively consistent with published values (Fig. 2.3).

2.4.2 Monte-carlo sensitivity analysis of cell cycle models reveals model agnostic trends in fragility

The published parameter sets, with fixed initial conditions, were used to generate families of random parameter sets (N=500, unless otherwise noted) where each nominal parameter was perturbed by up to ±50%, ± 1-order, or ± 2-orders of magnitude. Overall State Sensitivity Coefficients (OSSCs) were calculated over the random parameter families for each cell-cycle model using three different numerical algorithms. For each model, the mean OSSC values were ranked-ordered and plotted. The Area Under the Curve (AUC), calculated using the trapezoid rule, was used to measure the cumulative sensitivity contribution of

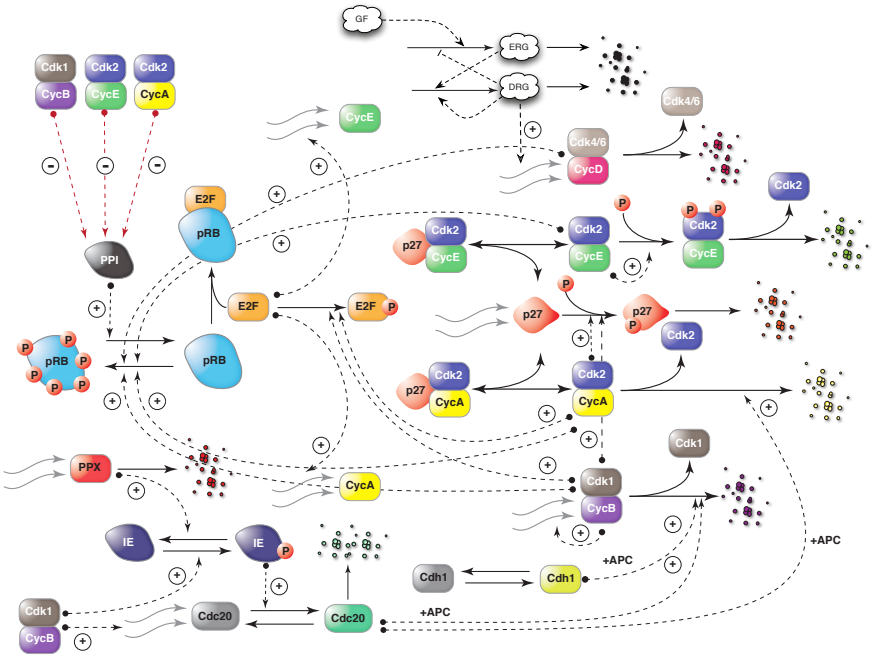

Figure 2.1: Schematic of the molecular logic of the whole-cycle model of Novak and Tyson used in this study. The Novak and Tyson model, composed of 18 dynamic species, 4 species constraints and 74 parameters, describes both the G1/S and G2/M checkpoints and programmed protein expression and degradation.

each parameter. A cumulative cutoff of 95% of the overall sensitivity was used to establish the list of mechanisms (Fig. 2.4) which were clustered into three groups using a k-means algorithm. The mechanism clusters were then compared with literature to determine the validity of fragility classification. Approximately 65% of the G1/S mechanisms were responsible for 95% of the sensitivity, conversely, the G2-DNA damage network showed a stronger dependence on a few mechanisms. Of the 44 mechanisms in the G1/S model, 29 were responsible for 95% of the sensitivity (Fig. 2.4A). The distribution of fragility was not specific to any single class of mechanism (Table A.1); 10 of the 29 mechanisms were associated with activation, phosphorylation/dephosphorylation,

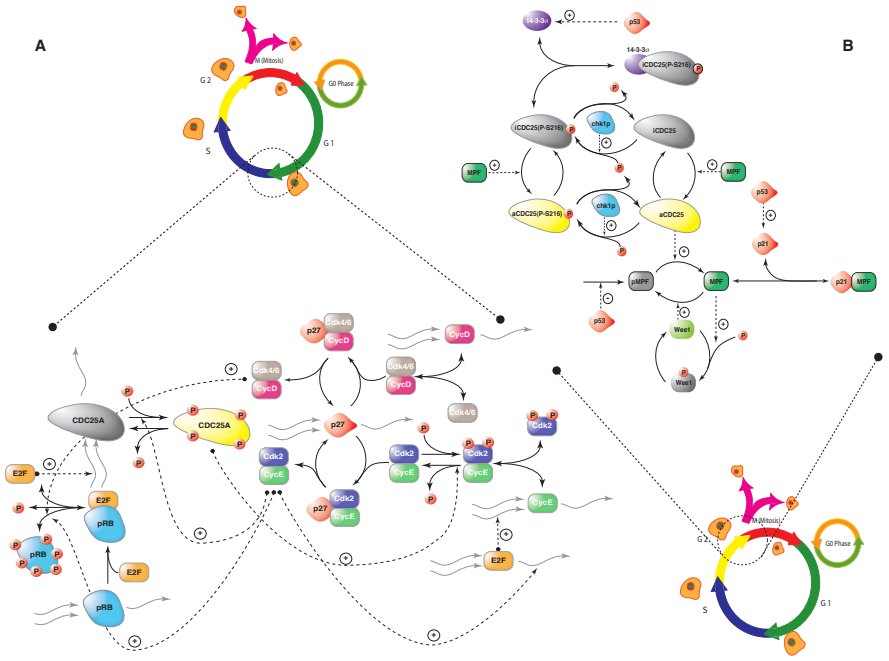

Figure 2.2: Schematic of the molecular logic of the G1/S (A) and G2/M (B) checkpoint models used in this study. The G1/S model of Qu et al., is composed of 16 dynamic protein balances, 2 species constraints and 44 parameters. The G2-DNA damage model of Aguda is composed of 15 dynamic protein balances 1constraint and 40 parameters. Both the G1/S and G2/M models employ mass action kinetics and the parameters are linear in the mass balances.

six of the 29 mechanisms were associated with degradation, seven of the 29 mechanisms were associated with expression or constraints on the total concentration of species in the model, while the remaining six of the 29 mechanisms were associated with binding interactions. The dephosphorylation of CDC25, the expression of cyclin E, the degradation of the cyclin E-CDK2 complex, and the concentration of the transcription factor E2F were classified as the most fragile mechanisms in the G1/S checkpoint (Table A.1, cluster I). The synthesis, activation and degradation of CKIs, the expression and degradation of CDC25, pRB concentration, the expression of cyclin D and cyclin E-CDK2 mechanisms

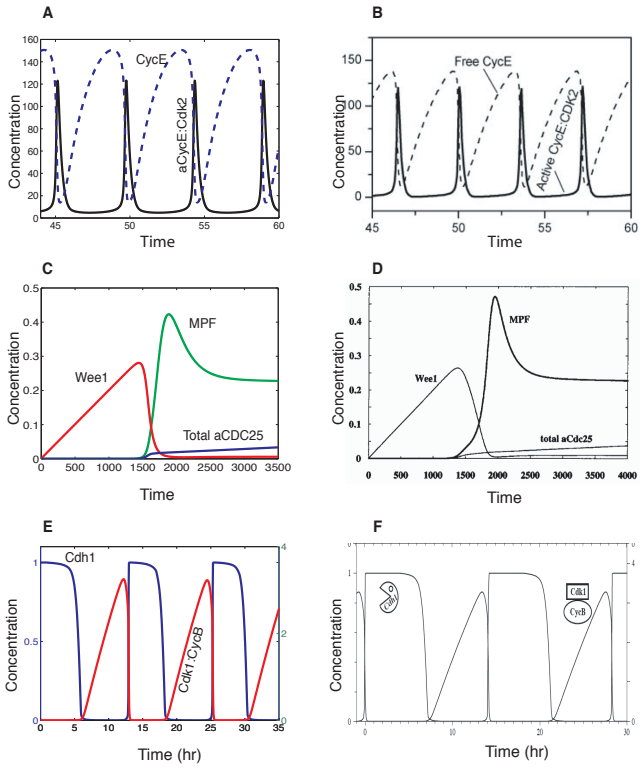

Figure 2.3: Qualitative comparison of simulations results of the model implementations used in this study. whole-cycle model of Novak and Tyson.

dominated the second-tier of G1/S fragility (Table A.1, cluster II). Tier-three involved several cyclin D mechanisms, cyclin E-CDK2 activity and E2F mediated cyclin E expression (Table A.1, cluster III). When taken together, the most heavily implicated G1/S protein was cyclin E, with 11 of 29 mechanisms, followed by CKIs with six, CDC25 and cyclin D were each involved in five fragile mechanisms and E2F and pRB were each listed twice. Cyclin E is the main restriction point cyclin, directly affecting E2F activation by phosphorylating pRb. Moreover, 16 of the 29 fragile parameters were functionally associated with cyclin E and cyclin E-CDK2 activity. As expected, the expression and degradation of

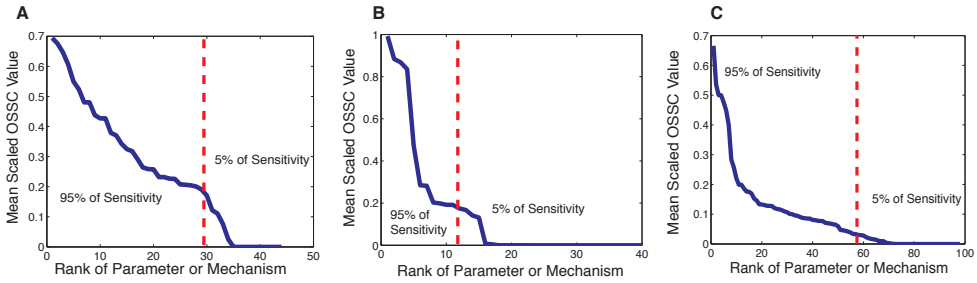

Figure 2.4: Cumulative Sensitivity as a function of parameter rank. The cumulative sensitivity contribution of each parameter was calculated by calculating the Area Under the Curve (AUC) using the trapazoid rule. Mechanisms responsible for 95% of the total sensitivity in each model were collected, clustered and analyzed. Panel A shows the result for G1/S model, Panel B - G2/DNA damage model and Panel C shows the plot for the whole cell model.

the G1/S-phase cyclins and their the associated CKIs were predicted to be important. However, the expression and degradation of cyclin E and all cyclin E interactions were ranked higher than the corresponding cyclin D mechanisms with the exception of the dissociation of the cyclin E-CDK2-CKI complex.

The G2-DNA damage network showed a stronger dependence on a few mechanisms when compared with G1/S. For the G2-DNA damage network, ~ 32% or 13 of 40 mechanisms accounted for 95% of the sensitivity (Fig. 2.4B). Consistent with G1/S, no single class of mechanism dominated the list of fragility. The most sensitive mechanisms were related to the generation and degradation of the cyclin B-CDK1 complex otherwise known as the Maturation Promoting Factor (MPF) and DNA repair mechanisms (Table A.2). The top five mechanisms were either directly or closely associated with the formation and activity of MPF while DNA repair mechanisms, e.g., the expression, degradation and activity of p21, 14-3-3σ and Wee1 phosphorylation dominated the

remaining eight mechanisms (Table A.2, cluster III). Activation of inactive MPF complex, which is negatively regulated by p53, was the most sensitive mechanism (Table A.2, cluster I), followed by pMPF generation, activation and transport of CDC25 into the nucleus (Table A.2, cluster II). Interestingly, while the generation of p53 itself was not predicted to be sensitive, interactions involving p53 were prevalent, e.g., the expression of inactive MPF and p21, both of which are up-regulated by p53, were predicted to be sensitive.

Approximately 77% of the Novak and Tyson parameters (57 of 74) were responsible for 95% of the sensitivity (Fig. 2.4C). However, because of the complex nature of the kinetics in the Novak and Tyson model in some cases multiple parameters which were functionally related with the same mechanism, were classified differently. Both global and local components of the model were predicted to be fragile. The most sensitive global mechanism was the translational efficiency while local mechanisms such as activation of IE (hypothetical protein which activates the E3-ligase CDC20), expression of cyclin B and CDH1 degradation were predicted to be the most fragile group (Table A.3, cluster I). The second-tier of fragile mechanisms were all associated with deregulation of programmed proteolysis (Table A.3, cluster II). Interestingly, while the percentage of mechanisms responsible for 95% of the sensitivity of the Novak and Tyson model was the largest of the three models, several mechanisms in cluster III were small, including most of the G1/S checkpoint logic. Thus, sampling the complex Novak and Tyson model produced less information than the mechanistic mass-action based G1/S and G2-DNA damage models.

If our fragility results were strictly artifacts of any particular model structure, then the classification of common mechanisms in each model would be

different; this was found not to be true (Table 2.1).

Table 2.1: Comparison of OSSC ranks for common mechanisms in the G1/S, G2-DNA damage and Novak and Tyson models.

Mechanism	G1/S (%)	G2-DNA (%)	Whole-cell model (%)
Generation of preMPF	–	93±2	80±18
Total concentrations			
Total E2F concentration	93±15	–	77±10
Total pRb concentration	86±15	–	43±16
Reactions of CKIs			
Generation of CKIs	86±10	85±2	68±12
CycE-Cdk2 associating with CKI	70±9	–	38±15
Dissociation of CycE-Cdk2-CKI	57±19	–	*(8±23, 5±19)*
CycD-Cdk4/6 associating with CKI	48±8	–	31±19
Dissociation of CycD-Cdk4/6-CKI	39±11	–	(47±14, *8±23, 4±19*)
Generation and Degradation			
Degradation of CycE	66±24	–	38±15
Degradation of CycD	55±15	–	47±14
CycE generation catalyzed by E2F	41±26	–	73±16

There were 11 mechanisms which appeared *exactly* in each model, 10 mechanisms were classified similarly while one mechanisms was ranked inconsistently across models. All 10 correctly classified mechanisms were fragile. Both mechanisms in the G2-DNA damage network that appeared in the Tyson and Novak model were correctly classified, while, one of the eight G1/S mechanisms was misclassified. Analysis of the G2-DNA damage and Novak and Tyson models predicted the formation of pMPF was an important mechanism and all three models predicted the expression of CKIs was fragile. Both the G1/S and Novak and Tyson models predicted that the total E2F and pRB concentra-

tions, the degradation of the G1/S phase cyclins, E2F driven cyclin E expression and the affinity of the cyclin D-CDK4/6-CKI complex were fragile. The models differed on the ranking of the off-rate of cyclin E-CDK2-CKI, analysis of the G1/S phase network predicted this to be important while Novak and Tyson did not. However, this discrepancy is likely an artifact of our insistence that mechanisms appear *exactly* in each model.

Table 2.2: Statistically significant shifts of OSSCs between solution methods using the Welch t-test. Only shifts recorded with a p-value of 0.01 and z-score of 1 are shown.

Mechanism	**ODE15s** $(\sigma \pm \mu)$	**BDF3** $(\sigma \pm \mu)$	**FD** $(\sigma \pm \mu)$
G1/S model			
Generation of CycE	0.6063 ± 0.3502	0.4583 ± 0.3364	0.5131 ± 0.3476
G2/M-DNA Damage model			
Generation of p21	0.2846 ± 0.1514	–	0.5016 ± 0.1954
Degradation of p21	0.2823 ± 0.1478	–	0.4847 ± 0.1835
Whole cell-cycle model			
CycE dependent CycE:Kip1 dissociation	0.1989 ± 0.2545	0.0463 ± 0.0798	0.0463 ± 0.0798
CycE:Kip1 dissociation giving Kip1	0.1988 ± 0.2545	0.0463 ± 0.0798	0.0463 ± 0.0798
CycE dependent Kip1 accumulation	0.1861 ± 0.2386	0.0438 ± 0.0744	0.0078 ± 0.0371
Degradation of DRGs	0.1461 ± 0.1720	0.0463 ± 0.1020	–
Synthesis of $p27^{Kip1}$	0.1274 ± 0.1232	0.0272 ± 0.0447	–
Total E2F concentration	0.1524 ± 0.1424	–	0.4249 ± 0.2385
Translational efficiency	0.6657 ± 0.3816	–	0.8647 ± 0.2372

2.4.3 The qualitative conclusions drawn from sampling the cell-cycle models were robust to the choice of solution method and the size of the parameter perturbation but sensitive to the number of parameter sets sampled.

Three different numerical techniques were used to solve the sensitivity equations to control for possible numerical artifacts. The ODE15s routine of Matlab (The Mathworks, Natick MA), a third-order backward-difference implicit method (BDF3) and forward finite difference (FD), all methods generated qualitatively similar sensitivity results (Fig. 2.5). The lowest Spearman rank between any two methods (ODE15s versus FD for the G1/S model) was 0.91 indicating a worse case correlation of approximately 91%. Interestingly, while the Spearman rank indicated good agreement between the solution methods, there were statistically significant shifts (See 2.2) in OSSC values indicating the solution methods systematically shifted mechanisms, i.e., different OSSC values were calculated but the order or ranking of mechanisms was maintained.

Second, the cumulative Spearman rank correlation between sensitivity results generated using the ODE15s, BDF3 and FD methods for each model was calculated as a function of the number of parameter sets sampled. While the cumulative Spearman rank converged to the population mean as the number of parameter sets increased, a strong population size dependence was observed (Fig. 2.7). For each model, the results reported were obtained in the region of convergence, hence, no additional information would have been gained if additional random parameter sets were sampled. Two additional sampling controls were conducted to verify the robustness of the qualitative conclusions drawn

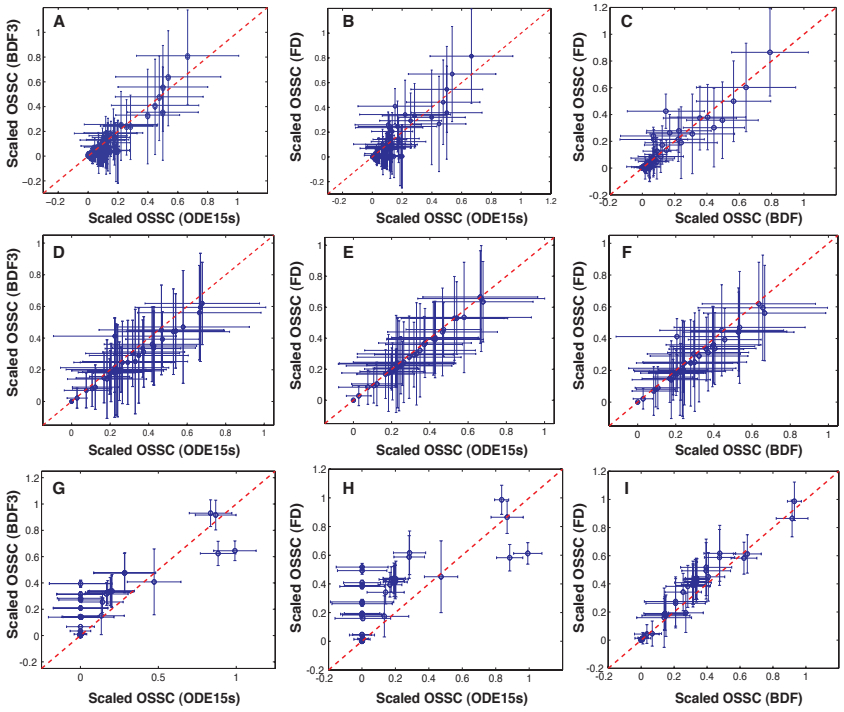

Figure 2.5: Sensitivity analysis results as a function of model and numerical method. Scaled Overall State Sensitvity Coefficients (OSSC) were calculated for each cell-cycle model over a family of random parameters sets (N=500 unless otherwise noted) generated by randomly pertubing the published set by ±1-order of magnitude. Three different numerical methods were used to solve the sensitivity equations to control for numerical artifacts.

from our analysis. First, the perturbation size used to generate the random parameter families was varied to test if different conclusions would have been drawn with different perturbation sizes; OSSC values computed over random parameter families generated using ±50%, ± 1-order and ± 2-orders of magnitude showed no qualitative difference as quantified by the Spearman rank correlation for the G1/S model (Fig. 2.6). The worst case correlation of 0.90 was observed between the ±50% and ± 2-orders of magnitude cases indicating on average 90% of the conclusions drawn between the two cases were consistent.

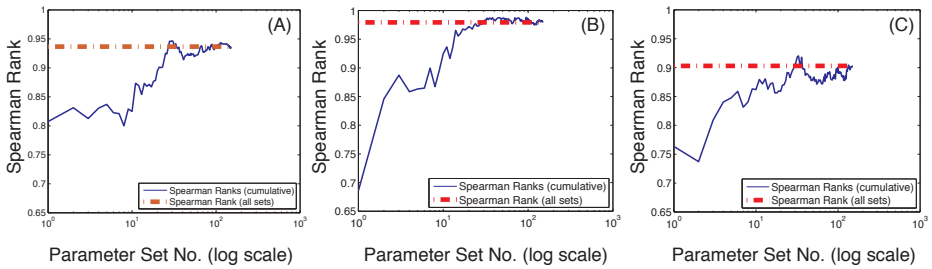

Figure 2.6: Effect of the parameter perturbation size on conclusions drawn from sensitivity analysis of the G1/S model. A family of random parameter sets was constructed (N=150) from the nominal set, where each parameter was perturbed by up to ±50%, ±1-order or ±2-orders of magnitude. The ODE15s routine of Matlab (The Mathworks, Natick MA) was used to solve the sensitivity equations.

2.5 Discussion

Multiple lines of experimental evidence support the assertion that cell-cycle control architectures are governed by the HOT paradigm. The single largest block of fragility predicted in the G1/S network was functionally associated with CDCD25 activity, cyclin E expression and activity of the cyclin E-CDK2 complex. Traditionally, cyclin E expression and cyclin E-CDK2 activity were thought to be critical for cell-cycle progression [72, 73]. For example, Ohtsubo *et al.*, have shown that cyclin E-CDK2 activity was maximum during the G1/S phase and over-expression of cyclin E accelerated cell-cycle progression [74]. Lucas *et al.*, showed that abnormal expression of cyclin E, but not Cyclin D1, was able to override G1 phase arrest by the INK4a family of CKIs [75]. Moreover, studies in cancer cell-lines and patients have suggested that cyclin E expression playes a strong role human breast cancer progression. Keyomarsi *et al.*, found, in human breast cancer tumors, that the cyclinE-CDK2 complex remains active

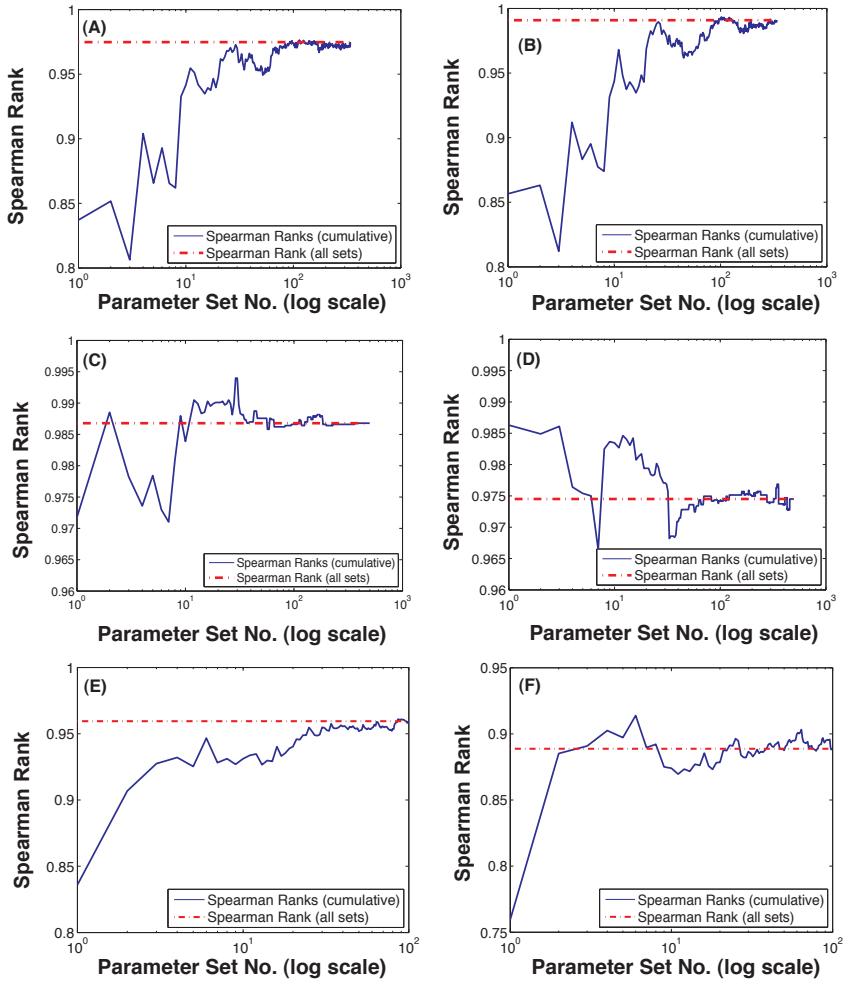

Figure 2.7: Spearman rank correlation as a function of the number of random parameter sets sampled. The red-dashed line in all cases denotes the cumulative Spearman Rank obtained by sampling all parameter sets for any two methods. A-B: Cumulative Spearman rank versus the number of parameter sets sampled for the G1-S model using the BDF3 and ODE15s methods (A) and Finite Difference (FD) and ODE15s methods (B), respectively. C-D: Cumulative Spearman rank versus the number of parameter sets sampled for the G2-M model using the BDF3 and ODE15s methods (C) and Finite Difference (FD) and ODE15s methods (D), respectively. E-F: Cumulative Spearman rank versus the number of parameter sets sampled for the whole-cycle model using the BDF3 and ODE15s methods (E) and Finite Difference (FD) and ODE15s methods (F), respectively.

throughout the cell-cycle suggesting a hypothesis, which was later confirmed by Porter *et al.,* [76], that truncated cyclin E variants, which were deregulated, might be responsible for the constitutive function of cyclin E-CDK2 in breast cancer tumors [77]. Keyomarsi *et al.,* demonstrated, in a retrospective study exploring the role of cyclin E in breast cancer patients, that cyclin E levels were strong clinical predictors of survival and mortality [78] while Span *et al.,* showed that cyclin E concentration was a strong predictor of endocrine therapy failure in breast cancer patients [79]. Recent studies, however, have challenged the traditional role of cyclin E. Geng *et al.,* have shown, in a mouse model, that while deletion of both cyclin E genes was lethal *in-utero*, deletion of cyclin E1 or cyclin E2 was tolerated with no obvious abnormalities [80]. Moreover, double cyclin E knockout mice were born alive if cyclin E was restored in the embroyoinc component of the placenta [80]. Ortega *et al.,* further challenged the role of cyclin E-CDK2 by showing that CDK2 null mice were born viable and healthy [81]. While the cyclin E and CDK2 knockout studies seem to contradict the essential role of cyclin E, the clinical evidence supporting the role of cyclin E in human cancer progression indicates that further studies are required.

In addition to cyclin E expression, the activity of the cyclin E-CDK2 complex and the generation, phosphorylation, dephosphorylation and degradation of CDC25 were predicted to occupy several positions in cluster(s) I and II of the G1/S checkpoint. Boutros *et al.,* recently reviewed the role of CDC25 phosphatases in cancer progression and summarized the progress of using CDC25 inhibitors in the treatment of several human cancers [82]. The overexpression of CDC25 at the mRNA and protein has been reported in primary tissue samples in several human cancers including breast [83], ovarian [84], prostate [85] and colorectal [86]. Hoffmann *et al.,* demonstrated, in human fibroblasts, that

expression of anti-CDC25 antibodies in the G1-phase prevented S-phase entry [87] while Hexl *et al.*, showed that CDC25 was a necessary protein for S phase entry by dephosphorylating the Thr-14 and Tyr-15 residues of CDK2, thereby activating the Cyclin E-CDK2 complex [88]. The concentration of E2F and pRB, which were constrained in both the G1/S and Novak and Tyson models, were also predicted to be critical components of the G1/S transition. The pRB protein has long been known to play a central role in the G1/S transition [89]. Richard *et al.*, showed that high expression as well as absence of pRb were associated with increased tumor progression and higher recurrence rates in bladder cancer [90] while Lucas *et al.*, showed that ectopic E2F expression was sufficient to induce S-phase entry and was able to override G1 phase arrest mediated by INK4 family of tumor suppressors [91, 92]. The sensitivity analysis of the cell-cycle models predicted that the off-rate of the cyclin D-CDK4/6 complex and the affinity and degradation of the cyclin D-CDK4/6-CKIs trimer were predicted to be robust or only moderately sensitive in the G1/S checkpoint while cyclin D expression was were predicted to be fragile. Overexpression of cyclin D variants, particularly cyclin D1, has been observed in several human cancers [93, 94] while cyclin $D1^{-/-}$ mice have been shown to display distinct tissue specific phenotypes including defective proliferation [95]. Tissue-specific defects were observed in cyclin D2 and cyclin D3 null mice along with proliferative malfunctions [96, 97]. Mice lacking all the cyclin D genes died prior to day E17.5 of gestation, however, most tissue and organs were formed by day E13.5 indicating that cyclin D was not required for embryogenies [98]. More generally, cyclin E expression and activity were ranked higher in our analysis than the respective cyclin D mechanisms. Keenan *et al.*, demonstrated in IIC9 Chinese hamster embryonic fibroblasts that cyclin E expression renders cyclin D-CDK4 dispensable for in-

activation of pRb, activation of E2F and for promoting G1-S progression [99]. When taken together, the cell-line, animal model and patient studies support the classification of fragile mechanisms obtained from sensitivity analysis of the cell-cycle models.

The hypothesis that computationally identified fragile mechanisms can be exploited as possible molecular targets, first explored using a model of the human extrinsic coagulation cascade by Luan *et al.,* [25], holds for cell-cycle control architectures. Consider the G1/S checkpoint prediction of the fragility of CDC25 mechanisms. While the inhibition of CDC25 as a cancer treatment strategy is still in the laboratory stage, several CDC25 inhibitors in development have shown promising results. The CDC25 inhibitor PM20 inhibited growth in human hepatoma-derived Hep3B cell-lines at a inhibitory concentration (IC) > 700 nM, PM-20 also inhibited the growth of MCF7 mammary carcinoma cells, FemX melanoma cells, PCI squamous cell carcinoma from tongue, albeit at a higher ICs [100]. BN82685, which inhibited CDC25A, B and C *in-vitro* and *in-vivo* and repressed the growth of HeLa and human pancreatic tumor Mia PaCa-2 xenografts in athymic nude mice, also inhibited the growth of human cell lines resistant to cytotoxic drugs e.g., the human myeloblastic leukemia cell-line HL-60 [101, 82]. The CDC25 antagonist, CPD-5, inhibited the growth of the rat hepatoma cell-line JM-1 *in-vitro* and the mouse cancer cell-line tsFT210 through selective inhibition of CDC25 [102, 103]. Orally administered IRC-083864, another CDC25 inhibitor, suppressed tumor growth in an LNCaP xenograft mouse model [104]. Inhibition and degradation of the active cyclin E-CDK2 complex, the second ranked mechanism in the G1/S network, has also been exploited as a treatment strategy. Bristol-Myers-Squibb (BMS) developed BMS-387032, a cyclin E-CDK2 inhibitor, with an IC50 of 95 nM [105]. Preclinical and phase I

studies exploring the use of BMS-387032 for the treatment of Ovarian cancer demonstrated that BMS-387032 possessed better efficacy than Flavopiridol, a promiscuous CDK inhibitor [106, 107]. More generally, the strategy of inhibiting CDKs, for example using molecules like Flavopiridol, has been an active area of research. Flavopiridol, which was the first cyclin dependent kinase inhibitor in clinical trials, alone or in combination with other drugs is currently being investigated in 52 active phase I or II trials [108, 109]. Flavopiridol has been proposed for the treatment of patients with recurrent, locally advanced, or metastatic soft tissue sarcoma [110], for the treatment of lymphoma and multiple myeloma [111], for the treatment, in combination with Trastumuzumab, of metastatic breast cancer [112] or in combination with other drugs such as Cisplatin and Carboplatin for the treatment of advanced solid tumors [113]. Another potent CDK2 inhibitor, CYC202, is in phase II trials for non-small cell lung cancer [114]. The fourth ranked mechanism in the G1/S model was the generation of cyclin E. E7070, a synthetic sulfonamide which depletes cyclin E, inhibits CDK2 in addition to modulating CKIs expression, is currently being evaluated in a phase I dose ranging study for the treatment of pancreatic and lung cancers [115, 116].

The correlation between fragility and treatment strategy was also found to hold for the G2/M-DNA damage network. The activation of preMPF (a complex of cyclin B and CDK1), catalyzed by CDC25, was predicted to be the most sensitive mechanism in the G2/M-DNA damage model while three of the four tier-two G2/M-DNA mechanisms were associated with CDC25 activity. The CDC25 inhibitors presented in the G1/S discussion, e.g., BN82685 could perhaps be used to modulate CDC25 activity in the G2/M phase of cell-division. Modulation of the formation of cyclin B-CDK1 Bryostatin-1, a pro-

tein kinase C (PKC) inhibitor and antagonist of the cyclin B-CDK1 complex, has been explored in phase II studies for the treatment of patients with multiple myeloma [117] or metastatic colorectal cancer [118] as well as a phase I study for the treatment of patients with relapsed non-Hodgkin's lymphoma and chronic lymphocytic leukemia [119]. In preclinical models, Bryostatin-1 has demonstrated single-agent activity against B16 melanoma, M5076 reticulum sarcoma and L10A B-cell lymphoma [120, 121]. Bryostatin-1 has been shown to disrupt cyclin B-CDK1 complex formation and activity by several different mechanisms. Hayun *et al.,* demonstrated, using an *in-vivo* HL-60 mouse leukemia model, that Bryostatin-1 in combination AS101 upregulated p21 expression, a cyclin dependent kinase inhibitor of CDK1 [122]. Aseiedu *et al.,* demonstrated that Bryostatin-1 was correlated with dephosphorylation of CDK2 [123] while Koutcher *et al.,* showed in both *in-vitro* and *in-vivo* models that Bryostatin-1 inhibited p34 kinase activator and decreased cyclin B1 expression [123, 124].

Modulation of translational efficiency, predicted to be the most important factor in the Novak and Tyson model, and manipulation of programmed protein degradation, which occupied seven of the top eight mechanisms in the Novak and Tyson model and was prominently featured in both the G1/S and G2/M-DNA damage networks, are both active areas of therapeutic development. Initiation of translation in Eukaryotes is thought to be rate limiting [125, 126] and overexpression of initiation components, for example the elongation factor elF4E, occurs frequently in human cancers [127, 128]. Eukaryotic translation occurs via two mechanisms, a CAP-dependent mechanism which accounts for processing of 95-97% of the total cellular mRNA [129] and an Internal Ribosome Entry Site (IRES) dependent route which is active during specific events, for example, apoptosis where many of the CAP-dependent factors have been de-

stroyed [129, 130]. Small molecule and peptide protein synthesis inhibitors, for example, cycloheximide, puromycin, emetine or PE38, a truncated *Pseudomonas* exotoxin lacking a cell binding domain, have been shown to induce apoptosis by downregulating the rate of macromolecular synthesis albeit with very different molecular mechanisms. Arnqvist and coworkers demonstrated downregulation of macromolecular synthesis in MCF-7 breast cancer cells following cycloheximide, puromycin or emetine exposure in the presence and absence of Insulin-like Growth Factor 1 (IGF-1) [131]. Addition of puromycin, cycloheximide and emetine to *in-vitro* cultures of MCF-7 cells, in the absence of IGF-1, resulted in increased apoptosis at 48 hr relative to the control. Conversely, in the presence of IGF-1, a concentration dependent reduction in apoptosis was observed for all three translation inhibitors. Bjornsti and Houghton recently reviewed another small molecule translation inhibitor under investigation as an antitumor agent, Rapamycin [132]. Rapamycin inhibits the Target of Rapamycin (TOR) protein, a serine/threonine kinase involved in several cellular functions, including CAP-mediated translation initiation. While Rapamycin has FDA approval as an immunosuppressant, development of anticancer therapies has been slow, despite antitumor activity against several solid-tumor models in the National Cancer Institute (NCI) screening program [133, 134, 135]. Several different Rapamycin analogs have been evaluated in clinical trials for the treatment of different indications including pediatric patients with relapsed or refractory acute leukaemia and renal-cell carcinoma where it resulted in a 7% objective response rate [132, 136]. Peptide inhibitors have also been used to downregulate translation; BL22, an immunotoxin developed and tested by Pastan, Krietman and coworkers at the National Cancer Institute (NCI) for the treatment of Chronic Lymphocytic Leukemia (CLL) [137], consists of the variable FV

fragment of the RFB4 antibody conjugated to the anti-translation peptide warhead PE38. Because PE38 lacks a cell-binding domain, it can only be incorporated into cells where the FV domain of BL22 binds. Once internalized, PE38 is liberated through a specific proteolytic cleavage mechanism and translocated via the KDEL receptor to the endoplasmic reticulum and eventually to the cytosol where it ribosylates components of the translation machinery. Siegall *et al.*, showed that ribosylation of translation components inhibited protein synthesis [138] often leading to apoptotic cell death [139], however other death mechanisms may have played a role in different cell types [140, 141]. When taken together, the anti-translation results demonstrate that inhibition of macromolecular synthesis which in turn induces cell-death could be a viable anti-cancer strategy which is unknowingly based upon the exploitation of a fragile mechanism. The second group of fragile mechanisms predicted in Novak and Tyson and more generally across the G1/S and G2/M-DNA damage networks involved deregulation of programmed protein degradation. Programmed proteolysis of cell-cycle components via the Ubiquitin Proteasome System (UPS), which is known to be a critical component driving cell-cycle progression [142], has been the target of several different therapeutic developments [143]. UPS operates in two discrete steps: first, the 8kDa peptide ubiquitin is attached to the protein substrate in an ATP dependent manner thereby marking the protein for destruction; second, the poly-ubiquinated proteins are degraded by the 26S proteasome complex [144]. The ubiquination of target proteins involves the coordinated activity of three families of enzymes; the ubiquitin activating enzyme family (E1), the ubiquitin-conjugating enzyme family (E2) and the ubiquitin ligase family (E3) [145]. While E1 malfunctions have not been observed in cancer, deregulation of E3 and to a lesser extent E2 activity has been directly linked to cancer

progression [145]. The Novak and Tyson model has only a skeleton representation of the UPS system, however, it does explicitly represent Cell Division Cycle protein 20 (CDC20), CDH1 and Anaphase Promoting Complex/Cyclostome (APC/C), all which are components of the E3 complex. APC/C is the core subunit to which the adapter proteins CDC20 and CDH1, which confer substrate specificity, bind [146, 147, 148]. Inhibition of specific E3 ligases remains a technical challenge [149], however, there have been some attempts to employ this strategy therapeutically. A class of cis-imidazoline analogs called Nutlins were synthesized which could displace p53 from the MDM2-p53 complex thereby inhibiting the programmed proteolysis of p53. Anti-tumor activity of Nutlins-3 against a human osteosarcoma xenograft model in nude mice showed 90% inhibition of tumor growth relative to control [150].

In this study, we tested the working hypothesis that cell-cycle control architectures are governed by the HOT paradigm by computationally probing models of protein-protein networks involved in cell-cycle regulation using monte-carlo sensitivity analysis. Consistent with the previous work of Luan *et al.,* and the conjecture of Kitano, the anecdotal comparison between the predicted group of fragile cell-cycle mechanisms and literature suggested that cell-cycle control architectures are HOT networks [25, 68]. However, while different controls were conducted to ensure the fidelity of the monte-carlo sampling protocol, the mathematical models being explored were coarse-grained and not structurally complete, hence, unknown factors not included in our analysis may influence our conclusions. Quantifying the impact of structural uncertainty on the qualitative conclusions drawn from our analysis remains a critical challenge. Certainly the correlation between efficacy and fragility is model independent; Luan *et al.*, demonstrated that fragile mechanisms correspond to current preclinical and

clinical treatment strategies for thrombosis using a similar monte-carlo sampling strategy applied to a model of the human extrinsic coagulation cascade [25]. What is less clear is when and why the classification of a mechanism might switch between fragile and robust or vice-versa. Initial results presented in this study suggest that while the quantitative values of sensitivity coefficients calculated between several different models with overlapping biology will change between models, the qualitative conclusions drawn are possibly invariant to the model description. However, this conclusion has not been generally established and is likely, as suggested by recent work by Luan *et al.,* to be true only for a subset of mechanisms [151]. A top-down strategy to explore the structural uncertainty issue would be to construct detailed subsystems models of the coarse-grained components which were determined by our analysis to be fragile, e.g., translation or the Ubiquitin Proteasome System. While a top-down strategy does not specifically address the theoretical aspects of the influence of structural uncertainty, it would allow the determination of the molecular interactions which are perhaps mediating fragility in the coarse-grained model. For example, if translational efficiency is in fact a fragile mechanism, then analysis of a detailed model of translation should produce a list of fragile mechanisms that have been observed experimentally. A similar argument could be made for programmed proteolysis. A second critical issue that was not addressed in this study was the safety of exploiting fragile mechanisms. The HOT paradigm suggests that fragile mechanisms are possible efficacious targets, however, nothing can be said regarding safety. There are several examples resident in the literature where highly efficacious strategies resulted in unwanted and possible harmful side effects, e.g., the association of rofecoxib with adverse cardiovascular events [152]. While there may be no direct and obvious linkage between

fragility and safety for single agents, sensitivity analysis could have a role to play when exploring drug combinations. Initial studies by Luan *et al.,* using combinations of coagulation inhibitors and a model of the coagulation cascade, have suggested that shifts in the ranking of mechanisms could be used to pinpoint the molecular nature of drug-drug synergies, however, this analysis is preliminary and at best would be retrospective [25].

CHAPTER 3

MODELING AND ANALYSIS OF AN ENSEMBLE OF EUKARYOTIC TRANSLATION INITIATION MODELS

3.1 Abstract

The programmed synthesis and degradation of proteins plays a central role in the regulation of cell cycle. Analogous to growth-factor stimulated gene expression, translation initiation is also up-regulated in the presence of growth factor signals. Deregulation of protein machinery involved in translation initiation has been implicated in many different cancers. In this study, we constructed a mathematical model describing the integration of growth factor and stress signals with the activation of translation initiation. Both kinetic parameters and unspecified initial conditions (a total of 431 parameters) were estimated using an adaptive step-size random search algorithm that minimized the residual between model simulations and 28 experimental data sets taken from multiple laboratories. We studied the effect of interactions and proteins on the entire network using systems-biology tools like sensitivity analysis and coupling coefficients in the presence and absence of growth factors. We found that whereas proteins Akt and mTor played an important role in the presence of growth factors, the effect of negative regulators such as PTEN and 4EBP1 assumed importance in their absence.

3.2 Introduction

The regulation of translation is a critical step in the control of eukaryotic proliferation and differentiation programs. Translation rates of many cell-cycle and survival proteins are modulated by growth factor, hormone and mitogenic signals [153]. These extracellular signals regulate the availability and activation of intracellular initiation factors required for the recognition of the 5′ cap on the mRNA. Given its central role in cell biology, evolutionarily optimized cellular infrastructure like translation might be expected to be robust. Robust systems or networks are able to maintain function despite component failures or perturbations. A robust translation architecture could provide cells with a secondary regulatory system in the event of transcriptional malfunctions. However, even in highly engineered or evolved subsystems, such as translation, malfunction of key components could result in program failure [61, 58, 60]. In fact, deregulated translation, especially involving initiation mechanisms, has been implicated in a spectrum of cancer types including breast and prostate cancer [154, 125, 155, 156, 157, 158, 127, 159].

The development of tools to estimate the robustness of network components has been an important outcome of systems biology. The assessment of robust and fragile features relies upon the computation of different measures of how networks respond to perturbation. Techniques such as monte-carlo sensitivity analysis have been applied to many systems to estimate network properties. Stelling *et al.* identified robust and fragile interactions in circadian rhythm by computing Overall State Sensitivity Coefficients (OSSCs) over a family of randomized parameters [23]. OSSCs measure how an infinitesimal change in the nominal value of a parameter influences all other network components dur-

ing a specified time-window. Luan *et al.* characterized the fragile components of the human coagulation cascade by computing OSSC values using randomized parameters [160]. The Luan *et al.* study demonstrated that sensitive interactions approximately corresponded with anti-coagulation therapeutic targets. Similarly, Nayak *et al.* showed that fragile interactions in cell-cycle control architectures were similar to anti-cancer targets [161]. Several other noteworthy studies have also demonstrated the utility of monte-carlo sensitivity analysis [26, 24]. However, sensitivity analysis does have limitations. First, the computation of sensitivity coefficients, especially by brute force methods such as finite difference, can be numerically problematic. Also, sensitivity analysis does not evaluate the ability of a network to maintain performance despite structural or operational perturbations. Other techniques, such as Structured Singular Values (SSVs) or direct simulation have been used to explore this question [162].

In this study, we investigated possible sources of structural fragility in the translation initiation architecture using computational tools. The motivation for this study was, in part, provided by an earlier work that suggested translation was a fragile subsystem in the eukaryotic cell cycle [161]. However, in the previous study the description of translation was course-grained and insight into which molecular components were critical could not be determined. To this end, we formulated and analyzed a canonical family of mechanistic eukaryotic translation initiation models compiled across multiple cell-lines. By exploring a consensus network, our analysis was perhaps more applicable to a wider range of cell-lines or primary tissues. Currently, we have only explored initiation mechanisms as translation regulation occurs primary at the initiation level [154]. The strategy and tools developed here are network agnostic and can be applied to other molecular networks easily. We tested the hypothesis that

malfunctions in only a few key proteins or interactions was likely responsible for translation deregulation. To this end, we analyzed a consensus mechanistic model of the eukaryotic translation initiation program, a canonical architecture compiled across multiple cell-lines [154]. Our initiation model was not specific to a cell-line or tissue. Rather, we explored a canonical initiation architecture compiled across multiple cell-lines. By exploring a consensus network, our analysis was more general and perhaps applicable to a wider range of tissues. Using literature, we formulated the model as a set of coupled non-linear Ordinary Differential Equations (ODEs). The model was deterministic and explained population averaged behavior as opposed to translation dynamics in a single-cell. Additionally, we assumed spatial homogeneity. However, we did differentiate between cytosolic and membrane localized processes. Translation model parameters and initial conditions were estimated by comparing simulations and experimental measurements. Twenty-eight data sets were compiled from *in-vitro* and *in-vivo* studies in multiple cell-lines [163, 164, 165]. Because of the complexity of initiation network, we were unable to estimate unique model parameters. Instead, we estimated an ensemble of possible model parameter sets [166, 167]. We identified over two-thousand probable sets based upon a similar simulation error. Each member of the parameter ensemble represented a different operational paradigm for the initiation network. By analyzing the model over these configurations, we identified structurally fragile components that were likely parameter independent.

3.2.1 A brief discussion of the initiation netwok

A mathematical model describing the integration of growth factor and stress signals with translation initiation was constructed . The model consisted of 145 proteins/protein-complexes and 286 reactions and its connectivity was assembled from literature [168, 129, 169, 170, 171, 172, 173, 174, 132, 175, 176, 177, 178]. While the model described both Cap and Internal Ribosome Entry Site (IRES) initiation mechanisms, we focused on Cap mediated translation as it is the dominant translation mechanism accounting for 95-97% of all translated mRNA [129]. Fig. 3.1 shows a schematic of the initiation network, whereas Table B.1) gives a description of all the reactions in the model. Two regulatory checkpoints control eukaryotic translation initiation following growth factor or hormone binding. We did not differentiate between the behavior of different kinds of receptors, for e.g., while in Platelet-derived growth factor receptor (PDGF) family the ligand is a dimer that cross-links the two receptors, in epidermal growth factor receptor family (EGFR) dimerization takes place through conformational change in the extracellular domain [44]. Binding of extracellular ligands to transmembrane surface receptors promotes the formation of multimeric adaptor complexes. These complexes composed of proteins such as Shc, Grb2, Ras and SoS promote the attachment and activation of Phosphoinositide 3-kinases (PI3K). PI3K and the tumor suppressor PTEN (phosphatase and tensin homolog) form the first of the two regulatory checkpoints controlling initiation. PI3K has a wide spectrum of effects in the cell and can regulate receptor originate MAPK signaling [179]. With respect to translation, PI3K catalyzes the conversion of plasma membrane lipid phosphatidylinositol-4,5-biphosphate (PIP2) to phosphatidylinositol-3,4,5-triphosphate (PIP3). Conversely, PTEN converts PIP3 back to PIP2. The ratio of PIP3 to PIP2 is critical because of the down-

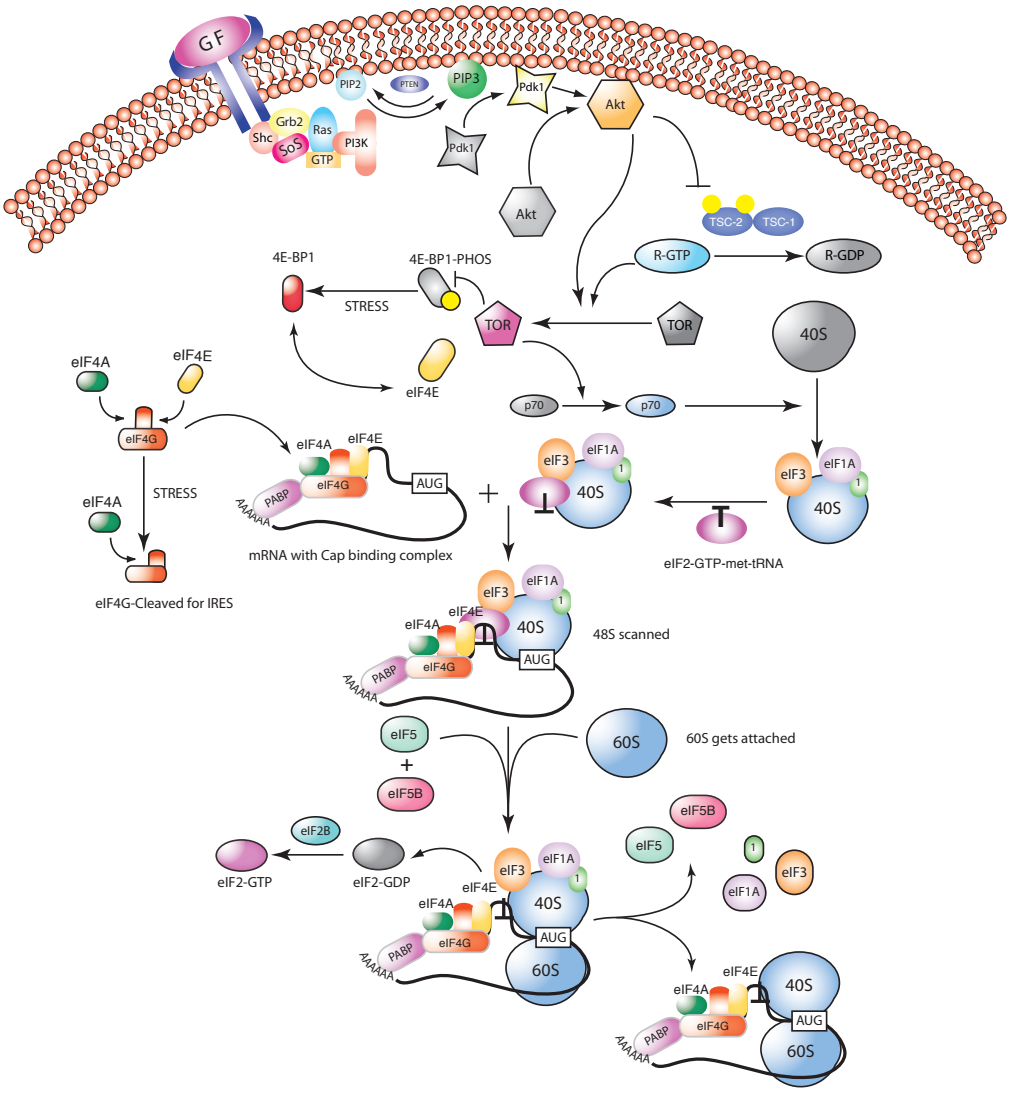

Figure 3.1: Schematic of the Eukaryotic translation initiation network governing the formation of the 80S initiation complex. A complete listing of all interactions and parameters used in this study is given in Table B.1

stream role of PIP3. PIP3 is responsible for recruiting key proteins such as Pdk1 and Akt to the plasma membrane where they become activated. Upon localization, Pdk1 phosphorylates and activates Akt [173, 172, 170]. Akt is a kinase involved in many different cellular processes [180]. In the context of translation, Akt activates another key kinase mTor (mammalian Target of Rapamycin) both directly by phosphorylation and indirectly by phosphorylating the TSC complex (TSC1-TSC2 dimer). The state of the TSC1/2 dimer is the effector of the second regulatory checkpoint. The TSC1/2 complex controls the balance between two forms of the Rheb protein, namely, Rheb-GTP and Rheb-GDP. Rheb-GTP directly activates mTor while the Rheb-GDP form is inactive. Once activated, mTor is responsible for initiating translation in two distinct ways. First, mTor activates the p70 protein (also called S6K) by phosphorylation at T-389 [181]. Activated p70 in turn activates the 40S ribosome. Second, mTor phosphorylates and inactivates 4E-BPx (Eukaryotic initiation factor 4E Binding Protein). In the absence of external signals, 4E-BPx sequesters eIF4E (Eukaryotic Initiation Factor 4E) and downregulates cap-binding complex assembly. Three 4E-BPx isoforms have been identified, all of which share a common eIF4E binding motif [182, 183, 184]. 4E-BPx is phosphorylated by mTor at multiple sites [185, 186]. Phosphorylated 4E-BPx realeases eIF4E which then promotes the formation of the eIF4F cap binding complex. The eIF4F-mRNA complex then binds 43S ribosomes. 43S ribosomes are composed of 40S ribosomes, initiation factors (eIF1, eIF3, etc) and the ternary eIF2-GTP-met-tRNA complex. The aggregate eIF4F-mRNA-43S complex is also called the 48S ribsome complex. Formation of 48S is followed by the mRNA scanning step and the subsequent hydrolysis and dissociation of eIF2-GTP. Removal of the eIF2-GTP promotes the binding of 60S ribosome with the 48S complex to form the final 80S initiation complex.

3.3 Materials and Methods

3.3.1 Formulation and solution of the model equations.

The translation initiation model was formulated as a set of coupled Ordinary Differential Equations (ODEs):

$$\frac{d\mathbf{x}}{dt} = \mathbf{S} \cdot \mathbf{r}\left(\mathbf{x}, \mathbf{p}\right) \qquad \mathbf{x}\left(t_o\right) = \mathbf{x}_o \tag{3.1}$$

The symbol $\mathbf{S}$ denotes the stoichiometric matrix (145×286). The quantity $\mathbf{x}$ denotes the concentration vector of proteins or protein complexes (145×1). The term $\mathbf{r}\left(\mathbf{x}, \mathbf{p}\right)$ denotes the vector of reaction rates (286×1). Each row in $\mathbf{S}$ described a protein while each column described the stoichiometry of network interactions. Thus, the (i, j) element of $\mathbf{S}$, denoted by σ_{ij}, described how protein i was involved in rate j. If $\sigma_{ij} < 0$, then protein i was consumed in r_j. Conversely, if $\sigma_{ij} > 0$, protein i was produced by r_j. Lastly, if $\sigma_{ij} = 0$, there was no protein i in rate j. We assumed mass-action kinetics for each interaction in the network. The rate expression for protein-protein interaction or catalytic reaction q:

$$\sum_{j \in \{\mathbf{R}_q\}} \sigma_{jq} x_j \rightarrow \sum_{p \in \{\mathbf{P}_q\}} \sigma_{pq} x_p \tag{3.2}$$

was given by:

$$r_q\left(\mathbf{x}, k_q\right) = k_q \prod_{j \in \{\mathbf{R}_q\}} x_j^{-\sigma_{jq}} \tag{3.3}$$

The set $\left\{\mathbf{R}_q\right\}$ denotes reactants for reaction q. The quantity $\left\{\mathbf{P}_q\right\}$ denotes the set of products for reaction q. The k_q term denotes the rate constant governing the qth interaction. Lastly, σ_{jq}, σ_{pq} denote stoichiometric coefficients (elements of the matrix $\mathbf{S}$). We treated every interaction in the model as non-negative. All reversible interactions were split into two irreversible steps. The mass-action formulation, while expanding the dimension of the initiation model, regularized

the mathematical structure. The regular structure allowed automatic generation of the model equations. In addition, an analytical Jacobian (**A**) and matrix of partial derivatives of the mass balances with respect to the model parameters (**B**) were also generated. Mass-action kinetics also regularized the model parameters. Unknown model parameters were one of only three types, association, dissociation or catalytic rate constants. Thus, although mass-action kinetics increased the number of parameters and species, they reduced the complexity of model analysis. In this study, we did not consider intracellular concentration gradients. However, we accounted for membrane and cytosolic proteins by explicitly incorporating separate membrane and cytosolic protein species.

3.3.2 Formulation of the objective function used to define the parameter ensemble and simulation error analysis.

Twenty-eight experimental constraints were used to define the parameter ensemble. These constraints consisted of *in-vitro* and *in-vivo* time-dependent and steady-state data sets. To compensate for different data time-scales, a weighting strategy was used in the error computation:

$$\mathcal{E}(\mathbf{p}) = \sum_{k \in \mathcal{A}} \epsilon_k^2(\mathbf{p}) + \gamma_\beta \left(\sum_{j \in \mathcal{B}} \epsilon_j^2(\mathbf{p}) \right) \tag{3.4}$$

The weighting coefficient $0 \leq \gamma_\beta \leq 1$ was a linear function of the fitting algorithm restart iteration β. An evolutionary algorithm minimized the error function $\mathcal{E}(\mathbf{p})$ by searching over different parameter vectors $\mathbf{p}$. The parameter vector $\mathbf{p}$ consisted of kinetic constants and unknown initial conditions. In the current model 431 model parameters were estimated. The sets $\mathcal{A}$, $\mathcal{B}$ denote groups of constraints. In this study, $\mathcal{A}$ consisted of the *in-vitro* time-series data of Lorsch

et al. [164]. The Garami *et al.* constraints made up $\mathcal{B}$. The terms ϵ_k^2 and ϵ_j^2 denote the squared error between simulations and experimental measurements. Steady-state values were estimated by allowing the simulation to run to steady-state. Parameter sets were accepted into the parameter ensemble based upon the overall error of the simulation. All parameter sets with error less than or equal to the median error were automatically accepted. Those sets with error larger than the median were accepted with the probability:

$$P(\mathbf{p}) = \exp\left(-\mathcal{E}(\mathbf{p})/\delta\right) \tag{3.5}$$

where $\delta = 0.5$. The form of the acceptance probability was similar to the previous work of Battogtokh *et al.* [167]. The scaled standard error was used to measure the agreement between the model and experiment:

$$s_E = \frac{1}{\max_k\left(Y(t_k)\right)}\left(\frac{\sum_{k=1}^{N_T}\left(Y(t_k) - \bar{Y}_m(t_k)\right)^2}{N_T}\right)^{1/2} \tag{3.6}$$

$Y(t_k)$ denotes the experimental measurement at time k. $\bar{Y}_m(t_k)$ denotes the mean simulated value over the parameter ensemble at time k. N_T denotes the number of experimental data points. The scaled standard error was taken from Spiegel [187].

3.3.3 Sensitivity analysis of the initiation network.

Overall State Sensitivity Coefficients (OSSC) were used to estimate which structural elements of the initiation network were sensitive [23]. OSSC values were determined by first calculating the first-order sensitivity coefficients at time t_k:

$$s_{ij}(t_k) = \left.\frac{\partial x_i}{\partial p_j}\right|_{t_k} \tag{3.7}$$

First-order sensitivity coefficients were computed by solving the matrix differential equation:

$$\frac{d\mathbf{s}_j}{dt} = \mathbf{A}(t)\,\mathbf{s}_j + \mathbf{b}_j(t) \qquad j = 1, 2, \ldots, P \tag{3.8}$$

subject to the initial condition $\mathbf{s}_j(t_0) = \mathbf{0}$. In Eqn. 6.10, j denotes the parameter index, P denotes the number of parameters in the model, $\mathbf{A}$ denotes the Jacobian matrix, and $\mathbf{b}_j$ denotes the jth column of the matrix of first-derivatives of the mass balances with respect to the parameter values (denoted by $\mathbf{B}$). An analytical Jacobian and matrix of first-derivatives of the mass balances w.r.t the parameters:

$$\mathbf{A} = \left.\frac{\partial \mathbf{f}_\mathbf{x}}{\partial \mathbf{x}}\right|_{(\mathbf{x}^*, \mathbf{p}^*)} \qquad \mathbf{B} = \left.\frac{\partial \mathbf{f}_\mathbf{x}}{\partial \mathbf{p}}\right|_{(\mathbf{x}^*, \mathbf{p}^*)} \tag{3.9}$$

were generated from the model equations. The quantity $\mathbf{f}_\mathbf{x} = \mathbf{S} \cdot \mathbf{r}(\mathbf{x}, \mathbf{p})$ and $(\mathbf{x}^*, \mathbf{p}^*)$ denotes a point along the unperturbed model solution. The sensitivity equations required that we solve the model equations to evaluate the $\mathbf{A}$ and $\mathbf{B}$ matrices. Thus, we formulated the sensitivity problem as an extended kinetic-sensitivity system of equations [188]:

$$\begin{pmatrix} \dot{\mathbf{x}} \\ \dot{\mathbf{s}}_j \end{pmatrix} = \begin{bmatrix} \mathbf{S} \cdot \mathbf{r}(\mathbf{x}, \mathbf{p}) \\ \mathbf{A}(t)\,\mathbf{s}_j + \mathbf{b}_j(t) \end{bmatrix} \qquad j = 1, 2, \ldots, P \tag{3.10}$$

where $\dot{\mathbf{x}} = d\mathbf{x}/dt$ and $\dot{\mathbf{s}}_j = d\mathbf{s}_j/dt$. We solved the kinetic-sensitivity system for multiple parameters in a single calculation using the LSODE routine of OCTAVE (www.octave.org). The first-order sensitivity coefficients were then used to calculate the OSSC value for parameter j:

$$O_j(t) = \frac{p_j}{N_s}\left(\sum_{k=1}^{N_T}\sum_{i=1}^{N_s}\left[\frac{1}{x_i}\left.\frac{\partial x_i}{\partial p_j}\right|_{t_k}\right]^2\right)^{1/2} \tag{3.11}$$

The terms N_T, N_s denote the number of time points considered and the state dimension of the model, respectively. To account for parametric uncertainty, OSSC values were calculated over a sparse sampling the parameter ensemble (N

= 77). The scaled parameter ranking was calculated based upon the magnitude of the OSSC value:

$$\theta_{sj} = \frac{N_P - R_{sj}}{N_P} \tag{3.12}$$

N_P denotes the number of kinetic parameters and R_{sj} denotes the ranking of parameter j calculated using parameter set s. We estimated the fragility of each protein or protein-complex in the network according to the relationship:

$$\mathcal{F}_s = |\mathbf{S}|\,\Theta_s \tag{3.13}$$

$|\mathbf{S}|$ denotes the absolute value of the stoichiometric matrix. Θ_s denotes the vector of scaled parameter rankings calculated using parameter set s.

3.3.4 Monte-carlo coupling analysis of the initiation architecture.

Coupling coefficients of the form:

$$\alpha\left(i, j, t_o, t_f\right) = \left(\int_{t_o}^{t_f} x_i\left(t\right) dt\right)^{-1} \left(\int_{t_o}^{t_f} x_i^{(j)}\left(t\right) dt\right) \tag{3.14}$$

were calculated to understand the regulatory connectedness of the initiation network. Here t_0 and t_f denote the initial and final simulation time respectively. i and j denote the indices for the reference species (here 80S complex) and the perturbed species respectively. The coupling coefficient $\alpha\left(i, j, t_o, t_f\right)$ is the ratio of the integrated concentration of a network output in the presence (numerator) and absence (denominator) of structural or operational perturbation. If $\alpha\left(i, j, t_o, t_f\right) > 1$, then the perturbation *increases* the output concentration. Conversely, if $\alpha\left(i, j, t_o, t_f\right) \ll 1$ the perturbation *decreases* the output concentration.

Lastly, if $\alpha\left(i, j, t_o, t_f\right) \sim 1$ the perturbation does not influence the output concentration. In this study, we used two structural perturbations to probe the regulatory connectedness of initiation. Protein knock-downs and over-expression was simulated where the network output was the concentration of 80S ribosomes. Because 80S concentration was a functions of the model parameters, coupling coefficients were calculated over the parameter ensemble.

3.4 Results

3.4.1 An ensemble model of the initiation network was able to capture formation of 80S and predict formation of 48S complexes

An ensemble of model parameters was constructed by minimizing the difference between model simulations and 28 experimental data sets. Both *in-vitro* and *in-vivo* dynamic and steady-state measurements were used to estimate model parameters. An initial best fit parameter set was randomized to form a family of seed parameters (N = 50). The seed parameters served as starting points for an adaptive step-size evolutionary algorithm [189]. The search algorithm minimized the residual between model simulations and the 28 experimental constraints simultaneously. Both kinetic parameters and unspecified initial conditions were estimated using the search algorithm (a total of 431 parameters). The search algorithm took 100 steps (approximately 4 error function evaluations per step) from each parameter seed. The error at each step

was stored along with the current parameter estimate. The error was calculated by comparing the simulated value or feature with experimental observations. Quantitative time-series data was directly compared with simulations. In addition, qualitative estimates of the phosphorylation state of key proteins were determined from published western blots. Western blot bands were assigned a value between (0,1) depending upon intensity (one being the maximum intensity band). The difference between these normalized intensity estimates and the simulated fraction of phosphorylated protein was minimized as part of the ensemble. While this was not ideal, it allowed us to train the model to reproduce published *qualitative* regulatory features. Parameter estimation generated a family of 5000 possible parameter sets each with a specified error (Fig. 3.2). In this study we used an error cutoff to decide whether a parameter set should be admitted into the ensemble. The median simulation error was used as a cutoff to include/exclude parameter sets in the ensemble (Fig. 3.2, dark circles). Parameter sets with error greater than the median were accepted with a probability (Fig. 3.2, light circles) similar to Battogtokh *et al.* [167]. All the parameters below the median error were selected. Parameter sets with error greater than the median were accepted with a probability < 1 (Fig. 3.2, light circles), with the exact probability calculated similar to Battogtokh *et al.* [167]. Approximately, 52% of the possible 5000 parameter sets generated by the fitting algorithm met the ensemble selection criteria (N = 2552). Analysis of the parameter ensemble showed that approximately 55% of the unknown parameters and initial conditions (240 of 431) were constrained with a Coefficient of Variation (CV) of less than or equal to 50% (Fig. 3.2, inset). Of the 240 constrained parameters, 82% were rate constants while the remaining 18% were initial conditions. The most highly constrained initial condition belonged to eIF4E. Conversely, parameters

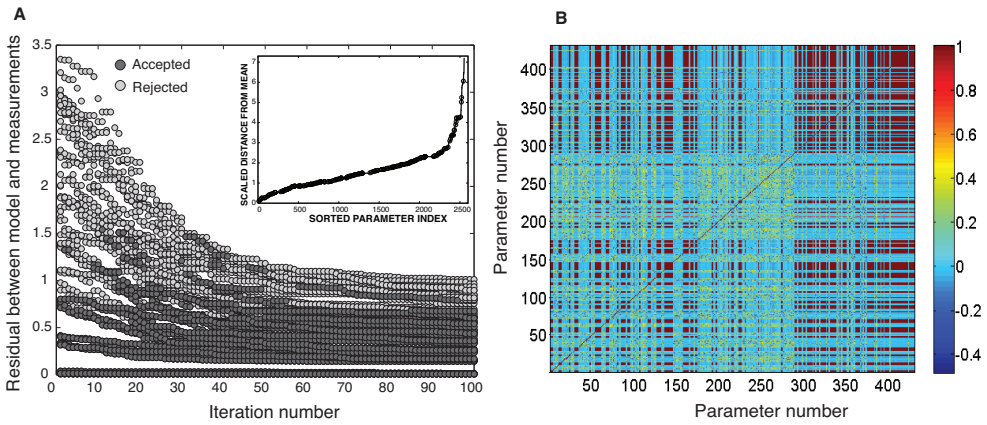

Figure 3.2: Ensemble error trajectories and Correlation Matrix of Parameters. **(A)** Model residual versus iteration number of the parameter fitting algorithm. Each point represents a possible parameter set. The dark circles denote parameter sets that met the ensemble selection criteria. Inset: The relative distance from the mean of sets chosen for sensitivity analysis is shown. **(B)** Correlation coefficients were calculated for each parameter over the entire ensemble.

governing the assembly of the adaptor complex, 48S assembly and p70 activation were the most constrained rate constants. Time dependent measurements with/without growth factors and inhibitors were used to estimate model parameters governing the rate of 80S assembly and the phosphorylation of Akt pathway proteins. The *in-vitro* study of Lorsch *et al.* was used to estimate model parameters governing the kinetics of 80S assembly. Conversely, 43S data taken from the same study was used for model validation [164]. Thus, while 80S initiation complex trajectory was used to constrain the model and used as training data. The trajectories of 43S-mRNA-GMP-PNP and 43S-mRNA-GTP generated by the model were compared with literature data for validation. Simulations of *in-vitro* 80S formation in the absence of stress had a scaled standard error (s_E) of approximately 8% (Fig. 3.3A). The *predicted* 43S-mRNA-GMP-PNP and 43S-mRNA-GTP trajectories had a scaled standard error of 21% and 39%, respec-

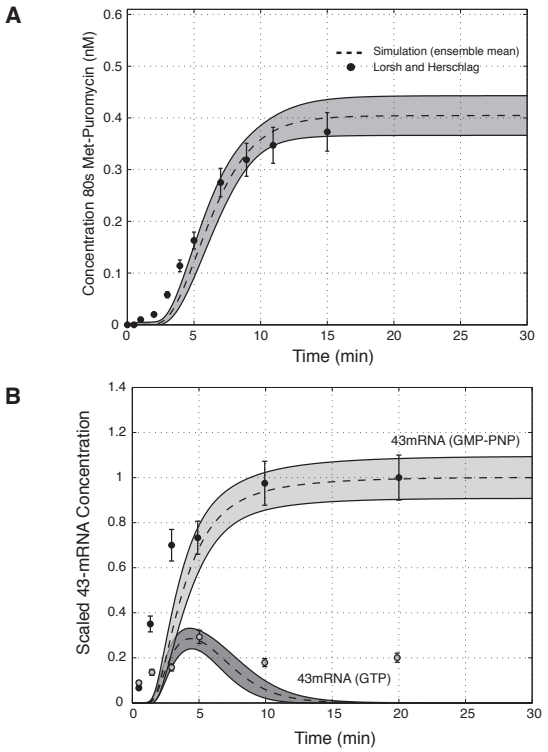

Figure 3.3: Simulation of *in-vitro* 80S formation. Dashed lines denote the mean simulation over the parameter ensemble while points denote experimental measurements. The shaded region denotes one ensemble standard deviation. **A**. *in-vitro* time-course for the 80S complex measured by the puromycin assay. **B**. *in-vitro* time-course for the formation of the 43S-mRNA complex (also called 48S) when the *in-vitro* translation reaction was quenched at the specified time-points by substitution of GMP-PNP in place of GTP. The GMP-PNP and GTP 43S-mRNA simulations were scaled by the simulated 43S-mRNA-GMP-PNP value at 20 min.

tively. The small standard fitting and prediction errors suggested the ensemble described the *in-vitro* kinetics of 80S formation.

3.4.2 A comparison of model predictions with experimental results obtained in conditions with and without serum

The study of Garami *et al.* was used to constrain the *in-vivo* phosphorylation of Akt (PKB), p70 (S6K) and 4E-BPx [165]. The Garami *et al.* study contained 14 steady-state and 12 time-dependent *in-vivo* constraints (Fig. 3.4 - 3.5). Approximately 73% (19 of 26) of the Garami *et al.* constraints were captured by the ensemble. The fraction of pAkt (S473) in serum-starved A14 NIH 3T3 cells with/without insulin was consistent with measurements (Fig. 3.4B). Without insulin no phosphorylated Akt was observed experimentally or in the simulation (Fig. 3.4B, lane 1). Thirty-minutes following insulin addition, the fraction of pAkt increased (Fig. 3.4B, lane 2). Reduced pAkt following the addition of the Wortmannin, a selective PI3K inhibitor, confirmed that Akt activation was dependent upon upstream PI3K signaling (Fig. 3.4B, lane 3). However, addition of Rapamycin, an inhibitor of mTor in the presence of insulin increased the fraction of pAkt (Fig. 3.4B, lane 4). The difference in uncomplexed pAkt with and without Rapamycin suggested that pAkt mediated mTor activation was significant in the simulations. The *in-vivo* kinetics of mTor phosphorylation were not directly constrained in the ensemble calculations. Rather, measurements of the Rheb-GTP/GDP ratio and the fraction of phosphorylated p70 were used to constrain mTor activation. p70 (also known as S6K) is a downstream target of mTor while Rheb-GTP directly activates mTor. The phosphorylation of p70 in serum starved A14 NIH 3T3 cells with/without insulin, wortmannin and rapamycin was captured (Fig. 3.4C, lane 2-4). However, the basal fraction of phosphorylated p70 (Fig. 3.4C, lane 1) was under-predicted by the model. Upstream of mTor/p70, the Rheb-GTP/GDP ratio with/without insulin, wortmannin or ra-

pamycin was also only partially constrained (Fig. 3.4A). The mean basal fraction of Rheb-GTP without insulin was consistent with observations (Fig. 3.4A, lane 1). However, the effect of insulin and insulin+wortmannin on the kinetics of the Rheb-GTP/GDP ratio was not well described (Fig. 3.4A, lane 2-3). Interestingly, the model was able to *predict* programming at the 4E-BPx-eIF4E node following H_2O_2 exposure (Fig. 3.4D, A1) and heat-shock (Fig. 3.4D, A2) in Chinese Hamster Ovary (CHO) cells [182, 163]. When taken together, these conflicting results suggested missing structural elements governing TSC1/2 heterodimer function and possible downregulation of phosphorylated p70 activity. The ensemble did not capture the dynamics of the Rheb-GTP/GDP ratio following insulin addition. However, the model did capture the steady-state behavior of several key nodes. Consistent with [^{32}P]-orthophosphate labeling studies without insulin in serum-deprived Mouse Embryo Fibroblasts (MEFs), the loss of TSC2 function led to increased Rheb-GTP (Fig. 3.5A). The agreement between simulation and experiment following TSC2 deletion suggested we were capturing the proper steady-state behavior of TSC1/2. The steady-state behavior of other key proteins upstream and downstream of TSC1/2 was also captured by the ensemble of models. Simulations of the ectopic expression of Akt, 4E-BPx or p70 with/without insulin exposure and Rheb overexpression in HeLa and A14 NIH 3T3 cells were compared with data as part of the ensemble calculation [165]. Ectopic expression was modeled by adding zero-order source and first-order degradation terms to the protein balance of interest. The ectopic expression and degradation rate constants were assumed to be the same for each protein explored. The steady-state phosphorylation of Akt, 4E-BPx and p70 with/without insulin was correctly captured by the model (Fig. 3.5A-C). Ectopic Rheb expression resulted in phosphorylated p70 in the absence of insulin

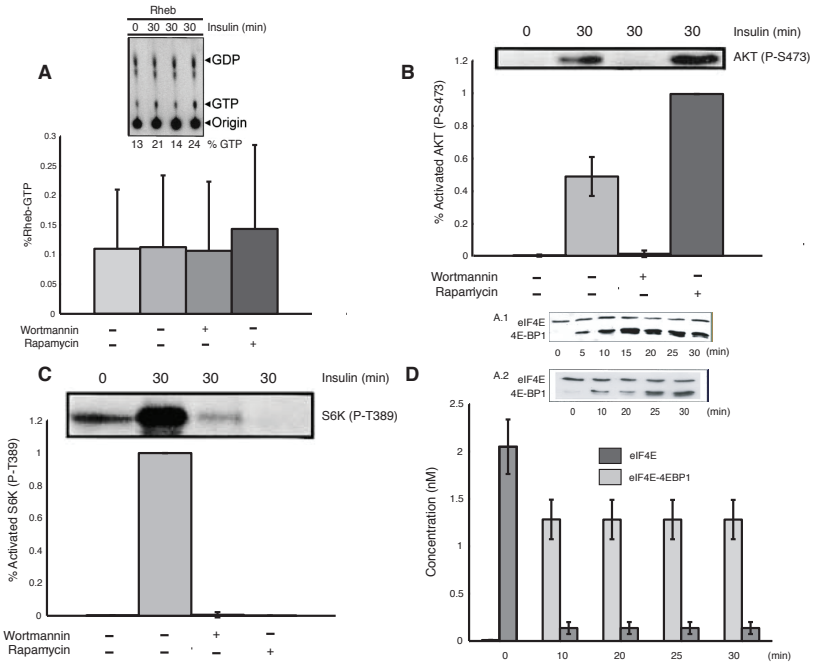

Figure 3.4: Comparison of model simulations with experimental data probing the time-dependent integration of insulin signals. All experimental data was taken from the study of Garami *et al.,* with the exception of D. All simulations were conducted over the entire parameter ensemble (N = 2552). The bars denote the mean fraction of activated (phosphorylated) target protein in the presence and absence of insulin and Wortmannin (PI3K inhibitor) or Rapamycin (mTor inhibitor). The error-bars denote one standard deviation over the ensemble. **A**: Comparison of the fraction of Rheb-GTP to Rheb-GDP following addition of insulin in the presence and absence of the translation inhibitors. **B**: Fraction of activated Akt following insulin addition in the presence and absence of the translation inhibitors. **C**: Fraction of activated p70 following the addition of insulin in the presence and absence of the translation inhibitors. **D**:Effect of physiological stress on 4E-BP1 and eIF4E binding.

(Fig. 3.5B). Phosphorylation of 4E-BPx with/without ectopic Rheb expression and insulin was also consistent with observations (Fig. 3.5C). However, the model only partially captured Akt (PKB) phosphorylation following Rheb expression with/without insulin (Fig. 3.5D, lane 3-4).

3.4.3 Monte-carlo Sensitivity Analysis of the initiation network shows the fragiltiy of Akt, mTOR and PI3K axis

Protein fragility was estimated based upon the sensitivity of the interactions a protein participated in and its connectivity (see Methods). If proteins were involved in several interactions with large sensitivity they had a high fragility score. Conversely, proteins involved in insensitive or only a few sensitive interactions were ranked lower. Protein fragility was computed over a sparse sampling of the parameter ensemble (N = 77) 5 min and 30 min after insulin addition (Fig. 3.6A and 3.6B). The fragility of some proteins was time-dependent. For example, proteins involved in receptor dimerization and adaptor complex assembly (Fig. 3.6A, green) and 80S assembly (Fig. 3.6A, black) were more sensitive during the early time-window. However, the fragility of translation regulators was time-invariant, Globally, the most sensitive proteins were regulatory proteins upstream of p70 activation (Fig. 3.6, red). Activated Akt, mTor, PIP3, TSC2/TSC2-complexes and Rheb-GTP were sensitive during both time periods following insulin addition. Activated Akt, mTor, PIP3, TSC2/TSC2-complexes and Rheb-GTP, all of which play a role in p70 activation of 4E-BPx phosphorylation, were sensitive during both time-periods following insulin addition (Fig. 3.6, red). To better understand the role of connectivity, we computed the aver-

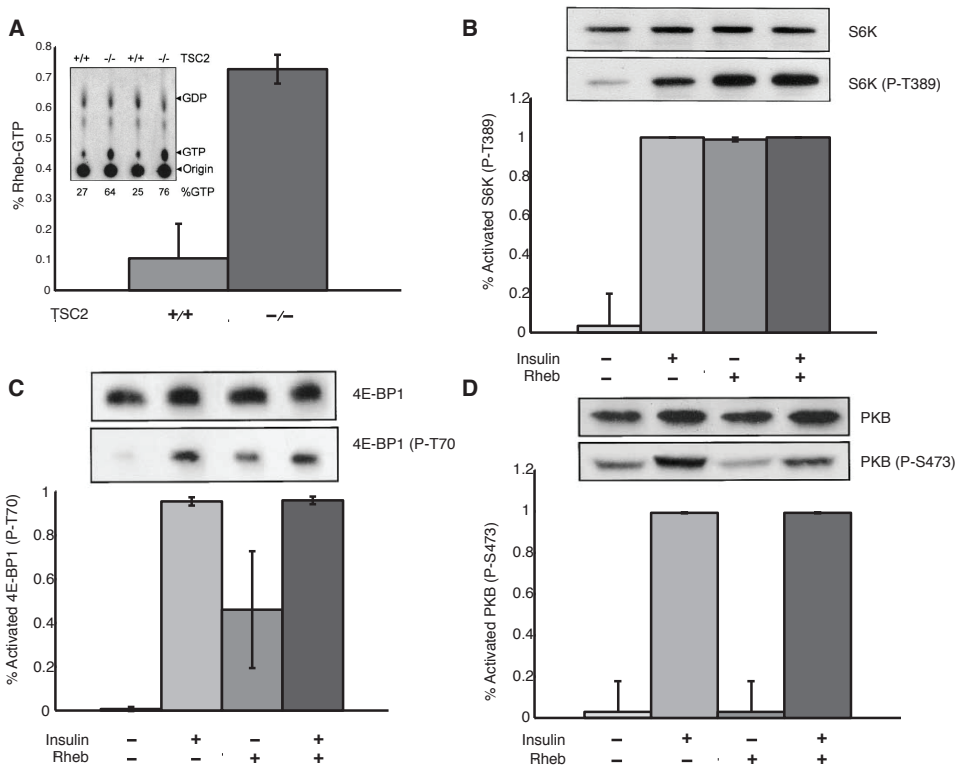

Figure 3.5: Comparison of model simulations with experimental data probing the steady-state integration of insulin signals. All experimental data was taken from the study of Garami *et al.*. All simulations were conducted over the entire parameter ensemble (N = 2552). The bars denote the mean fraction of activated (phosphorylated) target protein in the presence and absence of insulin and ectopic Rheb expression and the error-bars denote one standard deviation. **A**: Fraction of Rheb-GTP for TSC2 wt and knock-out MEFs. TSC2 knockout simulations were conducted by setting the initial TSC2 concentration and all source terms to zero. **B**: Fraction of activated p70 (S6K) in the presence and absence of ectopic Rheb expression and insulin. **C**: Fraction of activated 4E-BP1 in the presence and absence of ectopic Rheb expression and insulin. **D**: Fraction of activated Akt (PKB) in the presence and absence of ectopic Rheb expression and insulin.

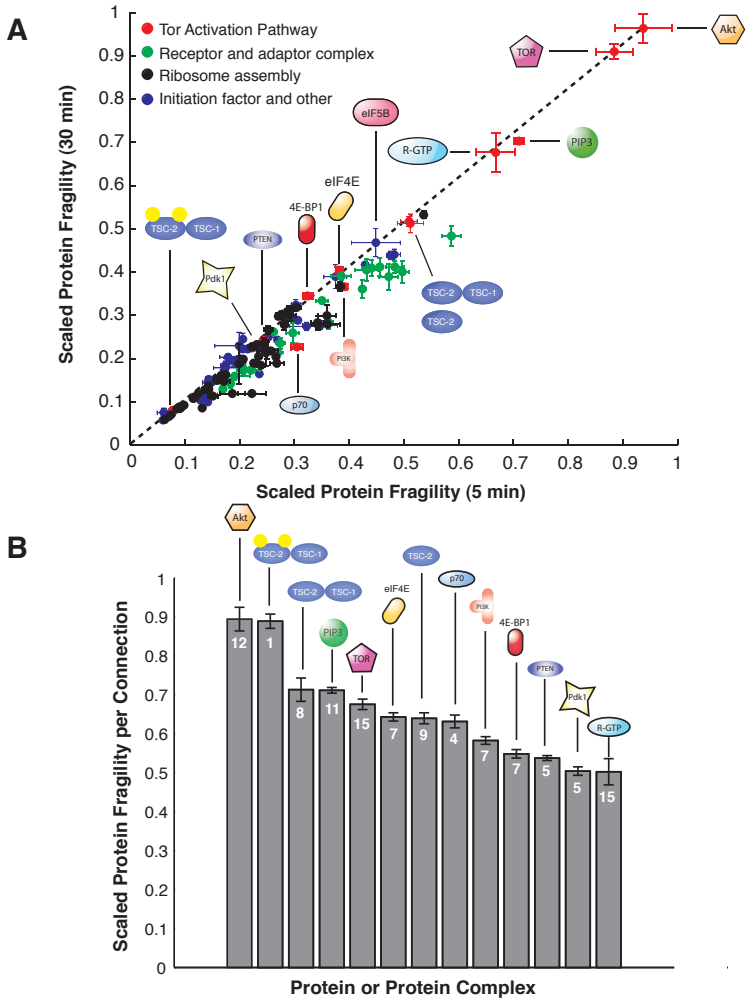

Figure 3.6: Sensitivity analysis of the initiation architecture. **(A)**. Estimated protein fragility in the initiation model calculated over a sparse sampling of the parameter ensemble (N = 77) for early (5 min) and late (30 min) time-windows following the addition of 100μM insulin. Overall State Sensitivity Coefficients (OSSCs) were used to estimate the scaled ranking of each interaction in the model from which the protein fragility was estimated. Points denote the mean value computed over the parameter sets sampled while the error bars denote one standard deviation. **(B)**. Estimated protein fragility normalized by the number of interactions per protein (indicated on bars) for the 30 min time-window. The bars denote the mean sensitivity calculated over a sparse sample of the ensemble (N = 77), error bars denote one standard ensemble deviation.

age protein fragility per connection for the mTor/p70 pathway (Fig. **??**B). On a per-connection basis, Akt was still the most sensitive protein in the initiation model. Akt was connected with 12 other proteins where each connection had an average ranking of approximately 0.90. mTor, which was connected with 15 other proteins, was ranked fourth with an average connection rank of 0.70. Rheb-GTP, with 15 interactions, was ranked last with an average connection rank of approximately 0.5. Thus, Rheb-GTP was estimated to be fragile largely because of its connectivity instead of its innate role in the network. Interestingly, pTSC1/2 and TSC1/2 were more sensitive on a per-connection basis than either mTor or Rheb-GTP. pTSC1/2 was not highly connected, however, its one connection (with Akt) was highly sensitive (scaled ranking of approximately 0.90).

3.4.4 Monte-carlo Coupling Analysis of the initiation network shows the difference in network operation with or without growth factors

The fragility of network components was further explored by coupling analysis. Coupling coefficients were computed over the entire parameter ensemble (see Methods). Protein knockdown analysis followed by k-means clustering segregated proteins into three groups with/without insulin (Fig. 3.7A and 3.7B, respectively). With insulin, the first group contained proteins whose knockdown resulted in null or positive changes in 80S formation (cluster I). All members of the second cluster were required to integrate insulin signals (cluster II). Lastly, the third cluster contained proteins strictly required for 80S formation (cluster

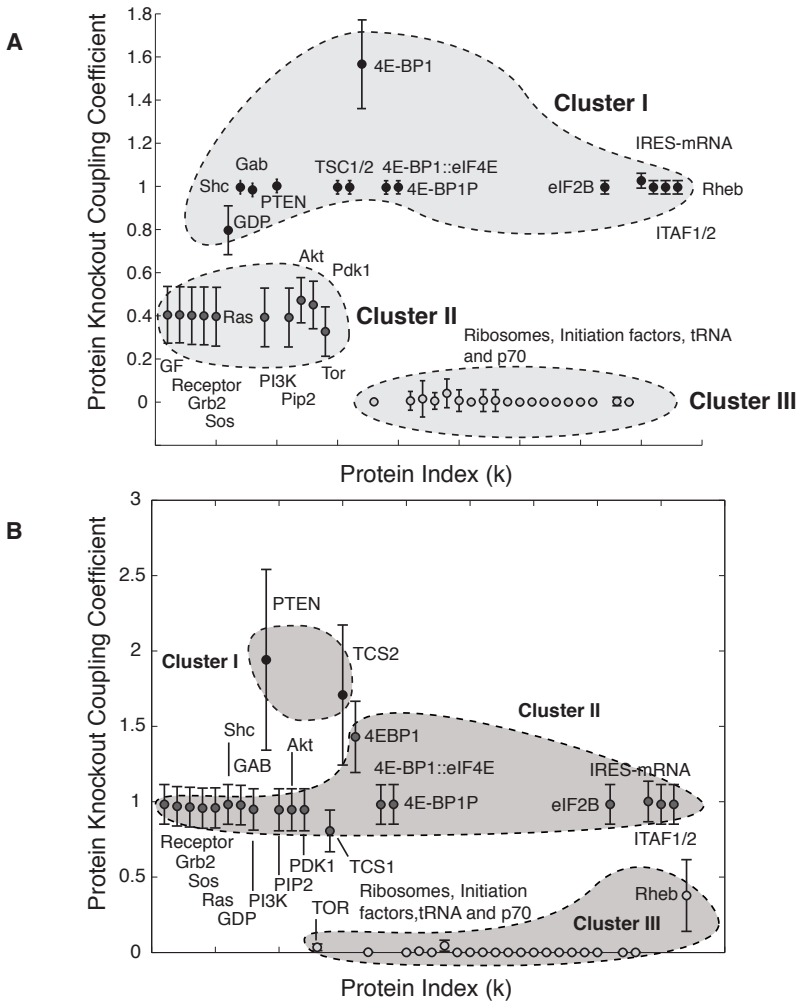

Figure 3.7: Knockdown coupling analysis of the translation initiation network. The protein knockdown coupling coefficient relative to nominal 80S complex formation was calculated for 43 different proteins over the parameter ensemble (N = 2552) following exposure to 200μM insulin for 6 hours. Coupling analysis was performed for the case when there was growth factor in the system (Panel A) and with no growth factor in the model (Panel B).

III). The knockdown of 14 proteins in cluster I had a limited or even a positive impact on 80S formation. In these cases, redundant interactions were available or the proteins were negative regulators of initiation. For example knockdown of 4E-BPx enhanced 80S formation by freeing eIF4E that would have otherwise

been bound. Knockdown of other proteins, such as PTEN, Rheb or TSC1/TSC2, were predicted to have a negligible effect on 80S formation following insulin addition. The minimal impact of the PTEN knockdown suggested the PIP2/PIP3 ratio was strongly in favor of PIP3 following insulin addition. Knockdown of Rheb and TSC1/TSC2 highlighted the existence of the redundant Akt-mediated route of mTor activation. Likewise, knockdown of the Shc and Gab adaptor proteins revealed a redundant dimerized-receptor/adaptor complex still capable of binding PI3K and catalyzing the formation of PIP3. Knockdown of proteins in cluster II, e.g., Akt and mTor reduced 80S formation to approximately basal levels and removed the ability to sense and integrate insulin signals. Decreased 80S initiation formation, following the knockdown of Akt and mTor, agreed with the sensitivity results, which predicted these proteins were fragile. In the absence of insulin, the regulatory connectedness of the initiation architecture was altered. Without insulin, most proteins were grouped similarly as the insulin positive case. However, key proteins such as PTEN, TSC2 and Rheb behaved differently (Fig. 3.7B). For example, a PTEN knockdown resulted in a two-fold increase in 80S formation without insulin. A TSC2 knockdown increased 80S formation by approximately 1.5 fold. Conversely, Rheb knockdown reduced 80S formation by approximately 60%.

3.4.5 *in-silico* overexpression studies of the initiation network reveals the roles of key initiation factors in conditions of with or without serum in the environment

In addition to knockdowns, the effect of overexpression of key proteins upon 80S formation was calculated with (Fig. 3.8A) and without (Fig. 3.8B) insulin. Again, coupling coefficients were computed over the entire parameter ensemble. Overexpression was modeled by adding a zero-order source and first-order degradation terms to each protein balance of interest, with the associated kinetic constants kept uniform throughout the model. In the presence of insulin, overexpression of 9 of the 33 proteins explored significantly influenced 80S formation (Fig. 3.8A). Statistical significance was established using a two-tailed student t-test assuming unequal variances. Overexpression of 4E-BPx, eIF1A and eIF5 in the presence of insulin reduced 80S formation to approximately 80% ± 11%, 70% ± 20% and 20% ± 10% of nominal levels. Conversely, overexpression of initiation factors (eIF4E, G, A, B and H) increased 80S formation by up to 1.5-fold with insulin. Without insulin, overexpression of initiation factors had almost no effect with the exception of eIF1A and eIF5. Overexpression of membrane phospholipid PIP3 or inactive regulatory proteins positively (mTor, TSC1, Rheb, p70, Akt and Pdk1) or negatively (TSC2, 4E-BPx) influenced 80S formation without insulin (Fig. 3.8B). On average the proteins explored were overexpressed by > 10-fold. While we are confident in the direction of coupling between 80S and proteins overexpression, the magnitude of the shifts in 80S could be dose dependent.

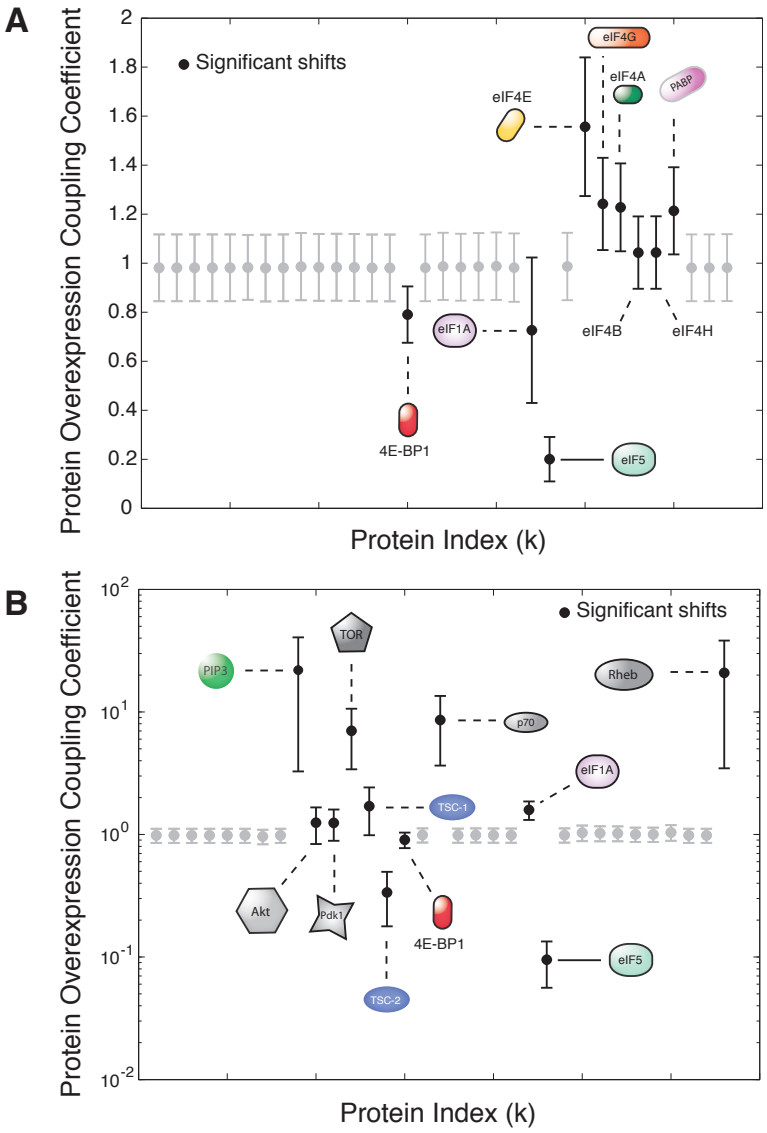

Figure 3.8: Overexpression coupling analysis of the translation initiation network with (**A**) and without (**B**) insulin. The protein overexpression coupling coefficient was computed relative to nominal 80S formation with and without insulin exposure (1hr 200μM). Thirty-three proteins were overexpresed where overexpression was modeled as a zero-order source term in the protein balance.

3.5 Discussion

Understanding the regulation of eukaryotic translation initiation could be an important step toward the development of novel anti-cancer drugs. In this study, we analyzed a model of translation initiation to better understand the role of key proteins like eIF4E. We estimated a family of model parameters by comparing simulations with 28 *in-vitro* and *in-vivo* data sets. We then analyzed the ensemble of initiation models to estimate qualitatively important regulatory and network features. Our analysis suggested that translation initiation was governed by a balance between two interconnected control programs. The first control element integrated growth-factor signals with the release of eIF4E thereby up-regulating translation. The second control element restrained initiation in the absence of stimulation by down-regulating the first loop and sequestering eIF4E. Sensitivity analysis, conducted over the parameter ensemble, suggested that Akt and mTor were structurally fragile and likely the key elements promoting the integration of growth factor signaling with initiation. The classification of Akt and mTor as sensitive was not a function of parameter values or time. Rather, it was a consequence of the network architecture. Interestingly, one of the components at the intersection of the two control programs, namely PIP3, was also estimated to be structurally fragile. The increased fragility of PIP3 versus the second element of the negative loop, 4E-BPx, suggested the balance between the promotion or restraint of initiation was controlled at the PI3K node, upstream of Akt and mTor. The PI3K/Akt/mTor pathway has long been known to be important in the oncogenic transformation of several tissues [172, 190]. Thus, our Akt/mTor results were consistent with the literature. Not suprisingly, sensitivity analysis also predicted eIF4E

was moderately sensitive given its role in the recognition of mRNA secondary structure. Overexpression of eIF4E is known to cause pro-survival pleiotropic effects and has been observed in several cancers including breast and prostate cancer [153, 125, 155, 156, 157, 158, 127, 191, 154]. The expression of several prominent proliferation and survival proteins e.g., cyclin D1, p27kip1, mdm2 and Bcl-2/Bcl-xL 9 (among others) are all translationally regulated, partly by eIF4E levels and its interactions with other initiation factors and proteins involved in translation initiation [153]. However, more studies to estimate the relative role of translation deregulation versus other factors such as transcriptional events or deregulated apoptosis should be conducted. Moreover, we expect that there are un-modeled effects that could influence our analysis results. For example, Akt is integrated into many cellular subsystems, including cell-survival pathways [172].

A limitation of sensitivity analysis is its inability to estimate the operational implications of structural or environmental perturbations. For example, eIF4E, 4E-BPx and PTEN were all predicted to be only moderately sensitive in the presence of insulin despite their key roles in initiation, as suggested by literature. However, we know from literature that structural perturbations involving these proteins e.g., overexpression of eIF4E or deletion of PTEN are common in several human cancers [153, 192]. In this study, we directly estimated the functional relationship between structural perturbations and initiation network operation using coupling analysis. Previously, coupling analysis has been used in several studies to understand the role of components in complex networks [193, 194]. We considered the coupling between the deletion/overexpression of network proteins and 80S formation with/without insulin. Our coupling analysis generated insight into the regulatory connectedness of the initiation

network as a function of growth factor as a driving force. The relationship between perturbed proteins and 80S formation was classified as either durable, perturbation-dependent, or growth factor dependent. For example, knockdown of Akt and mTor, consistent with the sensitivity analysis, removed the ability to up-regulate initiation with/without insulin. However, overexpression of inactive Akt and mTor increased 80S formation without insulin but resulted in no change in 80S with insulin present. Other notable examples include 4E-BPx, eIF4E and PTEN. For example, 4E-BPx was found to be a durable negative-regulator of 80S formation independent of perturbation or growth factor status. Overexpression of 4E-BPx with/without insulin reduced 80S formation albeit with different degrees of reduction. Conversely, knockdown of 4E-BPx increased 80S formation by approximately 1.5-fold with and without insulin. 4E-BPx shRNA studies in hypoxic Rh30 rhabdomyosarcoma cells confirm increased translation of markers such as cyclin-D1 following 4E-BPx knockdown [195]. The coupling between other proteins and 80S formation was depended upon the presence/absence of insulin or the type of structural perturbation. For example, knockdown of eIF4E was predicted to remove the ability of the network to form 80S with/without insulin. This finding was consistent with an earlier study showing that anti-sense knockdown of eIF4E disrupted the proliferation and morphology of HeLa cells [196]. Conversely, overexpression of eIF4E increased 80S formation by approximately 1.5-fold with insulin. The predicted increase in translation following eIF4E overexpression was consistent with the oncogenic role of eIF4E in immortalized cell-lines, primary tissue and patients [153]. Interestingly, eIF4E overexpression led to only a negligible 80S increase in the absence of insulin. Ectopic 4E-BP1 expression rescued tumorigenic 3T3 cells that overexpressed eIF4E, suggesting the ratio of free eIF4E to 4E-BPx is

a critical parameter controlling initiation [197]. Comparison of the simulation results with the 3T3 studies suggested that 4E-BPx levels in the model were sufficient to sequester free eIF4E. PTEN deletion had little effect in the presence of insulin but increased 80S exposure by 2-fold when insulin was absent. PTEN is an established negative regulator of PI3K signaling [198]. Moreover, PTEN mutations have been observed in a spectrum of cancer types [199]. In the presence of insulin the activity of PTEN was predicted to be overwhelmed by PI3K. Thus, a PTEN knockdown, in the presence of growth factors, resulted in little or no change to 80S because the network was programmed to promote initiation. However, a PTEN knockdown in the absence of insulin removed the ability of the network to downregulate Akt and mTor activation. If PIP3 is present in sufficient quantity in a PTEN mutant, Pdk1 and Akt could become activated allowing 80S complex formation in the absence of growth factors. Thus, the inability to modulate the level of PIP3 as a function of condition could be an important factor for malignant transformation. When taken together, the coupling results demonstrated the multifaceted nature of initiation regulation. Sensitivity analysis using a sparse sampling of the ensemble suggested structurally important proteins in the presence of insulin. Coupling analysis expanded our understanding of these proteins and provided a detailed portrait of the relationships between network nodes and 80S formation.

Sensitivity and coupling analysis using the ensembles of mechanistic models could be used to robustly rank-order the therapeutic value of molecular targets. Coupling coefficients describing conditions under which the network will fail could provide therapeutic insight. For example, knockdown of eIF4E was predicted to remove the ability of the network to form 80S with/without insulin. This finding was consistent with an earlier study showing that anti-sense

knockdown of eIF4E disrupted the proliferation and morphology of HeLa cells [196]. Recently, Soni *et al.* demonstrated the potential therapeutic effectiveness of targeting eIF4E in breast cancer, including in triple-negative (estorgen receptor/progesterone receptor/HER2) cancer cells [200]. Coupling analysis could also be used to generate falsifiable hypotheses regarding the role of network proteins. For example, 4E-BPx was found to be a durable negative-regulator of 80S formation independent of perturbation or growth factor status. 4E-BPx shRNA knockdown studies in hypoxic Rh30 rhabdomyosarcoma cells confirm increased translation of eIF4E-sensitive markers such as cyclin-D1 [195]. Conversely, ectopic 4E-BP1 expression reduced tumorigenic 3T3 cells [197]. For other proteins coupling dependend upon the presence/absence of growth factors or the type of structural perturbation. In these cases shifts in coupling gave insight into the role of a protein under different conditions. For example, the deletion of PTEN, an established negative regulator of PI3K signaling [198], had little effect in the presence of stimulation but increased 80S exposure by 2-fold when growth factors were absent. This suggests that PTEN activity in the presence of growth gactors may be overwhelmed by PI3K. However, a PTEN malfunction in the absence of stimulation could be a potentially important route on oncogenic transformation. Indeed, mutation in PTEN have been observed a spectrum of cancer types [199]. When taken together, these results support the use of mechanistic models to better understand the functional components of molecular networks relevant to human health. Perhaps, they are a first realizing the vision of Kitano who has suggested that insight into the fragility of networks could lead to new paradigms for drug discovery and the understanding of disease processes [68].

The translation architecture was assembled from an extensive literature anal-

ysis, however, they are likely missing model features. First, mTor was assumed to be activated and function in the absence of binding partners such as Raptor and LST8/GβL. The regulation of these binding partners and their role on mTor function needs to be explored. Moreover, Akt is integrated into many cellular subsystems, including cell-survival pathways [172]. Thus, we should reexamine the role of the Akt including these factors. Second, the activation of p70 by mTor was described as a single irreversible phosphorylation event at T-389. *In-vitro* studies support the phosphorylation of p70 at T-389 by mTor [201]. However, the *in-vivo* regulation of p70 may be far more complex with at least 12 distinct phosphorylation sites [202]. Proteins other than mTor may also play a role in p70 activation. For example, the PDK1 protein has been shown to phosphorylate p70 at T-229 both *in-vitro* and *in-vivo* [203]. It has also been hypothesized that perhaps mTor indirectly regulates p70 through secondary phosphatases [204]. Third, we modeled the regulation of 4E-BPx as a single phosphorylation event where phosphorylated 4E-BPx was unable to bind to eIF4E. In reality, 4E-BPx family members, such as 4E-BP1, have several phosphorylation sites [205] and the release of eIF4E is driven only after multiple conserved phosphorylation events [186]. In addition, eIF4E itself is phosphorylated at S-209 by MMK. While there is agreement that the phosphorylation of eIF4E does have a regulatory significance, the data is contradictory as to whether it is positive or negative [206]. Fourth, a generalized model of surface receptor activation, akin to the Epidermal Growth Factor Receptor (EGFR) family, was used in the study. Currently, the binding of extracellular ligands to transmembrane surface receptors promotes dimerization and the formation of multimeric adaptor complexes. These complexes composed of proteins such as Shc, Grb2, Ras and SoS promote the attachment and activation of Phosphoinositide 3-Kinase (PI3K). While we consid-

ered the formation of two independent adapter complexes, we did not include other types of growth factor sensitive receptors, e.g.. Platelet-derived Growth Factor (PDGF) receptors which signal by different mechanisms [44].

Lastly, the regulation and activity of phosphatases that down-regulate initiation after excitation need to be included in the model. This could involve adding new proteins to the network or updating the functionality to current proteins. For example, PTEN is known to dephosphorylate activated Platelet-derived Growth Factor (PDGF) receptors and attenuate their activity, a class of feature not included currently [207].

CHAPTER 4

ARSENIC TRIOXIDE (ATO) COOPERATES WITH ALL TRANS RETINOIC ACID (ATRA) TO ENHANCE MAPK ACTIVATION AND DIFFERENTIATION IN HUMAN MYELOBLASTIC LEUKEMIA (HL-60) CELLS

4.1 Abstract

Arsenic trioxide (ATO) synergistically promotes retinoic acid (RA)-induced differentiation of HL-60 myeloblastic leukemia cells, a PML-RARα negative cell line. In PML-RARα positive myeloid leukemia cells, ATO is known to cause degradation of PML-RARα with subsequent induced myeloid differentiation. We find now that ATO by itself does not cause differentiation of the PML-RAR? negative HL-60 cells, but enhances RA's capability to cause differentiation. RA-induced differentiation of HL-60 cells is known to be propelled by an induced hyperactive/persistent MAPK signal. ATO augmented RA-induced RAF/MEK/ERK axis signaling and expression of CD11b, an integrin receptor that is a myeloid differentiation marker. p47^{PHOX}, a component of the respiratory burst machinery and inducible oxidative metabolism, a functional differentiation marker, were also enhanced. However, ATO did not enhance RA-induced CD38 expression, an early cell surface differentiation marker. ATO enhanced RA-induced population growth retardation without evidence of apoptosis or an enhanced G1/0 growth arrest. But compared to RA, ATO plus RA showed reduced pAKT, suggesting that an overall biosynthetic/metabolic retardation was seminal to the apparent enhanced growth retardation due to ATO. In sum, our results indicate that ATO can augment the action of RA in causing

differentiation of myeloid leukemia cells through promoting MAPK signaling and independent of PML-RARα.

4.2 Introduction

Arsenic has historically been used as a medicinal agent for a variety of diseases such as psoriasis, eczema, asthma, malaria, ulcers, syphillis and leukemia. Arsenic and its derivatives have been used as antiseptics, antispasmodics, antipyretics, sedatives and tonics etc., especially in traditional Chinese medicine [208]. The most popular compound of Arsenic used in medicine is Arsenic Trioxide. Arsenic Trioxide (As_2O_3) or ATO is the active ingredient in the Fowler's solution developed in 18^{th} century and has been used to treat different malignancies for over a 100 years. In 1930s, before the introduction of chemotherapy and radiation therapy, arsenic was used as one of the standard treatments for chronic myeloid leukemia and other leukemias [208, 209]. Modern use of arsenic trioxide as a therapy for Acute Promyelocytic Leukemia (APL) started in China in 1990s [210]. In a study at the Shanghai Institute of Hematology (SIH) in 1999, patients with relapsed APL were treated with Arsenic Trioxide (ATO). Complete remission (CR) was achieved in 9/10 of the cases treated with ATO alone and 5/5 cases treated with ATO with chemotherapy (CT) or Retinoic Acid [210, 211, 212]. This suggests that ATO is potent as a single agent in APL. This was further proved by relatively high 2- and 3-year Disease Free Survival (DFS) rates seen recently in newly diagnosed leukemias also[213].

All Trans Retinoic Acid (ATRA) has been used as an inducer of differentiation therapy in APL cell lines since early 1980s [214, 215]. A recent clinical study of APL treatment with ATRA differentiation therapy in Japan resulted in

a complete remission (CR) rate of 94% and a 6-year Disease Free Survival rate of 68.5% and a 6-year overall survival (OS) rate of 83.9% [216]. Clinical studies performed for combination treatment of ATRA-ATO and ATRA alone in APL have revealed that the time required to achieve complete remission (CR) was statistically significantly different (25.5 days) than the ATRA treatment alone (40.5 days) or ATO treatment alone (31 days). The median disease free survival (DFS) rate had also increased to 20 months for the combination treatment as compared to ATRA alone (13 months) and ATO alone (16 months) [217]. Also, the disease burden, determined by fold change in PML-RARα was much shorter in the combination treatment as compared to monotherapy. Clinical studies thus show a synergistic effect of ATRA and ATO treatments, providing us with the motivation to probe the cause of this synergy at a biochemical level.

HL-60 is a myeloblastic leukemia cell line which serves as a model for differentiation therapy in cancer. HL-60 cells can undergo myeloid or monocytic differentiation along with G0/G1 growth arrest when treated with different inducers such as All Trans Retinoic Acid (ATRA) or 1-25-dihydroxyvitamin D3 (Vitamin D3) respectively. Previous studies in our lab have showed that ATRA induced differentiation and accompanying G0/G1 cell arrest is caused by sustained activation of proteins in the MAPK proteins [218, 219]. Various cell surface markers such as CD38, CD11b as well as functional markers such as inducible oxidative metabolism are seen to be enhanced as the cells proceed to their differentiation states.

HL-60 is negative for t(15:17), a hallmark of APL and lacks the PML-RARα fusion protein. However, it still undergoes differentiation when induced with agents such as ATRA, D3 etc. with enhanced MAPK activation being a necessary condition for differentiation. Buoyed by the synergy shown between ATRA

and ATO in clinical setting, in this study we tested the following hypothesis. If ATO's ability to promote differentiation is solely through the degradation of PML-RARα fusion protein, as seen in typical APL cell lines such as NB4 cells we should not see any enhanced differentiation in the combination treatment of ATRA and ATO. However, if in HL-60 the mechanism of ATO action impinges upon the mechanism of ATRA induced differentiation, e.g., by promoting sustained activation of MAPK, then addition of ATO to ATRA treatment should lead to augmented differentiation in HL-60 cells.

To test this hypothesis, we looked at well-established markers of differentiation and cell-cycle arrest to elucidate the role of cooperative synergy in the RAF/MEK/ERK axis of the MAPK pathway. Our investigations using low doses of ATO revealed that HL-60 cells treated with a combination of ATRA and ATO show augmented differentiation propelled by an enhanced activation of sustained MAPK proteins. Although MAPK proteins showed an increased activation, there was no such additive increase seen in their expression levels. This suggests that the synergy is at a protein interaction and phosphorylation level, not at a transcriptional level. Also, there was no similar cooperative increase seen in percentage of cells undergoing cell-cycle arrest. Additionally, it was seen that ATO alone treatment did not lead to differentiation in HL-60 cells, as shown before [220]. This study establishes that enhanced differentiation in case of combination treatment of ATRA-ATO is a result of increased sustained activation of MAPK proteins in HL-60 cells. Since ATO is already FDA approved (Trisenox ®), along with ATRA differentiation treatment for APL, we believe a more thorough understanding of its mechanism of action, especially on the MAPK proteins and related pathways will help in duplicating success in various other leukemias, or even non-hematologic cancers.

4.3 Methods and Materials

4.3.1 Cell Culture

HL-60, Human Leukemia Myeloblastic cells were grown in RPMI 1640 media supplemented with 5% heat-inactivated fetal bovine serum (Invitrogen, Carlsbad, CA, USA) in a 5% CO_2 humidified environment at 37°C and were maintained in an exponential growth phase. All the experimental cultures were initiated at a density of 0.2×10^6 cells/mL [221]. Cell viability was monitored by Trypan Blue Stain (Invitrogen) and it consistently exceeded 95%.

4.3.2 Reagents Used

All Trans Retinoic Acid (ATRA) (Sigma-Aldrich, St. Louis, MO, USA) and dissolved in 100% ethanol solution to a stock concentration of 5 nM. The concentration of ATRA used in cultures was 1 μM. Arsenic Trioxide (ATO) (Sigma-Adlrich) was diluted in water to a stock concentration of 5 nM. ATO was used at a final concentration of 2 μM, and was added at the same time as ATRA to the cultures. Anti-bodies for SDS-PAGE analysis against ERK1/2, phosphorylated ERK-1/2 (Thr-202/Tyr-204), MEK1/2, phosphorylated MEK1/2 (Ser-217/221), RAF1, phosphorylated Akt (Ser-473), phosphorylated Akt (Thr-308), PARP, $p47^{PHOX}$ and GAPDH were obtained from Cell Signaling (Beverly, MA, USA). PD98059 was added 16h before addition of ATRA and ATO to make its concentration in culture to be 1 μM. It was also re-added along with ATRA and ATO (at 0h) and finally at 16h after the addition of ATRA and ATO. The detailed procedure for addition of PD98059 has been explained here [218]. Antibody against

phosphorylated c-RAF1(Ser-621) was ordered from BIOSOURCE/Invitrogen.

4.3.3 Procedure for preparing Total Cell Lysates, Nuclear Fraction and Western Blots

Total cell lysates were prepared as follows. Cells were harvested at 24h and 48h time points and washed with PBS and centrifuged three times to wash away any culture medium. After washing away the media, cells were resuspended in 100 μl M-Per Mammalian Protein Extraction Reagent (Invitrogen) buffer mixed with a phosphatase and protease inhibitor. Western analysis of Akt phosphorylation was done on the nuclear fraction. The nuclear fraction was prepared by re-suspending the cells after centrifugation for 10 min in 100 μL of hypotonic propidium Iodide, sodium citrate (50 μg/mL propidium iodide (PI), 1 μL Triton-X100 and 1 mg/ml sodium citrate) solution. The cells were vortexed and kept on ice for 15 min, and the procedure was repeated 3 times. Nuclei were collected by centrifugation for 10 min, resuspended in 100 μL/sample RIPA buffer (Thermo Scientific, Rockford, IL USA) and freeze-thawed 3 times. Finally, the lysate was centrifuged (16060 x g) for 30 min and the supernatant was collected. Western analysis was done by resolving the lysates on 12% Tris-HCL gels (Bio Rad) and the membrane was blocked overnight with 5% w/V non-fat milk. The membrane was then probed using primary and secondary antibodies described in the Reagents section.

4.3.4 CD38 and CD11b Expression Studies by Flow Cytometry

At the 24h and 48h time points, 0.5×10^6 were collected, pelleted and resuspended in 100 μL PBS containing 5μL allophycocyanin(APC)-conjugated CD11b and 5μL of phycoerythrin(PE)-conjugated CD38 antibody. The cells were then incubated for 1 hr in a humidified atmosphere of 5% CO_2 at 37 °C and expression levels were measured in a BD LSR II flow cytometer. CD11b expression was measured by providing excitation by 633 nm red laser and collecting emission through a 735 long-pass dichroic and a 660/20 band-pass filter. For CD38 expression, excitation was provided by 488 nm laser and the emitted fluorescence was collected through a dichroic 550 long-pass and 576/26 band-pass filter. Gates to determine the shift in fluorescence intensity were set at the highest 5% of the control (untreated) cells.

4.3.5 Measurement of Inducible Oxidative Metabolism

Approximately 0.5×10^6 cells were collected at 48h, 72h time points, pelleted and resuspended in 200 μL PBS at 37°C containing 5μmol/L 5- (and 6)-chloromethyl-2′,7′-dichlorodihydro-fluorescence diacetate acetyl ester (H_2DCF, Molecular Probes) and 0.2 μg/mL 12-*O*-tetradecanoylphorbol-13-acetate (TPA, Sigma). H_2-DCF and TPA stock solutions were made in DMSO at concentrations of 0.2 mg/mL and 0.5 mg/mL respectively. Cells were incubated for 20 min in a humidified atmosphere of 5% CO_2 at 37°C. Flow cytometric analysis was done on a BD LSR II flow cytometer, using a 488 nm excitation laser and emission from oxidized DCF was collected through 505-nm long pass dichroic mirror and 530/30 nm band pass filter. The shift in fluorescence intensity in

response to TPA was used to determine the percentage of parent cells with the capability to generate inducible oxidative metabolites. Gates to determine percentage of positive cells were set at the highest 5% of the cells not treated with TPA.

4.3.6 Cell cycle analysis

About 0.5×10^6 cells were harvested at 72h by centrifugation and resuspended in 200 μL hypotonic staining solution (at 20°C) containing 50 μg/mL propidium iodide (PI), 1 μl Triton-X100 and 1 mg/ml sodium citrate. Cells were incubated at room temperature for 1 h and analyzed using flow cytometry (BD LSR II). Excitation was provided by a 488 nm laser and the emission was collected using 550 long-pass dichroic and a 576/26 band-pass filter.

4.3.7 Statistical Analysis

Statistical Analysis was done using MATLAB's statistical toolbox. Three independent repeats were performed in each case. Means of treatment cases were compared using paired-samples *t* test, using the `ttest2` function in MATLAB's statistical toolbox. The bar graphs show means of three independent repeats along with standard errors.

4.4 Discussion

In this report we studied the effect of ATO on ATRA induced differentiation in HL-60 cells. Earlier studies of biochemical effects of ATO treatment leukemia cells have concentrated on the PML-RARα protein and the Glutathione (GSH) redox system. In NB4 cells, ATO was seen to induce degradation of PML/RARα fusion protein, but not the mRNA in both retinoic acid sensitive and RA resistant cells lines [222]. ATO was also seen to affect the reorganization of PML and PML/RARα inside the nucleus in NB4 cells [222, 220]. Glutathione (GSH) redox system has also been known to be effected by Arsenic Trioxide (ATO) in various APL cell lines. The GSH redox system is an important component of cell's response to oxidative stress. Its function is to scavenge free radicals and neutralize the toxins in the cells. NB4 cells have the lowest levels of basal GSH and were found to be most sensitive to arsenic treatment. It was observed that in NB4 cells, ATO treatment modulated the GSH levels, which sensitized the cells towards apoptosis [223, 224]. In NB4 cells there is a dose dependent growth inhibitory, differentiation enhancing or apoptosis enhancing role of ATO, even though HL-60 cells were shown to be resistant to a treatment of ATO alone [225, 220]. Although the effects of ATO treatment has been studied in various APL cell lines, its mechanism of action is still not fully understood.

Clinically, a synergistic effect has been seen in the ATRA-ATO combination treatment, when compared with either ATRA or ATO monotherapies. We have tried to understand this synergy at a biochemical level, particularly in the MAPK pathway. Other studies for the biochemical effects of ATRA-ATO combination treatment have revealed additive effects in JNK/p38, TNF and cAMP/PKA pathways in APL cell lines[226, 227]. For e.g, in the cAMP/PKA

study, it was found that cAMP, which can induce monocytic differentiation in HL-60 cells was synergistically induced by ATRA and low doses of ATO [228, 227]. Our results showed that the combination treatment lead to an additive increase in molecular markers of differentiation such as CD11b and $p47^{PHOX}$. CD11b, a cell surface antigen, is a late stage marker of differentiation in HL-60 cells, which has been shown to be up-regulated with inducers such as Vitamin D3 and ATRA [229, 230]. $p47^{PHOX}$, on the other hand, is a part of the NADPH oxidase which catalyzes the ability to generate superoxides, a hallmark of neutrophils [231, 232]. Thus, an increased expression of CD11b, as seen by flow cytometry and $p47^{PHOX}$, as seen by SDS-PAGE analysis indicates enhanced differentiation in the combination treatment. Similar pattern of cooperative upregulation was observed in the measurement of inducible oxidative metabolism, as observed by generation of ROS in HL-60 cells. It is interesting to note that in these results, the ATO treatment behaved similar to the control (untreated) cells. This suggests that even though ATO is not able to induce differentiation on its own, it impinges on pathways responsible for ATRA induced differentiation, and modulates them to enhance the ATRA effect.

To understand the causes of this synergy we probed cellular pathways known to be affected by ATRA and looked for cooperative increase in them upon ATO treatment, starting with the MAPK pathway. Activation of RAF/MEK/ERK axis in MAPK pathway was seen to be enhanced synergistically in the combination treatment of ATRA and ATO. Increase in sustained phosphorylation of ERK1/2(Thr-202/Tyr-204) has been correlated with enhanced differentiation in HL 60 cells [219, 218]. We found that even though the activation of ERK1/2 (by phosphorylation) was enhanced by the combination treatment, there was no effect on expression of total ERK1/2 levels, either

in single treatments (ATRA and ATO), or in the combination treatments. We observed a similar trend in the activation of MEK1/2 (Ser-217/221), i.e., there was enhanced phosphorylation in the combination case but total MEK1/2 expression remained the same at 24h and 48h for all treatment cases. SDS-PAGE analysis of c-RAF and c-RAF(Ser621) followed the trend of enhanced activation and nearly constant expression levels. The activation and expression patterns of MAPK proteins suggest that the synergy between ATRA and ATO is at the protein-protein interaction level, rather than at the transcriptional level. This agrees with a recent systems level study which indicated that while the the effects of ATRA involved transcriptional remodeling ATO effects were seen at a proteome level, although the study was done for NB4 cells [226]. An intriguing result in our study was the slowing down of cell growth rate in treatments with ATO, without an increase in the percentage of cells arrested in G0/G1 phase. We hypothesized that the probable reason of low growth rate could be slowing down of proliferative process in the cell, which will elongate the cell cycle and hence decrease cell growth rate. To this end, we studied the phosphorylation of a key proliferative kinase Akt. Phosphorylation of Akt at Ser-473 and Thr-308 residues leads to activation of proliferative processes such as protein translation. SDS-PAGE analysis of phosphorylation of Akt(Ser473 and Thr308) revealed the combination treatment lead to lower phosphorylation, when compared with the control (intreated) and the ATRA treated case, especially at 48h. However, we did not see a similar reduction in ATO alone treatment, even though there was a growth rate reduction in that case. The reduction of pAkt phosphorylation seems to suggest a slow down on the translation machinery of the cell, since activated Akt plays a central role in the formation of the 80S translation initiation complex. However, this argument needs to be further explored as the effect of

ATO on other important regulators such as eIF4E, mTOR and p70SK needs to be clearly understood. Such studies, which aim to elucidate the role of ATRA in conjunction with ATO on the translation machinery of the cell form the basis of our future experiments on this topic. To understand this anomalous behavior in the ATO treated cells constitutes a part of our future work.

In sum, in PML-RARα negative HL-60 human myeloblastic leukemia cells, ATO causes MAPK signaling and augments ATRA-induced differentiation. The effects are more prominent as the MAPK signal augmentation increases, enhancing expression of later differentiation markers, but not the earliest, detected. A further potential contributor to the enhanced differentiation by ATO is the retardation of growth, possibly slowing down the self-renewal capacity of these progenitor cells and favoring differentiation. The results show that ATO may be of therapeutic use to augment the effects of ATRA.

4.5 Results

4.5.1 Arsenic Trioxide (ATO) leads to enhanced sustained activation of ATRA induced MAPK proteins

It is well known that transient activation of MAPK leads to proliferation, whereas a sustained activation of MAPK, especially ERK1/2 has been thought to drive differentiation in a variety of cell lines including HL-60 cells, [219, 218]. We investigated the effect of ATO in the sustained activation of MAPK, in order to better understand the biochemical effects of ATO. The most well characterized effect of ATO inside the cells is that on the glutathione (GSH) redox system.

GSH redox system is a critical modulator of cellular response to increase in oxidative stress. Action of ATO has been inversely correlated with levels of GSH or GSH-associated proteins with ATO treated cells showing low levels of reduced glutathione [233, 223, 234]. Previous studies have shown that addition of ATO in acute promyelocytic leukemia cells (NB4) cells leads to activation of stress-activated protein kinase, c-jun N-terminal kinase (JNK) [235]. This activation is directly related to apoptosis as inhibition of JNK was seen to reduce ATO induced apoptosis in NB4 cells. With regards to MAPK, the effect of ATO on p38MAPK has been widely studied, Verma *et al.*, showed that p38 is phosphorylated and activated by ATO in a sustained manner and that this activation is downstream of redox events activated by arsenic trioxide [236] in NB-4 cells. Activation of other MAPK proteins, such as Mkk 3 and Mkk 6 was also seen in NB-4 cells and in CML-derived KT-1 cell line, which was seen to be essential for p38MAPK activation.

We studied the effect of ATO on the RAF/MEK/ERK axis of MAPK signaling, in particular the potential synergistic effects of ATRA and ATO on these three central kinases. Treating cells with ATO plus ATRA enhanced the increase in phosphorylation at Thr-202/Tyr-204 and activation of ERK1/2 elicited by ATRA alone (Fig 4.1 (C)). This is seen in the comparison of Western blots of pERK1/2(Thr-202/Tyr-204) after 48 hrs of combination ATRA-ATO) treatment versus ATRA alone treatment. This enhanced activation was sustained and observed at both 24h and 48h. Interestingly, there was also increased activation of ERK1/2(Thr-202/Tyr-204) in the ATO alone treatment case compared to the control (untreated) case. The ATO induced increase could be compromised by addition of PD98059 (See Figure 4.1 (D)). Western analysis of ERK1/2 expression showed that there was no increase in the total expression of ERK1/2 in any

of the treatment cases. The expression levels of ERK1/2 were thus unaffected by treatment, although their activation increased.

Neither ATRA, not ATO or their combination seems to have an effect on the expression levels of ERK1/2, even though they increase its activation. Western blot analysis of other MAPK proteins showed similar results in MEK1/2 and RAF1. As seen in Fig. 4.1(B)., the combination treatment of ATO and ATRA lead to increased phosphorylation and activation of MEK (Ser-217/221), when compared with the ATRA treatment alone. Unlike ERK1/2 phosphorylation however, ATO treatment alone did not lead to an increase in phosphorylated MEK1/2 (Ser-217/221). SDS-PAGE analysis of the total MEK1/2 revealed that there is no effect of either ATRA or ATO treatment on its expression. These results suggest that the increase in phosphorylation of MEK1/2 in the combination treatment is solely due to increase in activation, and not due to increased expression of MEK1/2. Moving up the MAPK axis, we saw an increased phosphorylation of RAF1(Ser-621) residue, in both ATRA and ATRA-ATO combination treatments. As seen from Fig. 4.1(A), there is a synergy in the activation of RAF1(Ser-621) as the combination treatment of ATRA-ATO leads to more phosphorylation than the ATRA alone treatment.

It is interesting to note the ATO alone treatment did lead to an increase in p-RAF1(Ser621) and pERK1/2(Thr-202/Tyr-204) also, especially at 48h, when compared with the untreated (control) case, however this difference was not significant when compared with the ATRA alone treatment case. Having established enhanced activation of MAPK cascade in the combination treatment, we then proceeded to see if this augmentation translated to enhanced differentiation in HL-60 cells. Cells with ATO treatment alone did not show differentiation but a general decrease in growth rate. To investigate if combination treatment

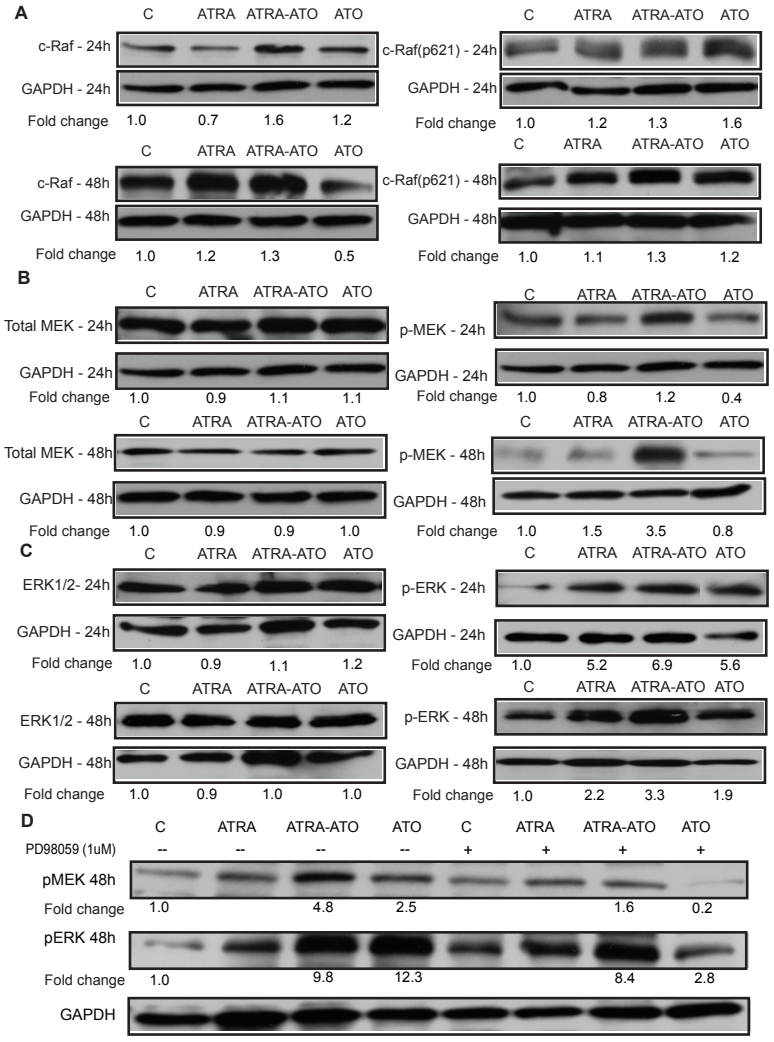

Figure 4.1: Western Blot analysis of MAPK proteins showed enhanced activation in the combination treatment of All Trans Retinoic Acid (ATRA) and Arsenic Trioxide (ATO), (ATRA-ATO) compared to ATRA treatment. (A), (B) and (C) show the effect of the different treatments on expression and activation levels of RAF1, MEK1/2 and ERK1/2 respectively. The left columns show the effect on expression levels at 24 h and 48h, whereas the right columns show the effect on activation of MAPK proteins. The lanes show control (untreated) cells, cells treated with ATRA, ATRA plus ATO, and ATO only. (D) shows the effect of adding MEK1 inhibitor (PD98059) on p-MEK and p-ERK at 48h time-point.

lead to enhanced differentiation we started by looking at the various cell surface markers of differentiation like CD38 and CD11b.

4.5.2 Arsenic Trioxide (ATO) enhances ATRA induced CD11b expression, but not CD38 expression

Having established enhanced activation of MAPK signaling in the combination treatment, we then proceeded to see if this augmentation translated into enhanced differentiation in HL-60 cells. A visual inspection of different treatments at 96h suggested that there was a synergy in the combination treatment which lead to enhanced differentiation. Figure 4.2 shows that there was an increase in the percentage of potentially differentiated irregularly shaped cells after the combination treatment compared to treatment with ATRA alone. Cells treated with ATO alone did not cause any apparent differentiation, but did exhibit a decrease in growth rate. To investigate if combination treatment lead to enhanced differentiation, we started by looking at the cell surface markers of differentiation, CD38 and CD11b.

CD38 is 45 kDa ectoenzyme receptor with a Retinoic Acid Receptor Element (RARE) in its first intron, which makes it responsive to ATRA [237]. CD38 is thought to be an activator of MAPK through activation of RAF, although the mechanism of its action is not fully understood. One possible mechanism is via the c-Cbl adaptor mechanism [238]. We measured expression of CD38 at an early time point (6 h) and at 24 h after various treatments using a PE-conjugated CD38 antibody. As seen in Figure 4.3, there was an increase in CD38 expression on treatment with ATRA as well as combination treatment of ATRA-ATO. There

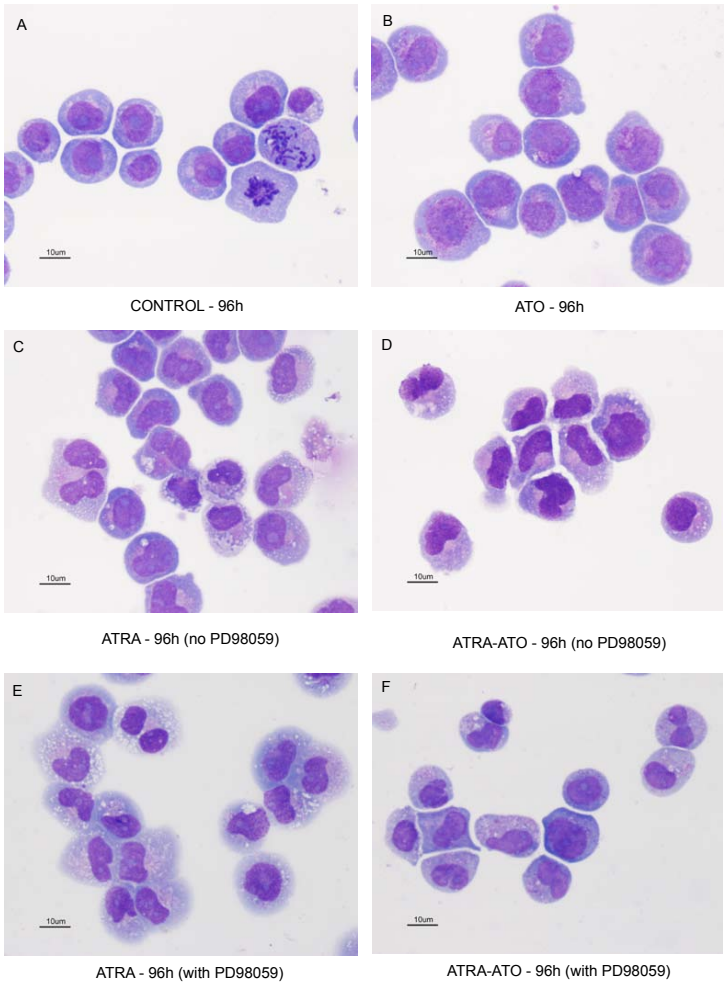

Figure 4.2: Change in cellular morphology induced by different treatments in the presence or absence of MEK1/ inhibitor PD98059. Wrights stained images showing morphological changes at 96h after different treatments are shown here. Panel A: In the control (untreated) case, mostly round cells were observed. Addition of All Trans Retinoic Acid (ATRA) lead to differentiated cells, seen here as the distorted cells (Panel C). Differentiation was more apparent in the combination treatment of ATRA and Arsenic Trioxide (ATO), whereas ATO alone treatment case shows a morphology similar to the control case, although a smaller number of cells are seen in this case (Panel D and B respectively). The effect of addition of MEK1 inhibitor PD98059 is seen in Panel E and F.

was no increase in CD38 expression in the case when cells were treated with ATO alone, when compared with the control case. There was no synergy seen in CD38 expression however, when we compared ATRA treatment with ATRA-ATO combination treatment at 24 h or at an earlier time point of 6h. These results suggested that ATO had no effect on CD38 expression, in combination with ATRA or by itself. Another cell surface marker, CD11b was used to measure the effect of Arsenic Trioxide (ATO) on ATRA induced cell differentiation. Measurement of CD11b expression was done by immunofluorescence using an APC-conjugated CD11b antibody. ATRA has been known to induce CD11b expression in HL-60 cells and other leukemic cell lines on its own [229, 230]. Effect of ATO on CD11b expression in HL-60 cells was determined by comparing expression levels in HL-60 untreated cells (control), cells treated with ATRA alone, cells treated with a combination of ATRA and ATO and cells treated with ATO alone. Measurements were taken at 48h and 74h time points using flow cytometry. Compared to untreated control cells, ATRA-treated cells showed an increase in CD11b expression, as expected. However, CD11b expression was consistently higher in the case of ATRA-ATO combination when compared with the ATRA alone case (Fig 4.3, Panel B). The difference between CD11b expression was statistically significant at both 48h ($p = 0.0006$) and 72h ($p = 0.016$), indicating that the differentiation machinery was affected by ATO during its both early and late stages. In contrast, the cells treated with ATO alone did not show an increase when compared with the untreated control case, indicating that ATO alone does not affect CD11b expression.

Increase in Reactive Oxygen Species (ROS) is one of the functional markers of differentiation. $p47^{PHOX}$ is one of the essential components of ROS generating machinery which gets activated in differentiated cells. We probed the effect of

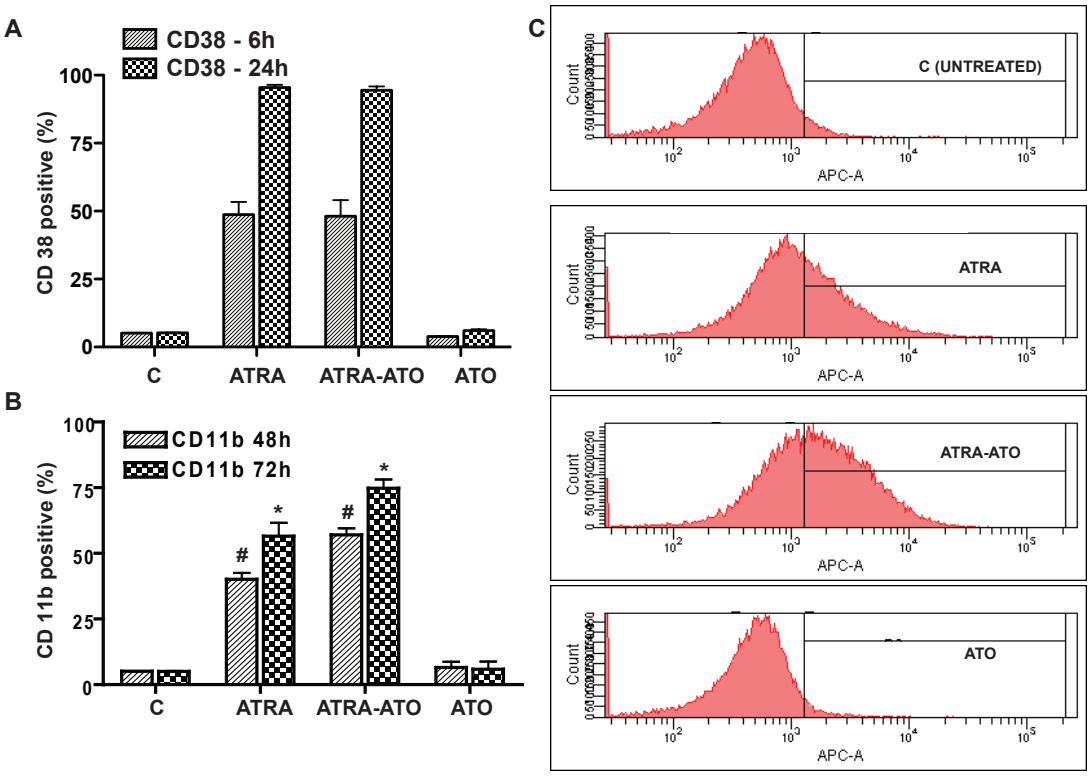

Figure 4.3: Arsenic Trioxide (ATO) enhanced ATRA-induced CD11b expression, but not CD38 expression. Panel A shows that there was no enhancement in CD38 expression in the combination treatment, but CD11b (Panel B) expression showed a synergistic increase in the ATRA-ATO combined treatment case. The y-axis shows percentage of CD38 positive cells (Panel A) and CD11b positive cells (Panel B) at indicated time points when compared with untreated cells with gates set to exclude 95% of the cells in the control case. (C) shows the representative CD11b histograms of untreated (control) and cells treated with ATRA, ATRA-ATO combination and ATO alone at 48h.

ATO on p47^{PHOX} to establish that it directly affects the differentiation machinery in HL-60 cells.

4.5.3 Arsenic Trioxide enhances ATRA induced differentiation by upregulating p47^{PHOX}

To determine whether the differentiation machinery is directly affected by the ATO treatment, we investigated the effect of ATO and ATRA on p47^{PHOX}. p47^{PHOX} is an essential component of the NADPH-oxidase complex which generates Reactive Oxygen Species (ROS) in neutrophils in response to agonists like phorbol-12-myristate-13-acetate (PMA) and Tumor Necrosis Factor (TNF) [239]. p47^{PHOX} is cytosolic, but upon its activation it translocates to the membrane where it acts as the scaffold for formation of the NADPH oxidase complex [231, 232]. Due to its central role in generating ROS, an increased amount of p47^{PHOX} is a indicator of a higher differentiated state of the cell. We analyzed and compared the expression of p47^{PHOX} in untreated cells (control), cells treated with ATRA, combination treatment of ATRA-ATO and ATO treatment alone. The control cells and ATO treatment alone cases did not show p47^{PHOX} at 24h or 48h (See Fig. 4.4). Consistent with the trend seen in activation of MAPK proteins, an enhanced expression was seen in case of the combination treatment as compared to ATRA treatment alone. Also, the difference in expression of p47^{PHOX} between ATRA and ATRA-ATO treatments was more prominent at 48h than at 24h. This result suggests that ATO synergizes with ATRA to directly affect the differentiation machinery in HL-60 cells, even though it does not seem to activate it on its own. Another interesting result was that we did not a signal

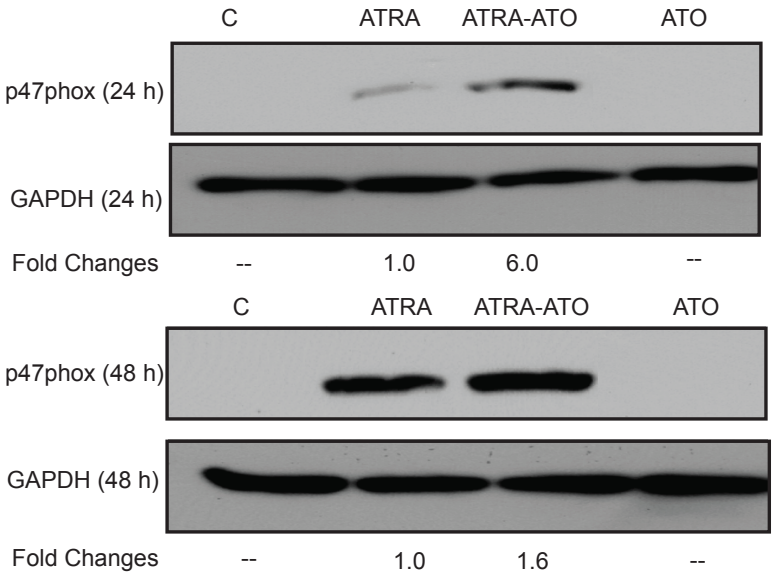

Figure 4.4: Arsenic Trioxide (ATO) leads to an increase in ATRA-induced expression in p47^{PHOX}. Western analysis of total expression of p47^{PHOX} is shown at 24h and 48h timepoints.

in the control (untreated) and ATO treatment alone. This corroborates with the results of the DCF assay which measured the inducible oxidative metabolism, a functional marker of terminal differentiation in HL-60 cells which showed that the ATO treatment alone did not lead to generation of ROS.

4.5.4 Arsenic Trioxide (ATO) enhances ATRA induced functional differentiation

To confirm the functional significance of the induced p47^{PHOX} expression, TPA inducible oxidative metabolism, a late functional differentiation marker that characterizes mature myelo-monocytic cells, was measured. When treated with

ATRA, HL-60 cells typically exhibit a functional inducible Reactive Oxygen Species (ROS) response. As before, cells were treated with ATO or ATRA alone or in combination. Inducible oxidative metabolism was measured by flow cytometry using 2',7'-dichloroduhydrofluorescein diacetate (H2DCFDA), a cell-permeant indicator of reactive oxygen species that is nonfluorescent until the acetate groups are removed by intercellular esterases when oxidation takes place within the cell. As shown by Fig 4.5 (A), HL-60 cells treated with a combination of ATRA-ATO showed increased functional differentiation at both 48h and 72h time-points when compared with cells treated with ATRA alone. For example, at 72h, 85.3 % of cells treated with ATO plus ATRA were able to produce ROS induced by TPA, compared to 60.9 % of cells treated with ATRA alone. The enhancement in ROS in case of ATO-ATRA was statistically significantly different than that of ATRA alone with 95% confidence ($p = 0.024$) at 72h. In the case of cells treated with ATO alone, there was no significant increase in ROS induction upon TPA treatment, indicating that ATO alone was unable to induce functional differentiation of HL-60 cells. This is consistent with the inability of ATO to induce the other differentiation markers measured. These results indicate that even though ATO by itself is unable to induce differentiation of HL-60 cells, it works synergistically to enhance ATRA induced differentiation. In the case of cells treated with ATO alone, there was no significant increase in DCF induction upon TPA treatment, suggesting that ATO alone was not able to induce differentiation in HL-60 cells. These results indicate that even though ATO by its own is not able to induce differentiation in HL-60 cells, it works synergistically to enhance ATRA induced differentiation. This result is consistent with the CD11b expression pattern seen in Fig. 4.3 which also showed enhanced ATRA induced expression upon ATO treatment.

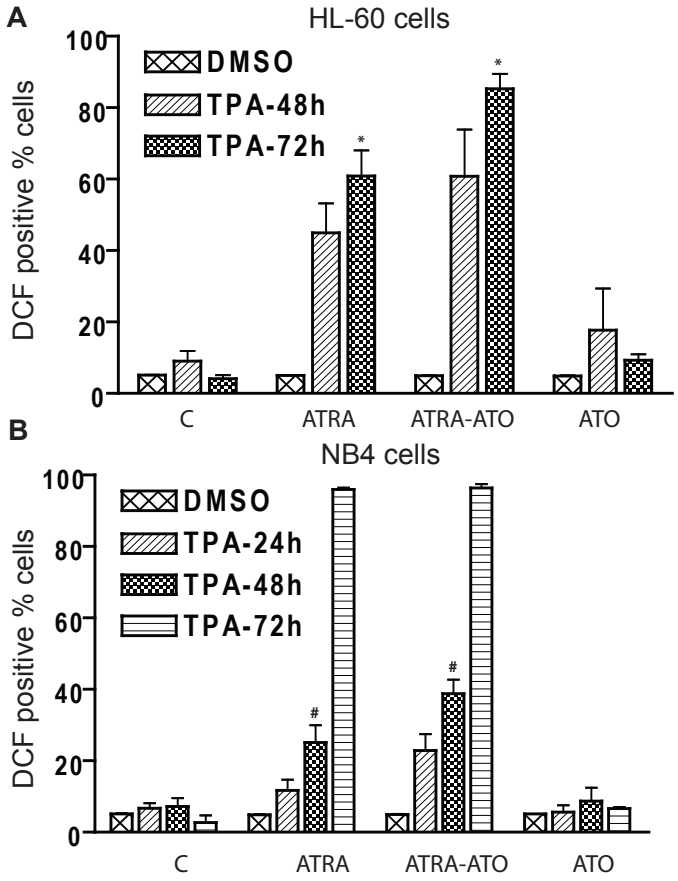

Figure 4.5: Arsenic Trioxide enhances ATRA-induced differentiation of HL-60 cells as well as NB4 cells. (A) shows the percentage of cells (y-axis) with capability for inducible oxidative metabolism at the indicated time points. Cells were treated with TPA to induce oxidative metabolism. The percentage of positive cells with TPA, when gates were set to exclude 95% of control cells (without TPA), is shown. There was no statistically significant difference in the percentage of differentiated cells in the ATRA alone versus ATRA-ATO combination treatments at 48h. However, at 72h the difference in DCF positive % cells was statistically significant between ATRA and ATRA-ATO combination treatment ($p = 0.024$). (B) shows the same for NB4 cells.

Similar enhancement in differentiation was obtained for NB4 cells in the combination treatment. There were some key differences however between the response of HL60 cells and NB4 cells. For e.g., NB4 cells showed much higher sensitivity towards ATO and massive apoptosis was observed in the cultures with ATO concentration more than 0.5 μM. Therefore a lower dose of ATO (0.5 μM) and ATRA (0.25 μM) was administered to NB4 cells in culture. This dosage was such as to preserve the ratio of ATRA to ATO same as that in HL-60 cells (2:1). Another difference in the response of the two cell lines was that almost 100% of the cells showed terminal differentiation at 72h in NB4 cells. Therefore, inducible oxidative mechanism was measured at earlier time points, i.e. 24h and 48h. An increase in terminal differentiation was observed at 24h and 48h in the combination treatment case, when compared to the ATRA alone case. Using a one-tailed t-test, we concluded that differentiation in the ATRA alone case was statistically less than that in the combination case at 48h ($p = 0.046$) (See Figure 4.5, Panel B). This result suggests that mechanisms involved in enhancement of differentiation in the combination are not HL-60 specific.

4.5.5 Arsenic Trioxide (ATO) leads to reduced growth in HL-60 cells

A persistent feature of HL-60 cells treated with Arsenic Trioxide (ATO) was their slower growth rates as compared with control (untreated) cells and All Trans Retinoic Acid (ATRA) treated cells. As seen from Fig. 4.5.5, addition of ATRA alone also decreased cell growth rate when compared with the untreated cells. However, addition of ATO had a more drastic effect on growth rate of cells than

ATRA, as cultures with ATO alone or the combination treatment of ATRA-ATO were seen to grow much slower than the cultures with ATRA alone. Microscopic images of the cultures at 72h showed differentiated cells in the ATRA and ATRA-ATO (Fig. 4.2) combination treatments, cells in the ATO alone cultures were not much different from the untreated cells morphologically. These results suggest ATO treatment alone, although leads to reduction in growth rate does not induce differentiation by itself. Three possible reasons for decrease in cell growth rates were hypothesized and tested, a decrease in cell growth rate could be due to apoptosis upon addition of ATO. Alternatively, an increase in the percentage of cells arrested in the G0/G1 phase could lead to overall decrease in cell growth rates or finally, an overall decrease in proliferative processes inside the cells could lead to a dilation of cell cycle and hence decrease in the cell doubling rates. We looked at phosphorylation of a key kinase Akt as a marker of metabolic processes inside the cell, cell-cycle assay using PI (Propidium Iodide) staining was used to measure the percentage of cells arrested in various treatments, whereas cleavage of PARP was used to determine the extent of apoptosis in various treatment cases.

4.5.6 Arsenic Trioxide dependent cleavage of PARP is abrogated by ATRA

To test our first hypothesis, i.e., if reduced growth rates are due to increased apoptosis, we looked at Poly (ADP)-ribose polymerase (PARP) cleavage. PARP acts as a molecular nick sensor and marks sections of damaged DNA for repair. PARP is a substrate for caspase-3 and caspase-7 which cleave it into two frag-

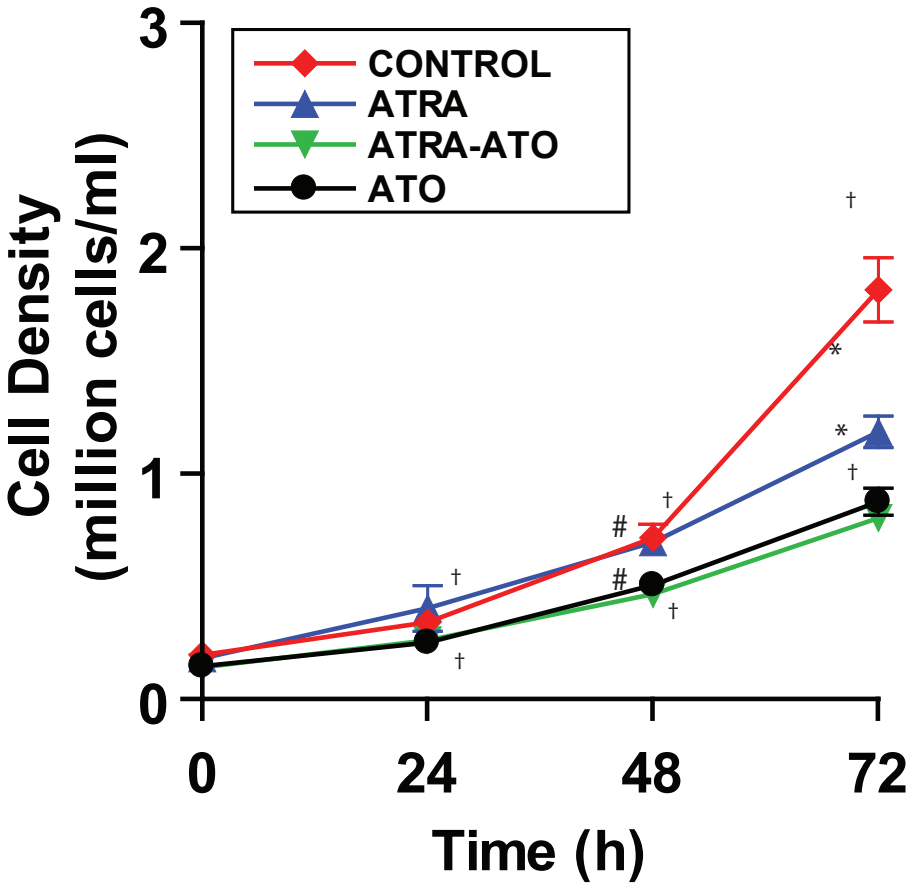

Figure 4.6: There is a decrease in cell growth rate upon addition of ATO. Cells growth rates were measured over a period of 72h after treatments. The cells were seeded at an initial concentration of 0.2 million cells/mL. Addition of ATRA also leads to decreased growth rate, however ATO addition has a more significant effect by itself or in combination with ATRA. # and *, the cell growth rates in ATO and ATRA-ATO combination treatment were statistically significantly different at both 48h ($p = 0.006$) and 72h ($p = 0.013$). †,

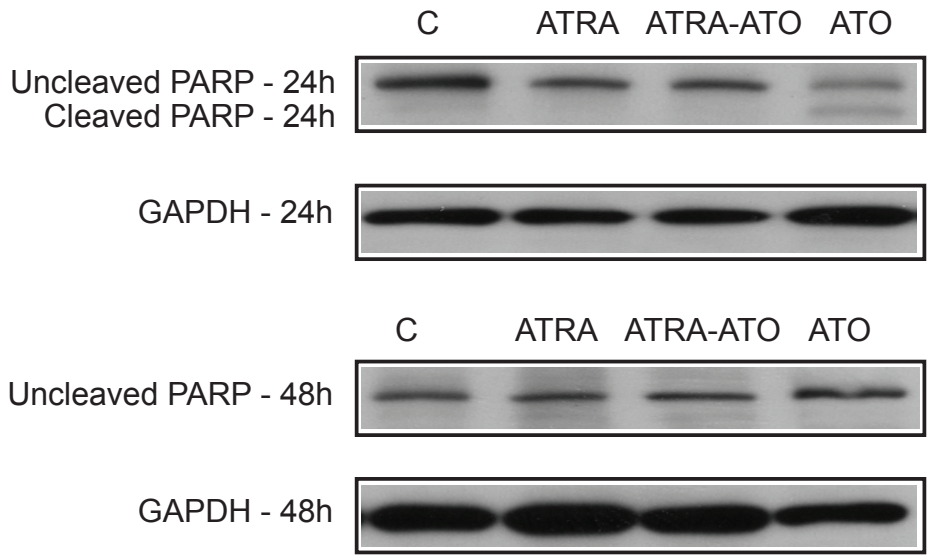

Figure 4.7: ATRA abrogates the apoptotic effect of ATO in HL-60 cells. Western analysis of cleaved and uncleaved PARP at 24 and 48 h is shown here. The different lanes are control (untreated) cells, and cells treated with ATRA, combination of ATRA-ATO, and ATO alone.

ments, a major fragment of 89 kDa and minor fragment of 24 kDa. Cleavage of PARP is a marker of proteolytic activity of caspase and measures progression of apoptosis. It has been shown that a high dose of ATO (10μM) leads to cleavage of PARP after 12h [240], which continues upto 24h in HL-60 cells and NB4 cells. In NB4 cells, a low dose (2 μM) ATO can lead to cleavage of PARP at 72h. However, it was also seen that chemical agents such as lipoic acid and N-acetylcysteine were able to block ATO induced cleavage of PARP and thus rescuing the cells from apoptosis, without affecting degradation of PML-RARα protein [223]. Figure 4.7 shows the SDS-PAGE analysis of the uncleaved and cleaved PARP. Our results suggest that there was some transient apoptosis in the ATO alone treatment case, but it did not continue at 48h. More importantly, we did not see apoptosis in the combination case of ATRA-ATO treatment. This

result shows that the effect of ATRA is to rescue cells from apoptosis caused by ATO. Thus we concluded that the decrease in growth rates in the combination treatment case is not due to death of cells. Next we tested if the decrease in growth rates was because of increase in the percentage of cells arrested in the G1/G0 phase using the Propidium Iodide (PI) cell-cycle arrest assay.

4.5.7 Arsenic Trioxide (ATO) did not accelerate ATRA induced cell-cycle arrest in HL-60 cells

ATRA treatment in HL-60 cells leads to myeloid differentiation as well as arrest of cells in G1/G0 phase. To determine the effect of Arsenic Trioxide (ATO) on cell-cycle arrest, the percentage of arrested cells was measured by flow cytometry in untreated (control) HL-60 cells, cells treated with ATRA, cells treated with ATRA-ATO combined and cells treated with ATO alone. Treatment with ATRA showed an increase in the percentage of cells arrested in G0/G1 phase, as seen before [229]. Treatment with ATO alone however, did not show an increase in the percentage of cells arrested as compared to the control case at 72h (see Fig. 4.8 (A)). The combination treatment also increased the percentage of cells arrested in the G0/G1 cell cycle phase. However, when compared with the ATRA induced cell-cycle arrest, the combination treatment did not lead to a statistically significant increase in the percentage of arrested cells. This indicates that the effect of ATO on cell-cycle arrest is minimal, both when acting alone or in combination with ATRA. The effect of ATO treatment on cell cycle arrest was studied at earlier time points also (24h and 48h, results not shown) and similar results were obtained. Thus, even though ATO treatment leads to enhanced

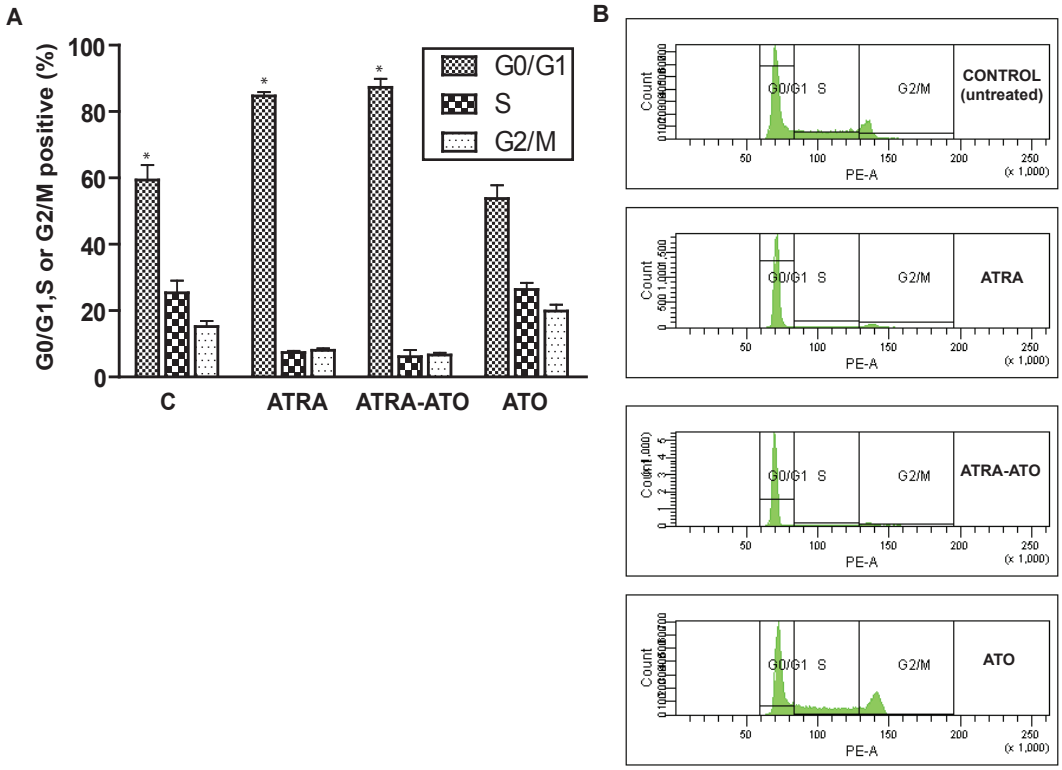

Figure 4.8: (A) Arsenic Trioxide did not accelerate ATRA-induced G0 arrest. The percentage of G1/G0, S and G2/M cells at 72 h after the treatment is shown for control (untreated), ATRA, ATRA-ATO combination treated and ATO alone treated cells. Y-axishere shows the percentage of cells in the different cell-cycle phases at 72h. *, treatment with ATRA or ATRA-ATO lead to statistically significant increase in percentage of cells in G1/0 w.r.t. control, as expected. (B) Representative DNA histograms for untreated (control) cells, cells treated with ATRA, cells treated with ATRA-ATO combination and cells treated ATO alone are shown at 72 h.

differentiation in HL-60 cells, our study indicates that it does not contribute to their arrest in the G0/G1 phase. Finally we tested our hypothesis that the reduced growth rate in ATO cells could be a result of overall slowing down of the proliferative mechanisms in the cells, leading to an increased cell cycle which would explain lower cell growth rate without an increase in apoptotic cells. To test this hypothesis we probed the activation levels of a key protein kinase, PKB or Akt which is involved in many important cellular signaling pathways related to growth.

4.5.8 Arsenic Trioxide (ATO) in combination with ATRA leads to decreased activation of Akt

The role of Akt phosphorylation (Ser-473/Thr-308) in cellular proliferation has been well documented [172]. In HL-60 cells, it has been shown that a constitutively active PI3K/Akt axis was responsible for resistance to ATO-induced apoptosis. Chemical inhibition of Akt activation was also seen to impart sensitivity to ATRA induced differentiation in HL-60 cells [241]. Previous studies have shown evidence of synergistic action between ATO and a flavinoid, quercetin in downregulating Akt phosphorylation in human leukemia cell lines such as U937 [242]. The cooperation between Quercetin and ATO was low in NB-4 cells, indicating that the synergy is cell-line dependent. We investigated the effect of the combination treatment of ATRA and ATO on Akt phosphorylation (Ser-473/Thr-308). As seen from Fig. 4.9, the combination treatment of ATRA and ATO leads to a decrease in Akt phosphorylation at both 24h and 48h. This decrease is seen at both the phosphorylation residues, Ser-473 and

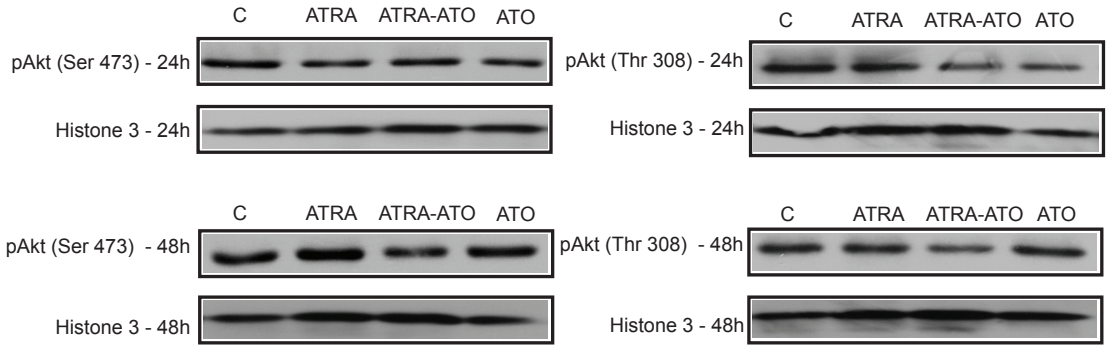

Figure 4.9: Arsenic Trioxide (ATO) in combination with ATRA leads to a decrease in the phosphorylation of Akt at the Ser-473 and Thr-308 residues. Western analysis of activation of Akt is shown here. (A) shows the activation at the Ser-473 residue whereas (B) shows the activation at the Thr-308 residues at 24h and 48h.

Thr-308, and is more prominent at 48h than at 24h. Since, we used only the nuclear fraction in Akt phosphorylation studies, Histone 3 was used as a loading control. Akt is a central kinase involved in many important cellular processes like proliferation, survival, growth as well as protein translation. For e.g., Akt upon phosphorylation and activation, activates mTOR which plays a key role in formation of the 80S translation initiation complex. Our results suggest that the due to reduction in Akt phosphorylation, there is a decrease in rates of proliferative processes in the cell leading to an overall decrease in cell growth rate. However, this result does not explain the fact that we saw a decrease in cell growth in the ATO alone treatment case without an apparent decrease in Akt phosphorylation, suggesting that there are other factors at play.

CHAPTER 5

MODELING AND ANALYSIS OF RETINOIC ACID INDUCED DIFFERENTIATION OF UNCOMMITTED PRECURSOR CELLS

5.1 Abstract

Manipulation of differentiation programs has therapeutic potential in a spectrum of human cancers and neurodegenerative disorders. In this study, we integrated computational and experimental methods to unravel the response of a lineage uncommitted precursor cell-line, HL-60, to Retinoic Acid (RA). HL-60 is a human myeloblastic leukemia cell-line used extensively to study human differentiation programs. Initially we focused on the role of the BLR1 receptor in RA-induced differentiation and G1/0-arrest in HL-60. BLR1, a putative G protein coupled receptor expressed following RA exposure, is required for RA-induced cell-cycle arrest and differentiation and causes persistent MAPK signaling. A mathematical model of RA-induced cell-cycle arrest and differentiation was formulated and tested against BLR1 wild-type (wt) knock-out and knock-in HL-60 cell-lines with and without RA. The current model described the dynamics of 729 proteins and protein complexes interconnected by 1356 interactions. An ensemble strategy was used to compensate for uncertain model parameters. The ensemble of HL-60 models recapitulated the positive feedback between BLR1 and MAPK signaling. The ensemble of models also correctly predicted Rb and p47phox regulation and the correlation between p21-CDK4 formation and G1/0-arrest following exposure to RA. Finally, we investigated the robustness of the HL-60 network architecture to structural perturbations and generated experimentally testable hypotheses for future study. Taken together,

the model presented here was a first step toward a systematic framework for analysis of programed differentiation. These studies also demonstrated that mechanistic network modeling can help prioritize experimental directions by generating falsifiable hypotheses despite uncertainty.

5.2 Introduction

A molecular understanding of proliferation and differentiation could lead to new treatments for cancer, spinal cord injuries or neurodegenerative disorders. However, the molecular basis of these fundamental programs has yet to be fully unraveled. To rationally reprogram these networks we must first understand their connectivity and regulation. One strategy toward this goal is to analyze the proliferation and differentiation behavior of a model system. Lessons learned in simple systems could perhaps inform analysis of more complex programs. One such model system for the study of differentiation is the lineage uncommitted human myloblastic cell line HL-60. HL-60 is an archetype *in-vitro* differentiation model studied since the late 1970's [243, 244, 245]. Depending upon the stimulus, HL-60 undergoes G1/0-arrest followed by either myeloid or monocytic differentiation. Retinoic Acid (RA) or Dimethyl Sufoxide (DMSO) causes G1/0-arrest and myeloid differentiation. On the other hand, 1,25-dihydroxy vitamin D3 (D3) or sodium butyrate causes arrest with monocytic differentiation. Stimuli such as RA or D3 drives MEK-dependent activation of the ERK1/2-MAPK pathway [218, 246, 247, 248]. Elevated MAPK signaling persists until cells G1/0-arrest and terminally differentiate. The onset of G1/0 arrest and terminal differentiation requires approximately 48 hr. During this period, HL-60 cells undergo approximately two division cycles [249, 250, 251, 252]. Interestingly, during the

first 24 hours of treatment, called a precommitment period, cells are primed to differentiate without lineage specificity. Lineage specificity is determined in the second 24 hr period. Disruption of MEK signaling leads to failure of ERK2 activation and HL-60 differentiation. Activation of both Retinoic Acid Receptor (RAR) and Retinoid X Receptor (RXR) is necessary for RA-induced G1/0-arrest, MAPK signal activation [253, 254, 255] and myeloid differentiation [246, 247, 248, 256]. RA-induced differentiation is contingent on the early transcriptional up-regulation of BLR1 (Burkitt's Lymphoma Receptor-1). BLR1, also known as CXCR5, is a putative serpentine heterotrimeric Gq protein-coupled receptor, with a sequence similar to IL-8 receptors [257]. It was first discovered in a screen for differentially expressed genes that conferred metastatic capability to human B-cell lymphomas [257, 258]. BLR1 was identified as an early RA (or D3)-inducible gene in HL-60 cells using differential display [245, 259], suggesting it had a broader function than lymphocyte regulation. Studies of the BLR1 promoter identified a 5' 17bp GT box approximately 1 kb upstream of the transcriptional start that conferred RA responsiveness [260]. Over expression of BLR1 in HL-60 cells enhanced ERK2 activation in both RA-untreated and treated cells and accelerated RA- and D3-induced differentiation and G1/0-arrest. Alternatively, BLR1 homologous knockout cells failed to produce a sustained MAPK response, arrest or differentiate. However, activation of MAPK signaling via constitutively active Raf over-expression was able to rescue the differentiation response. Furthermore, inhibiting MAPK activation via a Raf inhibitor or siRNA knockdown resulted in decreased BLR1 expression, and loss of differentiation and arrest [219]. Thus, RA-induced BLR1 expression appears to contribute to sustained ERK2 activation and propulsion of induced differentiation and G0 arrest.

To analyze RA-induced arrest and differentiation in HL-60 we integrated experimental and computational methods. Many have suggested that the integration of experimental and computational research is required to unravel critical questions facing modern cell biology [261, 262]. Toward this end, mathematical modeling has become an important tool to understand biological complexity [3]. A common method of modeling biological pathways is to formulate coupled Ordinary Differential Equations (ODEs). ODE models have been constructed for a range of signal transduction processes [263, 264, 171, 23, 265, 266, 267, 268, 269]. However, to formulate and solve these models both the network structure and parameter estimates are required. Yeast Two-Hybrid (Y2H) [270, 271, 272, 273], Fluorescence Resonance Energy Transfer (FRET) [274] or Chromatin Immunoprecipitation (ChIP)-DNA microarray techniques [275, 276, 277, 278] have all been used to identify network interactions. Although error prone [279, 280], these techniques along with traditional low-throughput Immunoprecipitation have been the basis for most experimental network discovery. Computational motif discovery [281, 282, 283], high-throughput network reconstruction [284, 285, 286, 287] or text processing [288], have also contributed significantly to network identification. The integration of these studies has led to comprehensive on-line network databases such as STRING [289], NetworKIN [290, 291] or KEGG [292, 293, 294]. However, while network structural knowledge continues to evolve, the identification of model parameters remains a fundamental challenge.

5.3 Materials and Methods

5.3.1 Cell culture, RA treatment and western blot analysis.

Human myeloblastic leukemia cells (HL-60) were grown in a humidified atmosphere of 5% CO2 at 37 C and maintained in RPMI 1640 supplemented with 5% fetal bovine serum (Invitrogen). The cells were cultured in constant exponential growth as previously described [295]. The experimental cultures were initiated at a cell density of 0.2×10^6 cells/ml. RA (Sigma) was dissolved in 100% ethanol with a stock concentration of 5 mM, and used at a final concentration of 1μM as previously described [295]. For Western blot analyses, 1.2×10^7 cells were lysed using 400μl of M-Per lysis buffer (Pierce) and lysates were cleared by centrifugation at 16,950 $\times$ g in a microcentrifuge for 20 min at 4^oC. Equal amounts of protein lysates (20μg) were resolved by 8% SDS-PAGE at 90 volts, transferred to nitrocellulose membranes, and probed with a primary and secondary antibodies for visualization. Antibody solutions contained 10μL of the appropriate antibody and 1g bovine serum albumin dissolved in 20mL 1X TBS, 0.1% Tween. The primary Retinoblastoma (Rb) antibody was purchased from Zymed. A GAPDH antibody (Cell Signaling, Beverly, MA) was used to check uniform loading. Anti-rabbit and anti-mouse horseradish peroxidase-linked secondary antibodies (Cell Signaling, Beverly, MA) were used for visualization.

5.3.2 Formulation and solution of the model equations.

The HL-60 model was formulated as a set of coupled Ordinary Differential Equations (ODEs):

$$\frac{d\mathbf{x}}{dt} = \mathbf{S} \cdot \mathbf{r}(\mathbf{x}, \mathbf{p}) \qquad \mathbf{x}(t_o) = \mathbf{x}_o \tag{5.1}$$

The symbol $\mathbf{S}$ denotes the stoichiometric matrix (729×1356). The quantity $\mathbf{x}$ denotes the concentration vector of proteins or protein complexes (729×1). The term $\mathbf{r}(\mathbf{x}, \mathbf{p})$ denotes the vector of reaction rates (1356×1). Each row in $\mathbf{S}$ described a protein while each column described the stoichiometry of network interactions. Thus, the (i, j) element of $\mathbf{S}$, denoted by σ_{ij}, described how protein i was involved in rate j. If $\sigma_{ij} < 0$, then protein i was consumed in r_j. Conversely, if $\sigma_{ij} > 0$, protein i was produced by r_j. Lastly, if $\sigma_{ij} = 0$, there was no protein i in rate j. We assumed mass-action kinetics for each interaction in the network. The rate expression for protein-protein interaction or catalytic reaction q:

$$\sum_{j \in \{\mathbf{R}_q\}} \sigma_{jq} x_j \rightarrow \sum_{p \in \{\mathbf{P}_q\}} \sigma_{pq} x_p \tag{5.2}$$

was given by:

$$r_q\left(\mathbf{x}, k_q\right) = k_q \prod_{j \in \{\mathbf{R}_q\}} x_j^{-\sigma_{jq}} \tag{5.3}$$

The set $\left\{\mathbf{R}_q\right\}$ denotes reactants for reaction q. The quantity $\left\{\mathbf{P}_q\right\}$ denotes the set of products for reaction q. The k_q term denotes the rate constant governing the qth interaction. Lastly, σ_{jq}, σ_{pq} denote stoichiometric coefficients (elements of the matrix $\mathbf{S}$). We treated every interaction in the model as non-negative. All reversible interactions were split into two irreversible steps. The mass-action formulation, while expanding the dimension of the initiation model, regularized the mathematical structure. The regular structure allowed automatic generation of the model equations. Mass-action kinetics also regularized the model param-

eters. Unknown model parameters were one of only three types, association, dissociation or catalytic rate constants. Thus, although mass-action kinetics increased the number of parameters and species, they reduced the complexity of model analysis. In this study, we did not consider intracellular concentration gradients. However, we accounted for membrane, cytosolic and nuclear species by explicitly incorporating separate protein species.

5.3.3 Simulation protocol.

A pseudo steady-state was used as the starting point ($t = 0$ hr) for all simulations presented in this study. For example, when calculating the response of HL-60 to the addition of RA, we first ran the model to steady-state and then simulated the addition of RA. We assumed that a pseudo steady-state was a reasonable approximation of the population average behavior of HL-60 growing in the exponential phase. The steady-state was estimated numerically by repeatedly solving the model equations and estimating the difference between two subsequent time points:

$$\|\mathbf{x}(t + \Delta t) - \mathbf{x}(t)\|_2 \leq \epsilon \tag{5.4}$$

The quantities $\mathbf{x}(t)$ and $\mathbf{x}(t + \Delta t)$ denote the simulated concentration vector at time t and $t + \Delta t$, respectively. The quantity $\|\cdot\|_2$ denotes the L_2 vector norm. In this study, we used $\Delta t = 50$ hrs of simulated time and $\epsilon = 0.01$ for all simulations.

5.3.4 Estimating an ensemble of model parameters.

The 1462 unknown model parameters (1356 kinetic constants and 106 non-zero initial conditions) were estimated using the experimental studies preformed by Wang and Yen [219]. The experimental work focused on the existence of a BLR1-MAPK positive feedback loop and included time course data and genetically engineered cell-lines to capture perturbations in both the BLR1 and MAPK signaling axis. The initial parameter guess $\mathbf{p}_0$ was used to generate an ensemble of parameters that maximized the likelihood of describing the training data. The difference between the measured and simulated value of species j at time or condition i, denoted by $\hat{x}_{i,j}$ and $x(\mathbf{p}_k)_{i,j}$ respectively, was quantified by the normalized mean squared error, η:

$$\eta(\mathbf{p}_k) = \frac{1}{N}\sum_{i,j}\frac{(\hat{x}_{i,j} - \beta_j x(\mathbf{p_k})_{i,j})^2}{\hat{\sigma}_{i,j}^2}, \tag{5.5}$$

where sum was carried out over all species j and observations i. The quantities N and $\hat{\sigma}_{i,j}$ denote the total number of observations and the measurement error of species j at time or condition i, respectively. If no experimental error was reported, we assumed a standard deviation equal to 10% of the reported observation. In cases where the quantification of the stimulus or observation was unclear an augmented error of 20%-100% was applied to compensate for the added uncertainty. The scaling factor β_j was chosen to minimize the normalized squared error for a given experiment and species j [296]:

$$\beta_j = \frac{\sum_i(\hat{x}_{i,j}x_{i,j}/\hat{\sigma}_{i,j}^2)}{\sum_i(x_{i,j}/\hat{\sigma}_{i,j})^2}. \tag{5.6}$$

Because of the scaling factor, the concentration units on simulation results were arbitrary (consistent with the arbitrary units associated with the majority of the training data). There was insufficient training data to properly constrain the

model parameters. To account for parametric uncertainty, a monte-carlo approach similar to Battogtokh *et al.* [167] was used to generate an ensemble of parameters. Consider a set of model parameters $\mathbf{p}_i$. Let the likelihood that model simulations with parameters $\mathbf{p}_i$ describe the training data be defined as:

$$\phi(\mathbf{p}_i) \equiv exp\{\frac{-\eta(\mathbf{p}_i)}{\mathcal{T}}\}, \tag{5.7}$$

where $\eta(\mathbf{p}_i)$ denotes the simulation error associated with parameter set $\mathbf{p}_i$. The quantity $\mathcal{T}$ is a parameter used to tune the rate of acceptance. Further let the acceptance probability, $P(\mathbf{p}'_{i+1}|\mathbf{p}_i)$, of a new parameter set, $\mathbf{p}'_{i+1}$, be $\frac{\phi(\mathbf{p}'_{i+1})}{\phi(\mathbf{p}_i)}$ if $\phi(\mathbf{p}'_{i+1}) < \phi(\mathbf{p}_i)$ and 1 otherwise. P denotes the probability that $\mathbf{p}'_{i+1}$ will be accepted as the starting point for consecutive monte-carlo steps. Parameter sets were generated by applying a small additive random perturbation in log space:

$$\log \mathbf{p}'_{i+1} = \log \mathbf{p}_i + \mathcal{N}(0, \nu) \tag{5.8}$$

where $\mathcal{N}(0, \nu)$ is a normally distributed random number with zero mean and variance ν. The perturbation was applied in log space to account for the large variation in parameter scales and to ensure positivity. Monte-carlo trajectories were generated starting from $\mathbf{p}_0$ where ν =0.05 or 0.1 and $\mathcal{T}$ =1 or 0.5. The autocorrelation function of each trajectory was calculated. The number of monte-carlo steps between parameter sets which were added to the ensemble was taken to be the number of steps after which the autocorrelation function dropped to 5% of its initial value. This was done to ensure independence between sets in the ensemble. To compensate for noise in the autocorrelation function an exponential fit was applied. We generated 2377 possible parameter sets from which we selected the 100 sets with the highest likely-hood for inclusion in the final ensemble.

5.3.5 Robustness analysis of the HL-60 architecture.

Robustness coefficients of the form:

$$\alpha\left(i, j, t_o, t_f\right) = \left(\int_{t_o}^{t_f} x_i\left(t\right) dt\right)^{-1} \left(\int_{t_o}^{t_f} x_i^{(j)}\left(t\right) dt\right) \tag{5.9}$$

were calculated to understand the regulatory connectedness of the HL-60 network. The robustness coefficient $\alpha\left(i, j, t_o, t_f\right)$ is the ratio of the integrated concentration of a network output in the presence (numerator) and absence (denominator) of structural or operational perturbation. Here t_0 and t_f denote the initial and final simulation time respectively. The network output was taken to be the network states. The quantity i denotes the index for a marker or reference species while j denotes the perturbation index, respectively. If $\alpha\left(i, j, t_o, t_f\right) > 1$, then the perturbation *increases* the output concentration. Conversely, if $\alpha\left(i, j, t_o, t_f\right) \ll 1$ the perturbation *decreases* the output concentration. Lastly, if $\alpha\left(i, j, t_o, t_f\right) \sim 1$ the perturbation does not influence the output concentration. Because of computational constraints, we calculated the robustness coefficients using a sub-ensemble (N = 47) selected from the full ensemble (N = 100). The sub-ensemble had a CV distribution similar to the full ensemble (Fig. 6.4.1B, circles). While we sampled a sub-ensemble, this subset had a diversity similar to the full ensemble. Thus, we expect results calculated using the sub-ensemble will be similar to the full ensemble.

5.4 Results

In this study, we tested the sufficiency of the BLR1-MAPK architecture to recapitulate persistent MAPK activation and to predict qualitative molecular fea-

tures of RA-induced arrest and differentiation in HL-60. The model was organized around the regulation of seven transcription factors by Erk1/2 and PKCα and the subsequent RA-induced transcriptional program (Table 5.1). The signaling and transcription factor network architecture was assembled by aggregating information from literature.

Table 5.1: Transcription factor, corresponding kinase and transcription factor target genes used in the transcription subnetwork.

TF	Kinase	Targets	Citation
ETS	ERK	IRF, SRPK, RhoGDI, p47Phox, CD45, EIF2AK, SIIIp15	[297, 298]
BRN	–	IRF, SRPK, RhoGDI, p47Phox, CD45, EIF2AK, SIIIp15	[297]
CREB	PKC	IRF, SRPK, RhoGDI, p47Phox, CD45, EIF2AK, SIIIp15, BLR1	[297, 219]
Oct1	–	IRF, SRPK, RhoGDI, p47Phox, CD45, EIF2AK, SIIIp15, BLR1	[297, 219]
NFATc3	ERK	BLR1	[299]
E2F	–	CycE, E2F	[300]
AP1	ERK	CycD	[298]

Model parameters and structure (if required) were re-identified to make the model HL-60 specific. The composite network included: steroid/hormone activated nuclear transcription factor receptors [301, 259]; MAPK driven transcription factor activation [302, 263, 171]; BLR1 mediated G coupled-protein receptor signaling [269, 303, 304]; PI3K/AKT/TOR mediated translation initiation [172, 154]; and G1/0 mammalian cell cycle regulation [161]. All molecular interactions, including transcription and translation, were modeled as elementary reactions using mass action kinetics. Mass balance equations describing the dynamics of network components were formulated as a system of non-linear Ordinary Differential Equations (ODEs). While we assumed spatial homogeneity, we differentiated between cytosolic, membrane and nuclear localized processes

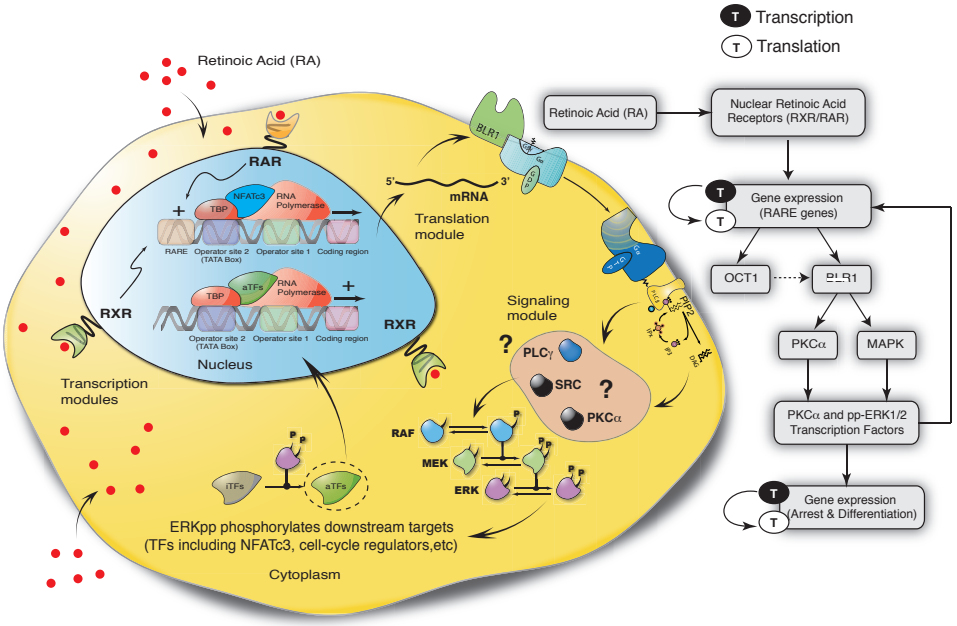

Figure 5.1: Schematic overview of BLR1-MAPK positive feedback loop driving RA induced HL-60 arrest and differentiation.

using segregated compartments. In total, the model described 729 species and 1356 interactions (Fig. 5.1). The model had 1462 unknown parameters (1356 kinetic constants and 106 initial conditions). The kinetic constants were of three types, association, dissociation or catalytic rate constants. Identification of these unknown model parameters posed a significant challenge. We addressed this challenge by identifying an *ensemble* of parameter sets consistent with the training data instead of a single best fit but uncertain parameter set. The ensemble of HL-60 models recapitulated the positive feedback between BLR1 and MAPK signaling. The ensemble of models was also capable of making important predictions. For example, the model ensemble correctly predicted Rb and p47phox regulation and the correlation between p21-CDK4 formation and G0 arrest. Finally, we investigated the robustness of the HL-60 network subjected to struc-

tural perturbations and generated experimentally testable hypothesis for future study.

5.4.1 Estimating an ensemble of HL-60 models.

Signal transduction models often exhibit complex behavior [305, 306, 307, 308]. It is often not possible to identify model parameters, even with extensive training data [309]. Thus, despite identification standards [310] and the integration of model identification with experimental design [311], parameter estimation remains challenging. In this study, an *ensemble* of plausible model parameters was estimated from the study of Wang and Yen [219]. Ensemble approaches have successfully addressed uncertainty in systems biology and other fields like weather prediction [167, 312, 269, 296, 313]. Their central value is the ability to constrain model predictions despite uncertainty. For example, Sethna and coworkers showed in a model of growth factor signaling that predictions were possible using ensembles despite incomplete parameter information (sometimes only order of magnitude estimates) [306]. They further showed that model ensembles were predictive using many different mathematical models [314]. The data sets used for model training and validation along with the model error are summarized in Table 5.2.

Table 5.2: Quantification of model training and validation error.

Species	Figure	Purpose	Cite
BLR1 mRNA	Fig. 3 A	training	[219]
pRaf	Fig. 3 B	training	[219]

Table 5.2 (Continued)

TF	Kinase	Targets	Citation
pMek	Fig. 3 C	training	[219]
pERK	Fig. 3 D	training	[219]
BLR1 mRNA	Fig. 4 A and B	training	[219]
pRaf	Fig. 4 C	training	[219]
Rb mRNA	Fig. C top	Validation	[315]
Rb	Fig. C bottom	Validation	in house
Cyclin D	Fig. C top	Validation	[315]
IRF	Table 1	Validation	[297]
SPRK2	Table 1	Validation	[297]
RhoGDI	Table 1	Validation	[297]
p47Phox	Table 1	Validation	[297]
CD45	Table 1	Validation	[297]
PRK	Table 1	Validation	[297]

We used the time-course of MAPK activation and BLR1 expression following RA treatment to generate the HL-60 ensemble (Fig. 5.4). In addition, measurements of the MAPK-BLR1 signaling axis in genetically engineered HL-60 cell-lines were also used (Fig. 5.5). We used a maximum likelihood random-walk strategy similar to Battogtokh *et al.* [167] to identify the ensemble (Fig. 6.4.1A). We generated 2377 possible parameter sets and selected the most likely sets (N = 100) for inclusion in the ensemble. The median binding affinity for interactions in the model (calculated over the ensemble) was approximately 100 nM, while the median $k_{cat} \simeq 0.5\ s^{-1}$. Thus, although no specific constraint was applied, the parameters were physiologically reasonable. Additionally, the correlation between ensemble parameter sets showed that we sampled from at least two local minima (Fig. 5.3). This suggested that the ensemble was diverse and explored multiple possible local solutions. Seventy-two percent of parameters in the en-

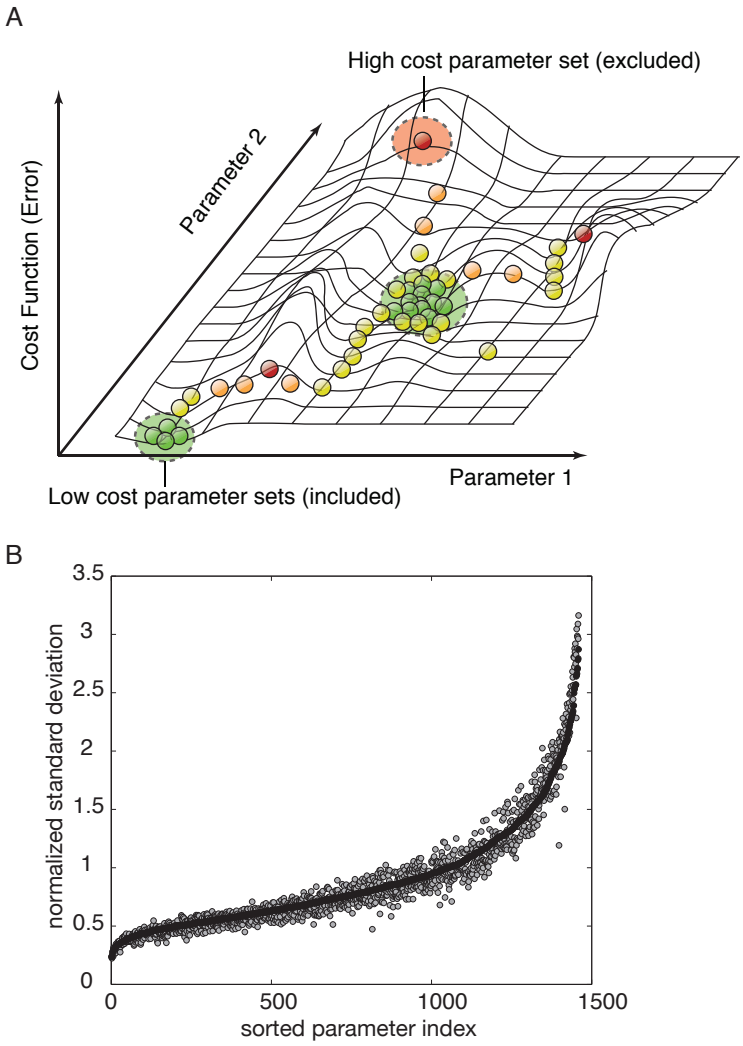

Figure 5.2: Parameter identification strategy. (A) Multiple monte-carlo trajectories were used to randomly explore parameter space. The simulation likelihood was used to generate a family of parameter sets used in the simulation study. We generated N = 2377 possible parameter sets and selected the 100 sets with the highest likelihood for inclusion in the ensemble. (B) Coefficient of Variation (CV; standard deviation of a parameter relative to its mean value) for the parameter ensemble used in this study.

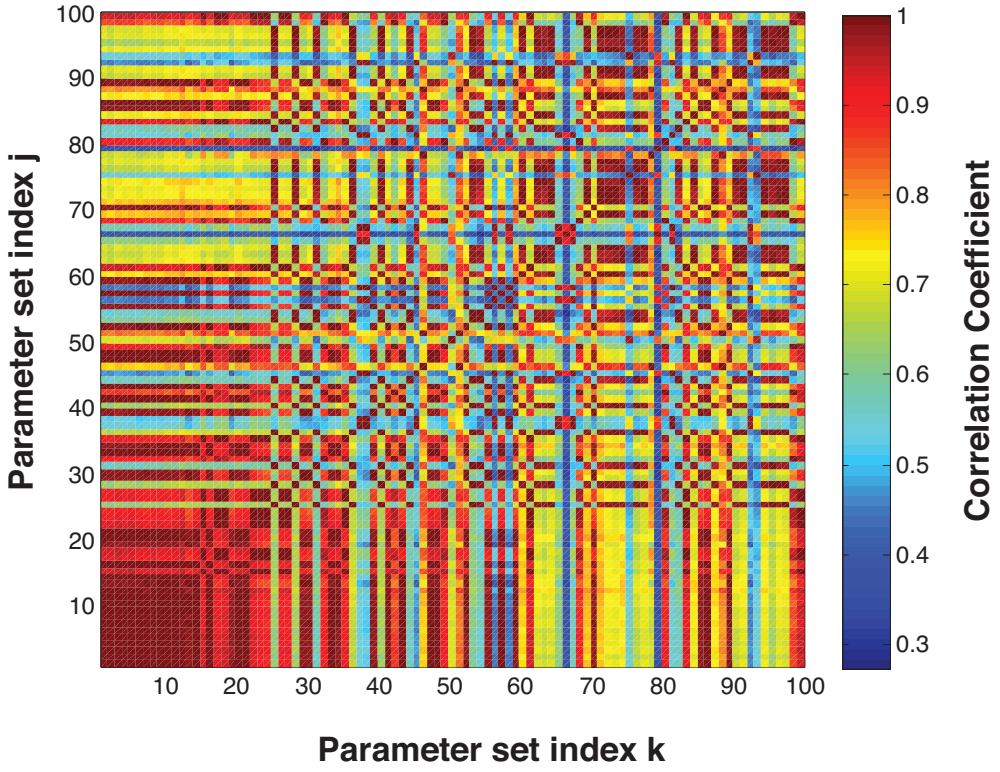

Figure 5.3: Correlation between parameter sets in the HL-60 ensemble. Regions of red indicate high correlation, while blue regions denote low correlation.

semble had a Coefficient of Variation (CV) of less than 100% (Fig. 6.4.1B). Thus, the order of magnitude of approximately three-quarters of the model parameters was identified from the training data. Unconstrained parameters typically involved processes not activated by RA or not associated with BLR1 signaling.

5.4.2 The ensemble of HL-60 models recapitulated RA-induced BLR1 expression and MAPK activation.

Wang and Yen demonstrated that RA-induced BLR1 expression was *necessary* for sustained MAPK activation [219]. In this study, we explored whether a BLR1 control element was *sufficient* for sustained MAPK activation. We incorporated a putative BLR1-MAPK feedback architecture supported by literature. Yen and coworkers established that RA treatment induces BLR1 expression through a non-canonical retinoic acid-responsive element (RARE) in the BLR1 promoter [260]. However, the mechanism by which BLR1 drives Raf1 activation in HL-60 remains uncertain. There is evidence suggesting that BLR1 acts as a Gq protein-coupled receptor [316, 317]. Moreover, Kolch *et al.* showed that protein kinase C activator (PKCα) phosphorylated Raf1, at several sites, in NIH 3T3 fibroblasts [304]. This suggested the hypothesis that BLR1 activates PKCα through its Gq protein-coupled receptor activity and PKCα in turn phosphorylates Raf1. We encoded this connectivity by re-identifying the Gq protein-coupled receptor model of Song and Varner [269] in HL-60. To complete the loop, MAPK family members must be connected in some way with BLR1 expression. Components of the BLR1 transcriptional activator complex e.g., NFATc3 and CREB can be phosphorylated by ERK, JNK or p38 MAPK family members [318]. In the model we encoded the simplest of the possible routes, namely the phosphorylation of NFATc3 by pERK1/2. The *in-vivo* phosphorylation of NFATc3 by ERK1/2 has been shown in a variety of blood cell types [318]. The HL-60 connectivity recapitulated RA-induced sustained MAPK activation and feedback between BLR1 and MAPK (Fig. 5.4 and Fig. 5.5). The ensemble of HL-60 models, following the addition of RA, captured the transient expression of

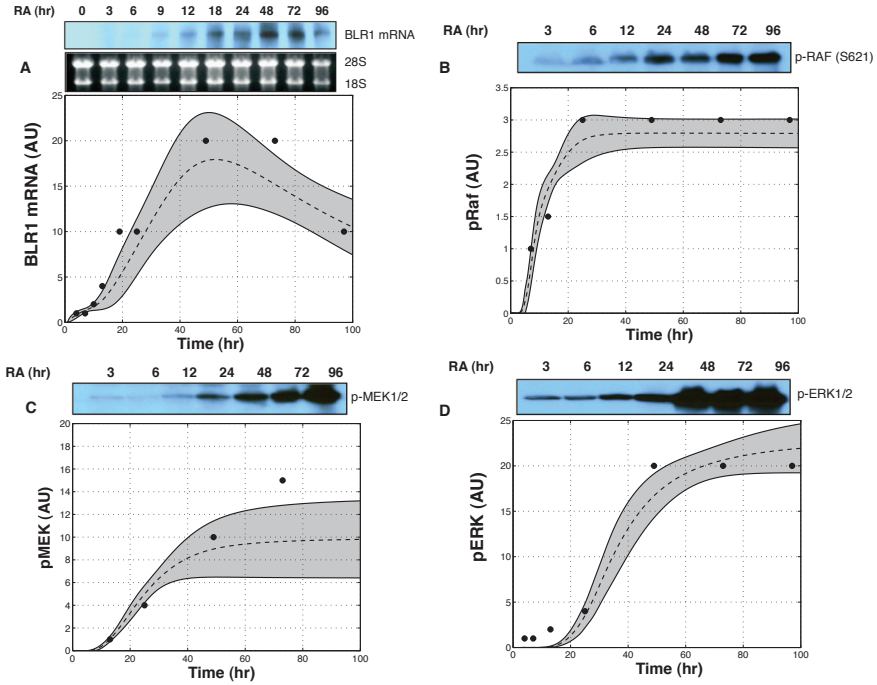

Figure 5.4: Model simulations over the parameter ensemble captured the sustained activation of MAPK following RA exposure (1μM) at time = 1 hour. Dashed lines denote the simulation mean. Shaded regions denote one ensemble standard deviation. (A) Experimental and simulated levels of BLR1 mRNA following RA exposure. (B) Time profile of phosphorylated RAF1 activation following RA exposure. (C) Simulated versus measured phosphorylated MEK activation following RA exposure. (D) Simulated versus measured phosphorylated ERK following RA exposure.

BLR1 (Fig. 5.4A). BLR1 then drove Raf1 phosphorylation through its hypothesized Gq protein-coupled activity (Fig. 5.4B). Activated Raf1 was then free to activate downstream MAPK kinases (Fig. 5.4C and 5.4D). The median training error for RA-induced BLR1/MAPK signaling was ~ 2, where pERK1/2 was the least constrained species (Table 5.2). An error of 1.0 indicated the model accuracy was equal to experimental error (assumed to be ± 20% for the training blots). Thus, the model recapitulated three of the four species to within

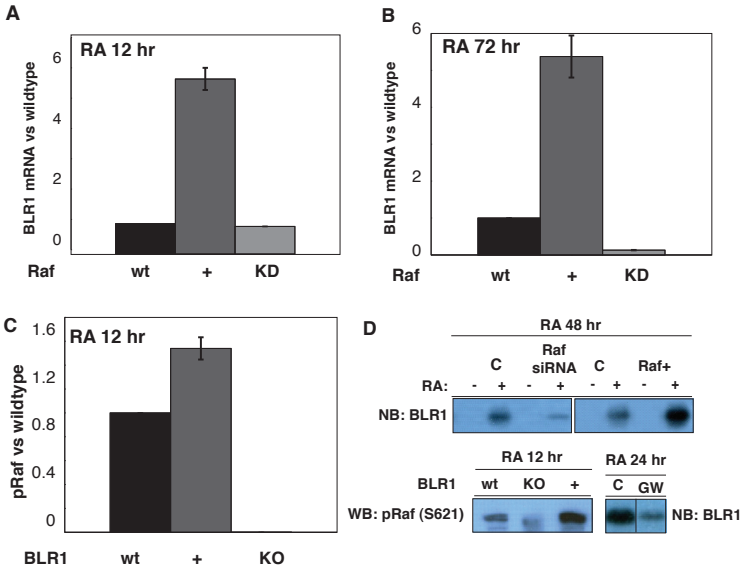

Figure 5.5: The model recapitulated RA-induced feedback between BLR1 expression and MAPK activation. (A) Simulated BLR1 expression normalized to wildtype (WT) with Raf overexpression (+, 50% increase in Raf initial condition) and inhibition (KD, 50% decrease in Raf initial condition) 12 hr after the addition of RA. (B) Simulated BLR1 expression normalized to wildtype (WT) with Raf overexpression (+) and inhibition (KD) 72 hr after the addition of RA. (C) Simulated phosphorylated Raf levels normalized to wildtype (WT) with BLR1 overexpression (+, 50% increase in BLR1 gene initial condition) and knockout (KO, BLR1 gene initial condition set to zero) 12 hr after the addition of RA. (D) Model training data adapted from Wang and Yen. First row: effect of Raf knockdown (left) and overexpression (right) on the expression of BLR1 (Northern). Second row: effect of BLR1 knockout and overexpression of the level of phosphorylated Raf (S621) (left) and the effect of the Raf inhibitor, GW5074 on BLR1 overexpression 12 and 24 hr after the addition of RA.

a neighborhood around the experimental error. The ensemble of models also recapitulated aspects of BLR1/MAPK signaling following Raf1 and BLR1 perturbations (Fig. 5.5). Because the perturbation magnitudes were not reported, we assumed ±50% for all changes, excluding the BLR1 homologous knockout.

A 50% increase in Raf1 expression increased BLR1 transcription after 12 hr of RA exposure (Fig. 5.5A). Conversely, a 50% decrease in Raf1 activation reduced the BLR1 message 72 hr post RA treatment (Fig. 5.5B). The perturbation of BLR1 played a similar role to Raf1. A 50% increase in BLR1 expression increased Raf1 activation (Fig. 5.5C, lane two), while a BLR1 knockout blocked RA-induced Raf1 activation (Fig. 5.5C, lane three). The BLR1-MAPK perturbation simulations were qualitatively consistent with experimental measurements (Fig. 5.5D). However, while the direction of the simulated shifts was consistent with measurements, the time-scale did not match for all cases. The time-scale of Raf1 activation following perturbations to BLR1 directly corresponded to measurements. On the other hand, the time-scale of the response of BLR1 to changes in Raf1 activation was not directly comparable to measurements.

5.4.3 The HL-60 ensemble predicted RA-induced expression shifts and qualitative features of G1/0 cell-cycle arrest.

We tested the ability of the model to predict qualitative features of RA-induced differentiation not included in the training data (Table 5.2).

Table 5.3: Predicted and measured RA-induced protein expression shifts at 3, 12 and 24 hrs after the addition of RA.

Protein TF	3hr Kinase	12hr Targets	24hr Citation
Cyclin D	-	+	-
IRF	-	-	-

Table 5.3 (Continued)

Protein TF	3hr Kinase	12hr Targets	24hr Citation
SPRK2	+	+	+
RhoGDI	+	-	-
p47Phox	+	+	+
CD45	+	-	-
PRK	+	+	-

We compared simulations of RA-induced protein expression with a panel of proteins found to be important following RA treatment [297]. In total, we captured approximately half of the significant RA-induced protein shifts at three different time points (Table 5.3). For example, the model ensemble predicted the up-regulation of p47Phox, a component of oxidative metabolism important in the functional differentiation of mature myeloid cells [319]. The model ensemble also predicted that Rb protein levels decreased following RA treatment (Fig. 5.6B). Down-regulation of the Rb protein level was consistent with western blot measurements 24 hrs after RA treatment (Fig. 5.6B, lower inset). Interestingly, Rb protein levels decreased despite a stable mRNA signal (Fig. 5.6B, top inset). The model thus correctly predicted an unanticipated experimental observation. The model ensemble predicted that competition for translational machinery resulted in the decreased Rb protein levels. Other factors not present in the model, for example, RA-induced degradation mechanisms could also play a role. In addition to shifts in Rb and p47Phox expression, the model ensemble also predicted other RA-induced cell-cycle responses. For example, the model ensemble predicted increased association of p21 with the CDK4-cyclin D complex following RA-treatment (Fig. 5.6A). Increased p21-CDK4-cyclin D levels were consistent with previous data on the kinetics of RA-induced G1/0-arrest

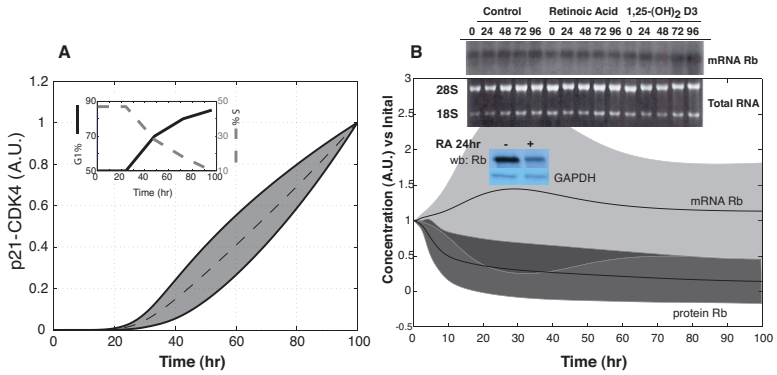

Figure 5

Figure 5.6: Computationally predicted markers of RA-induced phenotypic shift. (A) Predicted p21-CDK4-cyclinD complex formation was consistent with percentage of G1/0-arrested cells (insert). (B) Effect of RA on Rb expression. Rb transcript (top) remains constant while Rb protein (bottom) decreases. Rb transcript consistent with Northern analysis (top insert) while Rb protein levels were consistent with Western analysis (bottom insert).

(Fig. 5.6A, inset). However, there was some discrepancy between the previous arrest studies and the cyclin D expression data, as cyclin D expression levels were not consistently predicted (Table 5.3).

5.4.4 Robustness analysis identified essential nodes in RA-induced arrest and differentiation of HL-60.

Signal transduction architectures often contain redundancy, feedback and crosstalk. These and other features make signaling networks robust to perturbation. However, robust networks which are highly optimized for specific tasks may also contain hidden fragility [61]. Here, we generated falsifiable predictions about the fragility or robustness of structural features of the HL-60 net-

work using robustness analysis. We hypothesized that the concentration profiles of the network components following the addition of RA was indicative of network function. We calculated the direction of RA-induced concentration shifts for 729 markers following the deletion of 106 network components (Fig. 5.7A). Robustness coefficients were calculated over the ensemble to minimize parametric artifacts. The structural perturbations included the deletion of 80 constitutively expressed proteins, the genes for 20 regulated proteins or the removal of calcium, ATP, etc. We rank-ordered the results from least (rank = 1) to most (rank = 106) effective knock-down (x-axis) and least (rank = 1) to most (rank = 729) effected marker (y-axis). Effectiveness was defined as the number of expression shifts caused or the number of perturbations a marker was effected by.

The majority of structural perturbations resulted in only small changes in the network output following the addition of RA. The HL-60 network architecture was approximately scale-free (Fig. 5.8). A hub and spoke topology was consistent with the sparseness of the perturbation simulation results. Approximately 80% of the entries in the robustness matrix were equal to zero (Fig. 5.7A, green). For those species that did influence the network state, there was an approximately 30% correlation between connectivity and influence. Globally, the single largest impact was made by removing components of translation initiation and RNA polymerase (RNAp) from the model. For example, deletion of RNAp resulted in 468 statistically significant shifts, or 64% of the network components. This was consistent with the obvious expectation that stopping protein synthesis would interrupt the progress of induced differentiation. Interestingly, while deletion of translation components effected many markers, there were only a limited number of perturbations that impacted translation. This suggested that

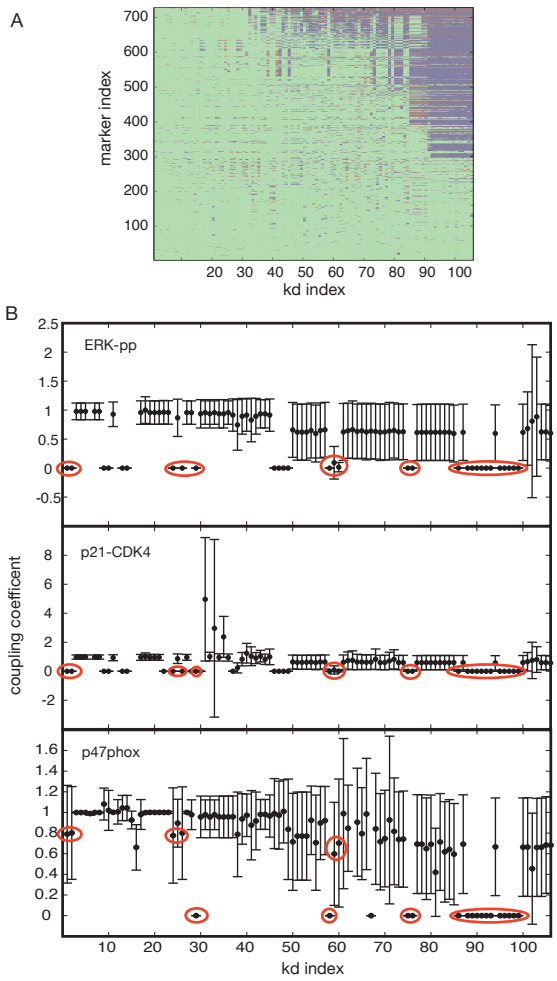

Figure 5.7: Robustness analysis. (A) Qualitative coupling results. Removed species are along the x-axis from lowest to largest impact and observed model species are along the y-axis from least to most effectived. Blue (red) markers depict a statistical decrease (increase) in area under the curve within a 90% confidence interval. (B) Coupling coefficients (area under the curve from the simulation with species removed over wild-type simulation) for three markers of differentiation: phosphorylated ERK, p47phox expression and p21-CDK4 complex.

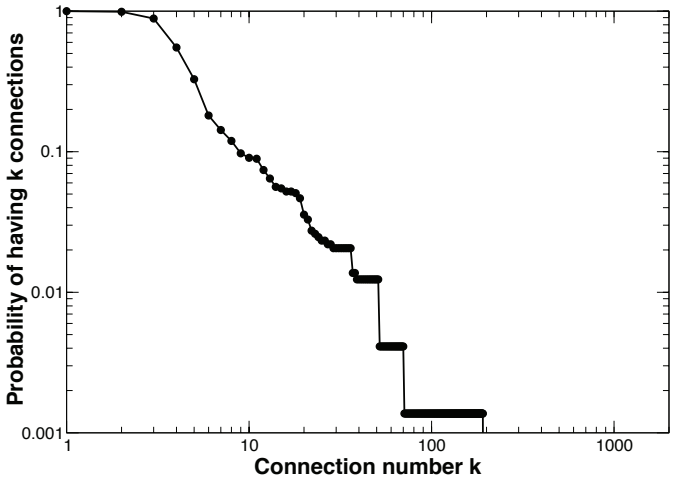

Figure 5.8: The HL-60 network architecture exhibits scale free properties.

translation was a fragile core subsystem similar to fragile subsystems in other 'bow-tie' type networks [320]. Anecdotally, RNAp was also the most connected component with 191 connections (connected to approximately 26% of the network species). However, the Spearman rank correlation between connectivity and knock-down effectiveness was only 0.32. This suggested there was a limited relationship between the direct connectivity of a node and the functional consequences of its removal. Deletion of other structural elements with much lower connectivity also produced global variation. For example, deletion of *blr1* or the *blr1* transcription factor complex effected on average 280 markers, or 38% of the network. BLR1 or components of its transcriptional activator complex had an average connectivity of 11, or just 1.5% of the network. Small molecules such as calcium ions, ATP and GDP were also structurally critical, on average effecting 185 markers. Interestingly, MAPK species appeared nearly midway through the ordered list with ERK at rank 43/106 and MEK at rank 46/106. The most influential MAPK component was Raf1 at rank 59/106.

No single structural deletion led to enhanced differentiation of HL-60 following RA exposure. We considered three markers to represent a significant tendency towards HL-60 differentiation and G1/0-arrest: ERK-$T^{203}Y^{205}$ phosphorylation represented sustained MAPK signaling; the p21-CDK4 complex represented initial aspects of cell cycle arrest; p47phox expression represented early aspects of the inducible reactive oxygen species machinery. Of the 106 deletions, none consistently up-regulated all three markers. Twenty-two network components (or 21% of those tested) were essential for differentiation (Fig. 5.7B). Seventeen of these involved translation and RNAp. The remaining five targets were members of the BLR1 transcription factor complex including RAR/RXR. Analysis of the shifts for the individual markers following the structural perturbations suggested functional relationships in the network. For example, deletion of 32 components (or 30% of those explored) reduced ERK-pp formation (Fig. 5.7B, top panel). These included BLR1, RXR/RAR, proteins in the Gq protein-coupled cascade connecting BLR1 with Raf1, upstream kinases and MAPK phosphatases. Thirty-six perturbations (or 34% of those explored) influenced p21-CDK4 formation (Fig. 5.7B, center panel). In addition to those perturbations associated with pERK1/2, deletion of components involved with cyclin D expression also influenced p21-CDK4-cyclin D levels. For example, deletion of the phosphatase responsible for de-phosphorylating AP1-p (transcription factor for cyclin D) increased p21-CDK4 levels. Twenty-seven perturbations (or 25% of those explored) shifted p47Phox expression (Fig. 5.7B, bottom panel). These structural perturbations were largely associated with the regulation of the transcription factors driving p47Phox expression.

5.5 Discussion

A grand challenge in tumor biology continues to be an understanding of the regulation of cell division and differentiation. The primary obstacle to understanding these programs has been their complexity and scale. Interrogating these complex systems species by species is intractable due to the number of species and their interactions. A computational approach that allows *in-silico* analysis versus experimental surveying would be a tool of widespread utility to push passed this hurdle. Perhaps, one such tool is mechanistic pathway modeling. The ultimate objective of this study was to develop a mathematical model of hormone/growth factor regulated cell division and differentiation. The mathematical model is eventually intended to be a cell-type agnostic tool generally applicable to any cell-type where division and differentiation are hormonally regulated. However, to develop an initial framework towards this goal we have focused model development on the archetype *in vitro* cell line HL-60. Upon RA treatment HL-60 undergoes growth arrest and myeloid differentiation. Our basic hypothesis has been that RA-induced cell differentiation is regulated by BLR1 which signals through a RAF/MEK/ERK axis. In turn, the MAPK cascade activates a limited number of transcription factors who then drive the expression of proteins mediating the phenotypic shift [260]. The current network incorporates these basic signaling features. We established that a literature based positive feedback loop between BLR1 and MAPK signaling was sufficient to generate the BLR1 expression and MAPK activation profiles observed experimentally (Fig. 5.4 and Fig. 5.5). Furthermore, we demonstrated that the current model was capable of making important predictions including the regulation of Rb and p47phox along with the correlation between the p21-cdk4 complex and

G0 arrest. Robust networks or systems maintain performance despite structural or operational perturbations.

In this study, we performed robustness analysis to estimate which architectural features of the HL-60 network promoted or destroyed differentiation. This analysis also generated falsifiable predictions on the role of individual model species and global insight into the network itself. For example, the core translation machinery was a robust yet fragile subsystem. Deletion of translation components effected roughly 60% of the entire network (Fig. 5.7A). However, translation was robust in that removal of other network species had little impact on its function. The majority of translation, save met-tRNA and eIF5, were in the lower third of effected markers. However, while necessary, the translation subnetwork may not be experimentally interesting. To focus on phenotypic conversion we considered three markers of programed differentiation and G1/0-arrest: pERK1/2, p21-CDK4-cyclin D and p47phox. These markers were representative of sustained MAPK activity, cell cycle arrest and early ROS machinery, respectively. Simulations of RA-induced phenotypic change in the wild-type model showed these markers were reliable compared to experimental data. None of the structural perturbations considered consistently up-regulated all three markers. This suggested that no single structural perturbation enhanced the effect of RA and that, given the current network, no components were blocking differentiation. Structural perturbations that consistently down-regulated all three markers were considered targets that would prevent differentiation. Again the translational core machinery along with RNAp proved to be necessary for differentiation. Beyond these global inhibitors, we also found that deletion of RAR, RXR, BLR1, NFATc3, Oct1 and CREB (Fig. 5.7B) also down-regulated differentiation. RAR and RXR were obvious candidates for mitigat-

ing the RA differentiation response [321]. Removal of BLR1 has previously been shown to prevent differentiation [219] and was indeed a motivating factor in the original model design. NFATc3, Oct1, and CREB were all required for transcriptional activation of the BLR1 gene and were therefore of similar importance [260]. This study identified key differentiation regulators, however, the list was not complete. For example, Yen *et al.* showed that Raf and MEK activation was also required for differentiation [219, 218]. In the current network, ERK1/2 deletion repressed only two (pERK1/2 and p21-CDK4) of the three differentiation markers, not effecting p47phox. While ERK1/2 may regulate p47phox expression, ERK1/2 may also impact inducible ROS response at other points in the network. A more detailed model, including other differentiation markers, is required to fully unravel the key species in the differentiation program.

The initial model presented here was a step toward a systematic framework for the organization and prediction of programed differentiation. However, there are several mathematical and experimental issues that should be addressed in subsequent studies. For example, a common criticism of large complex mathematical models is the poorly characterized effect of model uncertainty. Model uncertainty has two forms. Structural uncertainty is uncertainty in the biology, while parametric uncertainty is incomplete knowledge of model parameters. We used an ensemble approach to overcome parametric uncertainty. Consistent with previous ensemble studies [306], the HL-60 ensemble predicted the expression of a panel of markers found previously to be important [297]. These predictions were successful despite the large uncertainty in the model parameters. However, the prediction error rate was significant. This suggested that structural uncertainty was also important. It is likely that structural uncertainty was present both in terms of missing interactions (false

negatives) and incorrect interactions (false positives). We partially mitigated structural uncertainty by associating each interaction with experimental studies or previously validated network models. However, in some cases connectivity had to be hypothesized from literature. For example, the connectivity between BLR1 signaling and Raf1 activation was hypothesized from studies in fibroblasts. G coupled-protein receptor (GCPR) signaling and the subsequent activation of PKCα was modeled as a sequential series of activating events. This basic architecture was sufficient to generate an RA-induced sustained MAPK signal. However, this connectivity remains to be validated in HL-60. To validate the proposed architecture, our laboratory is employing biochemical strategies to characterize intermediate complexes in the BLR1 signaling axis. False negative structural defects also represent a significant challenge. Current computational and biological limitations render a full cell model intractable. Thus, the choice of scope is an important aspect to modeling protein interaction networks. In this study, we focused MAPK-BLR1 positive feedback. Inclusion of other signaling pathways or a more advanced transcriptional regulation network will be required to capture the RA-induced expression shifts missed here as well as other HL-60 differentiation data. The framework provided in this study is amenable to expansion. The inclusion of more experimental data and a more detailed network architecture could improve predictive power of the model and provide an *in silico* tool for understanding programed cellular differentiation.

CHAPTER 6

ANALYSIS OF THE MOLECULAR NETWORKS IN ANDROGEN DEPENDENT AND INDEPENDENT PROSTATE CANCER REVEALED FRAGILE AND ROBUST SUBSYSTEMS

6.1 Abstract

Androgen ablation therapy is currently the primary treatment for metastatic prostate cancer. Unfortunately, in nearly all cases androgen ablation fails to permanently arrest cancer progression. As androgens like testosterone are withdrawn, prostate cancer cells lose their androgen sensitivity and begin to proliferate without hormone growth factors. In this study, we constructed and analyzed a mathematical model of the integration between hormone growth factor signaling, androgen receptor activation and the expression of cyclin D and Prostate Specific Antigen in human LNCaP prostate adenocarcinoma cells. The objective of the study was to investigate which signaling systems were important in the loss of androgen dependence. The model was formulated as a set of ordinary differential equations which described 212 species and 384 interactions including both the mRNA and protein levels for key species. An ensemble approach was chosen to constrain model parameters and to estimate the impact of parametric uncertainty on model predictions. Model parameters were identified using 14 steady-state and dynamic LNCaP data sets taken from literature sources. Alterations in the rate of Prostatic Acid Phosphatase expression was sufficient to capture varying levels of androgen dependence. Analysis of the model provided insight into the importance of network components as a function of androgen dependence. The importance of androgen receptor avail-

ability and the MAPK/Akt signaling axes was independent of androgen status. Interestingly, androgen receptor was important even in androgen independent LNCaP cells. Translation became progressively more important in androgen independent LNCaP cells. Further analysis suggested a positive synergy between the MAPK and Akt signaling axes and the translation of key proliferative markers like cyclin D in androgen independent cells. Taken together, the results support the targeting of both the Akt and MAPK pathways. Moreover, the analysis suggested that direct targeting of the translational machinery, specifically eIF4E, could be efficacious in androgen independent prostate cancers.

6.2 Introduction

Prostate cancer is the most common cancer in men and the second leading cause of cancer-related death in the United States [322]. It has been known since the 1940s that androgens, such as testosterone, are required for prostate cancer growth [323]. Accordingly, androgen ablation in combination with radiation or traditional chemotherapy remains the primary non-surgical treatment for androgen-dependent prostate cancer. Androgen ablation initially leads to decreased tumor growth and reduced secretion of biomarkers such as Prostate Specific Antigen (PSA) [324, 325, 326]. However, in nearly all cases androgen ablation fails to permanently arrest cancer progression. As testosterone is withdrawn, malfunctioning prostate cells lose their sensitivity to androgen and begin to proliferate without hormone growth factor signals. These testosterone insensitive cells can then lead to Androgen-Independent Prostate Cancer (AIPC) [327]. The AIPC phenotype is closely related to metastasis and decreased survival. Unfortunately, current treatments for metastatic AIPC have demonstrated

only modest survival advantages [328]. Thus, an effective therepy for metastatic AIPC represents an unmet medical need and an ideal target for systems biology.

AIPC is characterized by androgen action in the absence of androgen stimulation. At the core of androgen action is the regulation of Androgen Receptor (AR) by hormones such as testosterone. AR is a cytosolic steroid hormone receptor belonging to the superfamily of ligand activated transcription factors. Other members of this family include Vitamin A/D, estrogen, progesterone and thyroid hormone receptors [329, 330]. In healthy prostate epithelial cells, androgens activate AR and drive an AR-dependent gene expression program. Sexual androgens such as testosterone typically circulate in the blood, bound to proteins such as the Sex Hormone Binding Globulin (SHBG) protein. Free testosterone enters prostate cells where the 5α-reductase enzyme converts it to activated dihydrotestosterone (DHT) [331]. Both cytosolic testosterone and DHT can bind AR, however DHT has a higher affinity for AR. Binding of DHT to AR promotes cytosolic AR activation and the translocation of activated AR to the nucleus. Nuclear AR drives the expression of target genes including PSA by binding to AR-responsive promoter elements [332, 333]. Because of its ligand dependence, one would expect AR activation and AR-driven gene expression to be absent without hormone stimulation. However, AIPC often has higher PSA expression and increased cell-proliferation compared to its androgen-dependent counterpart even without stimulation [334, 335].

AIPC's increased proliferation and PSA secretion in the absence of androgen suggests a failure in the regulation of androgen receptor activation. Feldman and Feldman reviewed several possible AR regulatory pathways perhaps responsible for androgen action in the absence of hormone stimulation [336]. One

hypothesis, referred to as the hypersensitivity pathway, suggests that AR may be more sensitive to androgen in AIPC. This would allow AR activation and AR-driven gene expression at much lower levels of extracellular testosterone signals. Another hypothesis, referred to as the promiscuous pathway, suggests that AR can be activated by non-androgen antagonists. A third hypothesis, explored here, suggests that AR can be activated by other pathways, for example, the Mitogen Activated Protein Kinase (MAPK) cascade. Several studies support this cross-talk hypothesis, sometimes referred to as the outlaw pathway. Culig *et al.* showed in DU-145 human prostatic tumor cells that growth factors e.g., IGF-I, KGF, and EGF could drive AR activation without androgen [337]. Nazareth and Weigel showed in human prostate PC-3 cells that AR could also be activated by the protein kinase A activator, forskolin in the absence of androgen [338]. Other studies have suggested a connection between Her2 induced activation of the primary MAPK cascade and AR activation [339]. For example, Her2 overexpression was positively correlated with diminished sensitivity to androgen ablation, increased AR dependent PSA expression, increased AR activation, increased tumor mass and shortened tumor latency [340, 339, 341, 335]. Thus, one would expect regulators of Her2 activation, for example the different forms of the 100 kDa glycoprotein Prostatic Acid Phosphatase (PAcP), could be important factors in androgen dependence and tumor grade [342, 343, 344, 345, 346, 347]. Intracellular PAcP (cPAcP) whose expression is AR responsive, downregulates Her2 by dephosphorylation. On the other had, secreted PAcP (sPAcP) promotes modest Her2 activation by an unknown mechanism [347].

6.3 Materials and Methods

Formulation and solution of the model equations.

The prostate model was formulated as a set of coupled Ordinary Differential Equations (ODEs):

$$\frac{d\mathbf{x}}{dt} = \mathbf{S} \cdot \mathbf{r}(\mathbf{x}, \mathbf{k}) \qquad \mathbf{x}(t_o) = \mathbf{x}_o \tag{6.1}$$

The symbol $\mathbf{S}$ denotes the stoichiometric matrix (212×384). The quantity $\mathbf{x}$ denotes the species concentration (212×1). The term $\mathbf{r}(\mathbf{x}, \mathbf{p})$ denotes the vector of reaction rates (384×1). Each row in $\mathbf{S}$ described a species while each column described the stoichiometry of network interactions. Thus, the (i, j) element of $\mathbf{S}$, denoted by σ_{ij}, described how protein i was involved in rate j. If $\sigma_{ij} < 0$, then protein i was consumed in r_j. Conversely, if $\sigma_{ij} > 0$, protein i was produced by r_j. Lastly, if $\sigma_{ij} = 0$, protein i was not involved in rate j.

We assumed mass-action kinetics for each interaction in the network. The rate expression for protein-protein interaction or catalytic reaction q:

$$\sum_{j \in \{\mathbf{R}_q\}} \sigma_{jq} x_j \rightarrow \sum_{p \in \{\mathbf{P}_q\}} \sigma_{pq} x_p \tag{6.2}$$

was given by:

$$r_q\left(\mathbf{x}, k_q\right) = k_q \prod_{j \in \{\mathbf{R}_q\}} x_j^{-\sigma_{jq}} \tag{6.3}$$

The set $\left\{\mathbf{R}_q\right\}$ denotes reactants for reaction q. The quantity $\left\{\mathbf{P}_q\right\}$ denotes the set of products for reaction q. The k_q term denotes the rate constant governing the qth interaction. Lastly, σ_{jq}, σ_{pq} denote stoichiometric coefficients (elements of the matrix $\mathbf{S}$). We treated every interaction in the model as non-negative. All reversible interactions were split into two irreversible steps. The mass-action for-

mulation, while expanding the dimension of the prostate model, regularized the mathematical structure. The regular structure allowed automatic generation of the model equations. In addition, an analytical Jacobian (**A**) and matrix of partial derivatives of the mass balances with respect to the model parameters (**B**) were also generated. Mass-action kinetics also regularized the model parameters. Unknown model parameters were one of only three types, association, dissociation or catalytic rate constants. Thus, although mass-action kinetics increased the number of parameters and species, they reduced the complexity of model analysis. In this study, we did not consider intracellular concentration gradients. However, we accounted for membrane and cytosolic proteins by explicitly incorporating separate membrane and cytosolic protein species. We did not consider a separate nuclear compartment.

6.3.1 Simulation protocol.

An approximate steady-state was used as the starting point ($t = 0$ hr) for all simulations presented in this study. For example, when calculating the response of LNCaP to the addition of DHT, we first ran the model to steady-state and then simulated the addition of DHT. Although no individual cell is likely to be at steady-state we assumed that steady-state was a reasonable approximation of the population average behavior of LNCaP cells growing in the exponential phase. The steady-state was estimated numerically by repeatedly solving the model equations and estimating the difference between two subsequent time points:

$$||\mathbf{x}(t + \Delta t) - \mathbf{x}(t)||_2 \leq \epsilon \tag{6.4}$$

The quantities $\mathbf{x}(t)$ and $\mathbf{x}(t + \Delta t)$ denote the simulated concentration vector at time t and $t + \Delta t$, respectively. The quantity $\| \cdot \|_2$ denotes the L_2 vector norm. In this study, we used $\Delta t = 50$ hrs of simulated time and $\epsilon = 0.01$ for all simulations.

6.3.2 Estimation of the prostate model parameter ensemble.

An initial set of model parameters, denoted by $\mathbf{p}_0$, was chosen by hand to replicate the training data. The training data consisted of 14 time-series and steady-state data sets taken from literature sources (Table C.2). The initial parameter guess $\mathbf{p}_0$ was used to generate an ensemble of parameters that maximized the likelihood of describing the training data. The difference between the measured and simulated value of species j at time or condition i, denoted by $\hat{x}_{i,j}$ and $x(\mathbf{p}_k)_{i,j}$ respectively, was quantified by the normalized mean squared error, η:

$$\eta(\mathbf{p}_k) = \frac{1}{N} \sum_{i,j} \frac{(\hat{x}_{i,j} - \beta_j x(\mathbf{p_k})_{i,j})^2}{\hat{\sigma}_{i,j}^2}, \tag{6.5}$$

where the sum was carried out over all species j and observations i. The quantities N and $\hat{\sigma}_{i,j}$ denote the total number of observations and the measurement standard deviation of species j at time or condition i, respectively. If no experimental error was reported, we assumed a standard deviation equal to 10% of the reported observation. In cases where the quantification of the stimulus or observation was unclear an augmented error of 20%-100% was applied to compensate for the added uncertainty. β_j is a scaling factor which is required when considering experimental data that is accurate only to a multiplicative constant (assumed here to be the case form immunoblotting analysis). The scaling factor was chosen to minimize the normalized squared error between a given experi-

ment and species j [166]:

$$\beta_j = \frac{\sum_i (\hat{x}_{i,j} x_{i,j} / \hat{\sigma}^2_{i,j})}{\sum_i (x_{i,j} / \hat{\sigma}_{i,j})^2}. \tag{6.6}$$

Because of the scaling factor, the concentration units on simulation results were arbitrary (consistent with the arbitrary units on the majority of the training data). All simulation outputs reported in this study were scaled by the corresponding β_j. There was insufficient training data to properly constrain the 420 model parameters. To account for parametric uncertainty, a monte-carlo approach similar to Battogtokh *et al.* [167] was used to generate an ensemble of parameters. Consider a set of model parameters $\mathbf{p}_i$. Let the likelihood that model simulations with parameters $\mathbf{p}_i$ describe the training data be defined as:

$$\phi(\mathbf{p}_i) \equiv exp\{\frac{-\eta(\mathbf{p}_i)}{\alpha}\}, \tag{6.7}$$

where $\eta(\mathbf{p}_i)$ denotes the simulation error associated with parameter set $\mathbf{p}_i$. The quantity α is a parameter used to tune the rate of acceptance. Further let the acceptance probability, $P(\mathbf{p}'_{i+1}|\mathbf{p}_i)$, of a new parameter set, $\mathbf{p}'_{i+1}$, be $\frac{\phi(\mathbf{p}'_{i+1})}{\phi(\mathbf{p}_i)}$ if $\phi(\mathbf{p}'_{i+1}) < \phi(\mathbf{p}_i)$ and 1 otherwise. P denotes the probability that $\mathbf{p}'_{i+1}$ will be accepted as $\mathbf{p}_i$ for consecutive monte-carlo steps. Parameter sets were generated by applying a small additive random perturbation in log space:

$$\log \mathbf{p}'_{i+1} = \log \mathbf{p}_i + \mathcal{N}(0, \nu) \tag{6.8}$$

where $\mathcal{N}(0, \nu)$ is a normally distributed random number with zero mean and variance ν. The perturbation was applied in log space to account for the large variation in parameter scales and to ensure positivity. Monte-carlo trajectories were generated starting from $\mathbf{p}_0$ where ν =0.05 or 0.1 and α =1 or 0.5. The autocorrelation function of each trajectory was calculated. The number of monte-carlo steps between parameter sets which were added to the ensemble was taken to be the number of steps after which the autocorrelation function

dropped to 5% of its initial value. This was done to ensure independence between sets in the ensemble. To compensate for noise in the autocorrelation function an exponential fit was applied. The final ensemble contained 107 parameter sets, which produced an ensemble η of 5.25.

6.3.3 Sensitivity analysis of the prostate network.

Overall State Sensitivity Coefficients (OSSC) were used to estimate which structural elements of the prostate network were sensitive [23]. OSSC values were determined by first calculating the first-order sensitivity coefficients at time t_k:

$$s_{ij}(t_k) = \left.\frac{\partial x_i}{\partial p_j}\right|_{t_k} \tag{6.9}$$

First-order sensitivity coefficients were computed by solving the matrix differential equation:

$$\frac{d\mathbf{s}_j}{dt} = \mathbf{A}(t)\,\mathbf{s}_j + \mathbf{b}_j(t) \qquad j = 1, 2, \ldots, P \tag{6.10}$$

subject to the initial condition $\mathbf{s}_j(t_0) = \mathbf{0}$. In Eqn. 6.10, j denotes the parameter index, P denotes the number of parameters in the model, $\mathbf{A}$ denotes the Jacobian matrix, and $\mathbf{b}_j$ denotes the jth column of the matrix of first-derivatives of the mass balances with respect to the parameter values (denoted by $\mathbf{B}$). An analytical Jacobian and matrix of first-derivatives of the mass balances w.r.t the parameters:

$$\mathbf{A} = \left.\frac{\partial \mathbf{f_x}}{\partial \mathbf{x}}\right|_{(\mathbf{x}^*,\mathbf{p}^*)} \qquad \mathbf{B} = \left.\frac{\partial \mathbf{f_x}}{\partial \mathbf{p}}\right|_{(\mathbf{x}^*,\mathbf{p}^*)} \tag{6.11}$$

were generated from the model equations. The quantity $\mathbf{f_x} = \mathbf{S} \cdot \mathbf{r}(\mathbf{x}, \mathbf{p})$ and $(\mathbf{x}^*, \mathbf{p}^*)$ denotes a point along the unperturbed model solution. The sensitivity equations required that we solve the model equations to evaluate the $\mathbf{A}$ and $\mathbf{B}$

matrices. Thus, we formulated the sensitivity problem as an extended kinetic-sensitivity system of equations [188]:

$$\begin{pmatrix} \dot{\mathbf{x}} \\ \dot{\mathbf{s}}_j \end{pmatrix} = \begin{bmatrix} \mathbf{S} \cdot \mathbf{r}(\mathbf{x}, \mathbf{p}) \\ \mathbf{A}(t)\,\mathbf{s}_j + \mathbf{b}_j(t) \end{bmatrix} \qquad j = 1, 2, \ldots, P \tag{6.12}$$

where $\dot{\mathbf{x}} = d\mathbf{x}/dt$ and $\dot{\mathbf{s}}_j = d\mathbf{s}_j/dt$. We solved the kinetic-sensitivity system for multiple parameters in a single calculation using the LSODE routine of OCTAVE (www.octave.org). The first-order sensitivity coefficients were then used to calculate the OSSC value for parameter j:

$$O_j(t) = \frac{p_j}{N_s}\left(\sum_{k=1}^{N_T}\sum_{i=1}^{N_s}\left[\frac{1}{x_i}\frac{\partial x_i}{\partial p_j}\bigg|_{t_k}\right]^2\right)^{1/2} \tag{6.13}$$

The terms N_T, N_s denote the number of time points considered and the state dimension of the model, respectively. To account for parametric uncertainty, OSSC values were calculated over the parameter ensemble. Parameters were ranked-ordered ($1 \leq \theta_j \leq 384$) based upon the magnitude of the OSSC value. Large values of θ_j indicated fragile or important interactions in the prostate network architecture. Conversely, small values of θ_j indicated robustness.

Each model in the ensemble was run to approximately steady state. At steady-state, 10nM DHT was added and the first order sensitivity coefficients were calculated for 100 seconds of simulated time. OSSC values were then calculated and the rank ordering determined. We collected interactions whose rank was at least one standard deviation above the mean rank calculated over all parameters. Highly ranked interactions were statistically significantly different between LNCaP clones if the null hypothesis could be rejected with 95% confidence via a t-test. To estimate significance, we performed a two variable unequal variance double tail t-test using the MATLAB (R) statistical toolbox (2007a, The Mathworks, Natick, MA).

6.3.4 Robustness analysis of functional protein markers.

Robustness coefficients of the form:

$$\alpha\left(i, j, t_o, t_f\right) = \left(\int_{t_o}^{t_f} x_i\left(t\right) dt\right)^{-1} \left(\int_{t_o}^{t_f} x_i^{(j)}\left(t\right) dt\right) \tag{6.14}$$

were calculated to understand the regulatory connectedness of functional protein markers in the LNCaP network. The robustness coefficient $\alpha\left(i, j, t_o, t_f\right)$ is the ratio of the integrated concentration of a network output in the presence (numerator) and absence (denominator) of structural or operational perturbation. Here t_0 and t_f denote the initial and final simulation time respectively. Simulations were taken of C-81 from approximate steady-state at t_0, 10nM of DHT was added at 1 hour and t_f was taken to be 72 hours after DHT addition. The network output was taken to be the network states. The quantity i denotes the index for a marker or reference species while j denotes the perturbation index, respectively. If $\alpha\left(i, j, t_o, t_f\right) > 1$, then the perturbation *increases* the output concentration. Conversely, if $\alpha\left(i, j, t_o, t_f\right) \ll 1$ the perturbation *decreases* the output concentration. Lastly, if $\alpha\left(i, j, t_o, t_f\right) \sim 1$ the perturbation does not influence the output concentration.

6.3.5 Calculation of steady-state synergy coefficients.

To understand the connectedness of subsystems in the prostate network following ERK and/or Akt knockdowns we computed synergy coefficients of the form:

$$\Delta_j = \frac{\delta x_{j,Erk+Akt} - \left(\delta x_{j,Erk} + \delta x_{j,Akt}\right)}{x_{j,total}} \tag{6.15}$$

The quantity $x_{j,total}$ denotes the steady-state concentration (flux) of species (interaction) j in wild-type C-81. The quantity $\delta x_{j,Erk}$ ($\delta x_{j,Akt}$) denotes the steady-state

concentration (flux) of species (interaction) j in the presence of an Akt (ERK) knock-out minus the basal value of quantity j. The term $\delta x_{j,Erk+Akt}$ denotes the steady-state concentration (flux) of species (interaction) j in wild-type C-81. If $\Delta_j > 0$, the quantity j has a positive synergy with Akt and ERK. In other words, the steady-state concentration (flux) of species (interaction) j in the wild-type was *greater* than the sum of the individual contributions in single Akt or ERK knock-downouts. Conversely, if $\Delta_j < 0$, the quantity j has a negative synergy with Akt and ERK. Lastly, if $\Delta_j \sim 0$ then there is no connection between quantity j and the Akt/ERK signaling axes.

6.4 Results

The objective of this study was to determine which signaling components were important in AI versus AD LNCaP cells. Toward this objective, we constructed and analyzed a mechanistic mathematical model of the androgen response of three different LNCaP prostate adenocarcinoma sub-lines. We investigated MAPK-dependent outlaw activation of AR in AD (C-33), mid-range (C-51) and AI (C-81) LNCaP cells [348, 334]. Our network model included: nuclear hormone and transmembrane growth factor receptor activation; transcriptional activity via the MAPK subsystem [302, 263, 171] together with outlaw activation of AR via MAPK [336, 339]; PI3K/AKT/TOR mediated translation initiation [172, 154]; the transcriptional and translational regulation of PSA, cyclin D and PAcP expression [341, 335]; and the regulation of Her2 activity by PAcP [347] (Fig. 6.4).

The network described 212 species and 384 interactions (Table C.1). Tran-

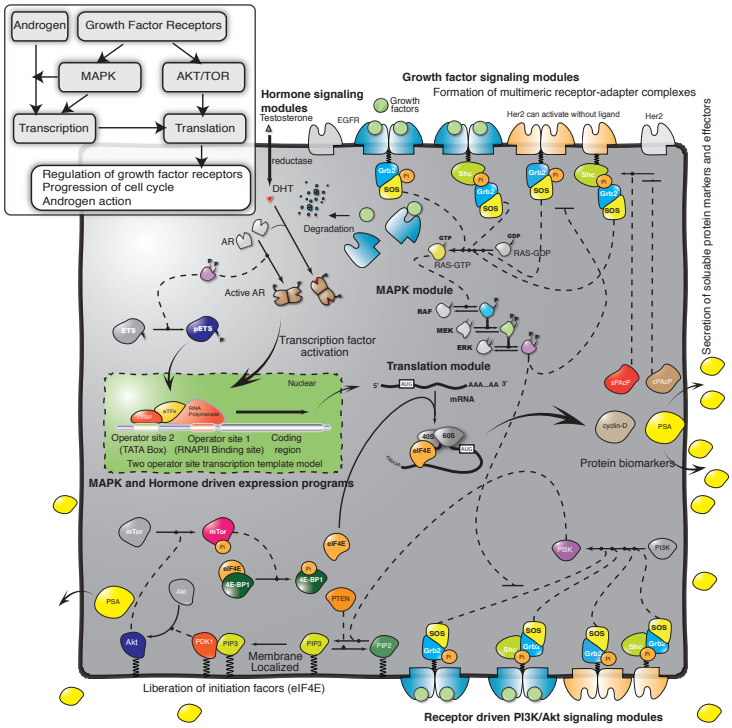

Figure 6.1: Schematic overview of the interaction network used in modeling the androgen response in prostate epithelial cells. The model architecture was formulated by aggregating molecular modules into a single network (see insert for high level details).

scription and translation were modeled using elementary reactions based on literature. Constitutive and regulated expression of PSA, cyclin D and the two forms of PAcP were considered in the model. The *total* level of all other model proteins was constant. We modeled the molecular interactions using mass action kinetic processes within an ordinary differential equation (ODE) framework. ODEs are a common method of modeling biological pathways and have been used to model a range of signal transduction processes [263, 264, 171, 23, 265, 266, 267, 268, 269, 349]. Mass action kinetics have also been used extensively, for example, to model receptor tyrosine kinase signaling [349], blood coagulation [268], pain networks [269] or Toll like receptor signaling

[350, 351]. They have also been a key component in the success of perturbation-response approaches which have shown that simple linear rules often govern the response behavior of biological networks [352]. The ODE model was deterministic and captured only population averaged behavior. While we assumed spatial homogeneity, we differentiated between cytosolic and membrane localized processes. We used mass-action kinetics to describe the rate of each molecular interaction. Thus, the 384 kinetic model parameters were mainly association, dissociation or catalytic rate constants. With one exception, model parameters were estimated and validated using LNCaP training data taken from literature sources (Table C.2). However, we were unable to estimate unique model parameters. Instead, we estimated a family or *ensemble* of parameters that was consistent with the training data. The ensemble allowed us to estimate the model uncertainty associated with the many poorly characterized parameters. We analyzed the model ensemble to better understand which architectural features were important in androgen dependent versus independence cells.

6.4.1 Estimating the ensemble of prostate model parameters.

Signal transduction models often exhibit complex behavior [305, 306, 307, 308]. It is often not possible to identify model parameters, even with extensive training data [309]. Thus, despite identification standards [310] and the integration of model identification with experimental design [311], parameter estimation remains challenging. In this study, an *ensemble* of plausible model parameters was estimated from AI and AD LNCaP sub-clones. Ensemble approaches have successfully addressed uncertainty in systems biology and other fields like weather prediction [167, 312, 269, 166, 313]. Their central value is the ability to con-

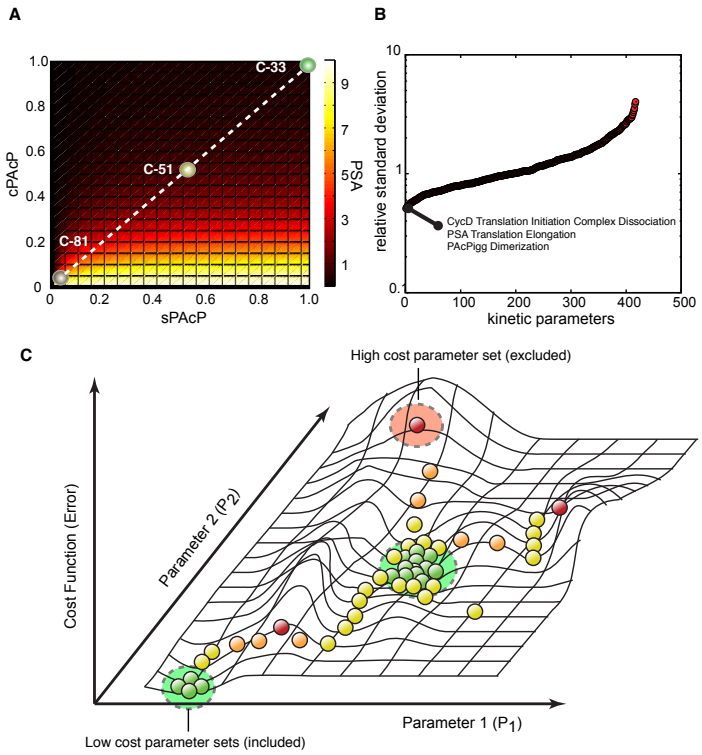

Figure 6.2: Identification and properties of the prostate model ensemble. **A**: Steady state PSA level as a function of cPAcP and sPAcP expression. The circles represent the values used to model the C-51 and C-81 LNCaP clones. All values are relative to C-33. **B**: Coefficient of Variation (CV; standard deviation of a parameter relative to its mean value) for the parameter ensemble used in this study. **C**: Parameter identification strategy. Multiple monte-carlo trajectories were used to randomly explore parameter space.

strain model predictions despite uncertainty. For example, Sethna and coworkers showed in a model of growth factor signaling that predictions were possible using ensembles despite incomplete parameter information (sometimes only order of magnitude estimates) [306]. They further showed that model ensembles were predictive using many different mathematical models [314]. The 420 unknown model parameters (384 kinetic constants and 36 non-zero initial conditions) were estimated using 14 time-series and steady-state training sets taken

from literature sources (Table S2). The parameter identification procedure used a maximum likelihood random-walk strategy with a correlation constraint to identify a diverse family of likely parameter sets (Fig. 6.4.1C). We generated 3210 possible parameter sets and selected 107 of these for inclusion in the final ensemble. The selection was made to minimize the correlation between possible sets (materials and methods). The majority of parameters had a Coefficient of Variation (CV) of greater than 100%. Thus, although the model qualitatively recapitulated the training data, many of the parameters were poorly constrained (Fig. 6.4.1B). However, parameters involved with key features such as cyclin-D and PSA expression were relatively well constrained (CV $\leq$ 50%). The low deviation of these parameters could be attributed to the abundance of PSA/cyclin D training data. Alternatively, it may suggest that these mechanisms had a large impact on model behavior. A single network structure described both Androgen Dependent (AD) and Androgen Independent (AI) training data with only two experimentally justified parameter changes. The parameters controlling the expression rate of cellular PAcP (cPAcP) and secreted PAcP (sPAcP) were reduced by a factor of 0.01 and 0.5, respectively, for the C-81 and C-51 cell-lines compared to C-33 (Fig. 6.4.1A). The PAcP expression scaling factors were chosen to correspond with measured steady-state PAcP expression ratios for the different cell-lines [353]. The kinetic parameters and non-zero initial conditions for C-33 are given in Table C.1 and Table C.3, respectively.

6.4.2 The ensemble of AI/AD LNCaP models recapitulated androgen action and the activity of the outlaw pathway.

AR can be activated by both hormone dependent and independent pathways. In this study, we considered both the traditional hormone dependent and MAPK mediated AR activation. We selected training data sets to constrain each mode of AR activation and the subsequent AR-driven gene expression program. The data of Lee *et al.,* was used to constrain the relationship between PSA expression and AR activation in AI and AD cells [335]. Activated AR was modeled as both a transcriptional activator of PSA expression [354] and a transcriptional represser of PAcP expression [341]. The model recapitulated the qualitative features of PSA expression at the protein level for C-81 and C-33 (Fig. 6.3B). Additionally, the basal and increased level of PSA mRNA following Her2 overexpression in C-33 was also well described (Fig. 6.4). The PSA mRNA data was taken from a separate LNCaP study [339]. The C-33 simulations recapitulated the observed lower PSA expression (~ 4 fold) compared to C-81 in the absence of androgen (Fig. 6.3B, initial point). Following DHT stimulation (10nM at t = 1 hr) PSA expression increased for both clones. However, the increase was more significant for C-33 (Fig. 6.3B). The study of Meng *et al.* was used to constrain the relationship between AR activation and PAcP expression [341]. The addition of DHT to C-33 cells decreased PAcP expression and increased Her2 phosphorylation (Fig. 6.3A). The model recapitulated the positive feedback between Her2 induced MAPK activation and androgen action. Several studies have demonstrated that MAPK can activate AR in the absence of hormone stimulation. Activated AR transcriptionally down-regulates cPAcP expression which in turn increases Her2 activation. Both Her2 dimerization along with the traditional

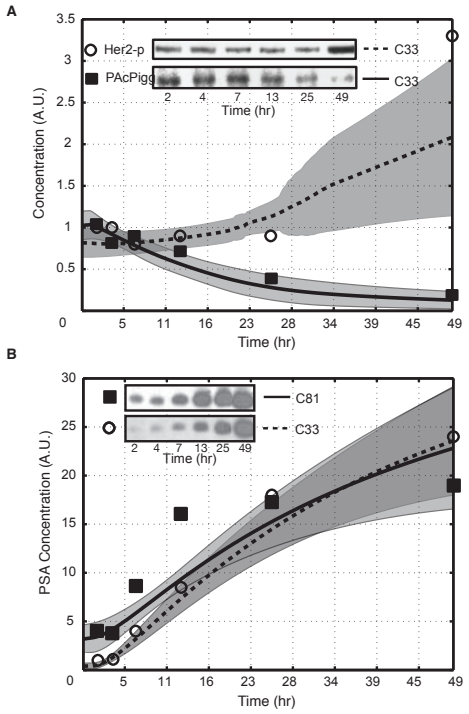

Figure 6.3: Simulation results for the addition of 10nm DHT at 1 hour to C-33 and C-81 LNCaP clones. **A**: Her2 phosphoralation (circles) and cPAcP expression (squares) for C-33 cells following the addition of DHT. **B**: PSA expression following the addition of DHT to C-81 (squares) and C-33 (circles) LNCaP clones.

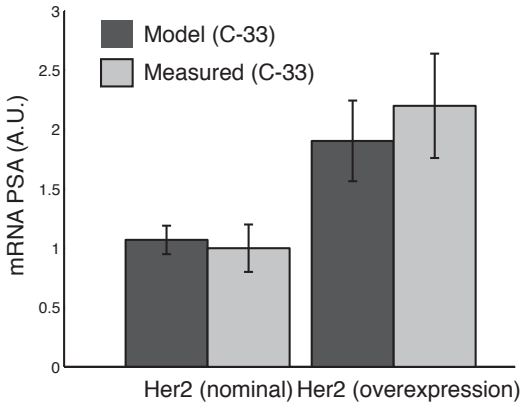

Figure 6.4: Simulated PSA mRNA levels in C-33 cells with and without Her2 overexpression. Her2 overexpression was modeled as a 50% increase in the expression rate of Her2.

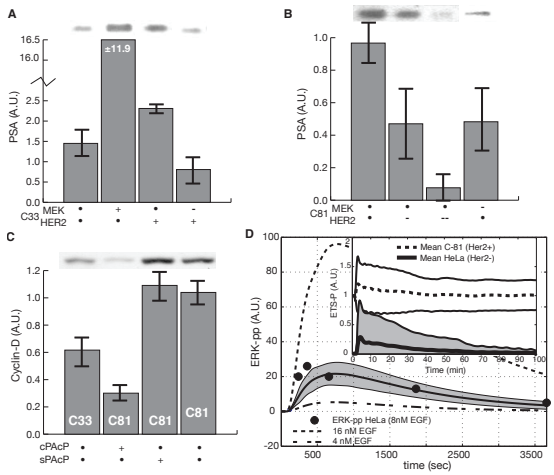

Figure 6.5: Simulation results for key species under androgen free conditions. **A**: Effect of HER2 and MEK overexpression on LNCaP C-33 steady state PSA levels. The inhibition of MEK blocks the effect HER2 overexpression. **B**: Effect of HER2 and MEK inhibition on LNCaP C-33 steady state PSA levels. The inhibition of either HER2 or MEK blocks high AIPC PSA levels. **C**: Effect of PAcP isoforms on LNCaP steady state cyclin D levels. Experimental data adapted from Lingappa and coworkers (Prosetta Corporation, unpublished data). **D**: Transient activation of ERK via ligand dependent EGF signaling (8nM EGF at t = 60s) in HeLa cells. Inset: Simulated phosphorylated ETS (ETSp) levels following the addition of 8nM EGF in the presence and absence of Her2.

EGFR-growth factor pathway can activate MAPK, leading to a positive feedback loop. However, typical growth factor induced MAPK activation is transient whereas de-regulated Her2 induced MAPK activation is persistent. The MAPK module in the model described both activation pathways. Growth factor dependent MAPK activation was constrained by dynamic measurements of phosphorylated ERK (ERKpp) levels following stimulation of EGFR with 8nM EGF (Fig. 6.5D). The EGF induced ERKpp data was taken from HeLa cells [171]. However, we expect transient EGF-induced MAPK activation in LNCaP cells will be qualitatively similar to HeLa given the conserved nature of mitogenic

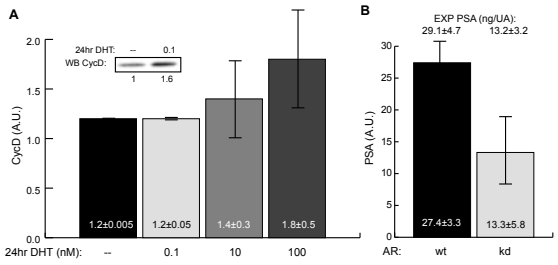

Figure 6.6: Independent model predictions versus experimental observations. **A** Ensemble prediction of cyclin D expression following the addition of DHT at 1 hour to C-33 clones. **B** Predicted effect of an AR knockdown on PSA expression following the addition of androgen at 1 hour to C-33 wild-type and C-33 AR knock-down clones.

signaling. We constrained Her2 induced MAPK activation using cyclin D protein expression data in C-33 and C-81 cells without androgen following PAcP expression (Fig. 6.5C). Cyclin D expression was coupled to ERK through the ETS and AP1 transcription factors, both of which activate cyclin D expression [298]. Her2 induced MAPK activation led to a persistent ETSp signal compared to ETS activation following EGFR-induced MAPK activation (Fig. 6.5D, inset). Nominally, C-33 cells have lower cyclin D expression compared to C-81 (Fig. 6.5C, lane 1 and 4). The difference in cyclin D expression between C-33 and C-81 cells was qualitatively consistent with increased C-81 proliferation [334]. While the expression of cPAcP in C-81 reduced cyclin D levels (Fig. 6.5C, lane 2), sPAcP expression resulted in no change (Fig. 6.5C, lane 3). Furthermore, the model *predicted* a dose dependent increase in C-33 cyclin D levels 24 hours after addition of DHT (Fig. 6.6A). Although the cyclin D increase is only notable in response to high levels of DHT (10 or 100nM) the prediction is qualitatively consistent with experimental data *not* included in the ensemble calculations [355]. To further constrain the relationship between MAPK, Her2 and AR activation, we used the Her2 perturbation study of Lee *et al.* [335] in the ensemble calcu-

lations. Because the perturbation magnitudes were not reported, we assumed ±50% for all changes. Where possible, this assumption was validated by analyzing the corresponding Western blots using the GelEval software package (v1.22, Frog Dance Software). The ±50% perturbation magnitude was approximately consistent with the published blots. A 50% increase in Her2 led to an approximately 50% increase in PSA expression in C-33 without androgen (Fig. 6.5A, lanes 1 and 3). While a 50% decrease in Her2 in C-81 led to a similar decrease in PSA secretion (Fig. 6.5B, lanes 1 and 2). Further disruption of Her2 effectively blocked PSA expression in C-81 without androgen (Fig. 6.5B, lane 3). A 50% reduction of MEK, one of the three primary protein kinases in MAPK, resulted in reduced PSA expression in C-81 (Fig. 6.5B, lane 4). While a 50% increase of MEK in C-33 increased PSA expression by 5-fold (Fig. 6.5A, lane 2). The combination of MEK inhibition and Her2 activation (50% increase in Her2 and a 50% decrease in MEK) decreased PSA expression in C-33 (Fig. 6.5A, lane 4). Furthermore, the model *predicted* an increase in C-33 PSA levels 72 hours after a 2nM addition of the androgen testosterone. Simulations performed with 10% of the AR initial condition predicted an approximate 50% decrease in testosterone stimulated PSA (Fig. 6.6B). The reduced PSA levels are consistent with reported experimental data on AR antisense knock-downs in androgen dependent LNCaP cells [356]. This data was *not* included in the ensemble calculations. Taken together, the model replicated qualitative features of the relationship between MAPK, AR activation and androgen action. In addition, the qualitative agreement between model and experiments for PSA and cyclin D expression suggested that the transcription and translation subsystem models were operating correctly.

6.4.3 Sensitivity analysis revealed key subsystems in AI and AD cells.

Sensitivity analysis identified interactions important in C-33, C-51 and C-81 cells (Fig. 6.7 and Table C.4). We calculated overall State Sensitivity Coefficients (OSSCs) for the three LNCaP clones over the parameter ensemble (materials and methods). The OSSC values were ranked-ordered based on their absolute magnitude. The dissociation of AR from Heat Shock Proteins (HSP), components of the Akt signaling axis and MAPK activation were important (top 2% of sensitive interactions) irrespective of androgen status. Sequestered AR was unable to become activated by androgens or MAPK. Thus, increased AR-HSP dissociation promoted increased AR activation and AR-driven gene expression. Several components of the MAPK cascade were also important including Ras binding to GAP and Raf, and the dephosphorylation of ERK. The sensitivity of MAPK was not unexpected. ERK was critical to outlaw activation of AR. Moreover, ERK activation was modeled as being Ras dependent. We also found the Akt signaling axis to have components in the top 2% of sensitive interactions irrespective of androgen status. For example, the formation of PIP3, an early step in the PI3K/Akt signaling axis regulated by PTEN, was found to be highly sensitive in all clones. Looking beyond the upper 2% of sensitive interactions, additional common mechanisms were identified. These included AR interactions with DHT, recruitment of adapter molecules by Her2, activation of ERK by MEKpp and additional regulation of PIP3 formation by PTEN.

Translation interactions became more fragile while transcription became more robust with increasing androgen independence. Her2 auto-activation and Her2 cPAcP interactions were also increasingly important with increasing an-

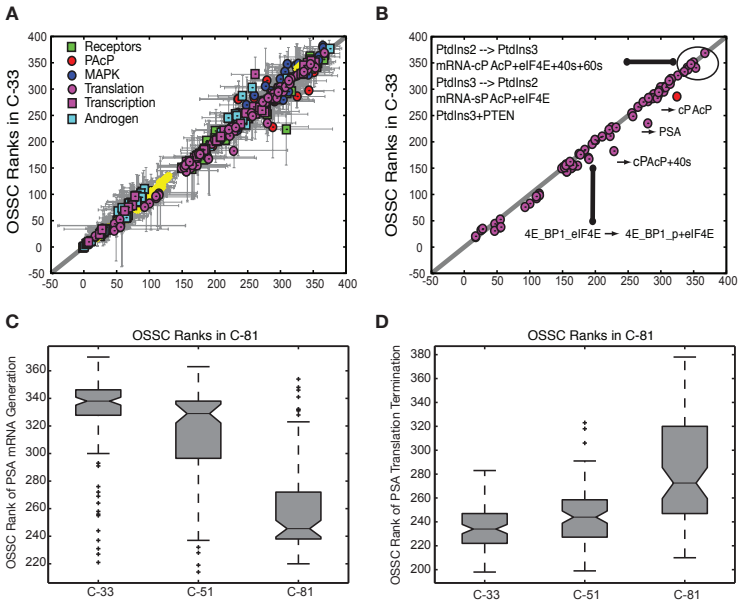

Figure 6.7: Sensitivity analysis of the model parameters. **A**: Comparison of the mean OSSC parameter ranks for the C-33 and C-81 LNCaP models. **B**: Comparison of the mean OSSC parameter ranks for translation mechanisms (including the role of Akt signaling in translation initiation) in C-33 versus C-81 LNCaP clones. **C**: The final mechanism in PSA transcription becomes increasingly more robust w.r.t cancer aggressiveness, as indicated by a significant reduction in mean OSSC Rank. **D**: The final mechanism in PSA translation (translation termination) was increasingly fragile w.r.t cancer aggressiveness, as indicated by a significant increase in mean OSSC rank.

drogen independence. The difference in the importance of interactions in AI versus AD LNCaP clones was estimated by computing shifts in the sensitivity rankings (Table C.5). In addition to considering C-33 and C-81, we analyzed a third clone, C-51, which was moderately androgen dependent. There were 117 statistically significant shifts (52 more and 65 less sensitive) between the C-81 and C-33 clones. However, only 14 shifts were larger than one standard above the mean shift. Of the 14 large shifts, 50% involved PSA and PAcP translation while the remainder were associated with Her2 and cPAcP. Conversely,

PSA transcription became more robust with increasing androgen independence. Similarly, when comparing C-33 to C-51, PSA translation and Her2 activity became more sensitive with increasing androgen independence. Inspection of the importance of the final step in PSA transcription and translation among the individual models in the ensemble showed a shift away from transcription (Fig. 6.7C) toward translation (Fig. 6.7D) across the population of models. The increasing importance of translation was not limited to PSA, although PSA was the most significant example. Globally, 16 of the 52 interactions that were more sensitive in C-81 involved translation while only 4 of 52 involved transcription. No translation mechanisms became more robust in C-81 compared to C-33. Similar to PSA, translation of other key proteins such as cPAcP became more sensitive in C-81 versus C-33. Of the statistically significant shifts, 7/9 of the cPAcP translation interactions were more sensitive in C-81. Additionally, both mechanisms for the phosphorylation of 4E-BP1 by TOR kinase, a key step in translation initiation that liberates eIF4E, were also more importance in C-81. Taken together, the sensitivity analysis suggested that the fragility of the translational subsystem directly correlated to androgen independence.

To quantify the effects of perturbing key species in C-81 clones we preformed robustness analysis on four functional protein markers. The initial conditions of seven key protein species were altered by a factor of 10, .1 or 0 for knock-in, knock-down or knock-out perturbations, respectively. We then calculated the effect of these perturbation on cyclin D and PSA expression levels along with ERK and AR activation levels. Perturbation of Raf, MEK or ERK had similar effects on the functional markers with ERK being the most notable (Fig 6.8 lanes 1, 2 and 3). Trivially, ERK perturbations directly effected ERK activation levels. However, more importantly, ERK perturbations greatly effected cyclin D

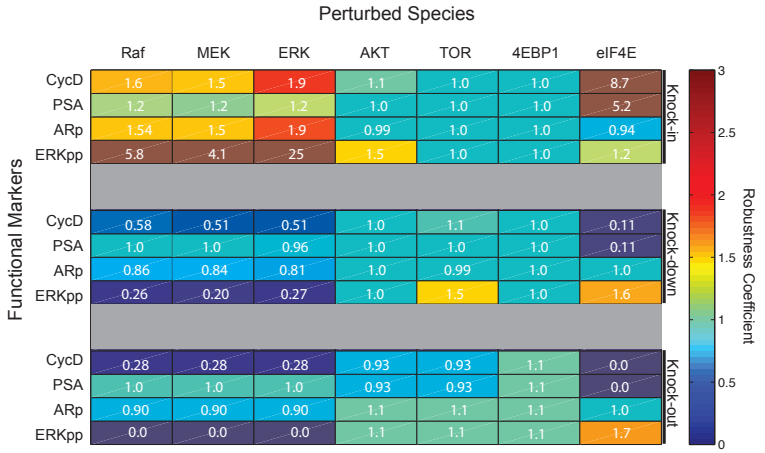

Figure 6.8: Robustness analysis of functional protein markers. The expression level of seven key proteins was altered by a factor of 10, .1 or 0 (knock-in, knock-down or knock-out) and robustness coefficients.

expression levels. ERK knock-ins approximately doubled cyclin D while ERK knock-outs reduced cyclin D to less then one third of wild-type levels. The functional markers were robust to perturbations in AKT and TOR with differing effects on ERK activity and slight decreases in expression levels upon AKT or TOR knock-out (Fig 6.8 lanes 4 and 5). Furthermore, the translation initiation factor eIF4E demonstrated a limiting reagent behavior in the expression of both cyclin D and PSA while perturbations in 4E-BP1 had little effect (Fig 6.8 lanes 6 and 7). However, the 4E-BP1 results could be an artifact of artificially high background levels of eIF4E as no direct eIF4E measurements were included in the training data. Knock-in simulations of eIF4E demonstrated an 8.7 and 5.2 fold increase in cyclin D and PSA expression. Reduction of eIF4E resulted in a 89% loss of expression and, full knock-out simulations predicted a complete loss of cyclin D and PSA.

6.4.4 The MAPK and Akt pathways synergistically activated cyclin D expression.

Complex systems composed of interacting subsystems can display emergent properties that are not explained by the individual subsystems alone [357]. In cancer biology, it is common to speak of signal transduction pathways as if they were isolated. In reality, these components are highly interconnected and can interact in a variety of ways sometimes leading to unpredictable behavior. In this study, we explored whether the MAPK and Akt signaling axes synergistically activated the expression of cyclin D. We compared the steady-state cyclin D expression in Akt and ERK knock-outs with wild-type C-81 cells in the absence of androgens. At steady-state, the MAPK and Akt pathways synergistically ($\Delta_{cycD} > 0$) activated cyclin D expression in C-81 cells without androgen (Fig. 6.9A). Thus, steady-state cyclin D expression was *greater* in wild-type cells (Akt^+-ERK^+) than the linear combination of cyclin D expression in Akt^--EKT^+ and Akt^+-ERK^- cells. The above-additive (superlinear) cyclin D expression was statistically significant within a 95% confidence interval. However, the relatively large standard deviation suggested that cyclin D expression varied widely across the ensemble. To address this, we inspected every model in the ensemble and found that each predicted an above-additive increase in cyclin D expression (data not shown). Superlinear cyclin D expression may be the result of positive synergy between the MAPK and translation subsystems. To elucidate the underlying mechanisms responsible for synergy we expanded the analysis to include all modeled species (both proteins and protein complexes) and rates. Many functional network subunits demonstrated no statistically significant deviations from additive behavior (Fig. 6.9C, grey). However, 22 species

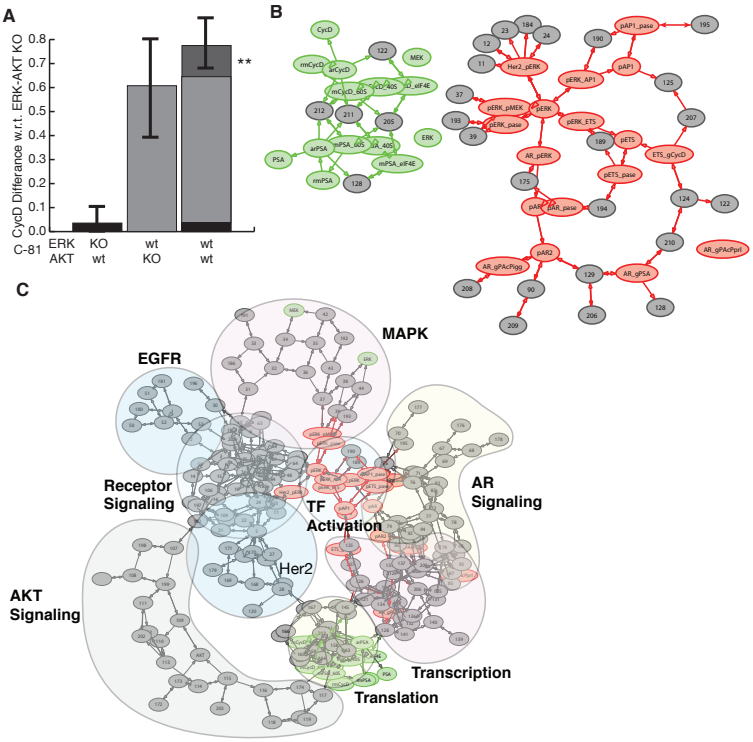

Figure 6.9: Synergy analysis between the ERK and Akt signaling axes in LNCaP C-81 cells. The double ERK and Akt knock-out was used as the control. **A**: The difference in steady state cyclin D expression (compared to the control) with the knock-in of Akt (left), ERK (center) and both (right). **B**: Species and interactions that demonstrated a positive (negative) synergy are shown as green (red) in the connectivity diagram. Species or interactions not effected are shown in grey. **C**: The full connectivity diagram qualitatively clustered in functional groups. Positive (negative) synergy are shown in green (red) in the connectivity diagram.

(79 interactions) were negatively coupled to Akt/ERK ($\Delta_j < 0$; Fig. 6.9B, red) while 14 species (37 interactions) had a positive synergy ($\Delta_j > 0$; Fig. 6.9B, green). Synergy between the MAPK and Akt signaling subsystems negatively effected transcription factor activation. Phosphorylated ERK (ERKpp) activated AR (pAR), and the transcription factors AP1 and ETS all showed a below additive response (Fig. 6.9B). Conversely, positive synergy was almost exclusively

limited to translation interactions. The binding of eIF4E, 40S and 60S ribosomes to form the mRNA initiation complex, elongation and termination steps all had positive synergy with ERK/Akt knockdowns (Fig. 6.9B).

6.5 Discussion

A critical milestone in prostate cancer progression is the onset of androgen independence. In this study, we formulated and analyzed an ensemble of mathematical models of the androgen response of AI and AD LNCaP prostate cancer epithelial cells. The model ensemble was identified using 14 different steady-state and dynamic data sets taken from literature. With the exception of one study, all the training data was generated in LNCaP cell-lines. We estimated which molecular subsystems were important in AI versus AD cells using sensitivity analysis. For example, the assembly and regulation of Her2 adapter complexes and the regulation of ERK were sensitive irrespective of androgen status. The dissociation of AR from HSP was also in the top 2% of sensitive interactions for both C-33 and C-81. On the surface, the importance of AR in C-81 was surprising as the proliferation of C-81 is androgen independent. However, AR can be activated independently of androgen, thus, the presence of androgen is not required for androgen action [336, 358]. The differentiating factor between the AI and AD models described here was the expression rate of PAcP conformers. We demonstrated the ability of decreased PAcP expression to describe the PSA levels of increasingly androgen independent sub-lines. Moreover, interactions involving Her2 auto-phopshporylation, cPAcP availability and cPAcP phosphatase activity were significantly more fragile in C-81 versus C-33. These results suggest that the regulation of the phosphorylation state of Her2 by cPAcP

may be a critical interaction controlling androgen action in the absence of hormone signals. Experimentally this has been demonstrated as forced expression of PAcP is sufficient to suppress C-81 xenograft tumor growth [359].

Model analysis suggested that translation interactions were more fragile and transcription more robust in AI versus AD cells. Globally, 16 of the 52 interactions that were more sensitive in C-81 involved translation while only 4 of 52 involved transcription. Moreover, no translation mechanisms became more robust in AI versus AD cells. The importance of translation in more aggressive cancers (increasing androgen independence) may be due, in-part, to synergies between the Akt and MAPK pathways. Simulations of ERK and/or Akt knockouts showed an above-additive response almost exclusively limited to translation upon the simultaneous reinstitution of Akt and ERK. *In-vivo* studies of AIPC have demonstrated positive synergies between the MAPK and Akt pathways. Gao *et al.* observed above-additive tumor growth rates in castrated and mock nude male mice upon the forced expression of constitutively active Akt and B-Raf^{V600E} [360]. These experiments suggest that cell proliferation may be regulated by a complex integration of the MAPK and Akt signaling axes. Our robustness analysis suggested that independent perturbations in TOR and AKT may have little or no effect on AIPC. However, we observed the possibility of an inverse relationship between TOR and ERK activation. This suggests that if TOR or Akt were to be independently targeted, AKT might be a more suitable therapeutic target. Additionally, we observed that perturbations in Raf, MEK and ERK had a similar effect on cyclin D but not PSA expression, with ERK being more pronounced. Current therapeutics such as trastuzumab or gefitinib, which target either Her2 or EGFR respectively, have had little efficacy against hormone-refractory prostate cancers [361, 362]. Our results suggest that

a possible factor in their lack of effectiveness is that they fail to address synergy between growth factor signaling, MAPK activation and the Akt signaling axes. Our analysis also demonstrated that translation mechanisms were generally more sensitive in increasingly androgen independent models. The translation results suggest that the direct targeting of the translation machinery may be useful for the treatment of AIPC. Our robustness analysis identified eIF4E as a limiting reagent in the expression of both cyclin D and PSA in C-81 clones. Soni *et al.* demonstrated the effectiveness of directly targeting eIF4E in breast cancer. Down-regulation of eIF4E resulted in decreased cyclin D expression and decreased growth rate without the deleterious effect of inhibitors such as rapamycin which act further upstream [363]. Previous modeling studies from our laboratory have also demonstrated the importance of translation beyond cyclin D [161]. However, the current model has only a basic description of translation initiation. Moreover, translation parameters were only indirectly trained from the PSA mRNA and protein data. Thus, while the initial robustness and sensitivity results are encouraging more studies are needed.

Analysis of the ensemble of AI models suggested the Akt and MAPK pathways synergistically enhanced cyclin D expression by up-regulating translation. Cyclin D is expressed early in the cell cycle and a point of convergence in the proliferative action of multiple receptors [364]. Many studies have identified a direct correlation between cyclin D regulation and prostate cancer, as well as breast and non-small cell lung cancer [365, 366, 367]. Balk *et al.* demonstrated that increased cyclin D expression in PTEN$^{-/-}$ LNCaP cells following DHT addition was largely because of increased translation [368]. PTEN loss and presumably the activation of Akt has been implicated with increased translation and the resistance to therapeutics which target Her2 and EGFR [369, 370]. However,

the underlying mechanism responsible for the increased translation in the Balk *et al.* study was not solely AKT dependent. Early translation activation was due to PI3K/Akt signaling but TOR activation at later time points was Akt independent. One key difference between the modeling and the Balk *et al.* study was the binding of activated AR with the regulatory subunit of PI3K. This interaction, which was not included in the model, was at least partially responsible for TOR activation and the eventual liberation of eIF4E. In addition to direct AR binding, PI3K (and subsequently TOR) can be activated through receptor adaptor complexes such as those associated with Her2. In the model, PI3K was activated by androgen (in the absence of growth factor) because of the down-regulation of cPAcP expression by activated AR. Upregulated PI3K then drove Akt dependent activation of TOR which led to enhanced liberation of eIF4E from 4E-BP1. Thus, while the initiating events driving TOR activation were different, the subsequent up-regulation of cyclin D translation was similar. This suggests that the model prediction of a complex synergy between interacting signaling axes may be valid. It also suggests a falsifiable hypothesis that cPAcP could be critical to enhanced translation following androgen stimulation.

The role of mechanistic mathematical modeling in drug design remains unclear. A common criticism of such techniques has been the poorly characterized effect of model uncertainty. Model uncertainty has two forms. Structural uncertainty is defined as uncertainty in the biology, while parametric uncertainty is defined as incomplete knowledge of parameter values. In this study, parametric uncertainty was minimized by considering a family of consistent models instead of a single best-fit but uncertain model. While model ensembles often poorly constrain individual parameter values, they may robustly constrain model predictions [314]. Structural uncertainty was addressed by considering

only molecular interactions supported by experimental evidence. However, the current model contained some abstracted pathways and should be expanded to include additional biology. For example, the analysis highlighted the importance of translation. However, the current model contains a limited description of initiation factor activation and the assembly of the 80S initiation complex. A more detailed translation interaction network could further refine which translation components were important in AI versus AD cells. Another example is the mechanism by which AR transcriptionally regulates the expression of target genes. In the current model we ignored the role of transcriptional co-regulators and assumed activated AR functioned alone. While this is a reasonable first approximation, well known co-repressors and activators [371] such as ARA70 [372] should be included. The regulation and activity of these co-regulators may be different in AI versus AD cells and could enhance the list of differentially important targets. Additionally, a nuclear compartment and enhanced cell cycle and cell death subnetworks should be added to the model. These additional networks could be critical to understanding cell proliferation and survival effects in AI versus AD cells. For example, androgen and AR are known to regulate several components of the G1-phase of the cell cycle in prostate cells, not just cyclin D [373]. Moreover, the model describes the activation of Akt in the context of translation initiation, but not its well know survival functions [374, 375]. Lastly, given the importance of EGFR and Her2 induced MAPK activation in the current study and the therapeutic emphasis on receptor inhibition we plan to include a more complete receptor signaling network. Other receptors, IGFR and IL-6R have also been implicated in prostate cancer [376, 377, 378]. Understanding the signaling associated with these receptors and their downstream targets should be considered and will provide a better representation of how

intra- extra-cellular communication drives cell fate decisions. Furthermore, the application of advanced sampling techniques may allow for a more exhaustive investigation of parameter space. For example, multi-objective optimization ensemble techniques could be used to balance conflicts in the training data [269]. Additionally, understanding the topological details of the cost function in an extended parameter space could provide statistical information on kinetic rates and initial conditions. Other techniques, for example the calculation of the mutual information matrix, could also provide insight into correlations between model interactions. Also, computation of second order sensitivity coefficients would allow the identification of possible synergies in the model. Thus, we expect that deeper insight could be generated by extending the network structure and through the application of advanced model analysis tools.

CHAPTER 7

CONCLUDING REMARKS AND FUTURE DIRECTIONS

7.1 Conclusions

This objective of this thesis was to understand the molecular mechanisms controlling critical cellular functions such as growth, reproduction and cell differentiation computationally and gain valuable insight which could be used directly in treatment strategies for various cancers. Towards this aim we first studied three different published models of cell cycle to show the validity of our modeling and analysis methods. Our computational analysis of these well-established systems suggested that cell-cycle models follow the Highly Optimized Tolerance (HOT) paradigm. They exhibit the "robust yet fragile" property, a common phenomenon exhibited by all evolved networks. Our work on these models also revealed a list of fragile proteins, which correlated well with the targets currently pursued in clinical trials. Thus, we showed that computationally derived novel targets are of potential therapeutic value. Our analysis of one of the cell cycle models revealed protein translation as a major fragile sub-sytem. We constructed a detailed mechanistic model of protein translation initiation and validated it using a novel ensemble approach. The ensemble approach allowed us to overcome several different challenges and offered many advantages over the traditional approach used in literature. For e.g., kinetic rates of biological interactions are often not exactly known and can vary order-of-magnitudes in their values. By using an ensemble of parameters we can better capture this diversity in rates and explore a variety of scenarios. Because of our approach we were able to faithfully replicate both steady state *in vivo* and dynamic *in vitro*

data within a common framework. It also enabled us to overcome the handicap of parametric uncertainty, a hallmark of such models. Innovative analysis methods such as coupling coefficients and *in silico* knockout and over-expression experiments allowed us to analyze the entire model on a system wide scale. We discovered the critical role of proteins such as Akt and eIF4E, emerging due to an interplay of connected sub-systems. A study of signaling pathways of importance in Prostate cancer was done to understand the change in the nature of the biological system as it underwent a transition towards increasing androgen independence. In the prostate study, we introduced a computational method to quantify the interdependence between any two states using coupling or robustness analysis. Our results revealed a synergy between the MAPK and the Akt pathway and the increasing importance of protein translation as cells moved towards androgen independence. Molecular mechanisms playing an important role in cell differentiation were studied in detail both computationally and experimentally. An experimental study elucidating the effects of Arsenic Trioxide on a myeloblastic cell line (HL-60) revealed that cellular differentiation is directly affected by sustained activation of MAPK. Our studies showed that Arsenic Trioxide cooperated with All Trans Retinoic Acid (ATRA) to enhance cellular differentiation. The increase in differentiation was a result of concomitant increase in the activation of components of MAPK signaling cascade. Our studies revealed a synergistic response in case of combined Arsenic Trioxide and ATRA treatment and suggested a direct role of sustained MAPK activation in cell differentiation logic. With computational modeling and analysis of differentiation program in HL-60 cells, we presented a systematic framework to study programmed differentiation. That the model was able to recapitulate experimental results qualitatively, despite structural and parametric uncertainty

suggests that our approach can be extended to study other cellular programs with confidence.

7.2 Future Directions

This thesis established a detailed framework for the study of cellular programs of critical importance in cancers. The tools presented here are easily extendable to a variety of biological systems and the computational tools developed are model agnostic. We would like to see the present work advanced both on a biological as well as computational level. With the advent of highly powerful computers, modeling ultra-scale networks is perhaps no longer intractable. Therefore, we would like to see much more biological details being added to the our networks. Specifically, the translation initiation network now describes the response to a generic growth factor input, we would like it to be tailored to model specific kinds of growth factors, e.g., Platelet Derived Growth Factors (PDGF) and Insulin. Similarly, adding components such as phosphorylation events of eIF4E and other binding partners of mTOR would give the model a much more solid biological basis. Addition of a full translation network to the present prostate cancer study and the HL-60 model to understand differentiation would contribute towards making them more faithful representations of underlying real events. As the response of cell surface markers like CD38 and CD11b is measured to study differentiation experimentally, addition of these markers and their interactions is needed to make the model more realistic. Apart from addition of biological complexity, novel mathematical and computational techniques would be required to handle and analyze these complex networks. Towards this end, application of fast solvers routines such as SUNDIALS

(https://computation.llnl.gov/casc/sundials/main.html) would help in reducing the computation time associated with solving and analyzing the models. This becomes a critical issue as the size of networks grows geometrically. Another area of possible improvement is the method to select parameter sets in the ensemble method. Incorporation of optimization techniques such as multi-objective thermal annealing sampling method would allow us to select more diverse parameter sets. This approach can thus allow us to explore more diversity in kinetic rate constants. Our experimental study was focussed on the co-operation between Arsenic Trioxide and Retinoic Acid to enhance cell differentiation. Our study also revealed that addition of Arsenic Trioxide leads to a reduction in the growth rate of HL-60 cells. Investigating the mechanistic basis of this decreased growth rate would help in clearly establishing the reasons behind stunted growth in HL-60 cells and would elucidate the effects of Arsenic Trioxide on cell differentiation programs better. As treatment with Arsenic Trioxide in case of relapsed cancers has shown positive results clinically, a laboratory study on the effects of Arsenic Trioxide on RA resistant cell lines is needed to fully understand the mechanisms behind its efficacy. The ultimate goal of this study is to computationally provide novel targets of therapeutic value in cellular systems. Towards this aim, it is important that the targets generated *in silico* are regularly tested in the laboratory to ultimately enhance clinical efficacy and increase therapeutic options.

APPENDIX A

CHAPTER 1 OF APPEDIX

Table A.1: Comparison of OSSCs calculated for G1/S model of Qu *et al.*,.

Reaction	Cluster	OSSC-BDF	OSSC-FD	OSSC-ODE15s
		$\mu \pm \sigma$	$\mu \pm \sigma$	$\mu \pm \sigma$
Dephosphorylation of *a*CDC25	I	0.6252 ± 0.2980	0.6314 ± 0.2667	0.6942 ± 0.2518
Degradation of *a*CycE-Cdk2	I	0.5854 ± 0.3452	0.6373 ± 0.3403	0.6756 ± 0.3423
Concentration of E2F	I	0.5710 ± 0.3247	0.6744 ± 0.3062	0.6469 ± 0.2958
Synthesis of CycE	I	0.4583 ± 0.3364	0.5131 ± 0.3476	0.6063 ± 0.3502
Generation of *a*CKIs	II	0.4513 ± 0.2577	0.5297 ± 0.2540	0.5494 ± 0.2320
Concentration of pRb	II	0.4429 ± 0.2982	0.5224 ± 0.2827	0.5238 ± 0.2725
Phosphorylation of *i*CDC25	II	0.4442 ± 0.3245	0.4349 ± 0.2905	0.4803 ± 0.2856
Synthesis of *i*CDC25	II	0.3952 ± 0.1934	0.4535 ± 0.2015	0.4801 ± 0.1690
Synthesis of CycD	II	0.3367 ± 0.2230	0.3984 ± 0.2340	0.4376 ± 0.2411
Formation of *i*CycE-Cdk2	II	0.3590 ± 0.2275	0.4053 ± 0.2656	0.4271 ± 0.2417
Dephosphorylation of *i*CKIs	II	0.3841 ± 0.2557	0.4101 ± 0.2428	0.4271 ± 0.2361
Degradation of *i*CDC25	II	0.3198 ± 0.2129	0.3711 ± 0.2436	0.3789 ± 0.2239
Formation of CycE-Cdk2-CKI	II	0.3410 ± 0.1997	0.3655 ± 0.2106	0.3706 ± 0.1731
Dissociation of CycE-Cdk2 complex	II	0.3023 ± 0.2626	0.3343 ± 0.2946	0.3428 ± 0.3002
Degradation of CycE	II	0.2671 ± 0.2791	0.3163 ± 0.3165	0.3250 ± 0.3262
Phosphorylation of *a*CKIs	II	0.2909 ± 0.2459	0.2705 ± 0.2017	0.3182 ± 0.2099
Degradation of CKIs	II	0.2678 ± 0.2556	0.2985 ± 0.2803	0.2921 ± 0.2618
Formation of CycD-Cdk4/6	III	0.1987 ± 0.1312	0.2325 ± 0.1410	0.2639 ± 0.1485
Dissociation of CycE-Cdk2-CKI	III	0.2623 ± 0.2512	0.2647 ± 0.2722	0.2585 ± 0.2563
Degradation of CycD	III	0.1867 ± 0.1654	0.2194 ± 0.1786	0.2575 ± 0.1910
Phosphorylation of CDC25 by *a*CycE-Cdk2	III	0.2096 ± 0.2617	0.2472 ± 0.3047	0.2322 ± 0.2888
*i*CycE-Cdk2 → *a*CycE-Cdk2	III	0.2057 ± 0.2446	0.2358 ± 0.2828	0.2318 ± 0.2893

Table A.1 (Continued)

Reaction	Cluster	OSSC-BDF	OSSC-FD	OSSC-ODE15s
		$\mu \pm \sigma$	$\mu \pm \sigma$	$\mu \pm \sigma$
Formation of CycD-Cdk4/6-CKI	III	0.1801 ± 0.1130	0.2054 ± 0.1164	0.2268 ± 0.1232
Rate constant for pRb dephosphorylation	III	0.3945 ± 0.3126	0.2016 ± 0.1152	0.2260 ± 0.1164
Degradation of *i*CKI	III	0.1678 ± 0.1646	0.1644 ± 0.1642	0.2077 ± 0.1815
E2F dependent CycE expression	III	0.2219 ± 0.2849	0.2432 ± 0.3064	0.2064 ± 0.3020
Dissociation of CycD-Cdk4/6-CKI	III	0.1867 ± 0.1654	0.1993 ± 0.1443	0.2046 ± 0.1376
*a*CycE-Cdk2 regulated pRb phosphorylation	III	0.1551 ± 0.1055	0.1812 ± 0.1122	0.2008 ± 0.1127
Rate constant for CKI phosphorylation	III	0.1638 ± 0.2232	0.1998 ± 0.2602	0.1911 ± 0.2547

Table A.2: Comparison of OSSCs for the G2-DNA damage model of Aguda.

Reaction	Cluster	OSSC-BDF	OSSC-FD	OSSC-ODE15s
		$\mu \pm \sigma$	$\mu \pm \sigma$	$\mu \pm \sigma$
pMPF → MPF, catalyzed by aCdc25	I	0.8759 ± 0.1475	0.8910 ± 0.1271	0.9924 ± 0.0739
aCdc25 → iCdc25	II	0.7676 ± 0.1442	0.7703 ± 0.1181	0.8845 ± 0.0920
Generation of preMPF	II	0.9413 ± 0.1214	0.9720 ± 0.0838	0.8684 ± 0.1130
$iCdc25_{cyto.}$ →$iCdc25_{nuc.}$	II	0.9270 ± 0.1164	0.9417 ± 0.0938	0.8356 ± 0.1014
iCdc25 → aCdc25, catalyzed by MPF	II	0.5728 ± 0.2291	0.5010 ± 0.1422	0.2835 ± 0.1517
Generation of p21	III	0.4860 ± 0.1784	0.5031 ± 0.1949	0.2835 ± 0.1517
Degradation of p21	III	0.4833 ± 0.1760	0.4854 ± 0.1838	0.2812 ± 0.1481
p21 + MPF → p21-MPF	III	0.3382 ± 0.1406	0.3413 ± 0.1504	0.2017 ± 0.1248
p21-MPF → p21 + MPF	III	0.3352 ± 0.1373	0.3254 ± 0.1438	0.1979 ± 0.1172
Generation of 14-3-3σ protein	III	0.3434 ± 0.1250	0.3802 ± 0.1459	0.1913 ± 0.1060
Degradation of 14-3-3σ protein	III	0.3421 ± 0.1247	0.3625 ± 0.1390	0.1909 ± 0.1059
Wee1 → Wee1P, catalyzed by MPF	III	0.3214 ± 0.1338	0.3274 ± 0.1489	0.1739 ± 0.0878
Wee1P → Wee1	III	0.3078 ± 0.1306	0.2993 ± 0.1381	0.1666 ± 0.0855

Table A.3: Comparison of OSSCs for Tyson and Novak model. Three different numerical methods were used to solve the sensitivity equations; OSSC-BDF: 3rd order fixed step-size backward difference method (implicit); OSSC-FD: forward-finite difference (explicit); and OSSC-ODE15s: 5th order variable step-size backward difference routine (implicit) from the Matlab (The Mathworks, Natick MA) ODE suite.

Reaction	**Cluster**	**OSSC-BDF**	**OSSC-FD**	**OSSC-ODE15s**
		$\mu \pm \sigma$	$\mu \pm \sigma$	$\mu \pm \sigma$
Translational efficiency (ϵ)	I	0.7904 ± 0.3264	0.8647 ± 0.2372	0.6657 ± 0.3816
Activation of 'IE'(k_{31})	I	0.6026 ± 0.3071	0.6026 ± 0.3071	0.5361 ± 0.3843
Generation of CycB(k_1)	I	0.5650 ± 0.3015	0.4993 ± 0.2299	0.5002 ± 0.3471
Cdh1 degradation(k_4)	I	0.4043 ± 0.2443	0.3805 ± 0.2361	0.4997 ± 0.3765
Degradation of 'IEP'(k_{32})	II	0.4958 ± 0.2863	0.3576 ± 0.2219	0.4759 ± 0.3417
Generation of Cdh1 (k'_3)	II	0.4434 ± 0.2934	0.3021 ± 0.1895	0.4482 ± 0.3853
CycA mediated degradation of Cdh1 (γ_A)	II	0.3567 ± 0.2381	0.3734 ± 0.2263	0.3985 ± 0.3823
Degradation of 'PPX'(k_{34})	II	0.2266 ± 0.1621	0.2788 ± 0.1995	0.2835 ± 0.2604
Generation of dephosphatase PPX (k_{33})	III	0.2224 ± 0.1652	0.2152 ± 0.1616	0.2572 ± 0.2240
Activation of Cdc20 (k_{13})	III	0.2441 ± 0.3096	0.2557 ± 0.2616	0.2202 ± 0.2782
CycE dependent CycE:Kip1 dissociation (k_8)	III	0.0463 ± 0.0798	0.0041 ± 0.0058	0.1989 ± 0.2545
CycE:Kip1 dissociation giving Kip1 (k'_8)	III	0.0463 ± 0.0798	0.0105 ± 0.0635	0.1988 ± 0.2545
CycE dependent Kip1 accumulation (ψ_E)	III	0.0438 ± 0.0744	0.0078 ± 0.0371	0.1861 ± 0.2386
Cdh1 dependent degradation of Cyc B (k'_2)	III	0.1143 ± 0.1189	0.0865 ± 0.1405	0.1759 ± 0.1690
Generation of Cyc B (k'_1)	III	0.1486 ± 0.0760	0.1333 ± 0.0672	0.1751 ± 0.1649
Degradation of Cdc20 (k_{14})	III	0.2402 ± 0.2678	0.1898 ± 0.2238	0.1692 ± 0.2057
Total E2F ($E2F_T$)	III	0.1460 ± 0.1282	0.4249 ± 0.2385	0.1524 ± 0.1424

Table A.3 (Continued)

Reaction	Cluster	OSSC-BDF	OSSC-FD	OSSC-ODE15s
		$\mu \pm \sigma$	$\mu \pm \sigma$	$\mu \pm \sigma$
Delay of DRGs (k_{18})	III	0.0463 ± 0.1020	0.0003 ± 0.0006	0.1461 ± 0.1720
Expression CycA, catalyzed by aE2F (k_{29})	III	0.1697 ± 0.1366	0.2639 ± 0.1444	0.1334 ± 0.1525
aE2F (k_7) mediate CycE expression	III	0.0367 ± 0.0625	0.0035 ± 0.0038	0.1325 ± 0.1489
Formation of 'GM' (k_{27})	III	0.0911 ± 0.1014	0.1276 ± 0.0863	0.1307 ± 0.1474
Degradation of Cdc20 (J_4)	III	0.0649 ± 0.0743	0.0743 ± 0.1348	0.1281 ± 0.1151
CycB dependent degradation of Cdh1 (γ_B)	III	0.0902 ± 0.1296	0.0478 ± 0.0563	0.1281 ± 0.1331
Synthesis of p27^{Kip1} (k_5)	III	0.0272 ± 0.0447	0.0032 ± 0.0041	0.1274 ± 0.1232
Synthesis of DRG products (k_{17})	III	0.0442 ± 0.0992	0.0003 ± 0.0005	0.1205 ± 0.1754
Maximum specific growth rate (μ)	III	0.1231 ± 0.1431	0.1724 ± 0.1096	0.1176 ± 0.1490
CycE dependent decrease in Kip1 (k_6)	III	0.0264 ± 0.0432	0.0030 ± 0.0038	0.1161 ± 0.1161
Decrease in E2F (k_{23})	III	0.0713 ± 0.0734	0.2138 ± 0.2094	0.1130 ± 0.1080
Degradation of Cdc20 (k_{12})	III	0.0686 ± 0.0969	0.0308 ± 0.0419	0.1091 ± 0.1041
Degradation of free E2F (aE2F (k_{22}))	III	0.0683 ± 0.0654	0.2401 ± 0.2031	0.1065 ± 0.1038
Total PP1$_T$ ($PP1_T$)	III	0.0220 ± 0.0394	0.0001 ± 0.0002	0.1011 ± 0.1034
Synthesis of CycB (J_1)	III	0.0577 ± 0.0356	0.0594 ± 0.0378	0.0999 ± 0.1341
Degradation of 'GM' (k_{28})	III	0.0841 ± 0.0957	0.1025 ± 0.0688	0.0961 ± 0.1092
CycE/A activation of PP1 (K_{21})	III	0.0206 ± 0.0370	0.0001 ± 0.0002	0.0945 ± 0.0972
Cdh1 dependent CycB degradation (k_2)	III	0.0706 ± 0.0676	0.0547 ± 0.0447	0.0911 ± 0.1137
CycD dependent E2F:Rb dissociation (k_{20})	III	0.0224 ± 0.0402	0.0022 ± 0.0208	0.0878 ± 0.0941
CycE dependent activation of PP1 (ϕ_E)	III	0.0183 ± 0.0324	0.0011 ± 0.0104	0.0865 ± 0.0911
Degradation of 'IEP' (J_{32})	III	0.0467 ± 0.0551	0.0313 ± 0.0428	0.0853 ± 0.0774
Degradation of CycD and CycD:Kip1 (k_{10})	III	0.0174 ± 0.0307	0.0002 ± 0.0004	0.0852 ± 0.0889
GF dependent synthesis of CycD (k_9)	III	0.0171 ± 0.0304	0.0012 ± 0.0104	0.0805 ± 0.0874
Degradation of ERG (k_{16})	III	0.0129 ± 0.0227	$7.194\times10^{-7} \pm 1.728\times10^{-6}$	0.0802 ± 0.0912
Total pRb concentration (Rb_T)	III	0.0179 ± 0.0321	0.0068 ± 0.0530	0.0780 ± 0.0817
PP1 dependent pRb activation (k_{19})	III	0.0179 ± 0.0321	0.0001 ± 0.0002	0.0772 ± 0.0807

Table A.3 (Continued)

Reaction	Cluster	OSSC-BDF	OSSC-FD	OSSC-ODE15s
		$\mu \pm \sigma$	$\mu \pm \sigma$	$\mu \pm \sigma$
CycB dependent Cdc20 formation (k_{11})	III	0.0138 ± 0.0230	0.0023 ± 0.0171	0.0770 ± 0.0826
Formation of Cdh1 (J_3)	III	0.0153 ± 0.0224	0.0118 ± 0.0136	0.0710 ± 0.1542
Formation of CycE-Cdk2-Kip1 (k_{25})	III	0.0142 ± 0.0246	0.0004 ± 0.0006	0.0695 ± 0.0687
Cdc20 dependent CycB degradation (k_2'')	III	0.0697 ± 0.1035	0.0489 ± 0.0944	0.0685 ± 0.1210
Formation of ERGs (k_{15})	III	0.0124 ± 0.0222	$8.593\times10^{-7} \pm 2.233\times10^{-6}$	0.0662 ± 0.0759
DRG dependent formation of ERG(J_{15})	III	0.0208 ± 0.0399	$4.998\times10^{-7} \pm 8.465\times10^{-7}$	0.0649 ± 0.0997
CycB dissociation of CKI complex(η_B)	III	0.0170 ± 0.0328	0.0003 ± 0.0004	0.0598 ± 0.0787
CycD-Cdk4/6-Kip1 association(k_{24})	III	0.0110 ± 0.0199	0.0002 ± 0.0004	0.0469 ± 0.0563
CycE dissociation of CKI complex(η_E)	III	0.0099 ± 0.0134	0.0021 ± 0.0022	0.0461 ± 0.0510
Cdh20 depdendent Cdh1 formation (k_3)	III	0.0732 ± 0.1007	0.0607 ± 0.1165	0.0439 ± 0.0851
CycE dependent pRb phosphorylation (λ_E)	III	0.0098 ± 0.0173	$7.812\times10^{-5} \pm 1.044\times10^{-4}$	0.0413 ± 0.0467
Cyclin dependent pRb phosphorylation (k_{26})	III	0.0112 ± 0.0199	0.0001 ± 0.0002	0.0383 ± 0.0470
CycB dependent pRb phosphorylation (λ_B)	III	0.0123 ± 0.0238	$5.447\times10^{-5} \pm 1.567\times10^{-4}$	0.0333 ± 0.0515
Cdc20 dependent CycA degradation (k_{30})	III	0.0182 ± 0.0289	0.0138 ± 0.0184	0.0329 ± 0.0458

APPENDIX B

CHAPTER 2 OF APPENDIX

Table B.1: Reactions and parameter values for the cap-dependent and cap-independent Initiation model developed in this study. For each parameter, the ensemble mean and one standard deviation are reported.

Reaction	$k_f \pm \sigma$ (**nM^{-1}min^{-1}**)	$k_b \pm \sigma$ (**min^{-1}**)	$k_c \pm \sigma$ (**min^{-1}**)	**Source**
Formation of the activated receptor complex				
∅ ⇋ GF	$2.6\times10^{-5} \pm 0.0$	$3.6\times10^{-5} \pm 0.0$	–	
∅ ⇋ R	$1.6\times10^{-5} \pm 0.0$	$9.7\times10^{-5} \pm 0.0$	–	
GF+R ⇋ GF-R	$1.8 \pm 3.6\times10^{-1}$	$2.4\times10^{-1} \pm 4.4\times10^{-2}$	–	[170, 171, 172]
2*GF-R ⇋ GF-R-2	3.9 ± 7.1	6.6 ± 1.2	–	[170, 171, 172]
GF-R-2 ⇋ GF-R-2-P	$6.3\times10^{1} \pm 1.1\times10^{1}$	$6.5\times10^{-1} \pm 1.1\times10^{-1}$	–	[170, 171, 172]
∅ ⇋ G	$5.6\times10^{-5} \pm 0.0$	$5.3\times10^{-5} \pm 0.0$	–	
∅ ⇋ So	$1.2\times10^{-4} \pm 0.0$	$1.2\times10^{-4} \pm 0.0$	–	
G+So ⇋ G-So	$9.4\times10^{-2} \pm 1.6\times10^{-2}$	$6.1\times10^{-3} \pm 1.1\times10^{-3}$	–	[170, 171, 172]
GF-R-2-P+G ⇋ GF-R-2-P-G	$1.8\times10^{-2} \pm 3.8\times10^{-3}$	$3.29 \pm 4.3\times10^{-1}$	–	[170, 171, 172]
GF-R-2-P-G+So ⇋ GF-R-2-P-G-So	$3.0\times10^{-1} \pm 4.7\times10^{-2}$	$3.86 \pm 7.1\times10^{-1}$	–	[170, 171, 172]
GF-R-2-P+G-So ⇋ GF-R-2-P-G-So	$2.9\times10^{-1} \pm 4.7\times10^{-2}$	$6.3\times10^{-1} \pm 1.5\times10^{-1}$	–	[170, 171, 172]
∅ ⇋ Ras	$3.5\times10^{-5} \pm 0.0$	$1.2\times10^{-4} \pm 0.0$	–	
Ras+GDP ⇋ R-GDP	$6.5\times10^{-1} \pm 1.1\times10^{-1}$	$3.76 \pm 7.1\times10^{-1}$	–	[170, 171, 172]
GF-R-2-P-G-So+R-GDP ⇋ GF-R-2-P-G-So-R-GDP	$2.3\times10^{-1} \pm 4.1\times10^{-2}$	$3.2 \pm 5.6\times10^{-1}$	–	[170, 171, 172]
GF-R-2-P-G-So-R-GDP → GF-R-2-P-G-So-R-GTP (Act-R)	–	–	61 ± 8.6	[170, 171, 172]
∅ ⇋ Sh	$2.4\times10^{-5} \pm 0.0$	$3.9\times10^{-5} \pm 0.0$	–	
∅ ⇋ GB	$8.9\times10^{-5} \pm 0.0$	$1.6\times10^{-6} \pm 0.0$	–	
GF-R-2-P+Sh ⇋ GF-R-2-P-Sh	5.6 ± 1.0	$3.8\times10^{1} \pm 5.9$	–	[170, 171, 172]
GF-R-2-P-Sh-G ⇋ GF-R-2-P-Sh+G	$1.9\times10^{-1} \pm 3.0\times10^{-2}$	$3.10 \pm 4.7\times10^{-1}$	–	[170, 171, 172]
GF-R-2-P-Sh-G+So ⇋ GF-R-2-P-Sh-G-So	$6.1\times10^{-1} \pm 1.2\times10^{-1}$	$3.74 \pm 6.2\times10^{-1}$	–	[170, 171, 172]
GF-R-2-P-Sh+G-So ⇋ GF-R-2-P-Sh-G-So	$6.0\times10^{-1} \pm 9.6\times10^{-2}$	$3.79 \pm 7.6\times10^{-1}$	–	[170, 171, 172]
GF-R-2-P-Sh-G-So+GB ⇋ GF-R-2-P-Sh-G-So-GB	$6.2\times10^{-1} \pm 9.4\times10^{-2}$	$3.8 \pm 7.9\times10^{-1}$	–	[170, 171, 172]
GF-R-2-P-Sh-G-So-GB+R-GDP ⇋ GF-R-2-P-Sh-G-So-GB-R-GDP	$2.1\times10^{-1} \pm 3.7\times10^{-2}$	$3.1\times10^{1} \pm 7.1$	–	[170, 171, 172]
GF-R-2-P-Sh-G-So-GB-R-GDP →				

Table B.1 (Continued)

Reaction	$k_f \pm \sigma$ ($\mathbf{nM^{-1}min^{-1}}$)	$k_b \pm \sigma$ ($\mathbf{min^{-1}}$)	$k_c \pm \sigma$ ($\mathbf{min^{-1}}$)	Source
GF-R-2-P-Sh-G-So-GB-R-GDP (Act-R)	–	–	61 ± 9.7	[170, 171, 172]
Activation of Akt and TOR				
$\varnothing \leftrightharpoons$ PI3K	$2.8\times10^{-5} \pm 0.0$	$7.4\times10^{-5} \pm 0.0$	–	
PI3K+GF-R-2-P-Sh-G-So-GB-R-GTP $\leftrightharpoons$ PI3K-Act-R	5.9 ± 1.1	$3.4\times10^{-1} \pm 6.9\times10^{-2}$	–	[170, 171, 172]
PI3K+GF-R-2-P-G-So-R-GTP $\leftrightharpoons$ PI3K-Act-R	6.0 ± 1.1	$2.1 \pm 4.5\times10^{-1}$	–	[170, 171, 172]
PI3K-Act-R $\leftrightharpoons$ Act-PI3K+R	6.5 ± 1.1	$1.2\times10^{-4} \pm 6.2\times10^{-4}$	–	[170, 171, 172]
$\varnothing \leftrightharpoons$ PTEN	$4.8\times10^{-5} \pm 0.0$	$1.7\times10^{-5} \pm 0.0$	–	
$\varnothing \leftrightharpoons$ PIP2	$7.7\times10^{-5} \pm 0.0$	$1.2\times10^{-4} \pm 6.0.0$	–	
$\varnothing \leftrightharpoons$ PIP3	$1.1\times10^{-5} \pm 0.0$	$1.1\times10^{-4} \pm 0.0$	–	
PIP2+Act-PI3K $\leftrightharpoons$ PIP2-Act-PI3K	9.2 ± 1.7	$1.0\times10^{-1} \pm 1.9\times10^{-2}$	–	[173, 172]
PIP2-Act-PI3K $\rightarrow$ PIP3+Act-PI3K	7.4 ± 1.9	–	–	[173, 172]
PIP3+PTEN $\leftrightharpoons$ PIP3-PTEN	8.6 ± 1.6	$5.2\times10^{-1} \pm 1.1\times10^{-1}$	–	[173, 172]
PIP3-PTEN $\rightarrow$ PIP2+PTEN	9.1 ± 1.4	–	–	
$\varnothing \leftrightharpoons$ Akt	$1.1\times10^{-4} \pm 0.0$	$9.8\times10^{-5} \pm 0.0$	–	[173, 172]
$\varnothing \leftrightharpoons$ Pdk1	$1.0\times10^{-4} \pm 0.0$	$7.6\times10^{-5} \pm 0.0$	–	[173, 172]
PIP3+Akt $\leftrightharpoons$ PIP3-Akt	9.7 ± 1.8	$2.7\times10^{-1} \pm 5.2\times10^{-2}$	–	[173, 172]
PIP3-Akt $\rightarrow$ PIP3+Akt$_m$	8.1 ± 1.4	–	–	[173, 172]
PIP3+Pdk1 $\leftrightharpoons$ PIP3-Pdk1	8.2 ± 1.6	$1.1\times10^{-1} \pm 1.8\times10^{-2}$	–	[173, 172]
PIP3-Pdk1 $\rightarrow$ PIP3+Pdk1$_m$	8.0 ± 1.3	–	–	[173, 172]
Pdk1$_m$+Akt$_m$ $\leftrightharpoons$ Pdk1$_m$-Akt$_m$	9.0 ± 1.9	$5.3\times10^{-1} \pm 1.0\times10^{-1}$	–	[173, 172]
Pdk1$_m$-Akt$_m$ $\rightarrow$ Pdk1+aAkt	–	–	8.3 ± 1.5	[173, 172]
$\varnothing \leftrightharpoons$ TOR	$3.5\times10^{-5} \pm 0.0$	$9.5\times10^{-5} \pm 0.0$	–	
aAkt+TOR $\leftrightharpoons$ aAkt-TOR	$4.2 \pm 8.1\times10^{-1}$	6.2 ± 1.1	–	[174]
aAkt-TOR $\leftrightharpoons$ Akt+aTOR	8.67 ± 1.56	$2.26\times10^{-5} \pm 1.1\times10^{-4}$	–	[174]
$\varnothing \leftrightharpoons$ TSC1	$9.3\times10^{-5} \pm 0.0$	$5.2\times10^{-5} \pm 0.0$	–	
$\varnothing \leftrightharpoons$ TSC2	$6.3\times10^{-5} \pm 0.0$	$6.2\times10^{-5} \pm 0.0$	–	[132]
TSC1+TSC2 $\leftrightharpoons$ TSC1-TSC2	8.65 ± 1.49	$3.3\times10^{-1} \pm 6.5\times10^{-2}$	–	[132]
$\varnothing \leftrightharpoons$ R-GDP	$9.6\times10^{-5} \pm 0.0$	$1.0\times10^{-4} \pm 0.0$	–	
$\varnothing \leftrightharpoons$ R-GTP	$1.0\times10^{-4} \pm 0.0$	$4.3\times10^{-5} \pm 0.0$	–	
R-GTP+TSC1-TSC2 $\leftrightharpoons$ R-GTP-TSC1-TSC2	$1.6\times10^{-1} \pm 2.9\times10^{-2}$	$1.86 \pm 3.0\times10^{-1}$	–	[132]
R-GTP-TSC1-TSC2 $\leftrightharpoons$ R-GDP+TSC1-TSC2	$4.5\times10^{-1} \pm 6.8\times10^{-2}$	$6.9\times10^{-5} \pm 3.5\times10^{-4}$	–	[132]
R-GTP+TOR $\leftrightharpoons$ R-GTP-TOR	$1.3\times10^{-2} \pm 2.9\times10^{-3}$	$1.0\times10^{1} \pm 1.71$	–	[132]
R-GTP-TOR $\rightarrow$ R-GTP+aTOR	–	–	$2.25 \pm 4.6\times10^{-1}$	[132]
TSC1-TSC2+aAkt $\leftrightharpoons$ TSC1-TSC2-aAkt	$2.1\times10^{-1} \pm 3.8\times10^{-2}$	6.72 ± 1.27	–	[132]
TSC1-TSC2-aAkt $\rightarrow$ TSC1-TSC2-P+aAkt	$9.9\times10^{-2} \pm 1.7\times10^{-2}$	–	–	[132]
4E-BP1 and eIF4E reactions				
$\varnothing \leftrightharpoons$ 4E-BP1	$7.8\times10^{-6} \pm 0.0$	$7.8\times10^{-5} \pm 0.0$	–	
4E-BP1-4E $\leftrightharpoons$ 4E-BP1+4E	6.57 ± 1.11	$9.6\times10^{-1} \pm 1.7\times10^{-1}$	–	[175, 176, 177]

Table B.1 (Continued)

Reaction	$k_f \pm \sigma$ ($\mathbf{nM^{-1}min^{-1}}$)	$k_b \pm \sigma$ ($\mathbf{min^{-1}}$)	$k_c \pm \sigma$ ($\mathbf{min^{-1}}$)	Source
4E-BP1+*a*TOR ⇋ 4E-BP1-*a*TOR	$1.1\times10^{-1} \pm 1.6\times10^{-2}$	$1.27 \pm 2.3\times10^{-1}$	–	[175, 176, 177]
4E-BP1→ 4E-BP1-P+*a*TOR	–	–	$5.2\times10^{1} \pm 1.0\times10^{1}$	[175, 176, 177]
4E-BP1-4E+*a*TOR ⇋ 4E-BP1-4E-*a*TOR	$4.3\times10^{-1} \pm 7.9\times10^{-2}$	$3.9\times10^{-1} \pm 7.6\times10^{-2}$	–	[175, 176, 177]
4E-BP1-4E-*a*TOR → 4E-BP1-P+4E+*a*TOR	–	–	$2.0\times10^{-1} \pm 4.3\times10^{-2}$	[175, 176, 177]
Formation of 43S complex				
∅ ⇋ $40S_I$	$1.1\times10^{-4} \pm 0.0$	$1.2\times10^{-5} \pm 0.0$	–	
∅ ⇋ p70	$1.0\times10^{-4} \pm 0.0$	$2.6\times10^{-5} \pm 0.0$	–	
p70+*a*TOR ⇋ p70-*a*TOR	8.74 ± 1.28	$1.09 \pm 1.9\times10^{-1}$	–	[178]
p70-*a*TOR → *a*p70+*a*TOR	8.00 ± 1.31	–	–	[178]
*a*p70+$40S_I$ ⇋ *a*p70-$40S_I$	7.52 ± 1.28	$6.5\times10^{-1} \pm 1.5\times10^{-1}$	–	
*a*p70-$40S_I$ → *a*p70+40S	$4.78 \pm 7.9\times10^{-1}$	–	–	
∅ ⇋ 2	$4.2\times10^{-5} \pm 0.0$	$3.6\times10^{-5} \pm 0.0$	–	
∅ ⇋ GTP	$9.4\times10^{-5} \pm 0.0$	$1.0\times10^{-4} \pm 0.0$	–	
∅ ⇋ *m*tRNA	$1.1\times10^{-4} \pm 0.0$	$3.6\times10^{-5} \pm 0.0$	–	
2+GTP ⇋ 2-GTP	9.71 ± 1.59	$7.6\times10^{-2} \pm 1.3\times10^{-2}$	–	[168, 129]
2-GTP+*m*tRNA ⇋ 2-GTP-*m*tRNA	$3.2\times10^{-1} \pm 6.1\times10^{-2}$	$5.3\times10^{-1} \pm 1.0\times10^{-1}$	–	[168, 129]
∅ ⇋ 3	$2.0\times10^{-5} \pm 0.0$	$8.6\times10^{-6} \pm 0.0$	–	
∅ ⇋ 1	$1.2\times10^{-4} \pm 0.0$	$1.0\times10^{-4} \pm 0.0$	–	
∅ ⇋ 1A	$1.2\times10^{-4} \pm 0.0$	$3.5\times10^{-5} \pm 0.0$	–	
∅ ⇋ 5	$9.5\times10^{-5} \pm 0.0$	$3.0\times10^{-5} \pm 0.0$	–	
∅ ⇋ 5B	$8.7\times10^{-5} \pm 0.0$	$6.5\times10^{-5} \pm 0.0$	–	
40S+3 ⇋ 40S-3	6.92 ± 1.55	$6.4\times10^{-2} \pm 1.3\times10^{-2}$	–	[168, 129]
40S-3+1 ⇋ 40S-3-1	8.80 ± 1.92	$4.2\times10^{-2} \pm 9.8\times10^{-3}$	–	[168, 129]
40S-3-1+1A ⇋ 40S-3-1-1A	$3.9\times10^{-2} \pm 6.4\times10^{-3}$	$5.9\times10^{-2} \pm 1.0\times10^{-2}$	–	[168, 129]
5+5B ⇋ 5-5B	$1.0\times10^{1} \pm 1.85$	$6.8\times10^{-2} \pm 1.0\times10^{-2}$	–	[379]
40S-3-1-1A+5-5B ⇋ 40S-3-1-1A-5-5B	$1.0\times10^{1} \pm 1.52$	$1.0\times10^{-2} \pm 1.7\times10^{-3}$	–	[379]
2-GTP-*m*tRNA+40S-3-1-1A-5-5B ⇋ 2-GTP-*m*tRNA-40S-3-1-1A-5-5B (43S)	7.17 ± 1.04	$5.0\times10^{-1} \pm 9.2\times10^{-2}$	–	[379]
Formation of the Cap Binding Complex (CBC) and it's binding to mRNA				
∅ ⇋ 4E	$6.2\times10^{-8} \pm 0.0$	$1.1\times10^{-4} \pm 0.0$	–	
∅ ⇋ 4G	$3.2\times10^{-5} \pm 0.0$	$1.0\times10^{-4} \pm 0.0$	–	
∅ ⇋ 4A	$1.0\times10^{-4} \pm 0.0$	$6.6\times10^{-5} \pm 0.0$	–	
4A+4G+4E ⇋ 4A-4G-4E	$7.7\times10^{-1} \pm 1.4\times10^{-1}$	$4.6 \pm 9.7\times10^{-1}$	–	[168, 129]
∅ ⇋ 4B	$1.5\times10^{-5} \pm 0.0$	$3.3\times10^{-5} \pm 0.0$	–	
∅ ⇋ 4H	$5.7\times10^{-5} \pm 0.0$	$8.3\times10^{-5} \pm 0.0$	–	
4A-4G-4E+4B+4H ⇋ 4A-4G-4E-4B-4H (CBC)	9.8 ± 2.0	$3.7\times10^{-1} \pm 7.1\times10^{-2}$	–	[168, 129]
∅ ⇋ PB	$5.8\times10^{-5} \pm 0.0$	$2.6\times10^{-5} \pm 0.0$	–	
∅ ⇋ $mRNA_C$	$7.8\times10^{-8} \pm 0.0$	$8.3\times10^{1} \pm 1.5\times10^{1}$	–	

Table B.1 (Continued)

Reaction	$k_f \pm \sigma$ ($nM^{-1}min^{-1}$)	$k_b \pm \sigma$ (min^{-1})	$k_c \pm \sigma$ (min^{-1})	Source
PB+mRNA$_C$ ⇋ mRNA$_C$-PB	$1.4\times10^{1} \pm 2.16$	9.15 ± 1.43	–	
CBC+mRNA$_C$-PB ⇋ CBC-mRNA$_C$-PB	8.96 ± 1.49	$2.4\times10^{-2} \pm 4.4\times10^{-3}$	–	
Formation of the 48S complex and scanning				
CBC-mRNA$_C$-PB+43S ⇋ CBC-mRNA$_C$-PB-43S (48S)	$5.78 \pm 9.1\times10^{-1}$	$3.3\times10^{-1} \pm 7.9\times10^{-2}$	–	
48S → 48S-AUG	–	–	$6.8\times10^{-1} \pm 1.0\times10^{-1}$	
Hydrolysis of GTP and release of eIF2-GDP				
48S-AUG+5 ⇋ 48S-AUG-5	$3.3 \pm 5.4\times10^{-1}$	$4.9\times10^{-1} \pm 1.0\times10^{-1}$	–	[379, 380]
48S-AUG-5+5B ⇋ 48S-AUG-5-5B	6.20 ± 1.04	$2.3\times10^{-2} \pm 3.6\times10^{-3}$	–	[379, 380]
48S-AUG+5-5B ⇋ 48S-5-5B-AUG-5-5B	6.34 ± 1.21	$5.1\times10^{-1} \pm 9.2\times10^{-2}$	–	[379, 380]
48S-(2-GTP)-5-5B-AUG-5-5B → 48S-(2-GDP)-5-5B-AUG-5-5B	–	–	6.66 ± 1.33	[379, 380]
48S-(2-GDP)-5-5B-AUG-5-5B → 48S-5-5B-AUG-5-5B+2-GDP	$7.1\times10^{1} \pm 1.2\times10^{1}$	–	–	[379, 380]
Conversion of eIF2-GDP to eIF2-GTP				
∅ ⇋ eIF2B	$1.1\times10^{-4} \pm 0.0$	$7.5\times10^{-5} \pm 0.0$	–	
2-GDP+eIF2B ⇋ 2-GDP-eIF2B	$5.9\times10^{-1} \pm 1.2\times10^{-1}$	$7.9\times10^{-2} \pm 1.3\times10^{-2}$	–	
2-GDP-eIF2B → 2-GTP+eIF2B	$3.6\times10^{-1} \pm 6.3\times10^{-2}$	–	–	
Addition of 60S and Puromycin Assay				
∅ ⇋ 60S	$2.2\times10^{-5} \pm 0.0$	$6.9\times10^{-7} \pm 0.0$	–	[164]
48S-5-5B-AUG-5-5B+60S ⇋ 48S-5-5B-AUG-5-5B-60S (80S)	$4.40 \pm 7.4\times10^{-1}$	$9.0\times10^{-2} \pm 1.7\times10^{-2}$	–	[164]
80S ⇋ 80S+5+5B	$1.0\times10^{1} \pm 1.62$	$4.6\times10^{-3} \pm 7.4\times10^{-4}$	–	[164]
80S ⇋ 80S+3+1+1A	$4.49 \pm 7.4\times10^{-1}$	$1.1\times10^{-1} \pm 1.9\times10^{-2}$	–	[164]
80S+GTP → 80S-star+GDP	–	–	$1.0\times10^{-1} \pm 1.9\times10^{-2}$	–
80S-star+Puro ⇋ 80S-star-Puro	$1.1\times10^{-3} \pm 2.8\times10^{-4}$	$6.6\times10^{1} \pm 1.3\times10^{1}$	–	[164]
80S-star-Puro → Cap-Met-Puro	–	–	$1.1\times10^{1} \pm 1.98$	[164]
80S+Puro ⇋ 80S-Puro	$1.0\times10^{-3} \pm 1.9\times10^{-4}$	$1.0\times10^{2} \pm 1.7\times10^{1}$	–	[164]
80S-Puro → Cap-Met-Puro	–	–	$3.3\times10^{-1} \pm 5.9\times10^{-2}$	[164]
Effect of physiological stress, e.g., hypoxia				
∅ ⇋ mRNA$_I$	$6.7\times10^{-5} \pm 0.0$	$9.7\times10^{1} \pm 2.0\times10^{1}$	–	
mRNA$_I$+PB ⇋ mRNA$_I$-PB	8.43 ± 1.80	$8.8\times10^{-1} \pm 1.5\times10^{-1}$	–	
∅ ⇋ Stress	$3.0\times10^{-5} \pm 1.5\times10^{-4}$	$6.7\times10^{-5} \pm 3.4\times10^{-4}$	–	
Stress+4G ⇋ Stress-4G	9.89 ± 1.80	$6.2\times10^{-2} \pm 1.1\times10^{-2}$	–	[381]
Stress-4G → 4G$_C$	–	–	9.46 ± 1.67	[381]
4E-BP1-P+Stress ⇋ 4E-BP1-P-Stress	$8.5\times10^{-1} \pm 1.4\times10^{-1}$	$9.4\times10^{-2} \pm 1.6\times10^{-2}$	–	[382]

Table B.1 (Continued)

Reaction	$k_f \pm \sigma$ ($nM^{-1}min^{-1}$)	$k_b \pm \sigma$ (min^{-1})	$k_c \pm \sigma$ (min^{-1})	Source
4E-BP1-P-Stress → 4E-BP1	–	–	$9.2\times10^{-1} \pm 1.7\times10^{-1}$	[382]
$\varnothing \leftrightharpoons$ I1	$8.2\times10^{-5} \pm 0.0$	$3.2\times10^{-5} \pm 0.0$	–	
$\varnothing \leftrightharpoons$ I2	$7.4\times10^{-5} \pm 0.0$	$4.0\times10^{-5} \pm 0.0$	–	
4A+4G$_C$+4B+4H+I1+I2 $\leftrightharpoons$ 4A-4G$_C$-4B-4H-I1-I2 (IBC)	$4.67 \pm 8.4\times10^{-1}$	$1.6\times10^{-2} \pm 2.7\times10^{-3}$	–	[383]
IBC+mRNA$_I$-PB $\leftrightharpoons$ IBC-mRNA$_I$-PB	$5.57 \pm 8.0\times10^{-1}$	$3.3\times10^{-4} \pm 3.2\times10^{-4}$	–	
IBC-mRNA$_I$-PB+43S $\leftrightharpoons$ IBC-mRNA$_I$-PB-43S (48S$_I$)	$5.31 \pm 8.6\times10^{-1}$	$2.5\times10^{-1} \pm 3.8\times10^{-2}$	–	
48S$_I$ → 48S$_I$-AUG	–	–	$7.1\times10^{-1} \pm 1.1\times10^{-1}$	–
48S$_I$-AUG+5 $\leftrightharpoons$ 48S$_I$-AUG-5	6.57 ± 1.00	$2.8\times10^{-1} \pm 5.1\times10^{-2}$	–	
48S$_I$-AUG-5+5B $\leftrightharpoons$ 48S$_I$-AUG-5-5B	5.50 ± 1.04	$8.7\times10^{-1} \pm 1.5\times10^{-1}$	–	
48S$_I$-AUG+5-5B $\leftrightharpoons$ 48S$_I$-AUG-5-5B	$1.0\times10^{1} \pm 2.05$	$1.0\times10^{-1} \pm 1.8\times10^{-2}$	–	
48S$_I$-(2-GTP)-AUG-5-5B → 48S$_I$-(2-GDP)-AUG-5-5B	–	–	6.56 ± 1.17	–
48S$_I$-(2-GDP)-AUG-5-5B → 48S$_I$-AUG-5-5B+2-GDP	–	–	$3.82 \pm 7.3\times10^{-1}$	–
48S$_I$-AUG-5-5B+60S $\leftrightharpoons$ 48S$_I$-AUG-5-5B-AUG-60S	$4.18 \pm 8.3\times10^{-1}$	$2.4\times10^{-1} \pm 4.3\times10^{-2}$	–	
48S$_I$-5-5B-AUG-60S → 48S$_I$-AUG-60S+5-5B	–	–	$1.12 \pm 2.1\times10^{-1}$	–
48S$_I$-AUG-60S → 48S$_I$-AUG-60S (IRES 80S) +1+1A+3	$4.7\times10^{-1} \pm 8.4\times10^{-2}$	$5.3\times10^{-5} \pm 2.7\times10^{-4}$	–	–
Characterization with Puromycin Assay				
IRES 80S+GTP → IRES 80S-star+GDP	–	–	$1.0\times10^{-1} \pm 2.3\times10^{-2}$	[164]
IRES 80S-star+Puro $\leftrightharpoons$ IRES 80S-star-Puro	$1.0\times10^{-3} \pm 2.0\times10^{-4}$	$6.4\times10^{1} \pm 1.2\times10^{1}$	–	[164]
IRES 80S-star-Puro → IRES-Met-Puro	–	–	$1.0\times10^{1} \pm 1.64$	[164]
80S+Puro $\leftrightharpoons$ IRES-80S-Puro	$1.0\times10^{-3} \pm 1.8\times10^{-4}$	$1.0\times10^{2} \pm 1.9\times10^{1}$	–	[164]
IRES-80S-Puro → IRES-Met-Puro	–	–	$3.1\times10^{-1} \pm 4.5\times10^{-2}$	[164]
Reactions of the Rheb-GTP/GDP, TSC subsystem				
R-GTP+TSC1 $\leftrightharpoons$ R-GTP-TSC1	$7.7\times10^{-2} \pm 1.7\times10^{-2}$	$1.0\times10^{1} \pm 1.89$	–	[384]
R-GTP-TSC1 → R-GDP+TSC1	$1.04 \pm 2.0\times10^{-1}$	–	–	[384]
R-GTP+TSC2 $\leftrightharpoons$ R-GTP-TSC2	$6.0\times10^{-1} \pm 1.2\times10^{-1}$	$3.16 \pm 5.6\times10^{-1}$	–	[384]
R-GTP-TSC2 → R-GDP+TSC2	–	–	$71.0\times10^{1} \pm 2.56$	[384]
TSC1+aAkt $\leftrightharpoons$ TSC1-aAkt	$2.2\times10^{-1} \pm 3.2\times10^{-2}$	6.61 ± 1.22	–	
TSC1-aAkt → TSC1-P+aAkt	–	–	$1.0\times10^{-1} \pm 1.7\times10^{-2}$	[384]
TSC2+aAkt $\leftrightharpoons$ TSC2-aAkt	$2.2\times10^{-1} \pm 4.4\times10^{-2}$	6.99 ± 1.45	–	
TSC2-aAkt → TSC2-P+aAkt	–	–	$1.0\times10^{-1} \pm 2.0\times10^{-2}$	[384]
R-GTP $\leftrightharpoons$ R-GDP	$1.0\times10^{-2} \pm 1.9\times10^{-3}$	$1.0\times10^{-2} \pm 1.9\times10^{-3}$	–	
aTOR → TOR	–	–	$1.1\times10^{1} \pm 1.96$	
Rheb+GDP $\leftrightharpoons$ R-GDP	$1.07 \pm 1.8\times10^{-1}$	$9.8\times10^{-2} \pm 1.7\times10^{-2}$	–	[384]
Rheb+GTP $\leftrightharpoons$ R-GTP	$1.03 \pm 2.0\times10^{-1}$	$1.0\times10^{-1} \pm 1.9\times10^{-2}$	–	[384]
$\varnothing \leftrightharpoons$ Rheb	$2.7\times10^{-5} \pm 0.0$	$1.2\times10^{-4} \pm 0.0$	–	

Table B.1 (Continued)

Reaction	$k_f \pm \sigma$ ($\mathbf{nM^{-1}min^{-1}}$)	$k_b \pm \sigma$ ($\mathbf{min^{-1}}$)	$k_c \pm \sigma$ ($\mathbf{min^{-1}}$)	Source
Reactions of PI3K (Wortmannin) and mTOR inhibitors (Rapamycin)				
Wx $\leftrightharpoons$ Wi	$1.0\times10^{2} \pm 2.5\times10^{1}$	$1.0\times10^{-1} \pm 1.7\times10^{-2}$	–	
Rx $\leftrightharpoons$ Ri	$1.0\times10^{2} \pm 1.7\times10^{1}$	$1.0\times10^{-1} \pm 2.0\times10^{-2}$	–	
Ri+TOR $\leftrightharpoons$ Ri-TOR	$1.0\times10^{1} \pm 2.27$	$9.9\times10^{-3} \pm 1.9\times10^{-3}$	–	
Wi+PI3K $\leftrightharpoons$ Wi-PI3K	$1.0\times10^{1} \pm 1.66$	$1.0\times10^{-2} \pm 1.7\times10^{-3}$	–	
Ri+*a*TOR $\leftrightharpoons$ Ri-*a*TOR	$1.0\times10^{1} \pm 1.89$	$1.0\times10^{-2} \pm 1.8\times10^{-3}$	–	
Wi+Act-PI3K $\leftrightharpoons$ Wi-Act-PI3K	$1.0\times10^{1} \pm 1.96$	$1.0\times10^{-2} \pm 1.8\times10^{-3}$		

APPENDIX C

CHAPTER 3 APPENDIX

Table C.1: Prostate model interactions and parameters for the C-33, C-51 and C-81 LNCaP clones.

Reactions	k_{on}	k_{off}	k_{cat}	cite
EGF+EGFR $\rightleftharpoons$ EGFR-EGF	2.215E0±3.1E0	1.3E-3±1.9E-3	-	[171]
2*EGFR-EGF $\rightleftharpoons$ EGFR-EGF-2	3.701E-1±3.586E-1	1.708E-1±1.377E-1	-	[171]
EGFR-EGF-2 $\rightleftharpoons$ EGFR-EGF-2-p	1.864E0±2.444E0	2.707E-2±7.107E-2	-	[171]
2*Her2 $\rightleftharpoons$ Her2-2	4.98E-2±2.815E-2	1.756E-1±2.654E-1	-	⋆
Her2-2 $\rightleftharpoons$ Her2-2-p	2.032E-2±2.204E-2	1.472E-5±1.213E-5	-	[385]
EGFR-EGF-2-p+Grb2 $\rightleftharpoons$ EGFR-EGF-2-p-Grb2	1.068E0±3.282E0	7.018E-1±4.517E-1	-	[302]
EGFR-EGF-2-p-Grb2+Sos $\rightleftharpoons$ EGFR-EGF-2-p-Grb2-Sos	4.244E-1±6.357E-1	3.506E0±5.793E0	-	[302]
EGFR-EGF-2-p-Grb2-Sos $\rightleftharpoons$ EGFR-EGF-2-p+Grb2-Sos	1.159E0±2.35E0	5.034E-2±6.075E-2	-	[302]
Grb2+Sos $\rightleftharpoons$ Grb2-Sos	4.104E-3±2.773E-3	2.548E-4±2.191E-4	-	[302]
EGFR-EGF-2-p-Grb2-Sos+Ras-GDP $\rightleftharpoons$ EGFR-EGF-2-p-Grb2-Sos-Ras-GDP	2.183E-2±1.842E-2	8.377E-1±9.551E-1	-	[263, 386]
EGFR-EGF-2-p-Grb2-Sos-Ras-GDP $\rightarrow$ EGFR-EGF-2-p-Grb2-Sos+Ras-GTP	-	-	4.28E0±3.525E0	[263, 386]
Her2-2-p+Grb2 $\rightleftharpoons$ Her2-2-p-Grb2	1.976E-2±2.734E-2	9.558E-1±8.677E-1	-	⋆
Her2-2-p-Grb2+Sos $\rightleftharpoons$ Her2-2-p-Grb2-Sos	2.395E-1±2.953E-1	1.49E0±2.296E0	-	⋆
Her2-2-p-Grb2-Sos $\rightleftharpoons$ Her2-2-p+Grb2-Sos	3.623E-2±2.45E-2	5.343E-2±5.586E-2	-	⋆
Her2-2-p-Grb2-Sos+Ras-GDP $\rightleftharpoons$ Her2-2-p-Grb2-Sos-Ras-GDP	3.053E-2±1.959E-2	4.568E-1±3.063E-1	-	⋆
Her2-2-p-Grb2-Sos-Ras-GDP $\rightarrow$ Her2-2-p-Grb2-Sos+Ras-GTP	-	-	5.685E0±5.969E0	⋆
EGFR-EGF-2-p+Shc $\rightleftharpoons$ EGFR-EGF-2-p-Shc	6.682E-1±7.743E-1	2.79E0±1.557E0	-	[302]
EGFR-EGF-2-p-Shc $\rightarrow$ EGFR-EGF-2-p-Shc-p	-	-	1.327E1±1.083E1	[302]
EGFR-EGF-2-p-Shc-p $\rightleftharpoons$ EGFR-EGF-2-p+Shc-p	1.464E0±1.058E0	6.464E-3±8.466E-3	-	[302]
Shc-p $\rightarrow$ Shc	-	-	5.153E0±5.371E0	[302]
EGFR-EGF-2-p-Shc-p+Grb2 $\rightleftharpoons$ EGFR-EGF-2-p-Shc-p-Grb2	6.308E-2±4.851E-2	8.773E-1±6.182E-1	-	[302]
EGFR-EGF-2-p-Shc-p-Grb2+Sos $\rightleftharpoons$ EGFR-EGF-2-p-Shc-p-Grb2-Sos	2.065E-1±3.931E-1	2.176E-1±2.282E-1	-	[302]
EGFR-EGF-2-p-Shc-p-Grb2-Sos $\rightleftharpoons$ EGFR-EGF-2-p+Shc-p-Grb2-Sos	9.887E-1±1.048E0	1.562E-3±1.142E-3	-	[302]
Shc-p+Grb2-Sos $\rightleftharpoons$ Shc-p-Grb2-Sos	3.755E-2±4.72E-2	1.613E-1±1.613E-1	-	[302]
EGFR-EGF-2-p-Shc-p-Grb2-Sos+Ras-GDP $\rightleftharpoons$ EGFR-EGF-2-p-Shc-p-Grb2-Sos-Ras-GDP	3.412E-2±3.79E-2	2.066E-1±2.164E-1	-	[263, 386]
EGFR-EGF-2-p-Shc-p-Grb2-Sos-Ras-GDP $\rightarrow$ EGFR-EGF-2-p-Shc-p-Grb2-Sos+Ras-GTP	-	-	4.399E0±7.045E0	[263, 386]
Her2-2-p+Shc $\rightleftharpoons$ Her2-2-p-Shc	1.208E-1±1.537E-1	9.921E0±2.087E1	-	⋆
Her2-2-p-Shc $\rightarrow$ Her2-2-p-Shc-p	-	-	2.995E1±6.778E1	⋆

Table C.1 (Continued)

Reactions	k_{on}	k_{off}	k_{cat}	cite
Her2-2-p-Shc-p ⇌ Her2-2-p+Shc-p	4.703E0±1.342E1	3.983E-3±4.616E-3	-	⋆
Her2-2-p-Shc-p+Grb2 ⇌ Her2-2-p-Shc-p-Grb2	5.805E-2±7.916E-2	1.127E0±1.51E0	-	⋆
Her2-2-p-Shc-p-Grb2+Sos ⇌ Her2-2-p-Shc-p-Grb2-Sos	1.359E-1±1.23E-1	2.241E0±7.899E0	-	⋆
Her2-2-p-Shc-p-Grb2-Sos ⇌ Her2-2-p+Shc-p-Grb2-Sos	9.861E-1±1.159E0	1.294E-2±3.787E-2	-	⋆
Her2-2-p-Shc-p-Grb2-Sos+Ras-GDP ⇌ Her2-2-p-Shc-p-Grb2-Sos-Ras-GDP	1.749E-2±1.219E-2	6.129E-1±1.44E0	-	⋆
Her2-2-p-Shc-p-Grb2-Sos-Ras-GDP → Her2-2-p-Shc-p-Grb2-Sos+Ras-GTP	-	-	1.882E1±4.063E1	⋆
Her2-2-p+cPAcP ⇌ Her2-2-p-cPAcP	1.707E1±1.581E1	5.325E-2±3.92E-2	-	⋆
Her2-2-p-cPAcP → Her2-2+cPAcP	-	-	2.012E1±2.021E1	[346]
Her2-2+sPAcP ⇌ Her2-2-sPAcP	8.951E0±9.414E0	1.248E-3±7.101E-4	-	[346]
Her2-2-sPAcP → Her2-2-p+sPAcP	-	-	2.288E1±2.252E1	†
Ras-GTP+GAP ⇌ Ras-GTP-GAP	1.032E-1±1.526E-1	1.149E0±1.23E0	-	†
Ras-GTP-GAP → Ras-GDP+GAP	-	-	4.785E-1±3.57E-1	[386]
Ras-GTP+Raf ⇌ Ras-GTP-Raf	5.455E-3±4.49E-3	2.097E-2±1.256E-2	-	[386]
Ras-GTP-Raf → Ras-GTP+Raf-p	-	-	5.858E0±6.133E0	[171]
Raf-p+Pase1 ⇌ Raf-p-Pase1	5.166E-1±5.821E-1	1.77E0±1.446E0	-	[171]
Raf-p-Pase1 → Raf+Pase1	-	-	3.978E0±2.632E0	[171]
MEK+Raf-p ⇌ MEK-Raf-p	6.055E-2±5.209E-2	9.006E-2±1.189E-1	-	[171]
MEK-Raf-p → MEK-p+Raf-p	-	-	1.409E1±2.857E1	[171]
MEK-p+Raf-p ⇌ MEK-p-Raf-p	2.145E-1±6.272E-1	1.056E-1±1.282E-1	-	[171]
MEK-p-Raf-p → MEK-pp+Raf-p	-	-	2.949E0±2.16E0	[171]
ERK+MEK-pp ⇌ ERK-MEK-pp	1.677E-3±1.72E-3	4.956E-1±3.873E-1	-	[171]
ERK-MEK-pp → ERK-p+MEK-pp	-	-	1.095E1±1.112E1	[171]
ERK-p+MEK-pp ⇌ ERK-p-MEK-pp	2.09E-3±1.47E-3	3.124E0±8.012E0	-	[171]
ERK-p-MEK-pp → ERK-pp+MEK-pp	-	-	8.435E0±6.538E0	[171]
MEK-p+Pase2 ⇌ MEK-p-Pase2	1.04E-3±1.072E-3	7.569E0±1.607E1	-	[171]
MEK-p-Pase2 → MEK+Pase2	-	-	7.221E-1±8.541E-1	[171]
MEK-pp+Pase2 ⇌ MEK-pp-Pase2	6.319E-2±4.223E-2	4.293E0±2.501E0	-	[171]
MEK-pp-Pase2 → MEK-p+Pase2	-	-	2.617E-2±2.29E-2	[171]
ERK-p+Pase3 ⇌ ERK-p-Pase3	2.408E0±2.499E0	3.366E-1±2.34E-1	-	[171]
ERK-p-Pase3 → ERK+Pase3	-	-	2.7E0±4.156E0	[171]
ERK-pp+Pase3 ⇌ ERK-pp-Pase3	5.008E-2±3.168E-2	5.499E0±8.337E0	-	[171]
ERK-pp-Pase3 → ERK-p+Pase3	-	-	2.789E0±5.206E0	[171]
EGFR-EGF-2-p-Grb2-Sos+ERK-pp ⇌ EGFR-EGF-2-p-Grb2-Sos-ERK-pp	2.239E0±2.85E0	6.502E-4±5.11E-4	-	[305]
EGFR-EGF-2-p-Grb2-Sos-ERK-pp → EGFR-EGF-2-p-Grb2+Sos+ERK-pp	-	-	1.351E0±1.222E0	[305]
Her2-2-p-Grb2-Sos+ERK-pp ⇌ Her2-2-p-Grb2-Sos-ERK-pp	1.856E0±1.211E0	1.559E-1±2.128E-1	-	⋆
Her2-2-p-Grb2-Sos-ERK-pp → Her2-2-p-Grb2+Sos+ERK-pp	-	-	3.075E0±3.738E0	⋆
EGFR-EGF-2-p-Shc-p-Grb2-Sos+ERK-pp ⇌ EGFR-EGF-2-p-Shc-p-Grb2-Sos-ERK-pp	1.185E0±1.099E0	8.315E-4±6.405E-4	-	[305]

Table C.1 (Continued)

Reactions	k_{on}	k_{off}	k_{cat}	cite
EGFR-EGF-2-p-Shc-p-Grb2-Sos-ERK-pp → EGFR-EGF-2-p-Shc-p-Grb2+Sos+ERK-pp	-	-	1.231E1±4.931E1	[305]
Her2-2-p-Shc-p-Grb2-Sos+ERK-pp ⇌ Her2-2-p-Shc-p-Grb2-Sos-ERK-pp	3.378E0±5.412E0	3.747E-1±8.356E-1	-	[171]
Her2-2-p-Shc-p-Grb2-Sos-ERK-pp → Her2-2-p-Shc-p-Grb2+Sos+ERK-pp	-	-	5.262E0±9.916E0	[171]
EGF → EGFi	-	-	0E0±0E0	[171]
EGFR ⇌ EGFRi	1.179E-2±1.056E-2	1.599E-1±2.308E-1	-	[171]
EGFR-EGF → EGFR-EGFi	-	-	1.579E-1±3.334E-1	[171]
EGFRi+EGFi ⇌ EGFR-EGFi	1.041E0±1.185E0	1.251E-1±4.785E-1	-	‡
EGFR-EGF-2 → EGFR-EGF-2i	-	-	6.648E-3±4.899E-3	[171]
2*EGFR-EGFi ⇌ EGFR-EGF-2i	1.432E-2±1.301E-2	4.332E0±7.81E0	-	‡
EGFR-EGF-2-p → EGFR-EGF-2-pi	-	-	7.456E-2±8.563E-2	[171]
EGFR-EGF-2i ⇌ EGFR-EGF-2-pi	2.347E0±3.074E0	1.54E-1±1.493E-1	-	‡
EGFR-EGF-2-p-Grb2 → EGFR-EGF-2-pi-Grb2	-	-	7.874E-2±9.134E-2	[171]
EGFR-EGF-2-pi+Grb2 ⇌ EGFR-EGF-2-pi-Grb2	3.449E-3±2.48E-3	3.572E-1±3.045E-1	-	‡
EGFR-EGF-2-p-Grb2-Sos → EGFR-EGF-2-pi-Grb2-Sos	-	-	1.541E-1±2.247E-1	[171]
EGFR-EGF-2-pi+Grb2-Sos ⇌ EGFR-EGF-2-pi-Grb2-Sos	3.954E-3±3.183E-3	3.359E-1±2.71E-1	-	‡
EGFR-EGF-2-pi-Grb2+Sos ⇌ EGFR-EGF-2-pi-Grb2-Sos	1.13E-2±1.034E-2	6.348E-1±6.501E-1	-	‡
EGFR-EGF-2-pi-Grb2-Sos+Ras-GDP ⇌ EGFR-EGF-2-pi-Grb2-Sos-Ras-GDP	3.459E-3±3.064E-3	7.339E-2±8.78E-2	-	‡
EGFR-EGF-2-pi-Grb2-Sos-Ras-GDP → EGFR-EGF-2-pi-Grb2-Sos+Ras-GTP	-	-	1.199E0±9.562E-1	‡
EGFR-EGF-2-pi-Grb2-Sos+ERK-pp ⇌ EGFR-EGF-2-pi-Grb2-Sos-ERK-pp	1.427E0±1.503E0	3.947E-4±2.363E-4	-	‡
EGFR-EGF-2-pi-Grb2-Sos-ERK-pp → EGFR-EGF-2-pi-Grb2+Sos+ERK-pp	-	-	1.617E0±1.465E0	‡
EGFR-EGF-2-pi+Shc ⇌ EGFR-EGF-2-pi-Shc	1 .367E-1±1.947E-1	6.82E0±6.97E0	-	‡
EGFR-EGF-2-p-Shc → EGFR-EGF-2-pi-Shc	-	-	1.652E-1±3.045E-1	[171]
EGFR-EGF-2-pi-Shc → EGFR-EGF-2-pi-Shc-p	-	-	9.176E0±1.724E1	‡
EGFR-EGF-2-p-Shc-p → EGFR-EGF-2-pi-Shc-p	-	-	9.441E-2±6.697E-2	[171]
EGFR-EGF-2-pi-Shc-p ⇌ EGFR-EGF-2-pi+Shc-p	6.97E0±1.16E1	1.036E-3±7.374E-4	-	‡
EGFR-EGF-2-pi-Shc-p+Grb2 ⇌ EGFR-EGF-2-pi-Shc-p-Grb2	4.201E-3±7.391E-3	2.866E0±6.449E0	-	‡
EGFR-EGF-2-p-Shc-p-Grb2 → EGFR-EGF-2-pi-Shc-p-Grb2	-	-	1.38E-1±1.346E-1	-
EGFR-EGF-2-pi-Shc-p-Grb2+Sos ⇌ EGFR-EGF-2-pi-Shc-p-Grb2-Sos	9.048E-3±4.866E-3	5.588E-1±7.609E-1	-	‡
EGFR-EGF-2-p-Shc-p-Grb2-Sos → EGFR-EGF-2-pi-Shc-p-Grb2-Sos	-	-	4.926E-1±1.139E0	-
EGFR-EGF-2-pi-Shc-p-Grb2-Sos ⇌ EGFR-EGF-2-pi+Shc-p-Grb2-Sos	3.537E0±3.537E0	3.606E-4±3.165E-4	-	‡
EGFR-EGF-2-pi-Shc-p-Grb2-Sos+Ras-GDP ⇌ EGFR-EGF-2-pi-Shc-p-Grb2-Sos-Ras-GDP	5.62E-3±4.616E-3	7.134E-1±1.236E0	-	‡

Table C.1 (Continued)

Reactions	k_{on}	k_{off}	k_{cat}	cite
EGFR-EGF-2-pi-Shc-p-Grb2-Sos-Ras-GDP → EGFR-EGF-2-pi-Shc-p-Grb2-Sos+Ras-GTP	-	-	1.142E0±8.919E-1	‡
EGFR-EGF-2-pi-Shc-p-Grb2-Sos+ERK-pp ⇌ EGFR-EGF-2-pi-Shc-p-Grb2-Sos-ERK-pp	1.924E0±2.013E0	5.668E-4±4.798E-4	-	‡
EGFR-EGF-2-pi-Shc-p-Grb2-Sos-ERK-pp → EGFR-EGF-2-pi-Shc-p-Grb2+Sos+ERK-pp	-	-	4.336E0±4.556E0	‡
AR+ERK-pp ⇌ AR-ERK-pp	1.873E-3±1.23E-3	3.88E-1±8.593E-1	-	[339]
AR-ERK-pp ⇌ AR-p+ERK-pp	2.57E-2±1.979E-2	-	-	[339]
T+Rase5a ⇌ T-Rase5a	2.171E-2±2.509E-2	3.308E-1±5.205E-1	-	[387]
T-Rase5a → DHT+Rase5a	-	-	1.374E0±1.034E0	[387]
AR+HSP ⇌ AR-HSP	9.162E-3±6.375E-3	1.01E-3±8.283E-4	-	[388]
AR+T ⇌ AR-T	5.289E-3±4.359E-3	9.361E-4±1.289E-3	-	[388]
AR-T ⇌ AR-p-T	5.458E-2±1.612E-1	-	-	[388]
AR-p+AR-p-T ⇌ AR-p-AR-p-T	5.32E-1±9.532E-1	6.128E-4±5.525E-4	-	[388]
2*AR-p-T ⇌ AR-p-T-2	5.835E-1±1.26E0	5.149E-4±2.812E-4	-	[388]
2*AR-p ⇌ AR-p-2	2.848E-1±4.904E-1	1.281E-1±2.018E-1	-	[388]
AR+DHT ⇌ AR-DHT	2.486E0±2.641E0	5.42E-5±6.636E-5	-	[388]
AR-DHT ⇌ AR-p-DHT	5.436E-1±4.693E-1	-	-	[388]
AR-p-DHT+AR-p-T ⇌ AR-p-DHT-AR-p-T	6.895E-1±1.445E0	7.915E-4±5.504E-4	-	[388]
AR-p-DHT+AR-p ⇌ AR-p-DHT-AR-p	6.064E-1±1.283E0	3.362E-3±6.635E-3	-	[388]
2*AR-p-DHT ⇌ AR-p-DHT-2	1.026E0±1.066E0	1.013E-3±1.461E-3	-	[388]
AR-p+Pase5 ⇌ AR-p-Pase5	5.409E-4±5.152E-4	4.6E-3±3.726E-3	-	[388]
AR-p-Pase5 → AR+Pase5	-	-	3.637E-3±2.758E-3	[388]
AR-p-T+Pase5 ⇌ AR-p-T-Pase5	1.671E-3±2.186E-3	7.194E-3±4.179E-3	-	[388]
AR-p-T-Pase5 → AR-T+Pase5	-	-	5.853E-3±5.596E-3	[388]
AR-p-DHT+Pase5 ⇌ AR-p-DHT-Pase5	7.907E-4±1.029E-3	7.667E-3±7.267E-3	-	[388]
AR-p-DHT-Pase5 → AR-DHT+Pase5	-	-	5.328E-2±1.285E-1	[388]
AR-p-2+g-cPAcP ⇌ AR-p-2-g-cPAcP	1.618E-3±1.482E-3	9.872E-5±6.594E-5	-	[341]
AR-p-DHT-2+g-cPAcP ⇌ AR-p-DHT-2-g-cPAcP	8.423E-4±1.136E-3	1.366E-7±1.582E-7	-	[341]
AR-p-DHT-AR-p+g-cPAcP ⇌ AR-p-DHT-AR-p-g-cPAcP	4.544E-3±3.674E-3	1.314E-7±1.111E-7	-	[341]
AR-p-T-2+g-cPAcP ⇌ AR-p-T-2-g-cPAcP	6.374E-2±3.979E-2	2.954E-4±4.596E-4	-	[341]
AR-p-AR-p-T+g-cPAcP ⇌ AR-p-AR-p-T-g-cPAcP	6.191E-2±4.34E-2	1.099E-4±1.07E-4	-	[341]
AR-p-DHT-AR-p-T+g-cPAcP ⇌ AR-p-DHT-AR-p-T-g-cPAcP	1.543E-1±1.874E-1	2.343E-4±3.372E-4	-	[341]
AR-p-2+g-sPAcP ⇌ AR-p-2-g-sPAcP	9.585E-2±1.272E-1	2.558E-2±3.325E-2	-	[341]
AR-p-DHT-2+g-sPAcP ⇌ AR-p-DHT-2-g-sPAcP	9.074E-6±1.236E-5	1.017E-1±6.467E-2	-	[341]
AR-p-DHT-AR-p+g-sPAcP ⇌ AR-p-DHT-AR-p-g-sPAcP	5.658E-6±4.624E-6	1.447E-1±1.972E-1	-	[341]
AR-p-T-2+g-sPAcP ⇌ AR-p-T-2-g-sPAcP	4.345E-3±2.721E-3	7.3E-2±1.85E-1	-	[341]
AR-p-AR-p-T+g-sPAcP ⇌ AR-p-AR-p-T-g-sPAcP	1.811E-2±5.092E-2	6.045E-3±4.406E-3	-	[341]
AR-p-DHT-AR-p-T+g-sPAcP ⇌ AR-p-DHT-AR-p-T-g-sPAcP	1.125E-2±3.516E-2	2.44E-2±3.7E-2	-	[341]
ERK-pp+ETS ⇌ ERK-pp-ETS	2.109E-3±3.444E-3	4.624E-1±3.654E-1	-	[298]
ERK-pp-ETS → ERK-pp+ETS-p	-	-	2.534E-2±1.687E-2	[298]

Table C.1 (Continued)

Reactions	k_{on}	k_{off}	k_{cat}	cite
ETS-p+Pase5 ⇌ ETS-p-Pase5	3.753E0±3.797E0	2.548E-3±6.034E-3	-	[298]
ETS-p-Pase5 → ETS+Pase5	-	-	8.124E0±9.856E0	[298]
ERK-pp+AP1 ⇌ ERK-pp-AP1	1.403E-3±1.096E-3	5.971E-1±4.652E-1	-	[298]
ERK-pp-AP1 → ERK-pp+AP1-p	-	-	2.556E-2±2.661E-2	[298]
AP1-p+Pase6 ⇌ AP1-p-Pase6	8.022E0±1.209E1	8.007E-4±7.727E-4	-	[298]
AP1-p-Pase6 → AP1+Pase6	-	-	1.54E1±2.376E1	[298]
Her2-2-p-Grb2-Sos+PI3K ⇌ Her2-2-p-Grb2-Sos-PI3K	2.125E-1±2.91E-1	1.412E-2±3.191E-2	-	[389, 171, 172]
Her2-2-p-Grb2-Sos-PI3K → Her2-2-p-Grb2-Sos+Act-PI3K	-	-	1.941E-1±3.754E-1	[389, 171, 172]
Her2-2-p-Shc-p-Grb2-Sos+PI3K ⇌ Her2-2-p-Shc-p-Grb2-Sos-PI3K	8.255E-2±8.716E-2	5.049E-3±7.031E-3	-	[389, 171, 172]
Her2-2-p-Shc-p-Grb2-Sos-PI3K → Her2-2-p-Shc-p-Grb2-Sos+Act-PI3K	-	-	1.93E-1±1.462E-1	[389, 171, 172]
EGFR-EGF-2-p-Grb2-Sos+PI3K ⇌ EGFR-EGF-2-p-Grb2-Sos-PI3K	4.34E-1±1.47E0	1.849E-2±4.73E-2	-	[389, 171, 172]
EGFR-EGF-2-p-Grb2-Sos-PI3K → EGFR-EGF-2-p-Grb2-Sos+Act-PI3K	-	-	1.684E-1±2.04E-1	[389, 171, 172]
EGFR-EGF-2-p-Shc-p-Grb2-Sos+PI3K ⇌ EGFR-EGF-2-p-Shc-p-Grb2-Sos-PI3K	1.722E-1±1.503E-1	8.976E-3±1.111E-2	-	[389, 171, 172]
EGFR-EGF-2-p-Shc-p-Grb2-Sos-PI3K → EGFR-EGF-2-p-Shc-p-Grb2-Sos+Act-PI3K	-	-	1.01E-1±1.081E-1	[389, 171, 172]
PtdIns2+Act-PI3K ⇌ PtdIns2-Act-PI3K	1.983E-1±1.959E-1	1.56E-2±9.585E-3	-	[172, 390]
PtdIns2-Act-PI3K → PtdIns3+Act-PI3K	-	-	9.81E-2±5.877E-2	[172, 390]
PtdIns3+PTEN ⇌ PtdIns3-PTEN	3.036E-1±3.942E-1	2.262E-2±3.503E-2	-	[172, 390]
PtdIns3-PTEN → PtdIns2+PTEN	-	-	3.081E-1±2.74E-1	[172, 390]
PtdIns3+Akt ⇌ PtdIns3-Akt	4.11E-1±7.091E-1	7.744E-3±1.008E-2	-	[172, 390]
PtdIns3-Akt → PtdIns3+Akt-m	-	-	2.839E-1±3.552E-1	[172, 390]
PtdIns3+Pdk1 ⇌ PtdIns3-Pdk1	2.436E-1±4.38E-1	4.369E-3±7.769E-3	-	[172, 390]
PtdIns3-Pdk1 → PtdIns3+Pdk1-m	-	-	7.83E0±2.249E1	[172, 390]
Pdk1-m+Akt-m ⇌ Pdk1-m-Akt-m	9.893E-2±6.529E-2	1.874E-2±4.907E-2	-	[172, 390]
Pdk1-m-Akt-m → Pdk1+Act-Akt	-	-	2.096E-1±3.052E-1	[172, 390]
Act-Akt+TOR ⇌ Act-Akt-TOR	1.389E-1±1.405E-1	1.102E-1±7.477E-2	-	[391]
Act-Akt-TOR → Akt+Act-TOR	-	-	2.551E-1±1.76E-1	[391]
4E-BP1+eIF4E ⇌ 4E-BP1-eIF4E	1.779E-1±1.65E-1	1.58E-1±3.496E-1	-	[392, 154, 177]
4E-BP1+Act-TOR ⇌ 4E-BP1-Act-TOR	1.347E-1±1.643E-1	1.947E-1±2.04E-1	-	[392, 154, 177]
4E-BP1-Act-TOR → 4E-BP1-P+Act-TOR	-	-	2.5E-1±2.358E-1	[392, 154, 177]
T-e ⇌ T	1.449E0±1.377E0	1.555E0±1.212E0	-	[388]
sPAcP → sPAcP-e	-	-	1.86E0±2.631E0	-
g-CycD+RNAp ⇌ g-CycD-RNAp	4.952E-5±5.451E-5	1.104E-1±9.207E-2	-	⋄
g-CycD-RNAp → g-CycD+RNAp+mRNA-CycD	-	-	1.099E-2±6.375E-3	⋄
g-CycD+ETS-p ⇌ g-CycD-ETS-p	1.38E-1±1.225E-1	1.26E0±1.424E0	-	[298],⋄
g-CycD-ETS-p+RNAp ⇌ g-CycD-ETS-p-RNAp	2.931E-1±7.426E-1	9.037E-3±9.077E-3	-	⋄
g-CycD-ETS-p-RNAp → g-CycD-ETS-p+RNAp+mRNA-CycD	-	-	1.156E-2±1.103E-2	⋄

Table C.1 (Continued)

Reactions	k_{on}	k_{off}	k_{cat}	cite
g-CycD+AP1-p ⇌ g-CycD-AP1-p	3.726E-1±7.298E-1	2.171E0±3.083E0	-	[298],⋄
g-CycD-AP1-p+RNAp ⇌ g-CycD-AP1-p-RNAp	4.288E-1±8.691E-1	2.945E-2±4.654E-2	-	⋄
g-CycD-AP1-p-RNAp → g-CycD-AP1-p+RNAp+mRNA-CycD	-	-	3.292E-2±5.52E-2	⋄
g-PSA+RNAp ⇌ g-PSA-RNAp	9.158E-9±5.822E-9	1.29E-4±9.22E-5	-	⋄
g-PSA-RNAp → g-PSA+RNAp+mRNA-PSA	-	-	2.873E-4±4.865E-4	⋄
g-PSA+AR-p-2 ⇌ g-PSA-AR-p-2	1.372E-1±4.477E-1	4.913E-3±3.906E-3	-	[354, 393],⋄
g-PSA-AR-p-2+RNAp ⇌ g-PSA-AR-p-2-RNAp	1.182E-4±9.273E-5	8.565E-5±6.869E-5	-	⋄
g-PSA-AR-p-2-RNAp → g-PSA-AR-p-2+RNAp+mRNA-PSA	-	-	8.167E-2±8.195E-2	⋄
g-PSA+AR-p-DHT-2 ⇌ g-PSA-AR-p-DHT-2	8.626E-2±5.139E-2	2.007E-4±2.664E-4	-	[354, 393],⋄
g-PSA-AR-p-DHT-2+RNAp ⇌ g-PSA-AR-p-DHT-2-RNAp	7.817E-2±7.669E-2	1.577E-4±3.931E-4	-	⋄
g-PSA-AR-p-DHT-2-RNAp → g-PSA-AR-p-DHT-2+RNAp+mRNA-PSA	-	-	2.238E-2±1.652E-2	⋄
g-PSA+AR-p-DHT-AR-p ⇌ g-PSA-AR-p-DHT-AR-p	1.025E-2±1.364E-2	1.353E-4±2.42E-4	-	[354, 393],⋄
g-PSA-AR-p-DHT-AR-p+RNAp ⇌ g-PSA-AR-p-DHT-AR-p-RNAp	1.091E-4±1.097E-4	1.029E-5±8.85E-6	-	⋄
g-PSA-AR-p-DHT-AR-p-RNAp → g-PSA-AR-p-DHT-AR-p+RNAp+mRNA-PSA	-	-	3.064E-4±2.688E-4	⋄
g-PSA+AR-p-T-2 ⇌ g-PSA-AR-p-T-2	9.22E-5±1.021E-4	8.384E-4±8.525E-4	-	[354, 393],⋄
g-PSA-AR-p-T-2+RNAp ⇌ g-PSA-AR-p-T-2-RNAp	4.362E-4±9.551E-4	2.375E-4±3.218E-4	-	⋄
g-PSA-AR-p-T-2-RNAp → g-PSA-AR-p-T-2+RNAp+mRNA-PSA	-	-	8.891E-5±5.851E-5	⋄
g-PSA+AR-p-AR-p-T ⇌ g-PSA-AR-p-AR-p-T	4.169E-5±3.125E-5	5.429E-3±1.32E-2	-	[354, 393],⋄
g-PSA-AR-p-AR-p-T+RNAp ⇌ g-PSA-AR-p-AR-p-T-RNAp	8.539E-5±1.306E-4	1.204E-4±1.07E-4	-	⋄
g-PSA-AR-p-AR-p-T-RNAp → g-PSA-AR-p-AR-p-T+RNAp+mRNA-PSA	-	-	1.959E-4±2.315E-4	⋄
g-PSA+AR-p-DHT-AR-p-T ⇌ g-PSA-AR-p-DHT-AR-p-T	2.392E-4±1.671E-4	5.202E-4±3.549E-4	-	[354, 393],⋄
g-PSA-AR-p-DHT-AR-p-T+RNAp ⇌ g-PSA-AR-p-DHT-AR-p-T-RNAp	2.092E-4±2.523E-4	1.516E-4±1.413E-4	-	⋄
g-PSA-AR-p-DHT-AR-p-T-RNAp → g-PSA-AR-p-DHT-AR-p-T+RNAp+mRNA-PSA	-	-	2.128E-4±2.825E-4	⋄
g-cPAcP+RNAp ⇌ g-cPAcP-RNAp	5.788E-2±8.352E-2	7.556E-2±7.697E-2	-	⋄
g-cPAcP-RNAp → g-cPAcP+RNAp+mRNA-cPAcP	-	-	1.311E-2±1.021E-2	⋄
g-sPAcP+RNAp ⇌ g-sPAcP-RNAp	4.894E-2±4.501E-2	1.238E-3±1.192E-3	-	⋄
g-sPAcP-RNAp → g-sPAcP+RNAp+mRNA-sPAcP	-	-	6.989E-1±8.214E-1	⋄
mRNA-CycD+eIF4E ⇌ mRNA-CycD-eIF4E	2.137E-2±2.447E-2	8.14E-3±7.613E-3	-	⋄
mRNA-CycD-eIF4E+40S ⇌ mRNA-CycD-eIF4E-40S	8.773E-2±8.511E-2	5.877E-3±2.975E-3	-	⋄
mRNA-CycD-eIF4E-40S+60S ⇌ mRNA-CycD-eIF4E-40S-60S	7.418E-1±6.638E-1	1.306E-3±1.249E-3	-	⋄
mRNA-CycD-eIF4E-40S-60S → Rm-CycD+eIF4E	-	-	1.194E0±9.078E-1	⋄
Rm-CycD → Ar-CycD	-	-	9.399E-1±6.401E-1	⋄
Ar-CycD → CycD+40S+60S+mRNA-CycD	-	-	1.781E0±1.759E0	⋄
mRNA-PSA+eIF4E ⇌ mRNA-PSA-eIF4E	1.278E-4±1.134E-4	5.894E-6±4.173E-6	-	⋄
mRNA-PSA-eIF4E+40S ⇌ mRNA-PSA-eIF4E-40S	9.861E-4±8.116E-4	4.486E-6±2.712E-6	-	⋄
mRNA-PSA-eIF4E-40S+60S ⇌ mRNA-PSA-eIF4E-40S-60S	7.736E-4±6.483E-4	6.108E-4±1.143E-3	-	⋄

Table C.1 (Continued)

Reactions	k_{on}	k_{off}	k_{cat}	cite
mRNA-PSA-eIF4E-40S-60S → Rm-PSA+eIF4E	-	-	3.98E-4±2.062E-4	⋄
Rm-PSA → Ar-PSA	-	-	7.268E-3±8.931E-3	⋄
Ar-PSA → PSA+40S+60S+mRNA-PSA	-	-	3.797E-2±1.084E-1	⋄
mRNA-cPAcP+eIF4E ⇌ mRNA-cPAcP-eIF4E	1.351E-2±7.272E-3	9.892E-3±1.443E-2	-	⋄
mRNA-cPAcP-eIF4E+40S ⇌ mRNA-cPAcP-eIF4E-40S	2.33E-1±3.139E-1	9.908E-3±9.67E-3	-	⋄
mRNA-cPAcP-eIF4E-40S+60S ⇌ mRNA-cPAcP-eIF4E-40S-60S	9.053E-1±5.338E-1	1.499E-3±1.438E-3	-	⋄
mRNA-cPAcP-eIF4E-40S-60S → Rm-cPAcP+eIF4E	-	-	1.185E0±1E0	⋄
Rm-cPAcP → Ar-cPAcP	-	-	1.31E0±2.102E0	⋄
Ar-cPAcP → cPAcP+40S+60S+mRNA-cPAcP	-	-	1.612E0±1.219E0	⋄
mRNA-sPAcP+eIF4E ⇌ mRNA-sPAcP-eIF4E	3.473E-4±2.456E-4	2.741E-2±7.506E-2	-	⋄
mRNA-sPAcP-eIF4E+40S ⇌ mRNA-sPAcP-eIF4E-40S	3.844E-1±8.881E-1	7.084E-3±7.617E-3	-	⋄
mRNA-sPAcP-eIF4E-40S+60S ⇌ mRNA-sPAcP-eIF4E-40S-60S	1.532E-2±2.378E-2	2.415E-3±2.381E-3	-	⋄
mRNA-sPAcP-eIF4E-40S-60S → Rm-sPAcP+eIF4E	-	-	1.089E0±8.417E-1	⋄
Rm-sPAcP → Ar-sPAcP	-	-	1.572E0±1.147E0	⋄
Ar-sPAcP → sPAcP+40S+60S+mRNA-sPAcP	-	-	1.474E0±1.459E0	⋄
mRNA-CycD → ∅	-	-	8.094E-1±6.348E-1	-
mRNA-PSA → ∅	-	-	1.389E-1±1.328E-1	-
CycD → ∅	-	-	6.123E-3±5.87E-3	-
PSA → ∅	-	-	9.309E-6±7.499E-6	-
EGFi → ∅	-	-	1.057E0±1.053E0	-
cPAcP → ∅	-	-	1.208E-2±8.088E-3	-
mRNA-cPAcP → ∅	-	-	1.3E0±1.39E0	-
sPAcP → ∅	-	-	7.162E-4±7.064E-4	-
mRNA-sPAcP → ∅	-	-	1.12E-1±1.224E-1	-
2*cPAcP ⇌ cPAcP-2	8.195E-2±1.868E-1	9.026E-2±6.808E-2	-	[347]
2*cPAcP-2 ⇌ cPAcP-4	8.039E-2±1.344E-1	6.186E-2±3.229E-2	-	[347]
2*Her2-2-p+cPAcP-2 ⇌ 2Her2-2-p-cPAcP-2	1.292E2±3.518E2	2.069E-1±2.448E-1	-	[347]
2Her2-2-p-cPAcP-2 → 2*Her2-2+cPAcP-2	-	-	9.256E0±6.196E0	[347]
4*Her2-2-p+cPAcP-4 ⇌ 4Her2-2-p-cPAcP-4	1.306E1±1.071E1	1.127E-2±1.019E-2	-	[347]
4Her2-2-p-cPAcP-4 → 4*Her2-2+cPAcP-4	-	-	7.811E0±5.607E0	[347]
Act-Akt+Pase7 ⇌ Act-Akt-Pase7	1.765E-3±1.65E-3	1.226E-3±2.158E-3	-	-
Act-Akt-Pase7 → Akt+Pase7	-	-	1.861E-3±3.179E-3	-
4E-BP1-eIF4E+Act-TOR ⇌ 4E-BP1-eIF4E-Act-TOR	1.603E-3±1.851E-3	7.501E-4±5.262E-4	-	[392, 154, 177]
4E-BP1-eIF4E-Act-TOR → 4E-BP1-P+eIF4E+Act-TOR	-	-	1.933E-3±4.962E-3	[392, 154, 177]

Table C.2: Experimental training data used to estimate the ensemble of prostate model parameters.

Experimental Setup	Observation	Simulation Setup	citation
C-81 transfection with WT PAcP	cyclin D 0.7 of C-81 WT	model of C-33	†
C-81 transfection with PAcP-IgG	cyclin D 0.3 of C-81	model of C-81 with gcPAcP + =1	†
C-81 transfection with PAcP-Prl	+cyclin D 1.1 of C-81	model of C-81 with gsPAcP +=1	†
Addition of 10nm DHT to C-81	PSA increase	Allowed SS of C-81 added 10nM DHT	[335]
Addition of 10nM DHT to C-33	PSA & Her2 activation increase and PAcP decrease	Allowed SS of C-33 added 10nM DHT	[335]
Overexpression of Her2 in C-33	PSA mRNA 2.2 of C-33 WT	model of C-33 with 50% more Her2	[339]
Overexpression of Her2 in C-33	PSA 2 fold of C-33 WT	model of C-33 with 50% more Her2	[335]
Transfection of constitutively active MEK in C-33	PSA 3 fold of C-33 WT	model of C-33 with 50% more MEK	[335]
1μM MEK inhibitor PD98059 in C-81	PSA 0.6 of C-81 WT	model of C-81 with 50% reduced MEK	[335]
MEK inhibitor PD98059 in C-33 with Her2 overexpression	PSA 1.86 of C-33 WT (compared to 2 with Her2 overexpression alone)	model of C-33 with 50% reduced MEK and 50% more Her2	[335]
0.5μM Her2 inhibitor AG879 in C-81	PSA 0.58 of C-81 WT	model of C-81 with 50% reduced Her2	[335]
10μM Her2 inhibitor	PSA 0.17	model of C-81 with	[335]

Table C.2 (Continued)

Experimental Setup	Observation	Simulation Setup	citation
AG879 in C-81	of C-81 WT	87.5% reduced Her2	
EGFR inhibitor	no PSA	Removed EGFR from	[335]
AG1478 in C-81	effect	model of C-81	
50ng/ml EGF to	transient increase	8nM EGF to model	[171]
HeLa cell culture	in Erk activity	of C-33 with no Her2	

Table C.3: Non-zero initial conditions estimated from the training data for the C-33 LNCaP clone. The mean (μ) and standard deviation (σ) calculated over the ensemble are shown.

species	initial condition ($\mu \pm \sigma$)
Pase7	24.71 ± 23.66
AR	192.40 ± 260.66
HSP	486.15 ± 659.55
Rase5a	81.11 ± 66.98
Her2	131.57 ± 111.41
EGFR	115.41 ± 82.19
Shc	91.19 ± 71.89
Grb2	80.32 ± 67.10
Sos	35.79 ± 29.37
Ras-GDP	233.39 ± 456.75
Raf	76.83 ± 54.31
MEK	1572.31 ± 2260.09
ERK	587.24 ± 401.24
ETS	133.52 ± 150.03
AP1	107.34 ± 172.51
Pase1	181.67 ± 513.24
Pase2	20.88 ± 11.78
Pase3	22.76 ± 12.44
Pase5	65.13 ± 82.13
Pase6	168.28 ± 234.48
GAP	60.71 ± 100.62
PI3K	174.54 ± 240.45
PtdIns2	131.27 ± 122.14
PtdIns3	119.05 ± 94.11

Table C.3 (Continued)

species	initial condition ($\mu \pm \sigma$)
PTEN	123.84 ± 142.99
Akt	332.36 ± 585.30
Pdk1	190.88 ± 237.37
TOR	121.80 ± 120.53
4E-BP1	136.67 ± 107.57
eIF4E	3707.42 ± 3178.77
g-PSA	3.29 ± 1.87
g-CycD	2.90 ± 4.98
g-cPAcP	0.09 ± 0.06
g-sPAcP	0.11 ± 0.09
RNAp	371.62 ± 314.59
40S	8203.19 ± 16956.30
60S	4732.73 ± 4700.66

Table C.4: Interactions determined to be significantly fragile for the C-33, C-51 and C-81 LNCaP clones. Overall State Sensitivity Coefficients (OSSCs) were calculated over the parameter ensemble. The OSSC values were ranked ordered.

Reaction	mean rank	st. dev rank	p-value
C-33			
AR-p-DHT-2+g-sPAcP→AR-p-DHT-2-g-sPAcP	302.4059406	15.97843734	0.039916369
Ras-GTP-Raf→Ras-GTP+Raf-p	302.7821782	18.9159705	0.046713871
AP1-p-Pase6→AP1+Pase6	302.8118812	9.99773526	0.00082649
ETS-p+Pase5→ETS-p-Pase5	303.0693069	17.82547816	0.02648256
mRNA-sPAcP-eIF4E+40S→mRNA-sPAcP-eIF4E-40S	303.4851485	11.65648068	0.000567415
Pdk1-m+Akt-m→Pdk1-m-Akt-m	303.960396	8.723384746	1.11E-06
ETS-p-Pase5→ETS+Pase5	304.3465347	12.61418002	0.000133415
AP1-p+Pase6→AP1-p-Pase6	309.0891089	31.45076272	0.001584816
mRNA-sPAcP-eIF4E-40S-60S→Rm-sPAcP+eIF4E	309.8118812	21.69943781	3.90E-06
2*AR-p-DHT→AR-p-DHT-2	313.5643564	27.07211339	6.11E-07
mRNA-sPAcP→[]	315.7524752	63.3152424	0.006070198
2*Her2-2-p+cPAcP-2→2Her2-2-p-cPAcP-2	315.8613861	33.36003113	2.00E-06
ERK-pp-Pase3→ERK-p+Pase3	318.5148515	49.25034329	0.000106094
mRNA-CycD-eIF4E-40S+60S→mRNA-CycD-eIF4E-40S-60S	318.8019802	31.76024659	1.25E-08
mRNA-CycD-eIF4E+40S→mRNA-CycD-eIF4E-40S	318.9306931	33.70966822	5.07E-08
AR-p-DHT+Pase5→AR-p-DHT-Pase5	319.3663366	26.60556138	1.80E-11
Her2-2-sPAcP→Her2-2-p+sPAcP	321.8217822	25.22037368	1.90E-14
Raf-p-Pase1→Raf+Pase1	323.7821782	22.38130583	8.18E-19
Act-Akt-Pase7→Akt+Pase7	325.4158416	60.54411162	2.25E-05
Her2-2-p-Shc-p-Grb2-Sos+ERK-pp→Her2-2-p-Shc-p-Grb2-Sos-ERK-pp	326.8811881	33.90589397	8.76E-13

Table C.4 (Continued)

Reaction	mean rank	st. dev rank	p-value
g-PSA-AR-p-DHT-2-RNAp→g-PSA-AR-p-DHT-2+RNAp+mRNA-PSA	327.990099	32.83064707	4.36E-14
g-PSA+AR-p-DHT-AR-p→g-PSA-AR-p-DHT-AR-p	328.1584158	15.42386775	2.07E-34
g-cPAcP-RNAp→g-cPAcP+RNAp	329.8217822	23.27042743	1.65E-23
AR-DHT→AR-p-DHT	330.039604	16.97809934	2.49E-33
ERK-pp-ETS→ERK-pp+ETS-p	330.4356436	22.63241163	7.61E-25
Her2-2-p-Shc-p-Grb2-Sos+Ras-GDP→Her2-2-p-Shc-p-Grb2-Sos-Ras-GDP	330.7425743	29.10705861	1.40E-18
Shc-p→Shc	331.5346535	14.6216741	3.60E-40
Her2-2-p+cPAcP→Her2-2-p-cPAcP	331.5346535	28.40846491	9.25E-20
ERK-pp+Pase3→ERK-pp-Pase3	332.1980198	31.79669944	1.34E-17
mRNA-cPAcP-eIF4E-40S+60S→mRNA-cPAcP-eIF4E-40S-60S	332.2871287	39.08921926	1.83E-13
AR+DHT→AR-DHT	335.4950495	28.38861289	8.88E-23
Ras-GTP-GAP→Ras-GTP+GAP	335.5049505	50.04604291	6.32E-11
ERK-pp-AP1→ERK-pp+AP1-p	336.960396	15.82823695	5.38E-43
mRNA-cPAcP-eIF4E+40S→mRNA-cPAcP-eIF4E-40S	336.980198	41.72896522	9.27E-15
Her2-2-p-Shc-p-Grb2+Sos→Her2-2-p-Shc-p-Grb2-Sos	338.0990099	35.12960585	3.83E-19
MEK-pp-Pase2→MEK-pp+Pase2	338.2871287	39.07173819	5.55E-17
ERK-pp-AP1→ERK-pp+AP1	338.7029703	18.00524926	5.81E-40
Her2-2+sPAcP→Her2-2-sPAcP	338.8415842	29.06930356	1.40E-24
ERK-pp-ETS→ERK-pp+ETS	339.5148515	23.01511078	3.15E-32
MEK-pp+Pase2→MEK-pp-Pase2	339.7227723	38.86613706	9.42E-18
mRNA-cPAcP+eIF4E→mRNA-cPAcP-eIF4E	339.8910891	35.54133028	5.79E-20
PtdIns3+PTEN→PtdIns3-PTEN	340.039604	27.87700028	1.17E-26
Grb2+Sos→Grb2-Sos	341.3564356	37.79192228	2.44E-19
Her2-2-p-Shc-p-Grb2→Her2-2-p-Shc-p+Grb2	341.3861386	30.78477517	9.83E-25
Her2-2-p-Grb2→Her2-2-p+Grb2	341.5742574	21.43160733	2.56E-36
ERK-MEK-pp→ERK-p+MEK-pp	342.2673267	31.13461386	5.26E-25

Table C.4 (Continued)

Reaction	mean rank	st. dev rank	p-value
MEK-p+Raf-p→MEK-p-Raf-p	343.5643564	37.26023438	5.78E-21
g-sPAcP+RNAp→g-sPAcP-RNAp	343.960396	21.50013622	3.89E-38
ERK-pp+AP1→ERK-pp-AP1	344.7227723	12.55571253	2.64E-59
AR-p-DHT+AR-p→AR-p-DHT-AR-p	345.8217822	17.42957316	2.33E-47
mRNA-sPAcP+eIF4E→mRNA-sPAcP-eIF4E	346.6435644	34.26818637	4.71E-25
ERK-p+Pase3→ERK-p-Pase3	346.9009901	24.64179214	1.26E-35
ERK-p+MEK-pp→ERK-p-MEK-pp	347.3465347	27.47147419	2.69E-32
sPAcP→sPAcP-e	348.2673267	27.44351213	5.87E-33
Her2-2-p-Shc-p+Grb2→Her2-2-p-Shc-p-Grb2	348.5346535	21.65689443	2.17E-41
g-PSA+AR-p-DHT-2→g-PSA-AR-p-DHT-2	348.7623762	17.48331511	1.32E-49
ERK-pp+ETS→ERK-pp-ETS	349.5346535	11.96328075	2.12E-65
g-cPAcP+RNAp→g-cPAcP-RNAp	349.8316832	6.127473123	7.84E-94
PtdIns3-PTEN→PtdIns2+PTEN	350.0990099	29.71098572	1.44E-31
g-sPAcP-RNAp→g-sPAcP+RNAp+mRNA-sPAcP	352.4851485	40.24617659	8.00E-24
Ras-GTP-GAP→Ras-GDP+GAP	353.2376238	19.0482184	1.17E-49
Her2-2-p-Grb2-Sos+ERK-pp→Her2-2-p-Grb2-Sos-ERK-pp	354.019802	21.93102608	7.57E-45
Her2-2-p-Shc-p→Her2-2-p+Shc-p	355.3168317	18.11565195	4.27E-53
Her2-2-p-Grb2-Sos+Ras-GDP→Her2-2-p-Grb2-Sos-Ras-GDP	355.4356436	18.33754782	1.06E-52
Her2-2-p+Grb2-Sos→Her2-2-p-Grb2-Sos	361.0792079	35.52873141	3.78E-32
Raf-p+Pase1→Raf-p-Pase1	361.6237624	16.52651724	4.71E-61
Her2-2-p+Shc→Her2-2-p-Shc	363.1485149	16.06569812	3.41E-63
Ras-GTP+Raf→Ras-GTP-Raf	366.8712871	9.359342626	3.28E-88
PtdIns2-Act-PI3K→PtdIns3+Act-PI3K	367.6732673	19.44024045	2.98E-58
Ras-GTP+GAP→Ras-GTP-GAP	368.3861386	6.688204923	1.46E-103
AR-HSP→AR+HSP	375.4950495	17.27851282	1.70E-67
ERK-p-Pase3→ERK+Pase3	377.1584158	15.50453953	6.74E-73
ERK+MEK-pp→ERK-MEK-pp	381.029703	4.115788113	7.95E-132

Table C.4 (Continued)

Reaction	mean rank	st. dev rank	p-value
C-51			
AP1-p-Pase6→AP1+Pase6	302.1578947	8.575750131	0.001745756
Ras-GTP-Raf→Ras-GTP+Raf-p	303	19.88599084	0.045952102
ETS-p+Pase5→ETS-p-Pase5	303.3157895	16.59502979	0.014236152
Pdk1-m+Akt-m→Pdk1-m-Akt-m	303.7368421	9.106632084	9.61E-06
ETS-p-Pase5→ETS+Pase5	303.9473684	11.5297039	0.000161664
mRNA-sPAcP-eIF4E+40S→mRNA-sPAcP-eIF4E-40S	304.9684211	15.17439161	0.000369539
Her2-2-p-cPAcP→Her2-2+cPAcP	308.5578947	24.48144981	0.000269085
AP1-p+Pase6→AP1-p-Pase6	310.2421053	25.34383172	4.28E-05
mRNA-sPAcP-eIF4E-40S-60S→Rm-sPAcP+eIF4E	313.2947368	22.27666879	1.83E-08
mRNA-CycD-eIF4E-40S+60S→mRNA-CycD-eIF4E-40S-60S	313.7052632	33.07913118	3.50E-05
g-PSA-AR-p-DHT-2-RNAp→g-PSA-AR-p-DHT-2+RNAp+mRNA-PSA	313.8421053	38.17282467	0.000222221
2*AR-p-DHT→AR-p-DHT-2	314.1263158	24.0220259	2.85E-08
ERK-pp-Pase3→ERK-p+Pase3	316.9157895	48.00365406	0.000338143
mRNA-sPAcP→[]	317.5684211	63.22635237	0.003381905
2*Her2-2-p+cPAcP-2→2Her2-2-p-cPAcP-2	317.8421053	33.02608723	2.69E-07
AR-p-DHT+Pase5→AR-p-DHT-Pase5	318.0736842	24.49156336	3.60E-11
mRNA-CycD-eIF4E+40S→mRNA-CycD-eIF4E-40S	318.5894737	34.67548648	3.28E-07
Raf-p-Pase1→Raf+Pase1	321.3578947	22.06922878	6.66E-16
Act-Akt-Pase7→Akt+Pase7	325.3684211	60.78799269	4.01E-05
Her2-2-sPAcP→Her2-2-p+sPAcP	326.5789474	27.72708307	1.28E-15
ERK-pp+Pase3→ERK-pp-Pase3	326.6526316	33.45374447	3.03E-12
Her2-2-p-Shc-p-Grb2-Sos+ERK-pp→Her2-2-p-Shc-p-Grb2-Sos-ERK-pp	327.9473684	37.42933508	3.32E-11
g-PSA+AR-p-DHT-AR-p→g-PSA-AR-p-DHT-AR-p	328.4842105	14.39799925	4.01E-35
AR-DHT→AR-p-DHT	329.1052632	16.30271123	8.22E-32
g-cPAcP-RNAp→g-cPAcP+RNAp	329.2736842	23.57449206	1.81E-21
Her2-2-p-Shc-p-Grb2-Sos+Ras-GDP→Her2-2-p-Shc-p-Grb2-Sos-Ras-GDP	331.3368421	29.15859015	5.32E-18

Table C.4 (Continued)

Reaction	mean rank	st. dev rank	p-value
mRNA-cPAcP-eIF4E-40S+60S→mRNA-cPAcP-eIF4E-40S-60S	331.4	39.66926425	4.29E-12
ERK-pp-ETS→ERK-pp+ETS-p	331.8	19.2636008	2.36E-29
Ras-GTP-GAP→Ras-GTP+GAP	333.0842105	51.16406287	3.58E-09
Shc-p→Shc	333.3684211	15.7600779	2.70E-37
ERK-pp-AP1→ERK-pp+AP1	336.7263158	20.51158446	8.55E-32
ERK-pp-AP1→ERK-pp+AP1-p	337.0736842	12.72150447	1.64E-48
MEK-pp-Pase2→MEK-pp+Pase2	337.2947368	37.76265872	3.96E-16
mRNA-cPAcP-eIF4E+40S→mRNA-cPAcP-eIF4E-40S	337.3157895	42.40786004	7.00E-14
ERK-pp-ETS→ERK-pp+ETS	337.3473684	23.58267358	4.79E-28
AR+DHT→AR-DHT	338.2	24.96844324	5.00E-27
MEK-pp+Pase2→MEK-pp-Pase2	338.7157895	37.64590232	5.70E-17
Her2-2-p-Shc-p-Grb2+Sos→Her2-2-p-Shc-p-Grb2-Sos	338.8105263	34.82597178	9.32E-19
Grb2+Sos→Grb2-Sos	338.9052632	39.71532216	6.11E-16
PtdIns3+PTEN→PtdIns3-PTEN	339.5684211	29.20838114	1.27E-23
Her2-2-p+cPAcP→Her2-2-p-cPAcP	340.0947368	29.00637813	3.67E-24
ERK-p+Pase3→ERK-p-Pase3	341.2842105	26.78949643	3.28E-27
Her2-2+sPAcP→Her2-2-sPAcP	342.4421053	30.45193479	2.28E-24
ERK-pp+AP1→ERK-pp-AP1	342.5894737	16.21597311	1.12E-44
Her2-2-p-Shc-p-Grb2→Her2-2-p-Shc-p+Grb2	342.7684211	25.81287016	2.40E-29
Her2-2-p-Grb2→Her2-2-p+Grb2	342.7789474	21.45407774	3.41E-35
g-sPAcP+RNAp→g-sPAcP-RNAp	342.9894737	21.4478534	2.31E-35
MEK-p+Raf-p→MEK-p-Raf-p	343.1578947	38.42622892	6.58E-19
ERK-MEK-pp→ERK-p+MEK-pp	343.7473684	27.89075245	1.05E-27
ERK-p+MEK-pp→ERK-p-MEK-pp	344.2315789	27.88791575	4.97E-28
mRNA-cPAcP+eIF4E→mRNA-cPAcP-eIF4E	345.6842105	36.12296635	8.80E-22
Her2-2-p-Shc-p+Grb2→Her2-2-p-Shc-p-Grb2	346.4315789	23.27666671	3.54E-35
AR-p-DHT+AR-p→AR-p-DHT-AR-p	346.8315789	16.13929669	2.98E-48

Table C.4 (Continued)

Reaction	mean rank	st. dev rank	p-value
g-PSA+AR-p-DHT-2→g-PSA-AR-p-DHT-2	347.2315789	16.73725918	3.13E-47
ERK-pp+ETS→ERK-pp-ETS	347.6736842	12.66611069	5.41E-58
mRNA-sPAcP+eIF4E→mRNA-sPAcP-eIF4E	347.7473684	35.32643812	1.66E-23
PtdIns3-PTEN→PtdIns2+PTEN	349.4105263	30.11608933	5.28E-29
g-cPAcP+RNAp→g-cPAcP-RNAp	349.7157895	6.308996347	4.17E-87
sPAcP→sPAcP-e	351.0105263	28.577317	1.40E-31
Ras-GTP-GAP→Ras-GDP+GAP	351.9473684	19.54340294	4.92E-45
g-sPAcP-RNAp→g-sPAcP+RNAp+mRNA-sPAcP	351.9578947	40.97365413	8.11E-22
Her2-2-p-Grb2-Sos+Ras-GDP→Her2-2-p-Grb2-Sos-Ras-GDP	352.1789474	20.4743634	1.57E-43
Her2-2-p-Shc-p→Her2-2-p+Shc-p	354.9894737	16.77372302	1.03E-52
Her2-2-p-Grb2-Sos+ERK-pp→Her2-2-p-Grb2-Sos-ERK-pp	355.8105263	19.06625276	1.64E-48
Her2-2-p+Grb2-Sos→Her2-2-p-Grb2-Sos	358.6631579	37.79657755	2.57E-27
Her2-2-p+Shc→Her2-2-p-Shc	361.2315789	19.83800321	1.95E-50
Raf-p+Pase1→Raf-p-Pase1	361.5157895	16.62646157	2.99E-57
Ras-GTP+Raf→Ras-GTP-Raf	366.5789474	9.591200954	6.39E-82
PtdIns2-Act-PI3K→PtdIns3+Act-PI3K	367.2210526	20.72790082	3.00E-52
Ras-GTP+GAP→Ras-GTP-GAP	367.8210526	7.643337584	8.85E-92
ERK-p-Pase3→ERK+Pase3	376.9894737	14.42986285	2.04E-71
AR-HSP→AR+HSP	377.8210526	5.201171826	6.56E-113
ERK+MEK-pp→ERK-MEK-pp	380.2315789	5.008314417	1.12E-115
C-81			
ETS-p-Pase5→ETS+Pase5	301.1604938	11.5297039	0.044372614
Pdk1-m+Akt-m→Pdk1-m-Akt-m	304.308642	9.106632084	6.31E-05
Her2-2-p-Shc-p-Grb2-Sos-ERK-pp→Her2-2-p-Shc-p-Grb2+Sos+ERK-pp	304.7160494	18.6392907	0.044183504
ETS-p+Pase5→ETS-p-Pase5	305.2222222	16.59502979	0.000259343
Rm-cPAcP→Ar-cPAcP	305.9259259	35.39776978	0.035058001

Table C.4 (Continued)

Reaction	mean rank	st. dev rank	p-value
ERK-pp+Pase3→ERK-pp-Pase3	306.8765432	33.45374447	0.006750525
mRNA-sPAcP-eIF4E+40S→mRNA-sPAcP-eIF4E-40S	306.8888889	15.17439161	0.000275699
AP1-p+Pase6→AP1-p-Pase6	309.037037	25.34383172	8.85E-10
Her2-2-p-Shc→Her2-2-p-Shc-p	309.5925926	28.82266729	0.001615564
AR-p-DHT+Pase5→AR-p-DHT-Pase5	310.0246914	24.49156336	9.34E-05
ERK-p+Pase3→ERK-p-Pase3	311.1234568	26.78949643	0.000360203
Her2-2-p-Grb2-Sos-ERK-pp→Her2-2-p-Grb2+Sos+ERK-pp	313.0123457	25.30996979	0.000134248
mRNA-CycD-eIF4E+40S→mRNA-CycD-eIF4E-40S	314.0123457	34.67548648	3.02E-05
mRNA-sPAcP-eIF4E-40S-60S→Rm-sPAcP+eIF4E	314.1358025	22.27666879	2.25E-06
mRNA-sPAcP→[]	314.1604938	63.22635237	0.010774155
2*AR-p-DHT→AR-p-DHT-2	314.2469136	24.0220259	3.92E-07
mRNA-CycD-eIF4E-40S+60S→mRNA-CycD-eIF4E-40S-60S	315	33.07913118	6.12E-06
Her2-2-sPAcP→Her2-2-p+sPAcP	315.3580247	27.72708307	3.46E-08
Her2-2-p-Grb2+Sos→Her2-2-p-Grb2-Sos	317.6296296	59.31322182	0.000564659
Raf-p-Pase1→Raf+Pase1	320.1481481	22.06922878	4.43E-16
MEK-p+Raf-p→MEK-p-Raf-p	320.8518519	38.42622892	8.15E-06
ERK-pp-AP1→ERK-pp+AP1	324.1975309	20.51158446	9.84E-12
Act-Akt-Pase7→Akt+Pase7	324.9382716	60.78799269	0.000162736
Ras-GTP-GAP→Ras-GTP+GAP	325.4691358	51.16406287	2.46E-06
Ar-cPAcP→cPAcP+40S+60S+mRNA-cPAcP	326.0246914	23.44263701	1.16E-07
ERK-p+MEK-pp→ERK-p-MEK-pp	327.0493827	27.88791575	1.06E-17
Grb2+Sos→Grb2-Sos	327.1604938	39.71532216	3.42E-08
Her2-2+sPAcP→Her2-2-sPAcP	327.3580247	30.45193479	1.27E-09
MEK-pp-Pase2→MEK-pp+Pase2	328.1604938	37.76265872	3.48E-10
ERK-pp-ETS→ERK-pp+ETS	328.1728395	23.58267358	8.85E-16
AR-DHT→AR-p-DHT	328.5061728	16.30271123	3.19E-20
MEK-pp+Pase2→MEK-pp-Pase2	329.691358	37.64590232	6.26E-11
g-PSA+AR-p-DHT-AR-p→g-PSA-AR-p-DHT-AR-p	330.1975309	14.39799925	6.17E-34

Table C.4 (Continued)

Reaction	mean rank	st. dev rank	p-value
ERK-pp+AP1→ERK-pp-AP1	330.8518519	16.21597311	2.17E-17
ERK-MEK-pp→ERK-p+MEK-pp	332.1975309	27.89075245	1.29E-22
ERK-pp-ETS→ERK-pp+ETS-p	332.7654321	19.2636008	5.16E-28
mRNA-cPAcP-eIF4E-40S+60S→mRNA-cPAcP-eIF4E-40S-60S	333.5802469	39.66926425	1.46E-11
g-cPAcP-RNAp→g-cPAcP+RNAp	334.0617284	23.57449206	2.04E-22
g-sPAcP+RNAp→g-sPAcP-RNAp	335.2345679	21.4478534	1.11E-25
ERK-pp-AP1→ERK-pp+AP1-p	336.5679012	12.72150447	1.21E-42
AR+DHT→AR-DHT	336.6419753	24.96844324	2.66E-19
Her2-2-p-Shc-p-Grb2-Sos+Ras-GDP→Her2-2-p-Shc-p-Grb2-Sos-Ras-GDP	338.382716	29.15859015	1.19E-20
ERK-pp+ETS→ERK-pp-ETS	339.3580247	12.66611069	3.29E-31
g-PSA+AR-p-DHT-2→g-PSA-AR-p-DHT-2	339.4567901	16.73725918	1.08E-33
PtdIns3+PTEN→PtdIns3-PTEN	339.5432099	29.20838114	4.00E-19
Shc-p→Shc	340.962963	15.7600779	2.34E-36
mRNA-cPAcP-eIF4E+40S→mRNA-cPAcP-eIF4E-40S	341.1234568	42.40786004	3.29E-14
Her2-2-p-Shc-p-Grb2-Sos+ERK-pp→Her2-2-p-Shc-p-Grb2-Sos-ERK-pp	341.345679	37.42933508	6.94E-17
Her2-2-p-cPAcP→Her2-2+cPAcP	343.345679	24.48144981	1.80E-16
sPAcP→sPAcP-e	343.4691358	28.577317	1.82E-18
Her2-2-p+Grb2-Sos→Her2-2-p-Grb2-Sos	344.4074074	37.79657755	5.91E-14
Her2-2-p-Grb2-Sos+Ras-GDP→Her2-2-p-Grb2-Sos-Ras-GDP	344.7654321	20.4743634	5.62E-29
mRNA-sPAcP+eIF4E→mRNA-sPAcP-eIF4E	345.8641975	35.32643812	2.14E-23
Her2-2-p-Shc-p-Grb2+Sos→Her2-2-p-Shc-p-Grb2-Sos	346.345679	34.82597178	2.39E-23
g-sPAcP-RNAp→g-sPAcP+RNAp+mRNA-sPAcP	346.7530864	40.97365413	1.22E-18
PtdIns3-PTEN→PtdIns2+PTEN	348.4814815	30.11608933	6.77E-23
AR-p-DHT+AR-p→AR-p-DHT-AR-p	348.7530864	16.13929669	2.31E-37
Ras-GTP-GAP→Ras-GDP+GAP	349.2222222	19.54340294	1.37E-41

Table C.4 (Continued)

Reaction	mean rank	st. dev rank	p-value
Her2-2-p+cPAcP→Her2-2-p-cPAcP	351.1358025	29.00637813	1.58E-26
Her2-2-p-Grb2→Her2-2-p+Grb2	351.308642	21.45407774	8.46E-36
g-cPAcP+RNAp→g-cPAcP-RNAp	351.7037037	6.308996347	7.31E-52
mRNA-cPAcP+eIF4E→mRNA-cPAcP-eIF4E	353.0493827	36.12296635	8.29E-22
Her2-2-p-Shc-p-Grb2→Her2-2-p-Shc-p+Grb2	354.4567901	25.81287016	2.21E-40
Her2-2-p-Shc-p+Grb2→Her2-2-p-Shc-p-Grb2	355.7530864	23.27666671	3.34E-44
Raf-p+Pase1→Raf-p-Pase1	356.7037037	16.62646157	1.53E-46
Her2-2-p-Grb2-Sos+ERK-pp→Her2-2-p-Grb2-Sos-ERK-pp	357.3333333	19.06625276	1.92E-52
ERK+MEK-pp→ERK-MEK-pp	363.691358	5.008314417	2.09E-35
ERK-p-Pase3→ERK+Pase3	364	14.42986285	3.04E-33
Ras-GTP+Raf→Ras-GTP-Raf	364.6296296	9.591200954	1.32E-59
Her2-2-p-Shc-p→Her2-2-p+Shc-p	364.9382716	16.77372302	1.25E-61
PtdIns2-Act-PI3K→PtdIns3+Act-PI3K	365.8395062	20.72790082	1.52E-39
Ras-GTP+GAP→Ras-GTP-GAP	366.2592593	7.643337584	4.45E-60
Her2-2-p+Shc→Her2-2-p-Shc	366.5555556	19.83800321	6.79E-53
AR-HSP→AR+HSP	373.962963	5.201171826	5.92E-56

Table C.5: Statistically significant sensitivity differences between AI and AD LNCaP clones. Negative changes in the mean rank denote interactions that were more sensitive in AI versus AD cells.

Reaction	p-value	Δ mean rank
rank(C-33) - rank(C-81)		
Her2-2→Her2-2-p	2.41E-14	-87.2565701
cPAcP→[]	2.97E-11	-60.05830583
Her2-2-p-cPAcP→Her2-2+cPAcP	1.11E-16	-46.32587703
Ar-PSA→PSA+40S+60S+mRNA-PSA	9.08E-14	-45.08495294
mRNA-cPAcP-eIF4E-40S-60S→mRNA-cPAcP-eIF4E-40S+60S	2.10E-05	-43.08984232
Ar-cPAcP→cPAcP+40S+60S+mRNA-cPAcP	8.00E-12	-40.0840973
MEK-pp-Pase2→MEK-p+Pase2	0.005304844	29.80992544
2*Her2-2-p+cPAcP-2→2Her2-2-p-cPAcP-2	2.34E-11	34.46632441
ERK-p+Pase3→ERK-p-Pase3	2.30E-14	35.77753331
cPAcP-4→2*cPAcP-2	1.74E-08	44.76995477
AR-p-DHT-2+g-sPAcP→AR-p-DHT-2-g-sPAcP	1.14E-14	44.86273072
2*cPAcP-2→cPAcP-4	9.22E-09	45.43002078
AR-p-DHT-AR-p+g-sPAcP→AR-p-DHT-AR-p-g-sPAcP	8.30E-10	46.80723628
g-PSA-AR-p-DHT-2-RNAp→g-PSA-AR-p-DHT-2+RNAp+mRNA-PSA	0	66.02713605
rank(C-33) - rank(C-51)		
Her2-2-p-cPAcP→Her2-2+cPAcP	0.000173573	-11.53809276
2Her2-2-p-cPAcP-2→2*Her2-2+cPAcP-2	0.005962433	-10.58394997
Her2-2-p+cPAcP→Her2-2-p-cPAcP	0.039330397	-8.560083377
4Her2-2-p-cPAcP-4→4*Her2-2+cPAcP-4	0.030899498	-7.999478895
Ar-PSA→PSA+40S+60S+mRNA-PSA	0.0163948	-7.574361647
g-CycD-RNAp→g-CycD+RNAp+mRNA-CycD	0.008798024	6.428035435
Her2-2-p-Grb2-Sos→Her2-2-p-Grb2+Sos	0.03404035	10.82219906

Table C.5 (Continued)

Reaction	p-value	Δ mean rank
4*Her2-2-p+cPAcP-4→4Her2-2-p-cPAcP-4	7.57E-05	14.0875456
g-PSA-AR-p-DHT-2-RNAp→g-PSA-AR-p-DHT-2+RNAp+mRNA-PSA	0.006362828	14.14799375
rank(C-51) - rank(C-81)		
Her2-2→Her2-2-p	2.28E-10	-73.21936322
cPAcP→[]	7.80E-07	-45.71812865
mRNA-cPAcP-eIF4E-40S-60S→mRNA-cPAcP-eIF4E-40S+60S	1.06E-05	-44.09317739
Ar-cPAcP→cPAcP+40S+60S+mRNA-cPAcP	1.22E-10	-37.77205978
Ar-PSA→PSA+40S+60S+mRNA-PSA	3.96E-10	-37.51059129
Her2-2-p-cPAcP→Her2-2+cPAcP	1.73E-10	-34.78778428
Her2-2-p-Shc-p-Grb2-Sos-ERK-pp→Her2-2-p-Shc-p-Grb2+Sos+ERK-pp	2.51E-09	-24.51604938
AR-p-DHT-AR-p-g-sPAcP→AR-p-DHT-AR-p+g-sPAcP	1.72E-05	25.18258609
4Her2-2-p-cPAcP-4→4*Her2-2+cPAcP-4	4.10E-05	29.57764782
ERK-p+Pase3→ERK-p-Pase3	1.68E-10	30.16075374
2*Her2-2-p+cPAcP-2→2Her2-2-p-cPAcP-2	3.71E-12	36.44704353
AR-p-DHT-2+g-sPAcP→AR-p-DHT-2-g-sPAcP	1.81E-13	42.27784276
cPAcP-4→2*cPAcP-2	4.06E-08	44.55932424
2*cPAcP-2→cPAcP-4	3.21E-08	44.70318389
AR-p-DHT-AR-p+g-sPAcP→AR-p-DHT-AR-p-g-sPAcP	2.05E-09	46.47654321
g-PSA-AR-p-DHT-2-RNAp→g-PSA-AR-p-DHT-2+RNAp+mRNA-PSA	5.55E-16	51.8791423

BIBLIOGRAPHY

[1] American Cancer Society. Cancer facts & figures 2009. Technical report, American Cancer Society, 2009.

[2] M Garcia, A Jemal, EM Ward, MM Center, Y Hao, RL Siegel, and MJ Thun. Global cancer facts & figures 2007. Technical report, American Cancer Society, 2007.

[3] H. Kitano. Computational systems biology. *Nature*, 420:206 – 210, 2002.

[4] M.I. Davidich and S. Bornholdt. Boolean network model predicts cell cycle sequence of fission yeast. *PLoS One*, 3(2), 2008.

[5] S. Bornholdt. Boolean network models of cellular regulation: prospects and limitations. *Journal of The Royal Society Interface*, 5(Suppl 1):S85, 2008.

[6] CJ Firth and D. Bray. Stochastic simulation of cell signaling pathways. *Computational modeling of genetic and biochemical networks. MIT Press, Cambridge, MA*, pages 263–286, 2000.

[7] A. Arkin, J. Ross, and H.H. McAdams. Stochastic kinetic analysis of developmental pathway bifurcation in phage {lambda}-infected Escherichia coli cells. *Genetics*, 149(4):1633, 1998.

[8] P. D'haeseleer, S. Liang, and R. Somogyi. Genetic network inference: from co-expression clustering to reverse engineering. *Bioinformatics*, 16(8):707, 2000.

[9] F. Li, T. Long, Y. Lu, Q. Ouyang, and C. Tang. The yeast cell-cycle network is robustly designed. *Proceedings of the National Academy of Sciences*, 101(14):4781, 2004.

[10] K. Sachs, D. Gifford, T. Jaakkola, P. Sorger, and D.A. Lauffenburger. Bayesian network approach to cell signaling pathway modeling. *Science's STKE*, 2002(148), 2002.

[11] N. Friedman, M. Linial, I. Nachman, and D. Pe'er. Using Bayesian networks to analyze expression data. *J. Comp. Biol.*, 7:601, 2000.

[12] JJ Tyson. Modeling the cell division cycle: cdc2 and cyclin interactions. *Proceedings of the National Academy of Sciences*, 88(16):7328, 1991.

[13] K.C. Chen, A. Csikasz-Nagy, B. Gyorffy, J. Val, B. Novak, and J.J. Tyson. Kinetic analysis of a molecular model of the budding yeast cell cycle. *Molecular Biology of the Cell*, 11(1):369, 2000.

[14] B. Novak, Z. Pataki, A. Ciliberto, and J.J. Tyson. Mathematical model of the cell division cycle of fission yeast. *Chaos: An Interdisciplinary Journal of Nonlinear Science*, 11:277, 2001.

[15] F.R. Cross, V. Archambault, M. Miller, and M. Klovstad. Testing a mathematical model of the yeast cell cycle. *Molecular biology of the cell*, 13(1):52, 2002.

[16] A. Zetterberg and O. Larsson. Kinetic Analysis of Regulatory Events in G1 Leading to Proliferation or Quiescence of Swiss 3T3 Cells. *Proceedings of the National Academy of Sciences USA*, 82(16):5365–5369, 1985.

[17] J.J. Tyson, K. Chen, and B. Novak. Network dynamics and cell physiology. *Nature Reviews Molecular Cell Biology*, 2(12):908–16, 2001.

[18] J.J. Tyson and B. Novak. Regulation of the eukaryotic cell cycle: molecular antagonism, hysteresis, and irreversible transitions. *Journal of Theoretical Biology*, 210(2):249–63, 2001.

[19] N. Barkai and S. Leibler. Robustness in simple biochemical networks. *Nature*, 387:913 – 917, 1997.

[20] U. Alon, M. G. Surette, N. Barkai, and S. Leibler. Robustness in bacterial chemotaxis. *Nature*, 397:168 – 171, 1999.

[21] K. H. Cho, S. Y. Shin, W. Kolch, and O. Wolkenhauer. Experimental Design in Systems Biology, Based on Parameter Sensitivity Analysis Using a Monte Carlo Method: A Case Study for the TNFα-Mediated NF-β-Signal Transduction Pathway. *Simul.-Trans. Soc. Model. Simul. Int.*, 79:726 – 739, 2003.

[22] T. Eissing, F. Allgöwer, and E. Bullinger. Robustness properties of apoptosis models with respect to parameter variations and intrinsic noise. *IEE Proc. Sys. Biol.*, 152:221 – 228, 2005.

[23] Jrg Stelling, Ernst Dieter Gilles, and Francis J Doyle. Robustness properties of circadian clock architectures. *Proc Natl Acad Sci U S A*, 101(36):13210–13215, Sep 2004.

[24] A. Mahdavi, R. E. Davey, P. Bhola, T. Yin, and P. W. Zandstra. Sensitivity Analysis of Intracellular Signaling Pathway Kinetics Predicts Targets for Stem Cell Fate Control. *PLoS Comp. Biol.*, 3:e130, 2007.

[25] D. Luan, M. Zai, and J. Varner. Computationally Derived Points of Fragility of a Human Cascade are Consistent with Current Therapeutic Strategies. *PLoS Comput. Biol.*, 3:1347 – 1359, 2007.

[26] A. Kremling, S. Fischer, K. Gadkar, F. J. Doyle III, T. Sauter, E. Bullinger, F. Allgöwer, and E. D. Gilles. A Benchmark for Methods in Reverse Engineering and Model Discrimination: Problem Formulation and Solutions. *Genome Res.*, 14:1773 – 1785, 2004.

[27] K. G. Gadkar, J. Varner, and F. J. Doyle III. Model identification of signal transduction networks from data using a state regulator problem. *IEE Proc. Syst. Biol.*, 2:17 – 30, 2005.

[28] K.G. Gadkar, R. Gunawan, and F. J. Doyle III. Iterative approach to model identification of biological networks. *BMC Bioinformatics*, 6:155 – 175, 2005.

[29] B. N. Kholodenko, A. Kiyatkin, F. J. Bruggeman, E. Sontag, H. V. Westerhoff, and J. B. Hoek. Untangling the wires: a strategy to trace functional interactions in signaling and gene networks. *Proc. Natl. Acad. Sci. USA*, 99:12841 – 12846, 2002.

[30] E. Sontag, A. Kiyatkin, and B. N. Kholodenko. Inferring dynamic architecture of cellular networks using time series of gene expression, protein and metabolite data. *Bioinformatics*, 20:1877 – 1886, 2004.

[31] K. Cho, S. M. Choo, P. Wellstead, and O. Wolkenhauer. A unified framework for unraveling the functional interaction structure of a biomolecular network based on stimulus-response experimental data. *FEBS Letters*, 579:4520 – 4528, 2005.

[32] J.T. Hwang, E.P. Dougherty, S. Rabitz, and H. Rabitz. The Green's function method of sensitivtiy analysis in chemical kinetics. *J. Chem. Phys.*, 69:5180 – 5191, 1978.

[33] E.P. Dougherty and H. Rabitz. A computational algorithm for the Green's function method of sensitvity analysis in chemical kinetics. *Int. J. Chem. Kinet.*, 11:1237 – 1248, 1979.

[34] M. Kramer, J.M. Calo, and H. Rabitz. An improved computational method for the sensitivity analysis - Green's function method with aim. *Appl. Math. Model*, 5:432 – 441, 1981.

[35] B. Lojek. Sensitivity analysis of systems of differential and algebraic equations. *IEE Proc.-G Circuits Devices and Systems*, 129:85 – 88, 1982.

[36] M.A. Kramer, H. Rabitz, J.M. Calo, and R.J. Kee. Sensitivity analysis in chemical kinetics: Recent developments and computational comparisons. *Int. J. Chem. Kinet.*, 16:559 – 578, 1984.

[37] A.M. Dunker. The decoupled direct method for calculating sensitivity coefficients in chemical kinetics. *J. Chem. Phys.*, 81:2385 – 2393, 1984.

[38] J. R. Leis and M. A. Kramer. Sensitivity analysis of systems of differential and algebraic equations. *Comput. Chem. Eng.*, 9:93 – 96, 1985.

[39] M. Caracotsios and W.E. Stewart. Sensitivity analysis of initial value problems with mixed odes and algebraic equations. *Comput. Chem. Eng.*, 9:359 – 365, 1985.

[40] R. Gunawan, Y. Cao, L. Petzold, and F. J. Doyle III. Sensitivity Analysis of Discrete Stochastic Systems. *Biophys. J.*, 88:2530 – 2540, 2005.

[41] D. Kim, B. J. Debusschere, and H. N. Najm. Spectral Methods for Parametric Sensitivity in Stochastic Dynamical Systems. *Biophys. J.*, 92:379 – 393, 2007.

[42] M Fussenegger and James E Bailey. Molecular regulation of cell-cycle progression and apoptosis in mammalian cells: Implications for biotechnology. *Biotechnology Progress*, 14:807–833, 1998.

[43] C.J. Sherr. Cancer cell cycles. *Science*, 274:1672–1677, 1996.

[44] B Alberts, A Johnson, J Lewis, M Raff, K Roberts, and P Walters. *Molecular Biology of The Cell*. Garland Publishing, 2002.

[45] K Collins, T Jacks, and Nikola P Pavletich. The cell cycle and cancer. *Proceedings of the National Academy of Sciences USA*, 94:2776–2778, 1997.

[46] Leland H Hartwell and Michael B Kastan. Cell cycle control and cancer. *Science*, 266(5192):1821–1828, 1994.

[47] B.D. Aguda and Y. Tang. The kinetic origins of the restriction point in the mammalian cell cycle. *Cell Proliferation*, 32(5):321–335, 1999.

[48] B. Novak and J.J. Tyson. A model for restriction point control of the mammalian cell cycle. *Journal of theoretical biology*, 230(4):563–579, 2004.

[49] Z. Qu, J.N. Weiss, and W.R. MacLellan. Regulation of the mammalian cell cycle: a model of the G1-to-S transition. *American Journal of Physiology-Cell Physiology*, 284(2):C349–C364, 2003.

[50] V. Hatzimanikatis, K. H. Lee, and J. E. Bailey. A mathematical description of regulation of the g1-s transition of the mammalian cell cycle. *Biotechnology and Bioengineering*, 65(6):631–637, December 1999.

[51] C Norbury and P Nurse. Animal Cell Cycle and their Control. *Annual Review of Biochemistry*, 61(1):441–470, 1992.

[52] B. D. Aguda. A qualitative analysis of the kinetics of the g2 dna damage checkpoint system. *Proceedings of the National Academy of Sciences USA*, 96:11352–11357, September 1999.

[53] W.R. Taylor and G.R. Stark. Regulation of the G2/M transition by p53. *Oncogene*, 20(15):1803–1815, 2001.

[54] A. Ciechanover, A. Orian, and A.L. Schwartz. Ubiquitin-mediated proteolysis: biological regulation via destruction. *BioEssays*, 22(5):442–451, 2000.

[55] D.M. Koepp, J.W. Harper, and S.J. Elledge. How the Cyclin Became a Cyclin, Minireview : Regulated Proteolysis in the Cell Cycle. *Cell*, 97:431–434, 1999.

[56] Keiichi I. Nakayama and Keiko Nakayama. Ubiquitin ligases: cell-cycle control and cancer. *Nature Reviews Cancer*, 6:369–381, 2006.

[57] M. E. Csete and J. C. Doyle. Reverse Engineering of Biological Complexitys. *Science*, 295:1664 – 1669, 2002.

[58] H. Kitano. Biological robustness. *Nat. Rev. Genet.*, 5:826 – 837, 2004.

[59] M. Csete and J. Doyle. Bow ties, metabolism and disease. *Trends Biotechnol.*, 22:446 – 450, 2004.

[60] J. Stelling, U. Sauer, Z. Szallasi, F. J. Doyle III, and J. Doyle. Robustness of cellular function. *Cell*, 118:675 – 685, 2004.

[61] J. M. Carlson and J. Doyle. Complexity and robustness. *Proc. Natl. Acad. Sci. USA*, 99(2358 - 2545), 2002.

[62] V. Venkatasubramanian, S. Katare, P. R. Patkar, and F. P. Mu. Spontaneous emergence of complex optimal networks through evolutionary adaptation. *Comput. Chem. Eng.*, 28:1789 – 1798, 2004.

[63] L. You and J. Yin. Evolutionary design on a budget: robustness and optimality of bacteriophage T7. *IEE Proc. Sys. Biol.*, 153:46 – 52, 2006.

[64] M. Fussenegger and J. E. Bailey. Molecular regulation of cell-cycle progression and apoptosis in mammalian cells: implications for biotechnology. *Biotechnol. Prog.*, 14:807 – 833, 1998.

[65] C. J. Sherr. Cancer cell cycles. *Science*, 274:1672 – 1677, 1996.

[66] H. Kitano. Cancer as a robust system: implications for anticancer therapy. *Nat. Rev. Cancer*, 4:227 – 235, 2004.

[67] A. R. A. Anderson, A. M. Weaver, P. T. Cummings, and Vito Quaranta. Tumor Morphology and Phenotypic Evolution Driven by Selective Pressure from the Microenvironment. *Cell*, 127:905 – 915, 2006.

[68] H. Kitano. A robustness based approach to systems-oriented drug design. *Nat. Rev. Drug Discov.*, 6:202 – 210, 2007.

[69] G. N. Newsam and J. D. Ramsdell. Estimation of Sparse Jacobian Matrices. *Siam J. Alg. Disc. Meth.*, 4:404 – 418, 1983.

[70] B. L. Welch. The generalization of students problem when several different population variances are involved. *Biometrika*, 34:28 – 35, 1947.

[71] T. Kanungo, D. M. Mount, N. S. Netanyahu, C. D. Piatko, R. Silverman, and A. Y. Wu. An efficient k-means clustering algorithm: Analysis and implementation. *IEEE Trans. Pattern Anal. Mach. Intell.*, 24:881 – 892, 2002.

[72] A. Koff, A. Giordano, D. Desai, K. Yamashita, J. W. Harper, S. Elledge, T. Nishimoto, D. O. Morgan, B. R. Franza, and J. M. Roberts. Formation

and activation of a cyclin E-cdk2 complex during the G1 phase of the human cell cycle. *Science*, 257(5077):1689 – 1694, 1992.

[73] V. Dulic, E. Lees, and S. I. Reed. Association of human cyclin E with a periodic G1-S phase protein kinase. *Science*, 257(5078):1958 – 1961, 1992.

[74] M. Ohtsubo, A. M. Theodoras, J. Schumacher, J. M. Roberts, and M. Pagano. Human cyclin E, a nuclear protein essential for the G1-to-S phase transition. *Mol. Cell. Biol.*, 15(5):2612 – 2624, 1995.

[75] J. Lukas, T. Herzinger, K. Hansen, M. C. Moroni, D. Resnitzky, K. Helin, S. I. Reed, and J. Bartek. Cyclin E-induced S phase without activation of the pRb/E2F pathway. *Genes Dev.*, 11(11):1479 – 1492, 1997.

[76] D. C. Porter, N. Zhang, C. Danes, M. J. McGahren, R. M. Harwell, S. Faruki, and K. Keyomarsi. Tumor-specific proteolytic processing of cyclin E generates hyperactive lower-molecular-weight forms. *Mol. Cell. Biol.*, 21:6254 – 6269, 2001.

[77] K. Keyomarsi, D. Conte, W. Toyofuku, and M. P. Fox. Deregulation of cyclin E in breast cancer. *Oncogene*, 11:941 – 950, 1995.

[78] K. Keyomarsi, S. L. Tucker, T. A. Buchholz, M. Callister, Y. Ding, G. N. Hortobagyi, I. Bedrosian, C. Knickerbocker, W. Toyofuku, M. Lowe, T. W. Herliczek, and S. S. Bacus. Cyclin E and survival in patients with breast cancer. *N. Engl. J. Med.*, 347:1566 – 1575, 2002.

[79] P. N. Span, V. C. G. Tjan-Heijnen, P. Manders, L. V. A. M. Beex, and C. G. J. Sweep. Cyclin-E is a strong predictor of endocrine therapy failure in human breast cancer. *Oncogene*, 22:4898 – 4904, 2003.

[80] Y. Geng, Q. Y. Yu, E. Sicinska, M. Das, J. E. Schneider, S. Bhattacharya, W. M. Rideout, R. T. Bronson, H. Gardner, and P. Sicinski. Cyclin E ablation in the mouse. *Cell*, 114:431 – 443, 2003.

[81] S. Ortega, I. Prieto, J. Odajima, A. Martín, P. Dubus, R. Sotillo, J. L. Barbero, M. Malumbres, and M. Barbacid. Cyclin-dependent kinase 2 is essential for meiosis but not for mitotic cell division in mice. *Nature Genet.*, 35:25 – 31, 2003.

[82] R. Boutros, V. Lobjois, and B. Ducommun. CDC25 phosphatases in cancer cells: key players? Good targets? *Nat. Rev. Cancer*, 7:495 – 507, 2007.

[83] Y. Ito, H. Yoshida, T. Uruno, Y. Takamura, A. Miya, K. Kuma, and A. Miyauchi. Expression of cdc25A and cdc25B phosphatase in breast carcinoma. *Breast Cancer.*, 11:295 – 300, 2004.

[84] M. Broggini, G. Buraggi, A. Brenna, L. Riva, A. M. Codegoni, V. Torri, A.A. Lissoni, C. Mangioni, and M. D'Incalci. Cell cycle-related phosphatases CDC25A and B expression correlates with survival in ovarian cancer patients. *Anti-Cancer Res.*, 20:4835 – 4840, 2000.

[85] E. S. W. Ngan, Y. Hashimoto, Z. Q. Ma, M. J. Tsai, and S. Y. Tsai. Overexpression of Cdc25B, an androgen receptor coactivator, in prostate cancer. *Oncogene*, 22:734 – 739, 2003.

[86] I. Takemasa, H. Yamamoto, M. Sekimoto, M. Ohue, S. Noura, Y. Miyake, T. Matsumoto, T. Aihara, N. Tomita, Y. Tamaki, I. Sakita, N. Kikkawa, N. Matsuura, H. Shiozaki, and M. Monden. Overexpression of CDC25B phosphatase as a novel marker of poor prognosis of human colorectal carcinoma. *Cancer Res.*, 60:3043 – 3050, 2000.

[87] I. Hoffmann, G. Draetta, and E. Karsenti. Activation of the phosphatase activity of human cdc25A by a cdk2-cyclin E dependent phosphorylation at the G1/S transition. *EMBO J.*, 13(18):4302–4310, 1994.

[88] V. Sexl, J. A. Diehl, C. J. Sherr, R. Ashmun, D. Beach, and M. F. Roussel. A rate limiting function of cdc25A for S phase entry inversely correlates with tyrosine dephosphorylation of Cdk2. *Oncogene*, 18(3):573 – 582, 1999.

[89] R. A. Weinberg. The retinoblastoma protein. *Cell*, 81:323 – 330, 1995.

[90] R. J. Cote, M. D. Dunn, S. J. Chatterjee, J. P. Stein, S. R. Shi, Q. C. Tran, S. X. Hu, H. J. Xu, S. Groshen, C. R. Taylor, D. G. Skinner, and W. F. Benedict. Elevated and Absent pRb Expression Is Associated with Bladder Cancer Progression and Has Cooperative Effects with p53. *Cancer Res.*, 58(6):1090 – 1094, 1998.

[91] J. Lukas, B. O. Petersen, K. Holm, J. Bartek, and K. Helin. Deregulated expression of E2F family members induces S-phase entry and overcomes p16INK4A-mediated growth suppression. *Mol. Cell. Biol.*, 16(3):1047–1057, 1996.

[92] D. G. Johnson, J. K. Schwarz, W. D. Cress, and J. R. Nevins. Expression of transcription factor E 2 F 1 induces quiescent cells to enter S phase. *Nature*, 365(6444):349 – 352, 1993.

[93] S. Fredersdorf, J. Burns, A. M. Milne, G. Packham, L. Fallis, C. E. Gillett, J. A. Royds, D. Peston, P. A. Hall, A. M. Hanby, D. M. Barnes, S. Shousha, M. J. O'Hare, and X. Lu. High level expression of p27kip1 and cyclin D1 in some human breast cancer cells: Inverse correlation between the expression of p27kip1 and degree of malignancy in human breast and colorectal cancers. *Proc. Natl. Acad. Sci. U. S. A.*, 94:6380 – 6385, 1997.

[94] R. Donnellan and R. Chetty. Cyclin D1 and human neoplasia. *J. Clin. Pathol.*, 51:1–7, 1998.

[95] P. Sicinski, J. L. Donaher, S. B. Parker, T. Li, A. Fazeli, H. Gardner, S. Z. Hasiam, R. T. Bronson, S. J. Elledge, and R. A. Weinberg. Cyclin D1 provides a link between development and oncogenesis in the retina and the breast. *Cell*, 82:621 – 630, 1995.

[96] P. Sicinski, J. L. Donaher, Y. Geng, S. B. Parker, H. Gardner, M. Y. Park, R. L. Robker, J. S. Richards, L. K. McGinnis, J. D. Biggers, J. J. Eppig, R. T. Bronson, S. J. Elledge, and R. A. Weinberg. Cyclin D2 is an FSH-responsive gene involved in gonadal cell proliferation and oncogenesis. *Nature*, 384:470 – 474, 1996.

[97] M. A. Ciemerych, A. M. Kenney, E. Sicinska, I. Kalaszczynska, R. T. Bronson, D. H. Rowitch, H. Gardner, and P. Sicinski. Development of mice expressing a single D-type cyclin. *Genes Dev.*, 16:3277 – 3289, 2002.

[98] K. Kozar, M. A. Ciemerych, V. I. Rebel, H. Shigematsu, A. Zagozdzon, E. Sicinska, Y. Geng, Q. Y. Yu, S. Bhattacharya, R. T. Bronson, K. Akashi, and P. Sicinski. Mouse Development and Cell Proliferation in the Absence of D-Cyclins. *Cell*, 118:477 – 491, 2004.

[99] S. M. Keenan, N. H. Lents, and J. J. Baldassare. Expression of Cyclin E Renders Cyclin D-CDK4 Dispensable for Inactivation of the Retinoblastoma Tumor Suppressor Protein, Activation of E2F, and G1-S Phase Progression. *J. Biol. Chem.*, 279:5387 – 5396, 2004.

[100] S. Kar, M. F. Wang, W. Yao, C. J. Michejda, and B. I. Carr. PM-20, a novel inhibitor of Cdc25A, induces extracellular signal-regulated kinase 1/2 phosphorylation and inhibits hepatocellular carcinoma growth in vitro and in vivo. *Mol. Cancer Ther.*, 5(6):1511 – 1519, 2006.

[101] M. C. Brezak, M. Quaranta, M. O. Contour-Galcera, O. Lavergne, O. Mondesert, P. Auvray, P. G. Kasprzyk, G. P. Prevost, and B. Ducommun. In-

hibition of human tumor cell growth in vivo by an orally bioavailable inhibitor of CDC25 phosphatases. *Mol. Cancer Ther.*, 4(9):1378 – 1387, 2005.

[102] K. Tamura, E. C. Southwick, J. Kerns, K. Rosi, B. I. Carr, C. Wilcox, and J. S. Lazo. Cdc25 Inhibition and Cell Cycle Arrest by a Synthetic Thioalkyl Vitamin K Analogue 1. *Cancer Res.*, 60(5):1317 – 1325, 2000.

[103] S. Kar, M. F. Wang, C. S. Wilcox, and B. I. Carr. Antitumor and anticarcinogenic actions of Cpd 5: a new class of protein phosphatase inhibitor. *Carcinogenesis*, 24(3):411 – 416, 2003.

[104] G. P. Prevost, M. C. Brezak, F. Goubin, O. Mondesert, M. O. Galcera, M. Quaranta, F. Alby, O. Lavergne, and B. Ducommum. Inhibitors of the CDC25 phosphatases. *Progress in Cell Cycle Research*, 5:225 – 234, 2003.

[105] G. K. Schwartz and M. A. Shah. Targeting the Cell Cycle: A New Approach to Cancer Therapy. *J. Clin. Oncol.*, 23(36):9408 – 9421, 2005.

[106] J. McCormick, SM Gadgeel, W. Helmke, R. Chaplen, B. van Leeuwen, M. Woo, H. Youssoufian, A. DeCiliis, S. Letrent, and P. LoRusso. Phase I study of BMS-387032, a cyclin dependent kinase (CDK) 2 inhibitor. *Proc. Am. Soc. Clin. Oncol.*, 22:208, 2003.

[107] R. N. Misra, H. Y. Xiao, K. S. Kim, S. F. Lu, W. C. Han, S. A. Barbosa, J. T. Hunt, D. B. Rawlins, W. F. Shan, S. Z. Ahmed, L. G. Qian, B. C. Chen, R. L. Zhao, M. S. Bednarz, K. A. Kellar, J. G. Mulheron, R. Batorsky, U. Roongta, A. Kamath, P. Marathe, S. A. Ranadive, J. S. Sack, J. S. Tokarski, N. P. Pavletich, F. Y. F. Lee, K. R. Webster, and S. D. Kimball. N-(cycloalkylamino)acyl-2-aminothiazole inhibitors of cyclin-dependent kinase - 2. n-[5-[[[5-(1,1-dimethylethyl)-2-oxazolyl]methyl]thio]-2-thiazolyl]-4-pip eridinecarboxamide (bms-387032), a highly efficacious and selective antitumor agent. *J. Med. Chem.*, 47(7):1719 – 1728, 2004.

[108] A. M. Senderowicz. Flavopiridol: the First Cyclin-Dependent Kinase Inhibitor in Human Clinical Trials. *Invest. New Drugs*, 17(3):313 – 320, 1999.

[109] A. M. Senderowicz. Small-molecule cyclin-dependent kinase modulators. *Oncogene*, 22:6609–6620, 2003.

[110] National Cancer Institute (NCI). A Phase II Study of Flavopiridol (HMR 1275; NSC 649890) in Patients With Previously Untreated Metastatic or Locally Advanced Soft Tissue Sarcoma (Trial NCT00005974), 2007.

[111] National Cancer Institute (NCI). A Pilot Study of Flavopiridol Administered as a 30-Minute Bolus Followed by a 4-Hour Infusion in Lymphomas and Multiple Myeloma (Trial NCT00112723), 2007.

[112] National Cancer Institute (NCI). A Phase I Study Of Herceptin/Flavopiridol In HER-2 Positive Metatatic Breast Cancer (Trial NCT00039455)., 2007.

[113] National Cancer Institute (NCI). Flavopiridol Plus Cisplatin or Carboplatin in Treating Patients With Advanced Solid Tumors (Trial NCT00003690), October 2007.

[114] Cyclacel Pharmaceuticals, Inc. A Phase IIb Randomized Study of Oral Seliciclib in Patients With Previously Treated Non-Small Cell Lung Cancer (Trial NCT00372073), 2007.

[115] National Cancer Institute (NCI). Phase I Dose-Finding Study of E7070 in Combination With Irinotecan (Trial NCT00060567).

[116] C. Van Kesteren, J. H. Beijnen, and J. H. M. Schellens. E7070: a novel synthetic sulfonamide targeting the cell cycle progression for the treatment of cancer. *Anti-Cancer Drugs*, 13(10):989 – 997, 2002.

[117] National Cancer Institute (NCI). Phase II Clinical Evaluation of BRYOSTATIN 1 in Patients with Relaped Multiple Myeloma (Trial NCT00002907), 2007.

[118] National Cancer Institute (NCI). Phase II Study of Bryostatin 1 in Patients With Metastatic Colo-Rectal Adenocarcinoma (Trial NCT00003220), 2007.

[119] M. L. Varterasian, R. M. Mohammad, D. S. Eilender, K. Hulburd, D. H. Rodriguez, P. A. Pemberton, J. M. Pluda, M. D. Dan, G. R. Pettit, B. D Chen, and A. M. Al-Katib. Phase I study of bryostatin 1 in patients with relapsed non-Hodgkin's lymphoma and chronic lymphocytic leukemia. *J. Clin. Oncol.*, 16:56 – 62, 1998.

[120] L. M. Schuchter, A. H. Esa, W. S. May, M . K. Laulis, G. R. Pettit, and A. D. Hess. Successful treatment of murine melanoma with bryostatin-1. *Cancer Res.*, 51:682 – 687, 1991.

[121] R. L. Hornung, J. W. Pearson, M. Bechwith, and D. L. Longo. Preclinical evaluation of bryostatin-1 as an anticancer agent against several murine

tumor cell lines: in vitro versus in vivo activity. *Cancer Res.*, 52:101 – 107, 1992.

[122] M. Hayun, E. Okun, R. Hayun, U. Gafter, M. Albeck, D. L. Longo, and B. Sredni. Synergistic effect of AS101 and Bryostatin-1 on myeloid leukemia cell differentiation in vitro and in an animal model. *Leukemia*, 21:1504 – 1513, 2007.

[123] C. Asiedu, J. Biggs, M. Lilly, and A. S. Kraft. Inhibition of leukemic cell growth by the protein kinase C activator bryostatin 1 correlates with the dephosphorylation of cyclin dependent kinase 2. *Cancer Res.*, 55:3716 – 3720, 1995.

[124] J. A. Koutcher, M. Motwani, K. L. Zakian, X. K. Li, C. Matei, J. P. Dyke, D. Ballon, H. H. Yoo, and G. K. Schwartz. The *in-vivo* effect of Bryostatin-1 on Paclitaxel-induced tumor growth, mitotic entry, and blood flow. *Clin. Cancer Res.*, 6:1498 – 1507, 2000.

[125] J.W.B. Hershey. Translational Control in Mammalian Cells. *Annual Review of Biochemistry*, 60(1):717–755, 1991.

[126] J. D. Richter and N. Sonenberg. Regulation of cap-dependent translation by eIF4E inhibitory proteins. *Nature*, 433:477 – 480, Feb 2005.

[127] B.D.L. Li, L. Liu, M. Dawson, and A. De Benedetti. Overexpression of eukaryotic initiation factor 4 E(eIF 4 E) in breast carcinoma. *Cancer*, 79(12):2385–2390, 1997.

[128] S. Franklin, T. Pho, F. W. Abreo, R. Nassar, A. De Benedetti, F. J. Stucker, and C. A. O. Nathan. Detection of the Proto-oncogene eIF4E in Larynx and Hypopharynx Cancers. *Arch. Otolaryngol. Head Neck Surg.*, 125(2):177 – 182, 1999.

[129] William C Merrick. Cap-dependent and cap-independent translation in eukaryotic systems. *Gene*, 332:1–11, 2004.

[130] K. A. Spriggs, M. Bushell, S. A. Mitchell, and A. E. Wills. Internal ribosome entry segment-mediated translation during apoptosis - the role of ires-*trans*-acting factors. *Cell Death Differ.*, 12:585 – 591, 2005.

[131] G. Soderlund, M. Haarhaus, S. Chisalita, and H. J. Arnqvist. Inhibition of

puromycin-induced apoptosis in breast cancer cells by igf-1 occurs simultaneously with increase protein synthesis. *Neoplasma*, 51:1 – 11, 2004.

[132] MA Bjornsti and PJ Houghton. The TOR pathway: a target for cancer therapy. *Nat Rev Cancer*, 4(5):335–48, 2004.

[133] J. Douros and M. Suffness. New antitumor substances of natural origin. *Cancer Treat. Rev.*, 8:63 – 87, 1981.

[134] D. P. Houchens, A. A. Ovejera, S. M. Riblet, and D. E. Slagel. Human brain tumor xenografts in nude mice as a chemotherapy model. *Eur. J. Cancer Clin. Oncol*, 19:799 – 805, 1983.

[135] C. P. Eng, S. N. Sehgal, and C. Vezina. Activity of rapamycin (AY-22,989) against transplanted tumors. . *J. Antibiot*, 37:1231 – 1237, 1984.

[136] M. B. Atkins, M. Hidalgo, W. M. Stadler, T. F. Logan, J. P. Dutcher, G. R. Hudes, Y. Park, S-H. Liou, B. Marshall, J. P. Boni, G. Dukart, and M. L. Sherman. Randomized Phase II Study of Multiple Dose Levels of CCI-779, a Novel Mammalian Target of Rapamycin Kinase Inhibitor, in Patients With Advanced Refractory Renal Cell Carcinoma. *J. Clin. Oncol.*, 22:909 – 918, 2004.

[137] S. Bang, S. Nagata, M. Onda, R. J. Kreitman, and I. Pastan. HA22 (R490A) is a recombinant immunotoxin with Increased Antitumor Activity without and increase in Animal Toxicity. *Clin. Cancer Res.*, 11:1545 – 1550, 2005.

[138] C. B. Siegall, V. K. Chaudhary, D. J. FitzGerald, and I. Pastan. Functional analysis of domains ii, ib and iii of *Psuedomonas* exotoxin. *J. Biol. Chem.*, 264:14256 – 14261, 1989.

[139] T. Decker, M. Oelsner, R. J. Kreitman, G. Salvatore, Q. C. Wang, I. Pastan, C. Peschel, and T. Licht. Induction of caspase-dependent programmed cell death in b-cell chronic lymphocytic leukemia by anti-cd22 immunotoxins. *Blood*, 103:2718 – 2726, 2004.

[140] A. Keppler-Hafkemeyer, U. Brinkmann, and I. Pastan. Role of caspases in immunotoxin-induced apoptosis of cancer cells. *Biochemistry*, 37:16934 – 16942, 1998.

[141] A. Keppler-Hafkemeyer, R. J. Kreitman, and I. Pastan. Apoptosis induced

by immunotoxins used in the treatment of hematologic malignancies. *Int. J. Cancer*, 87:86 – 94, 2000.

[142] M. Glotzer, A. W. Murray, and M. W. Kirschner. Cyclin is degraded by the ubiquitin pathway. *Nature*, 349:132 – 138, 1991.

[143] G. Nalepa, M. Rolfe, and J. W. Harper. Drug discovery in the ubiquitin–proteasome system. *Nat. Rev. Drug Discov.*, 5:596 – 613, 2006.

[144] A. Hershko. Ubiquitin - roles in protein modification and breakdown. *Cell*, 34:11 – 12, 1983.

[145] K. I. Nakayama and K. Nakayama. Ubiquitin ligases - cell-cycle control and cancer. *Nat. Rev. Cancer*, 6:369 – 381, 2006.

[146] A. Hershko, H. Heller, S. Elias, and A. Ciechanover. Components of ubiquitin-protein ligase system. Resolution, affinity purification, and role in protein breakdown. *J. Biol. Chem.*, 258(13):8206 – 8214, 1983.

[147] J. W. Harper, J. L. Burton, and M. J. Solomon. The anaphase promoting complex - its not just for mitosis any more. *Genes Dev.*, 16:2179 – 2206, 2002.

[148] A. Castro, C. Bernis, S. Vigneron, J. C. Labbe, and T. Lorca. The anaphase-promoting complex - a key factor in the regulation of cell-cycle. *Oncogene*, 24:314 – 325, 2005.

[149] K. Garber. Missing the Target - Ubiquitin Ligase Drugs Stall. *J. Natl. Cancer Inst.*, 97:166 – 167, 2005.

[150] L.T. Vassilev, B. T. Vu, B. Graves, D. Carvajal, F. Podlaski, Z. Filipovic, N. Kong, U. Kammlott, C. Lukacs, C. Klein, N. Fotouhi, and E. A. Liu. In Vivo Activation of the p53 Pathway by Small-Molecule Antagonists of MDM2. *Science*, 303(5659):844 – 848, 2004.

[151] D. Luan, D. Kudelas, and J. Varner. The Assessment of Robustness and Fragility of Mechanisms in a Human Cascade is Sensitive to Structural Uncertainty. In *Foundations of Systems Biology in Engineering*, pages 393 – 404, Stuttgart, Germany, 2007.

[152] R. S. Bresalier, R. S. Sandler, H. Quan, J. A. Bolognese, B. Oxenius, K. Horgan, C. Lines, R. Riddell, D. Morton, A. Lanas, M. A. Konstam, and J. A.

Baron. Cardiovascular Events Associated with Rofecoxib in a Colorectal Adenoma Chemoprevention Trial. *N. Engl. J. Med.*, 352:1092 – 1102, 2005.

[153] Arrigo De Benedetti and Jeremy R Graff. eif-4e expression and its role in malignancies and metastases. *Oncogene*, 23(18):3189–3199, 2004.

[154] Joel D Richter and Nahum Sonenberg. Regulation of cap-dependent translation by eif4e inhibitory proteins. *Nature*, 433(7025):477–480, 2005.

[155] J.R. Graff, B.W. Konicek, A.M. McNulty, Z. Wang, K. Houck, S. Allen, J.D. Paul, A. Hbaiu, R.G. Goode, G.E. Sandusky, et al. Increased AKT Activity Contributes to Prostate Cancer Progression by Dramatically Accelerating Prostate Tumor Growth and Diminishing p27Kip1 Expression. *Journal of Biological Chemistry*, 275(32):24500–24505, 2000.

[156] M.D. Ringel, N. Hayre, J. Saito, B. Saunier, F. Schuppert, H. Burch, V. Bernet, K.D. Burman, L.D. Kohn, and M. Saji. Overexpression and Overactivation of Akt in Thyroid Carcinoma 1. *Cancer Research*, 61(16):6105–6111, 2001.

[157] X. Zhou, M. Tan, V. Stone Hawthorne, K.S. Klos, K.H. Lan, Y. Yang, W. Yang, T.L. Smith, D. Shi, and D. Yu. Activation of the Akt/Mammalian Target of Rapamycin/4E-BP1 Pathway by ErbB2 Overexpression Predicts Tumor Progression in Breast Cancers. *Clinical Cancer Research*, 10(20):6779–6788, 2004.

[158] C. Bauer, N. Brass, I. Diesinger, K. Kayser, F.A. Graesser, and E. Meese. Overexpression of the eukaryotic translation initiation factor 4 G(eIF 4 G-1) in squamous cell lung carcinoma. *International Journal of Cancer*, 98(2):181–185, 2002.

[159] M.A. Bjornsti and P.J. Houghton. Lost in translation: dysregulation of cap-dependent translation and cancer. *Cancer Cell*, 5(6):519–523, 2004.

[160] Deyan Luan, Michael Zai, and Jeffrey D Varner. Computationally derived points of fragility of a human cascade are consistent with current therapeutic strategies. *PLoS Comput Biol*, 3(7):e142, 2007.

[161] Satyaprakash Nayak, Saniya Salim, Deyan Luan, Michael Zai, and Jeffrey D Varner. A test of highly optimized tolerance reveals fragile cell-cycle mechanisms are molecular targets in clinical cancer trials. *PLoS ONE*, 3(4):e2016, 2008.

[162] JE Shoemaker and 3rd Doyle FJ. Identifying fragilities in biochemical networks: Robust performance analysis of fas signaling-induced apoptosis. *Biophys J*, 95(6):2610–2623, 2008.

[163] R G Vries, A Flynn, J C Patel, X Wang, R M Denton, and C G Proud. Heat shock increases the association of binding protein-1 with initiation factor 4e. *J Biol Chem*, 272(52):32779–32784, 1997.

[164] J R Lorsch and D Herschlag. Kinetic dissection of fundamental processes of eukaryotic translation initiation in vitro. *EMBO J*, 18(23):6705–6717, 1999.

[165] Attila Garami, Fried J T Zwartkruis, Takahiro Nobukuni, Manel Joaquin, Marta Roccio, Hugo Stocker, Sara C Kozma, Ernst Hafen, Johannes L Bos, and George Thomas. Insulin activation of rheb, a mediator of mtor/s6k/4e-bp signaling, is inhibited by tsc1 and 2. *Mol Cell*, 11(6):1457–1466, 2003.

[166] Kevin S Brown and James P Sethna. Statistical mechanical approaches to models with many poorly known parameters. *Phys Rev E Stat Nonlin Soft Matter Phys*, 68(2 Pt 1):021904, 2003.

[167] D Battogtokh, D.K. Asch, M.E. Case, J Arnold, and H-B Shüttler. An ensemble method for identifying regulatory circuits with special reference to the qa gene cluster of neurospora crassa. *P Natl Acad Sci USA*, 99(26):16904–16909, December 2002.

[168] A. Marintchev and G. Wagner. Translation initiation: structures, mechanisms and evolution. *Quarterly Reviews of Biophysics*, 37(3-4):197–284, 2005.

[169] N.K. Gray and M. Wickens. Control of Translation Initiation in Animals. *Annual Review of Cell and Developmental Biology*, 14(1):399–458, 1998.

[170] L.C. Cantley. The Phosphoinositide 3-Kinase Pathway. *Science*, 296(5573):1655–1657, May 2002.

[171] B. Schoeberl, C. Eichler-Jonsson, E.D. Gilles, and G. Mueller. Computational modeling of the dynamics of the map kinase cascade activated by surface and internalized egf receptors. *Nat Biotechnol*, 20(4):370–375, Apr 2002.

[172] Igor Vivanco and Charles L Sawyers. The phosphatidylinositol 3-kinase akt pathway in human cancer. *Nat Rev Cancer*, 2(7):489–501, Jul 2002.

[173] J. Paez and W.R. Sellers. PI3K/PTEN/Akt pathway. *A critical mediator of oncogenic signaling. CancerTreat Res*, 115:145–67, 2003.

[174] A. Sekulic, C.C. Hudson, J.L. Homme, P. Yin, D.M. Otterness, L.M. Karnitz, and R.T. Abraham. A Direct Linkage between the Phosphoinositide 3-Kinase-AKT Signaling Pathway and the Mammalian Target of Rapamycin in Mitogen-stimulated and Transformed Cells 1. *Cancer Research*, 60(13):3504–3513, 2000.

[175] TA Lin, X. Kong, TA Haystead, A. Pause, G. Belsham, N. Sonenberg, and JC Lawrence. PHAS-I as a link between mitogen-activated protein kinase and translation initiation. *Science*, 266(5185):653–656, 1994.

[176] J.D. Richter and N. Sonenberg. Regulation of cap-dependent translation by eIF 4 E inhibitory proteins. *Nature*, 433(7025):477–480, 2005.

[177] G.J. Brunn, C.C. Hudson, et al. Phosphorylation of the Translational Repressor PHAS-I by the Mammalian Target of Rapamycin. *Science*, 277(5322):99, 1997.

[178] T. Schmelzle and M.N. Hall. TOR, a Central Controller of Cell Growth. *Cell*, 103(2):253–262, 2000.

[179] Tzvetanka Bondeva, Luciano Pirola, Ginette Bulgarelli-Leva, Ignacio Rubio, Reinhard Wetzker, and Matthias P. Wymann. Bifurcation of Lipid and Protein Kinase Signals of PI3K to the Protein Kinases PKB and MAPK. *Science*, 282(5387):293–296, 1998.

[180] D.P. Brazil and B.A. Hemmings. Ten years of protein kinase B signalling: a hard Akt to follow. *Trends in Biochemical Sciences*, 26(11):657–664, 2001.

[181] Marina K Holz, Bryan A Ballif, Steven P Gygi, and John Blenis. mtor and s6k1 mediate assembly of the translation preinitiation complex through dynamic protein interchange and ordered phosphorylation events. *Cell*, 123(4):569–580, 2005.

[182] A Pause, G J Belsham, A C Gingras, O Donze, T A Lin, J C Jr Lawrence, and N Sonenberg. Insulin-dependent stimulation of protein synthesis by

phosphorylation of a regulator of 5'-cap function. *Nature*, 371(6500):762–767, 1994.

[183] C Hu, S Pang, X Kong, M Velleca, and J C Jr Lawrence. Molecular cloning and tissue distribution of phas-i, an intracellular target for insulin and growth factors. *Proc Natl Acad Sci U S A*, 91(9):3730–3734, 1994.

[184] F Poulin, A C Gingras, H Olsen, S Chevalier, and N Sonenberg. 4e-bp3, a new member of the eukaryotic initiation factor 4e-binding protein family. *J Biol Chem*, 273(22):14002–14007, 1998.

[185] A C Gingras, S P Gygi, B Raught, R D Polakiewicz, R T Abraham, M F Hoekstra, R Aebersold, and N Sonenberg. Regulation of 4e-bp1 phosphorylation: a novel two-step mechanism. *Genes Dev*, 13(11):1422–1437, 1999.

[186] A C Gingras, B Raught, S P Gygi, A Niedzwiecka, M Miron, S K Burley, R D Polakiewicz, A Wyslouch-Cieszynska, R Aebersold, and N Sonenberg. Hierarchical phosphorylation of the translation inhibitor 4e-bp1. *Genes Dev*, 15(21):2852–2864, 2001.

[187] M. R. Spiegel. *Statistics: Schaum's Easy Outlines*. McGraw-Hill, 2000.

[188] R. P. Dickinson and R. J. Gelinas. Sensitivity analysis of ordinary differential equation systems - a direct method. *J Comp Phys*, 21:123 – 143, 1976.

[189] M. Schumer and K. Steiglitz. Adaptive step size random search. *IEE Trans Automatic Control*, 13:270 – 276, 1968.

[190] Y Mamane, E Petroulakis, O LeBacquer, and N Sonenberg. mtor, translation initiation and cancer. *Oncogene*, 25(48):6416–6422, 2006.

[191] B D Li, L Liu, M Dawson, and A De Benedetti. Overexpression of eukaryotic initiation factor 4e (eif4e) in breast carcinoma. *Cancer*, 79(12):2385–2390, 1997.

[192] Megan Cully, Han You, Arnold J Levine, and Tak W Mak. Beyond pten mutations: the pi3k pathway as an integrator of multiple inputs during tumorigenesis. *Nat Rev Cancer*, 6(3):184–192, 2006 Mar.

[193] Boris N Kholodenko, Anatoly Kiyatkin, Frank J Bruggeman, Eduardo Sontag, Hans V Westerhoff, and Jan B Hoek. Untangling the wires: a

strategy to trace functional interactions in signaling and gene networks. *Proc Natl Acad Sci U S A*, 99(20):12841–12846, 2002.

[194] Michael Andrec, Boris N Kholodenko, Ronald M Levy, and Eduardo Sontag. Inference of signaling and gene regulatory networks by steady-state perturbation experiments: structure and accuracy. *J Theor Biol*, 232(3):427–441, 2005.

[195] BC Barnhart, JC Lam, RM Young, PJ Houghton, B Keith, and MC Simon. Effects of 4e-bp1 expression on hypoxic cell cycle inhibition and tumor cell proliferation and survival. *Cancer Biol Ther*, 7(9), 2008.

[196] A De Benedetti, S Joshi-Barve, C Rinker-Schaeffer, and R E Rhoads. Expression of antisense rna against initiation factor eif-4e mrna in hela cells results in lengthened cell division times, diminished translation rates, and reduced levels of both eif-4e and the p220 component of eif-4f. *Mol Cell Biol*, 11(11):5435–5445, 1991.

[197] D Rousseau, R Kaspar, I Rosenwald, L Gehrke, and N Sonenberg. Translation initiation of ornithine decarboxylase and nucleocytoplasmic transport of cyclin d1 mrna are increased in cells overexpressing eukaryotic initiation factor 4e. *Proc Natl Acad Sci U S A*, 93(3):1065–1070, 1996.

[198] V Stambolic, A Suzuki, J L de la Pompa, G M Brothers, C Mirtsos, T Sasaki, J Ruland, J M Penninger, D P Siderovski, and T W Mak. Negative regulation of pkb/akt-dependent cell survival by the tumor suppressor pten. *Cell*, 95(1):29–39, 1998.

[199] J Li, C Yen, D Liaw, K Podsypanina, S Bose, S I Wang, J Puc, C Miliaresis, L Rodgers, R McCombie, S H Bigner, B C Giovanella, M Ittmann, B Tycko, H Hibshoosh, M H Wigler, and R Parsons. Pten, a putative protein tyrosine phosphatase gene mutated in human brain, breast, and prostate cancer. *Science*, 275(5308):1943–1947, 1997.

[200] A. Soni, A. Akcakanat, G. Singh, D. Luyimbazi, Y. Zheng, D. Kim, A. Gonzalez-Angulo, and F. Meric-Bernstam. eIF4E knockdown decreases breast cancer cell growth without activating Akt signaling. *Molecular Cancer Therapeutics*, 7(7):1782, 2008.

[201] P B Dennis, N Pullen, S C Kozma, and G Thomas. The principal rapamycin-sensitive p70(s6k) phosphorylation sites, t-229 and t-389, are differentially regulated by rapamycin-insensitive kinase kinases. *Mol Cell Biol*, 16(11):6242–6251, 1996 Nov.

[202] O J Shah, J C Anthony, S R Kimball, and L S Jefferson. 4e-bp1 and s6k1: translational integration sites for nutritional and hormonal information in muscle. *Am J Physiol Endocrinol Metab*, 279(4):E715–29, 2000 Oct.

[203] N Pullen, P B Dennis, M Andjelkovic, A Dufner, S C Kozma, B A Hemmings, and G Thomas. Phosphorylation and activation of p70s6k by pdk1. *Science*, 279(5351):707–710, 1998 Jan 30.

[204] S Volarevic and G Thomas. Role of s6 phosphorylation and s6 kinase in cell growth. *Prog Nucleic Acid Res Mol Biol*, 65:101–127, 2001.

[205] B Raught, A C Gingras, S P Gygi, H Imataka, S Morino, A Gradi, R Aebersold, and N Sonenberg. Serum-stimulated, rapamycin-sensitive phosphorylation sites in the eukaryotic translation initiation factor 4gi. *EMBO J*, 19(3):434–444, 2000 Feb 1.

[206] Gert C Scheper and Christopher G Proud. Does phosphorylation of the cap-binding protein eif4e play a role in translation initiation? *Eur J Biochem*, 269(22):5350–5359, 2002 Nov.

[207] Lenin Mahimainathan and Goutam Ghosh Choudhury. Inactivation of Platelet-derived Growth Factor Receptor by the Tumor Suppressor PTEN Provides a Novel Mechanism of Action of the Phosphatase. *J. Biol. Chem.*, 279(15):15258–15268, 2004.

[208] S. Waxman and K.C. Anderson. History of the development of arsenic derivatives in cancer therapy, 2001.

[209] A.M. Evens, M.S. Tallman, and R.B. Gartenhaus. The potential of arsenic trioxide in the treatment of malignant disease: past, present, and future. *Leukemia research*, 28(9):891–900, 2004.

[210] Z.Y. Wang and Z. Chen. Acute promyelocytic leukemia: from highly fatal to highly curable. *Blood*, 111(5):2505, 2008.

[211] Z.X. Shen, G.Q. Chen, J.H. Ni, X.S. Li, S.M. Xiong, Q.Y. Qiu, J. Zhu, W. Tang, G.L. Sun, K.Q. Yang, et al. Use of arsenic trioxide (As2O3) in the treatment of acute promyelocytic leukemia (APL): II. Clinical efficacy and pharmacokinetics in relapsed patients. *Blood*, 89(9):3354, 1997.

[212] C. Niu, H. Yan, T. Yu, H.P. Sun, J.X. Liu, X.S. Li, W. Wu, F.Q. Zhang, Y. Chen, L. Zhou, et al. Studies on treatment of acute promyelo-

cytic leukemia with arsenic trioxide: remission induction, follow-up, and molecular monitoring in 11 newly diagnosed and 47 relapsed acute promyelocytic leukemia patients. *Blood*, 94(10):3315, 1999.

[213] V. Mathews, B. George, K.M. Lakshmi, A. Viswabandya, A. Bajel, P. Balasubramanian, R.V. Shaji, V.M. Srivastava, A. Srivastava, and M. Chandy. Single-agent arsenic trioxide in the treatment of newly diagnosed acute promyelocytic leukemia: durable remissions with minimal toxicity. *Blood*, 107(7):2627–2632, 2006.

[214] TR Breitman, SJ Collins, and BR Keene. Terminal differentiation of human promyelocytic leukemic cells in primary culture in response to retinoic acid. *Blood*, 57(6):1000, 1981.

[215] ME Huang, YC Ye, SR Chen, JR Chai, JX Lu, L. Zhoa, LJ Gu, and ZY Wang. Use of all-trans retinoic acid in the treatment of acute promyelocytic leukemia. *Blood*, 72(2):567, 1988.

[216] Norio Asou, Yuji Kishimoto, Hitoshi Kiyoi, Masaya Okada, Yasukazu Kawai, Motohiro Tsuzuki, Kentaro Horikawa, Mitsuhiro Matsuda, Katsuji Shinagawa, Tohru Kobayashi, Shigeki Ohtake, Miki Nishimura, Masatomo Takahashi, Fumiharu Yagasaki, Akihiro Takeshita, Yukihiko Kimura, Masako Iwanaga, Tomoki Naoe, Ryuzo Ohno, and for the Japan Adult Leukemia Study Group. A randomized study with or without intensified maintenance chemotherapy in patients with acute promyelocytic leukemia who have become negative for PML-RARalpha transcript after consolidation therapy: The Japan Adult Leukemia Study Group (JALSG) APL97 study. *Blood*, 110(1):59–66, 2007.

[217] Z.X. Shen, Z.Z. Shi, J. Fang, B.W. Gu, J.M. Li, Y.M. Zhu, J.Y. Shi, P.Z. Zheng, H. Yan, Y.F. Liu, et al. All-trans retinoic acid/As2O3 combination yields a high quality remission and survival in newly diagnosed acute promyelocytic leukemia. *Proceedings of the National Academy of Sciences*, 101(15):5328–5335, 2004.

[218] A. Yen, M. S. Roberson, S. Varvayanis, and A. T. Lee. Retinoic acid induced mitogen-activated protein (map)/extracellular signal-regulated kinase (erk) kinase-dependent map kinase activation needed to elicit hl-60 cell differentiation and growth arrest. *Cancer Res*, 58(14):3163–3172, Jul 1998.

[219] Jianrong Wang and Andrew Yen. A mapk-positive feedback mechanism

for blr1 signaling propels retinoic acid-triggered differentiation and cell cycle arrest. *J Biol Chem*, 283(7):4375–4386, Feb 2008.

[220] GQ Chen, J. Zhu, XG Shi, JH Ni, HJ Zhong, GY Si, XL Jin, W. Tang, XS Li, SM Xong, et al. In vitro studies on cellular and molecular mechanisms of arsenic trioxide (As2O3) in the treatment of acute promyelocytic leukemia: As2O3 induces NB4 cell apoptosis with downregulation of Bcl-2 expression and modulation of PML-RAR alpha/PML proteins. *Blood*, 88(3):1052, 1996.

[221] SC Brooks 3rd, S. Kazmer, AA Levin, and A. Yen. Myeloid differentiation and retinoblastoma phosphorylation changes in HL-60 cells induced by retinoic acid receptor-and retinoid X receptor-selective retinoic acid analogs. *Blood*, 87(1):227, 1996.

[222] W. Shao. Arsenic trioxide as an inducer of apoptosis and loss of PML/RAR alpha protein in acute promyelocytic leukemia cells. *J Natl Cancer I*, 90(2):124–133, 1998.

[223] J. Dai, R.S. Weinberg, S. Waxman, and Y. Jing. Malignant cells can be sensitized to undergo growth inhibition and apoptosis by arsenic trioxide through modulation of the glutathione redox system. *Blood*, 93(1):268, 1999.

[224] A.M. Ramos, C. Fernandez, D. Amran, P. Sancho, E. de Blas, and P. Aller. Pharmacologic inhibitors of PI3K/Akt potentiate the apoptotic action of the antileukemic drug arsenic trioxide via glutathione depletion and increased peroxide accumulation in myeloid leukemia cells. *Blood*, 105(10):4013–4020, 2005.

[225] G.Q. Chen, X.G. Shi, W. Tang, S.M. Xiong, J. Zhu, X. Cai, Z.G. Han, J.H. Ni, G.Y. Shi, P.M. Jia, et al. Use of arsenic trioxide (As2O3) in the treatment of acute promyelocytic leukemia (APL): I. As2O3 exerts dose-dependent dual effects on APL cells. *Blood*, 89(9):3345, 1997.

[226] P.Z. Zheng, K.K. Wang, Q.Y. Zhang, Q.H. Huang, Y.Z. Du, Q.H. Zhang, D.K. Xiao, S.H. Shen, S. Imbeaud, E. Eveno, et al. Systems analysis of transcriptome and proteome in retinoic acid/arsenic trioxide-induced cell differentiation/apoptosis of promyelocytic leukemia. *Proceedings of the National Academy of Sciences*, 102(21):7653–7658, 2005.

[227] Q. Zhao, J. Tao, Q. Zhu, PM Jia, AX Dou, X. Li, F. Cheng, S. Waxman, GQ Chen, SJ Chen, et al. Rapid induction of cAMP/PKA pathway during

retinoic acid-induced acute promyelocytic leukemia cell differentiation. *Leukemia*, 18(2):285–292, 2003.

[228] Q. Zhu, J.W. Zhang, H.Q. Zhu, Y.L. Shen, M. Flexor, P.M. Jia, Y. Yu, X. Cai, S. Waxman, M. Lanotte, et al. Synergic effects of arsenic trioxide and cAMP during acute promyelocytic leukemia cell maturation subtends a novel signaling cross-talk. *Blood*, 99(3):1014, 2002.

[229] M. Shen and A. Yen. Nicotinamide Cooperates with Retinoic Acid and 1, 25-Dihydroxyvitamin D 3 to Regulate Cell Differentiation and Cell Cycle Arrest of Human Myeloblastic Leukemia Cells. *Oncology*, 76:91–100, 2009.

[230] G. Reiterer, R.P. Bunaciu, J.L. Smith, and A. Yen. Inhibiting the platelet derived growth factor receptor increases signs of retinoic acid syndrome in myeloid differentiated HL-60 cells. *FEBS Letters*, 582(17):2508–2514, 2008.

[231] BM Babior, JD Lambeth, and W. Nauseef. The neutrophil NADPH oxidase. *Archives of Biochemistry and Biophysics*, 397(2):342–344, 2002.

[232] J. Hua, T. Hasebe, A. Someya, S. Nakamura, K. Sugimoto, and I. Nagaoka. Evaluation of the expression of NADPH oxidase components during maturation of HL-60 cells to neutrophil lineage. *Journal of Leukocyte Biology*, 68(2):216–224, 2000.

[233] K. Davison, S. Cote, S. Mader, and WH Miller. Glutathione depletion overcomes resistance to arsenic trioxide in arsenic-resistant cell lines. *Leukemia*, 17(5):931–940, 2003.

[234] C.H. Yang, M.L. Kuo, J.C. Chen, and Y.C. Chen. Arsenic trioxide sensitivity is associated with low level of glutathione in cancer cells. *British journal of cancer*, 81(5):796–799, 1999.

[235] K. Davison, K.K. Mann, S. Waxman, and W.H. Miller. JNK activation is a mediator of arsenic trioxide-induced apoptosis in acute promyelocytic leukemia cells. *Blood*, 103(9):3496–3502, 2004.

[236] A. Verma, M. Mohindru, D.K. Deb, A. Sassano, S. Kambhampati, F. Ravandi, S. Minucci, D.V. Kalvakolanu, and L.C. Platanias. Activation of Rac1 and the p38 mitogen-activated protein kinase pathway in response to arsenic trioxide. *Journal of Biological Chemistry*, 277(47):44988–44995, 2002.

[237] H. Kishimoto, S. Hoshino, M. Ohori, K. Kontani, H. Nishina, M. Suzawa, S. Kato, and T. Katada. Molecular mechanism of human CD38 gene expression by retinoic acid Identification of retinoic acid response element in the first intron. *Journal of Biological Chemistry*, 273(25):15429–15434, 1998.

[238] M. Shen and A. Yen. c-Cbl Interacts with CD38 and Promotes Retinoic Acid-Induced Differentiation and G0 Arrest of Human Myeloblastic Leukemia Cells. *Cancer Research*, 68(21):8761, 2008.

[239] J.M. Li, A.M. Mullen, S. Yun, F. Wientjes, G.Y. Brouns, A.J. Thrasher, and A.M. Shah. Essential role of the NADPH oxidase subunit p47phox in endothelial cell superoxide production in response to phorbol ester and tumor necrosis factor-α. *Circulation research*, 90(2):143–150, 2002.

[240] X.J. Huang, P.H. Wiernik, R.S. Klein, and R.E. Gallagher. Arsenic trioxide induces apoptosis of myeloid leukemia cells by activation of caspases. *Cancer Immunology, Immunotherapy*, 16(1):58–64, 1999.

[241] G. Tabellini, A. Cappellini, P.L. Tazzari, F. Fala, A.M. Billi, L. Manzoli, L. Cocco, and A.M. Martelli. Phosphoinositide 3-kinase/Akt involvement in arsenic trioxide resistance of human leukemia cells Giovanna Tabellini and Alessandra Cappellini equally contributed to this work. *Journal of cellular physiology*, 202(2), 2005.

[242] A.M. Ramos and P. Aller. Quercetin decreases intracellular GSH content and potentiates the apoptotic action of the antileukemic drug arsenic trioxide in human leukemia cell lines. *Biochemical Pharmacology*, 75(10):1912–1923, 2008.

[243] S. J. Collins, R. C. Gallo, and R. E. Gallagher. Continuous growth and differentiation of human myeloid leukaemic cells in suspension culture. *Nature*, 270(5635):347–349, Nov 1977.

[244] T. R. Breitman, S. E. Selonick, and S. J. Collins. Induction of differentiation of the human promyelocytic leukemia cell line (hl-60) by retinoic acid. *Proc Natl Acad Sci U S A*, 77(5):2936–2940, May 1980.

[245] A. Yen. HL-60 cells as a model of growth control and differentiation - The significance of variant cells. *Hemat. Rev.*, 4:5 – 46, 1990.

[246] A. Yen, R. Sturgill, and S. Varvayanis. Retinoic acid increases amount of phosphorylated RAF. Ectopic expression of cFMS reveals that retinoic

acid induced differentiation is more strongly dependent on ERK2 signaling that induced G0 arrest is. *In Vitro Cell Dev. Biol.*, 36:249 – 255, 2000.

[247] H. Y. Hong, S. Varvayanis, and A. Yen. Retinoic acid causes mek-dependent raf phosphorylation through raralpha plus rxr activation in hl-60 cells. *Differentiation*, 68(1):55–66, Aug 2001.

[248] X. Wang and G. P. Studzinski. Activation of extracellular signal-regulated kinases (ERKs) defines the first phase of 1,25-dihydroxyvitamin D3-induced differentiation of HL-60 cells. *J. Cell Biochem.*, 80:471 – 482, 2001.

[249] A. Yen, S. L. Reece, and K. L. Albright. Dependence of hl-60 myeloid cell differentiation on continuous and split retinoic acid exposures: precommitment memory associated with altered nuclear structure. *J Cell Physiol*, 118(3):277–286, Mar 1984.

[250] A. Yen, M. Forbes, G. deGala, and J. Fishbaugh. Control of HL-60 cell differentiation lineage specificity - A late event occurring after precommitment. *Cancer Res.*, 47:129 – 134, 1987.

[251] A. Yen, D. Brown, and J. Fishbaugh. Precommitment states induced during HL-60 myeloid differentiation - Possible similarities of retinoic acid and DMSO induced early events. *Exp. Cell Res.*, 173:80 – 84, 1987.

[252] A. Yen and M. E. Forbes. C-myc down regulation and precommitment in HL-60 cells due to bromodeoxyuridine. *Cancer Res.*, 50:1411 – 1420, 1990.

[253] A. Yen, V. Cherington, B. Schaffhausen, K. Markes, and S. Varvayanis. Transformation defective polyoma middle t antigen mutants defective in plc-gamma, pi-3 or src kinase activation enhance erk2 activation and promote retinoic acid induced cell differentiation like wild type middle t. *Exp. Cell Res.*, 248:538 – 551, 1991.

[254] T. E. Battle, R. A. Levine, and A. Yen. Retinoic acid-induced blr1 expression promotes erk2 activation and cell differentiation in hl-60 cells. *Exp Cell Res*, 254(2):287–298, Feb 2000.

[255] A. Yen, A. W. Norman, and S. Varvayanis. Nongenomic vitamin d3 analogs activating erk2 in hl-60 cells show that retinoic acid induced differentiation and cell-cycle arrest require early concurrent mapk and rar and rxr activation. *In Vitro Cell Dev. Biol-Animal*, 37:93 – 99, 2001.

[256] T. E. Battle, M. S. Roberson, T. Zhang, S. Varvayanis, and A. Yen. Retinoic acid induced blr1 expression requires RARa, RXR and MAPK activation and uses ERK2 but not JNK/SAPK to accelerate cell differentiation. *Eur. J. Cell Biol.*, 80:59 – 67, 2001.

[257] T. Dobner, I. Wolf, T. Emrich, and M. Lipp. Differentiation-specific expression of a novel G protein-coupled receptor from Burkitt's lymphoma. *Eur. J. Immunol.*, 22:2795 – 2799, 1992.

[258] T. Emrich, R. Forster, and M. Lipp. Transmembrane topology of the lymphocyte-specific G protein-coupled receptor BLR1: analysis by flow cytometry and immunocytochemistry. *Cell Mol. Biol.*, 40:413 – 419, 1994.

[259] D. J. Mangelsdorf, U. Kazaukiko, and R. M. Evans. *The retinoid receptors.* The Retinoids. Raven Press, 2 edition, 1994.

[260] J. Wang and A. Yen. A novel retinoic acid-responsive element regulates retinoic acid induced BLR1 expression. *Mol. Cell. Biol.*, 24:2423 – 2443, 2004.

[261] H. E. Assmus, R. Herwig, K. H. Cho, and O. Wolkenhauer. Dynamics of biological systems: role of systems biology in medical research. *Exp. Rev. Molec. Diagn.*, 6:891 – 902, 2006.

[262] C. A. Arnaud. Systems Biology's Clinical Future. *Chem. Eng. News*, 84:17 – 26, 2006.

[263] C. Y. Huang and J. E. Ferrell. Ultrasensitivity in the mitogen-activated protein kinase cascade. *Proc Natl Acad Sci U S A*, 93(19):10078–10083, Sep 1996.

[264] M. Fussenegger, J. E. Bailey, and J. Varner. A mathematical model of caspase function in apoptosis. *Nat Biotechnol*, 18(7):768–774, Jul 2000.

[265] Ethel Queralt, Chris Lehane, Bela Novak, and Frank Uhlmann. Down-regulation of pp2a(cdc55) phosphatase by separase initiates mitotic exit in budding yeast. *Cell*, 125(4):719–732, May 2006.

[266] Hu Li, Choong Yong Ung, Xiao Hua Ma, Xiang Hui Liu, Bao Wen Li, Boon Chuan Low, and Yu Zong Chen. Pathway sensitivity analysis for detecting pro-proliferation activities of oncogenes and tumor suppressors of epidermal growth factor receptor-extracellular signal-regulated protein

kinase pathway at altered protein levels. *Cancer*, 115(18):4246–4263, Sep 2009.

[267] Edward C Stites, Paul C Trampont, Zhong Ma, and Kodi S Ravichandran. Network analysis of oncogenic ras activation in cancer. *Science*, 318(5849):463–467, Oct 2007.

[268] Deyan Luan, Michael Zai, and Jeffrey D Varner. Computationally derived points of fragility of a human cascade are consistent with current therapeutic strategies. *PLoS Comput Biol*, 3(7):e142, Jul 2007.

[269] Sang Ok Song and Jeffrey Varner. Modeling and analysis of the molecular basis of pain in sensory neurons. *PLoS One*, 4(9):e6758, 2009.

[270] S. Fields and R. Sternglanz. The two-hybrid system: an assay for protein-protein interactions. *Trends Genet.*, 10:282 – 292, 1994.

[271] G. Cagney, P. Uetz, and S. Fields. High-throughput screening for protein-protein interactions using two-hybrid assay. *Methods Enzymol*, 328:3 – 14, 2000.

[272] P. Uetz, L. Giot, G. Cagney, T. A. Mansfield, R. S. Judson, J. R. Knight, D. Lockshon, V. Narayan, M. Srinivasan, P. Pochart, A. Qureshi-Emili, Y. Li, B. Godwin, D. Conover, T. Kalbfleisch, G. Vijayadamodar, M. Yang, M. Johnston, S. Fields, and J. M. Rothberg. A comprehensive analysis of protein–protein interactions in *Saccharomyces cerevisiae*. *Nature*, 420:623 – 627, 2000.

[273] T. Ito, T. Chiba, R. Ozawa, M. Yoshida, M. Hattori, and Y. Sakaki. A comprehensive two-hybrid analysis to explore the yeast protein interactome . *Proc. Natl. Acad. Sci. USA*, 98:4569 – 4574, 2001.

[274] X. You, A. W. Nguyen, A. Jabaiah, M. A. Sheff, K. S. Thorn, and P. S. Daugherty. Intracellular protein interaction mapping with FRET hybrids. *Proc. Natl. Acad. Sci. USA*, 103:18458 – 18463, 2006.

[275] T. B. Farmer and R. M. Caprioli. Determination of protein-protein interactions by matrix-assisted laser desorption/ionization mass spectrometry. *J. Mass Spectrom.*, 33:697 – 704, 1998.

[276] A. Gavin, M. Bosche, R. Krause, P. Grandi, M. Marzioch, A. Bauer, J. Schultz, J. Rick, A. Michon, and C. Cruciat *et al.,*. Functional organi-

zation of the yeast proteome by systematic analysis of protein complexes. *Nature*, 415:141 – 147, 2002.

[277] Yuen Ho, Albrecht Gruhler, Adrian Heilbut, Gary D. Bader, Lynda Moore, Sally-Lin L. Adams, Anna Millar, Paul Taylor, Keiryn Bennett, Kelly Boutilier, Lingyun Yang, Cheryl Wolting, Ian Donaldson, Søren Schandorff, Juanita Shewnarane, Mai Vo, Joanne Taggart, Marilyn Goudreault, Brenda Muskat, Cris Alfarano, Danielle Dewar, Zhen Lin, Katerina Michalickova, Andrew R. Willems, Holly Sassi, Peter A. Nielsen, Karina J. Rasmussen, Jens R. Andersen, Lene E. Johansen, Lykke H. Hansen, Hans Jespersen, Alexandre Podtelejnikov, Eva Nielsen, Janne Crawford, Vibeke Poulsen, Birgitte D. Sørensen, Jesper Matthiesen, Ronald C. Hendrickson, Frank Gleeson, Tony Pawson, Michael F. Moran, Daniel Durocher, Matthias Mann, Christopher W. Hogue, Daniel Figeys, and Mike Tyers. Systematic identification of protein complexes in saccharomyces cerevisiae by mass spectrometry. *Nature*, 415(6868):180–183, Jan 2002.

[278] T. I. Lee, N. J. Rinaldi, F. Robert, D. T. Odom, Z. Bar-Joseph, G. K. Gerber, N. M. Hannett, C. T. Harbison, C.M. Thompson, I.Simon, J.Zeitlinger, E.G. Jennings, H.L. Murray, D. B. Gordon, B.Ren, J.J. Wyrick, J-B. Tagne, T.L. Volkert, E.Fraenkel, D.K. Gifford, and R. A. Young. Transcriptional Regulatory Networks in *Saccharomyces cerevisiae*. *Science*, 298:799 – 804, 2002.

[279] S. Fields. High-throughput two-hybrid analysis. The promise and the peril. *FEBS J.*, 272:5391 – 5399, 2005.

[280] Christian von Mering, Roland Krause, Berend Snel, Michael Cornell, Stephen G Oliver, Stanley Fields, and Peer Bork. Comparative assessment of large-scale data sets of protein-protein interactions. *Nature*, 417(6887):399–403, May 2002.

[281] R Milo, S Shen-Orr, S Itzkovitz, N Kashtan, D Chklovskii, and U Alon. Network motifs: simple building blocks of complex networks. *Science*, 298(5594):824–827, Oct 2002.

[282] Esti Yeger-Lotem, Shmuel Sattath, Nadav Kashtan, Shalev Itzkovitz, Ron Milo, Ron Y Pinter, Uri Alon, and Hanah Margalit. Network motifs in integrated cellular networks of transcription-regulation and protein-protein interaction. *Proc Natl Acad Sci U S A*, 101(16):5934–9, Apr 2004.

[283] N Kashtan, S Itzkovitz, R Milo, and U Alon. Topological generalizations of

network motifs. *Phys Rev E Stat Nonlin Soft Matter Phys*, 70(3 Pt 1):031909, Sep 2004.

[284] M K Stephen Yeung, Jesper Tegnér, and James J Collins. Reverse engineering gene networks using singular value decomposition and robust regression. *Proc Natl Acad Sci U S A*, 99(9):6163–8, Apr 2002.

[285] Jesper Tegner, M K Stephen Yeung, Jeff Hasty, and James J Collins. Reverse engineering gene networks: integrating genetic perturbations with dynamical modeling. *Proc Natl Acad Sci U S A*, 100(10):5944–9, May 2003.

[286] A. Gupta, J.D. Varner, and C.D. Maranas. Large-scale inference of the transcriptional regulation of *Bacillus subtilis*. *Comp. and Chem. Eng.*, 29:565 – 576, 2005.

[287] Jason W Locasale and Alejandro Wolf-Yadlin. Maximum entropy reconstructions of dynamic signaling networks from quantitative proteomics data. *PLoS One*, 4(8):e6522, 2009.

[288] Sophia Ananiadou, Douglas B Kell, and Jun-ichi Tsujii. Text mining and its potential applications in systems biology. *Trends Biotechnol*, 24(12):571–9, Dec 2006.

[289] Lars J Jensen, Michael Kuhn, Manuel Stark, Samuel Chaffron, Chris Creevey, Jean Muller, Tobias Doerks, Philippe Julien, Alexander Roth, Milan Simonovic, Peer Bork, and Christian von Mering. String 8–a global view on proteins and their functional interactions in 630 organisms. *Nucleic Acids Res*, 37(Database issue):D412–6, Jan 2009.

[290] Rune Linding, Lars Juhl Jensen, Gerard J Ostheimer, Marcel A T M van Vugt, Claus Jørgensen, Ioana M Miron, Francesca Diella, Karen Colwill, Lorne Taylor, Kelly Elder, Pavel Metalnikov, Vivian Nguyen, Adrian Pasculescu, Jing Jin, Jin Gyoon Park, Leona D Samson, James R Woodgett, Robert B Russell, Peer Bork, Michael B Yaffe, and Tony Pawson. Systematic discovery of in vivo phosphorylation networks. *Cell*, 129(7):1415–26, Jun 2007.

[291] Rune Linding, Lars Juhl Jensen, Adrian Pasculescu, Marina Olhovsky, Karen Colwill, Peer Bork, Michael B Yaffe, and Tony Pawson. Networkin: a resource for exploring cellular phosphorylation networks. *Nucleic Acids Res*, 36(Database issue):D695–9, Jan 2008.

[292] Kiyoko F Aoki-Kinoshita and Minoru Kanehisa. Gene annotation and pathway mapping in kegg. *Methods Mol Biol*, 396:71–91, 2007.

[293] Minoru Kanehisa, Michihiro Araki, Susumu Goto, Masahiro Hattori, Mika Hirakawa, Masumi Itoh, Toshiaki Katayama, Shuichi Kawashima, Shujiro Okuda, Toshiaki Tokimatsu, and Yoshihiro Yamanishi. Kegg for linking genomes to life and the environment. *Nucleic Acids Res*, 36(Database issue):D480–4, Jan 2008.

[294] Shujiro Okuda, Takuji Yamada, Masami Hamajima, Masumi Itoh, Toshiaki Katayama, Peer Bork, Susumu Goto, and Minoru Kanehisa. Kegg atlas mapping for global analysis of metabolic pathways. *Nucleic Acids Res*, 36(Web Server issue):W423–6, Jul 2008.

[295] S. C. Brooks, S. Kazmer, A. A. Levin, and A. Yen. Myeloid differentiation and retinoblastoma phosphorylation changes in hl-60 cells induced by retinoic acid receptor- and retinoid x receptor-selective retinoic acid analogs. *Blood*, 87(1):227–237, Jan 1996.

[296] Kevin S Brown and James P Sethna. Statistical mechanical approaches to models with many poorly known parameters. *Phys Rev E Stat Nonlin Soft Matter Phys*, 68(2 Pt 1):021904, Aug 2003.

[297] Andrew Yen, David M Lin, Thomas J Lamkin, and Susi Varvayanis. Retinoic acid, bromodeoxyuridine, and the delta 205 mutant polyoma virus middle t antigen regulate expression levels of a common ensemble of proteins associated with early stages of inducing hl-60 leukemic cell differentiation. *In Vitro Cell Dev Biol Anim*, 40(7):216–241, 2004.

[298] M. G. Wilkinson and J. B. Millar. Control of the eukaryotic cell cycle by map kinase signaling pathways. *FASEB J*, 14(14):2147–2157, Nov 2000.

[299] T.T.C. Yang, Q. Xiong, H. Enslen, R.J. Davis, and C.W. Chow. Phosphorylation of nfatc4 by p38 mitogen-activated protein kinases. *Mol Cell Biol*, 22(11):3892–3904, Jun 2002.

[300] K. Ohtani, J. DeGregori, and J. R. Nevins. Regulation of the cyclin e gene by transcription factor e2f1. *Proc Natl Acad Sci U S A*, 92(26):12146–12150, Dec 1995.

[301] D. J. Mangelsdorf, E. S. Ong, J. A. Dyck, and R. M. Evans. Nuclear receptor that identifies a novel retinoic acid response pathway. *Nature*, 345(6272):224–229, May 1990.

[302] B. N. Kholodenko, O. V. Demin, G. Moehren, and J. B. Hoek. Quantification of short term signaling by the epidermal growth factor receptor. *J Biol Chem*, 274(42):30169–30181, Oct 1999.

[303] L. L. Lin, M. Wartmann, A. Y. Lin, J. L. Knopf, A. Seth, and R. J. Davis. cpla2 is phosphorylated and activated by map kinase. *Cell*, 72(2):269–278, Jan 1993.

[304] W Kolch, G Heidecker, G Kochs, R Hummel, H Vahidi, H Mischak, G Finkenzeller, D Marme, and U R Rapp. Protein kinase c alpha activates raf-1 by direct phosphorylation. *Nature*, 364(6434):249–252, 1993 Jul 15.

[305] A. R. Asthagiri and D. A. Lauffenburger. A computational study of feedback effects on signal dynamics in a mitogen-activated protein kinase (mapk) pathway model. *Biotechnol Prog*, 17(2):227–239, 2001.

[306] K S Brown, C C Hill, G A Calero, C R Myers, K H Lee, J P Sethna, and R A Cerione. The statistical mechanics of complex signaling networks: nerve growth factor signaling. *Phys Biol*, 1(3-4):184–95, Dec 2004.

[307] Kapil Mayawala, Claudio A Gelmi, and Jeremy S Edwards. Mapk cascade possesses decoupled controllability of signal amplification and duration. *Biophys J*, 87(5):L01–2, Nov 2004.

[308] Jorrit J Hornberg, Bernd Binder, Frank J Bruggeman, Birgit Schoeberl, Reinhart Heinrich, and Hans V Westerhoff. Control of mapk signalling: from complexity to what really matters. *Oncogene*, 24(36):5533–42, Aug 2005.

[309] K. G. Gadkar, J Varner, and F J Doyle. Model identification of signal transduction networks from data using a state regulator problem. *Syst Biol (Stevenage)*, 2(1):17–30, Mar 2005.

[310] Peter Gennemark and Dag Wedelin. Benchmarks for identification of ordinary differential equations from time series data. *Bioinformatics*, 25(6):780–6, Mar 2009.

[311] S Bandara, J.P Schlöder, R Eils, H. G Bock, and T Meyer. Optimal Experimental Design for Parameter Estimation of a Cell Signaling Model. *PLoS Comput Biol*, 5:e1000558, 2009.

[312] L. Kuepfer, M. Peter, U Sauer, and J. Stelling. Ensemble modeling for analysis of cell signaling dynamics. *Nat Biotech*, 25(9):1001–1006, 2007.

[313] T.N Palmer, G.J Shutts, R Hagedorn, F.J Doblas-Reyes, Y Jung, and M. Leutbecher. Representing model uncertainty in weather and climate prediction. *Ann Rev Earth and Planetary Sci*, 33:163–193, 2005.

[314] Ryan N Gutenkunst, Joshua J Waterfall, Fergal P Casey, Kevin S Brown, Christopher R Myers, and James P Sethna. Universally sloppy parameter sensitivities in systems biology models. *PLoS Comput Biol*, 3(10):1871–78, Oct 2007.

[315] A. Yen, M. Williams, J. D. Platko, C. Der, and M. Hisaka. Expression of activated raf accelerates cell differentiation and rb protein down-regulation but not hypophosphorylation. *Eur J Cell Biol*, 65(1):103–113, Oct 1994.

[316] E Kaiser, R Förster, I Wolf, C Ebensperger, W M Kuehl, and M Lipp. The g protein-coupled receptor blr1 is involved in murine b cell differentiation and is also expressed in neuronal tissues. *Eur J Immunol*, 23(10):2532–9, Oct 1993.

[317] R. Forster, I. Wolf, E. Kaiser, and M. Lipp. Selective expression of the murine homologue of the G protein-coupled receptor BLR1 in B cell differentiation, B cell neoplasia and defined areas of the cerebellum. *Cell Mol. Biol.*, 40:381 – 387, 1994.

[318] Teddy T C Yang, Qiufang Xiong, Hervé Enslen, Roger J Davis, and Chi-Wing Chow. Phosphorylation of nfatc4 by p38 mitogen-activated protein kinases. *Mol Cell Biol*, 22(11):3892–904, Jun 2002.

[319] S J Collins, F W Ruscetti, R E Gallagher, and R C Gallo. Normal functional characteristics of cultured human promyelocytic leukemia cells (hl-60) after induction of differentiation by dimethylsulfoxide. *J Exp Med*, 149(4):969–74, Apr 1979.

[320] M.E. Csete and J.C. Doyle. Reverse Engineering of Biological Complexity. *Science*, 295:1664 – 1669, 2002.

[321] N Yang, R Schüle, D J Mangelsdorf, and R M Evans. Characterization of dna binding and retinoic acid binding properties of retinoic acid receptor. *Proc Natl Acad Sci U S A*, 88(9):3559–63, May 1991.

[322] Ahmedin Jemal, Rebecca Siegel, Elizabeth Ward, Taylor Murray, Jiaquan Xu, and Michael J Thun. Cancer statistics, 2007. *CA Cancer J Clin*, 57(1):43–66, 2007.

[323] Charles Huggins and Clarence V Hodges. Studies on prostatic cancer: I. the effect of castration, of estrogen and of androgen injection on serum phosphatases in metastatic carcinoma of the prostate. *Cancer Research*, 3(1):293–297, Jul 1941.

[324] L. D. Papsidero, M. C. Wang, L. A. Valenzuela, G. P. Murphy, and T. M. Chu. A prostate antigen in sera of prostatic cancer patients. *Cancer Res*, 40(7):2428–2432, Jul 1980.

[325] M. Kuriyama, M. C. Wang, C. L. Lee, C. S. Killian, L. D. Papsidero, H. Inaji, R. M. Loor, M. F. Lin, T. Nishiura, N. H. Slack, G. P. Murphy, and T. M. Chu. Multiple marker evaluation in human prostate cancer with the use of tissue-specific antigens. *J Natl Cancer Inst*, 68(1):99–105, Jan 1982.

[326] M. D. Sadar, M. Hussain, and N. Bruchovsky. Prostate cancer: molecular biology of early progression to androgen independence. *Endocr Relat Cancer*, 6(4):487–502, Dec 1999.

[327] M. A. Eisenberger, B. A. Blumenstein, E. D. Crawford, G. Miller, D. G. McLeod, P. J. Loehrer, G. Wilding, K. Sears, D. J. Culkin, I. M. Thompson, A. J. Bueschen, and B. A. Lowe. Bilateral orchiectomy with or without flutamide for metastatic prostate cancer. *N Engl J Med*, 339(15):1036–1042, Oct 1998.

[328] Ian F Tannock, Ronald de Wit, William R Berry, Jozsef Horti, Anna Pluzanska, Kim N Chi, Stephane Oudard, Christine Theodore, Nicholas D James, Ingela Turesson, Mark A Rosenthal, and Mario A Eisenberger. Docetaxel plus prednisone or mitoxantrone plus prednisone for advanced prostate cancer. *N Engl J Med*, 351(15):1502–1512, 2004 Oct 7.

[329] R. M. Evans. The steroid and thyroid hormone receptor superfamily. *Science*, 240:889 – 895, 1988.

[330] M. A. Carson-Junica, W. T. Schrader, and B. W. O'Malley. Sterioid receptor family: structure and functions. *Endocr. Rev.*, 11:201 – 220, 1990.

[331] J. D. McConnell. Prostatic growth: new insights into hormonal regulation. *Br. J. Urol.*, 76:5 – 10, 1955.

[332] P H Riegman, R J Vlietstra, J A van der Korput, A O Brinkmann, and J Trapman. The promoter of the prostate-specific antigen gene contains a functional androgen responsive element. *Mol Endocrinol*, 5(12):1921–1930, 1991 Dec.

[333] Edward P Gelmann. Molecular biology of the androgen receptor. *J Clin Oncol*, 20(13):3001–3015, 2002 Jul 1.

[334] Tsukasa Igawa, Fen-Fen Lin, Ming-Shyue Lee, Dev Karan, Surinder K Batra, and Ming-Fong Lin. Establishment and characterization of androgen-independent human prostate cancer lncap cell model. *Prostate*, 50(4):222–235, Mar 2002.

[335] Ming-Shyue Lee, Tsukasa Igawa, Ta-Chun Yuan, Xiu-Qing Zhang, Fen-Fen Lin, and Ming-Fong Lin. Erbb-2 signaling is involved in regulating psa secretion in androgen-independent human prostate cancer lncap c-81 cells. *Oncogene*, 22(5):781–796, Feb 2003.

[336] B. J. Feldman and D. Feldman. The development of androgen-independent cancer. *Nature Rev Cancer*, 1:34–45, 2001.

[337] Z. Culig, A. Hobisch, M. V. Cronauer, C. Radmayr, J. Trapman, A. Hittmair, G. Bartsch, and H. Klocker. Androgen receptor activation in prostatic tumor cell lines by insulin-like growth factor-i, keratinocyte growth factor, and epidermal growth factor. *Cancer Res*, 54(20):5474–5478, Oct 1994.

[338] L. V. Nazareth and N. L. Weigel. Activation of the human androgen receptor through a protein kinase a signaling pathway. *J Biol Chem*, 271(33):19900–19907, Aug 1996.

[339] S. Yeh, H. K. Lin, H. Y. Kang, T. H. Thin, M. F. Lin, and C. Chang. From her2/neu signal cascade to androgen receptor and its coactivators: a novel pathway by induction of androgen target genes through map kinase in prostate cancer cells. *Proc Natl Acad Sci U S A*, 96(10):5458–5463, May 1999.

[340] N. Craft, Y. Shostak, M. Carey, and C. L. Sawyers. A mechanism for hormone-independent prostate cancer through modulation of androgen receptor signaling by the her-2/neu tyrosine kinase. *Nat Med*, 5(3):280–285, Mar 1999.

[341] T. C. Meng, M. S. Lee, and M. F. Lin. Interaction between protein tyrosine phosphatase and protein tyrosine kinase is involved in androgen-promoted growth of human prostate cancer cells. *Oncogene*, 19(22):2664–2677, May 2000.

[342] P. Vihko. Human prostatic acid phosphatases: purification of a minor enzyme and comparisons of the enzymes. *Invest Urol*, 16(5):349–352, Mar 1979.

[343] M. F. Lin and G. M. Clinton. The epidermal growth factor receptor from prostate cells is dephosphorylated by a prostate-specific phosphotyrosyl phosphatase. *Mol Cell Biol*, 8(12):5477–5485, Dec 1988.

[344] A. A. Sinha, D. F. Gleason, M. J. Wilson, M. R. Wick, P. K. Reddy, and C. E. Blackard. Relationship of prostatic acid phosphatase localization in human prostate by a monoclonal antibody with the gleason grading system. *Prostate*, 13(1):1–15, 1988.

[345] H. Sakai, K. Shiraishi, Y. Minami, Y. Yushita, H. Kanetake, and Y. Saito. Immunohistochemical prostatic acid phosphatase level as a prognostic factor of prostatic carcinoma. *Prostate*, 19(3):265–272, 1991.

[346] T. C. Meng and M. F. Lin. Tyrosine phosphorylation of c-erbb-2 is regulated by the cellular form of prostatic acid phosphatase in human prostate cancer cells. *J Biol Chem*, 273(34):22096–22104, Aug 1998.

[347] S. Veeramani, T. Yuan, S. Chen, F. Lin, J. E. Petersen, S. Shaheduzzaman, S. Srivastava, R. G. MacDonald, and M. Lin. Cellular prostatic acid phosphatase: a protein tyrosine phosphatase involved in androgen-independent proliferation of prostate cancer. *Endocrine-Related Cancer*, 12:805–822, 2005.

[348] J. S. Horoszewicz, S. S. Leong, E. Kawinski, J. P. Karr, H. Rosenthal, T. M. Chu, E. A. Mirand, and G. P. Murphy. Lncap model of human prostatic carcinoma. *Cancer Res*, 43(4):1809–1818, Apr 1983.

[349] William W Chen, Birgit Schoeberl, Paul J Jasper, Mario Niepel, Ulrik B Nielsen, Douglas A Lauffenburger, and Peter K Sorger. Input-output behavior of erbb signaling pathways as revealed by a mass action model trained against dynamic data. *Mol Syst Biol*, 5:239, 2009.

[350] Mohamed Helmy, Jin Gohda, Jun-Ichiro Inoue, Masaru Tomita, Masa

Tsuchiya, and Kumar Selvarajoo. Predicting novel features of toll-like receptor 3 signaling in macrophages. *PLoS One*, 4(3):e4661, 2009.

[351] Kumar Selvarajoo, Yasunari Takada, Jin Gohda, Mohamed Helmy, Shizuo Akira, Masaru Tomita, Masa Tsuchiya, Jun-Ichiro Inoue, and Koichi Matsuo. Signaling flux redistribution at toll-like receptor pathway junctions. *PLoS One*, 3(10):e3430, 2008.

[352] Kumar Selvarajoo, Masaru Tomita, and Masa Tsuchiya. Can complex cellular processes be governed by simple linear rules? *J Bioinform Comput Biol*, 7(1):243–68, Feb 2009.

[353] M. F. Lin, M. S. Lee, R. Garcia-Arenas, and F. F. Lin. Differential responsiveness of prostatic acid phosphatase and prostate-specific antigen mrna to androgen in prostate cancer cells. *Cell Biol Int*, 24(10):681–689, 2000.

[354] Joshua Kim and Gerhard A Coetzee. Prostate specific antigen gene regulation by androgen receptor. *J Cell Biochem*, 93(2):233–241, Oct 2004.

[355] S Barnes-Ellerbe, KE Knudsen, and A Puga. 2,3,7,8-tetrachlorodibenzo-p-dioxin blocks androgen-dependent cell proliferation of LNCaP cells through modulation of pRB phosphorylation. *MOLECULAR PHARMACOLOGY*, 66(3):502–511, SEP 2004.

[356] IE Eder, Z Culig, R Ramoner, M Thurnher, T Putz, C Nessler-Menardi, M Tiefenthaler, G Bartsch, and H Klocker. Inhibition of LNCaP prostate cancer cells by means of androgen receptor antisense oligonucleotides. *CANCER GENE THERAPY*, 7(7):997–1007, JUL 2000.

[357] Alan Aderem. Systems biology: its practice and challenges. *Cell*, 121(4):511–513, May 2005.

[358] Cynthia A Heinlein and Chawnshang Chang. Androgen receptor in prostate cancer. *Endocr Rev*, 25(2):276–308, Apr 2004.

[359] Tsukasa Igawa, Fen-Fen Lin, Prathibha Rao, and Ming-Fong Lin. Suppression of lncap prostate cancer xenograft tumors by a prostate-specific protein tyrosine phosphatase, prostatic acid phosphatase. *Prostate*, 55(4):247–258, Jun 2003.

[360] Hui Gao, Xuesong Ouyang, Whitney A Banach-Petrosky, William L Gerald, Michael M Shen, and Cory Abate-Shen. Combinatorial activities of

akt and b-raf/erk signaling in a mouse model of androgen-independent prostate cancer. *Proc Natl Acad Sci U S A*, 103(39):14477–14482, Sep 2006.

[361] Ali Ziada, Albaha Barqawi, L. Michael Glode, Marileila Varella-Garcia, Frances Crighton, Susan Majeski, Mark Rosenblum, Madeleine Kane, Lin Chen, and E. David Crawford. The use of trastuzumab in the treatment of hormone refractory prostate cancer; phase ii trial. *Prostate*, 60(4):332–337, Sep 2004.

[362] C. M. Canil, M. J. Moore, E. Winquist, T. Baetz, M. Pollak, K. N. Chi, S. Berry, D. S. Ernst, L. Douglas, M. Brundage, B. Fisher, A. McKenna, and L. Seymour. Randomized phase ii study of two doses of gefitinib in hormone-refractory prostate cancer: a trial of the national cancer institute of canada-clinical trials group. *J Clin Oncol*, 23(3):455–460, Jan 2005.

[363] Alpana Soni, Argun Akcakanat, Gopal Singh, David Luyimbazi, Yuhuan Zheng, Doyil Kim, Ana Gonzalez-Angulo, and Funda Meric-Bernstam. eif4e knockdown decreases breast cancer cell growth without activating akt signaling. *Mol Cancer Ther*, 7(7):1782–1788, Jul 2008.

[364] J. Lukas, J. Bartkova, and J. Bartek. Convergence of mitogenic signalling cascades from diverse classes of receptors at the cyclin d-cyclin-dependent kinase-prb-controlled g1 checkpoint. *Mol Cell Biol*, 16(12):6917–6925, Dec 1996.

[365] Craig J Burd, Christin E Petre, Lisa M Morey, Ying Wang, Monica P Revelo, Christopher A Haiman, Shan Lu, Cecilia M Fenoglio-Preiser, Jiwen Li, Erik S Knudsen, Jiemin Wong, and Karen E Knudsen. Cyclin d1b variant influences prostate cancer growth through aberrant androgen receptor regulation. *Proc Natl Acad Sci U S A*, 103(7):2190–2195, Feb 2006.

[366] Q. Yu, Y. Geng, and P. Sicinski. Specific protection against breast cancers by cyclin d1 ablation. *Nature*, 411(6841):1017–1021, Jun 2001.

[367] S. Kobayashi, T. Shimamura, S. Monti, U. Steidl, C.J. Hetherington, A.M. Lowell, T. Golub, M. Meyerson, D.G. Tenen, G.I. Shapiro, et al. Transcriptional profiling identifies cyclin d1 as a critical downstream effector of mutant epidermal growth factor receptor signaling. *Cancer Res*, 66(23):11389–11398, Dec 2006.

[368] Youyuan Xu, Shao-Yong Chen, Kenneth N Ross, and Steven P Balk. Androgens induce prostate cancer cell proliferation through mammalian tar-

get of rapamycin activation and post-transcriptional increases in cyclin d proteins. *Cancer Res*, 66(15):7783–92, Aug 2006.

[369] Roberto Bianco, Incheol Shin, Christoph A Ritter, F. Michael Yakes, Andrea Basso, Neal Rosen, Junji Tsurutani, Phillip A Dennis, Gordon B Mills, and Carlos L Arteaga. Loss of pten/mmac1/tep in egf receptor-expressing tumor cells counteracts the antitumor action of egfr tyrosine kinase inhibitors. *Oncogene*, 22(18):2812–2822, May 2003.

[370] Yoichi Nagata, Keng-Hsueh Lan, Xiaoyan Zhou, Ming Tan, Francisco J Esteva, Aysegul A Sahin, Kristine S Klos, Ping Li, Brett P Monia, Nina T Nguyen, Gabriel N Hortobagyi, Mien-Chie Hung, and Dihua Yu. Pten activation contributes to tumor inhibition by trastuzumab, and loss of pten predicts trastuzumab resistance in patients. *Cancer Cell*, 6(2):117–127, Aug 2004.

[371] E R Sampson, S Y Yeh, H C Chang, M Y Tsai, X Wang, H J Ting, and C Chang. Identification and characterization of androgen receptor associated coregulators in prostate cancer cells. *J Biol Regul Homeost Agents*, 15(2):123–129, Apr-Jun 2001.

[372] Yueh-Chiang Hu, Shuyuan Yeh, Shauh-Der Yeh, Erik R Sampson, Jiaoti Huang, Peng Li, Cheng-Lung Hsu, Huei-Ju Ting, Hui-Kuan Lin, Liang Wang, Eungseok Kim, Jing Ni, and Chawnshang Chang. Functional domain and motif analyses of androgen receptor coregulator ara70 and its differential expression in prostate cancer. *J Biol Chem*, 279(32):33438–33446, Aug 2004.

[373] Steven P Balk and Karen E Knudsen. Ar, the cell cycle, and prostate cancer. *Nucl Recept Signal*, 6:e001, 2008.

[374] Paul L de Souza, Pamela J Russell, and John Kearsley. Role of the akt pathway in prostate cancer. *Curr Cancer Drug Targets*, 9(2):163–175, Mar 2009.

[375] Marek Los, Subbareddy Maddika, Bettina Erb, and Klaus Schulze-Osthoff. Switching akt: from survival signaling to deadly response. *Bioessays*, 31(5):492–495, May 2009.

[376] I.H. Koumakpayi, J.S. Diallo, C. Le Page, L. Lessard, M. Gleave, L.R. Bégin, A.M. Mes-Masson, and F. Saad. Expression and nuclear localization of erbb3 in prostate cancer. *Clin Cancer Res*, 12(9):2730–2737, May 2006.

[377] Maria Rosaria Cardillo, Salvatore Monti, Franco Di Silverio, Vincenzo Gentile, Francesco Sciarra, and Vincenzo Toscano. Insulin-like growth factor (igf)-i, igf-ii and igf type i receptor (igfr-i) expression in prostatic cancer. *Anticancer Res*, 23(5A):3825–3835, 2003.

[378] L. Tam, L. M. McGlynn, P. Traynor, R. Mukherjee, J. M S Bartlett, and J. Edwards. Expression levels of the jak/stat pathway in the transition from hormone-sensitive to hormone-refractory prostate cancer. *Br J Cancer*, 97(3):378–383, Aug 2007.

[379] T.V. Pestova, V.G. Kolupaeva, I.B. Lomakin, E.V. Pilipenko, I.N. Shatsky, V.I. Agol, and C.U.T. Hellen. Molecular mechanisms of translation initiation in eukaryotes. *PNAS*, 98(13):7029–2036, 2001.

[380] A. Unbehaun, S.I. Borukhov, C.U.T. Hellen, and T.V. Pestova. Release of initiation factors from 48S complexes during ribosomal subunit joining and the link between establishment of codon-anticodon base-pairing and hydrolysis of eIF2-bound GTP. *Genes & Development*, 18(24):3078–3093, 2004.

[381] M. Holcik and N. Sonenberg. Translational control in stress and apoptosis. *Nature Reviews Molecular Cell Biology*, 6(4):318–327, 2005.

[382] R.G.J. Vries, A. Flynn, J.C. Patel, X. Wang, R.M. Denton, and C.G. Proud. Heat Shock Increases the Association of Binding Protein-1 with Initiation Factor 4E. *Journal of Biological Chemistry*, 272(52):32779–32784, 1997.

[383] M. Stoneley and A.E. Willis. Cellular internal ribosome entry segments: structures, trans-acting factors and regulation of gene expression. *Oncogene*, 23:3200–3207, 2004.

[384] A. Garami, F.J.T. Zwartkruis, T. Nobukuni, M. Joaquin, M. Roccio, H. Stocker, S.C. Kozma, E. Hafen, J.L. Bos, and G. Thomas. Insulin Activation of Rheb, a Mediator of mTOR/S6K/4E-BP Signaling, Is Inhibited by TSC1 and 2. *Molecular Cell*, 11(6):1457–1466, 2003.

[385] B. P. Zhou, M. C. Hu, S. A. Miller, Z. Yu, W. Xia, S. Y. Lin, and M. C. Hung. Her-2/neu blocks tumor necrosis factor-induced apoptosis via the akt/nf-kappab pathway. *J Biol Chem*, 275(11):8027–8031, Mar 2000.

[386] F. A. Brightman and D. A. Fell. Differential feedback regulation of the mapk cascade underlies the quantitative differences in egf and ngf signalling in pc12 cells. *FEBS Lett*, 482(3):169–174, Oct 2000.

[387] P. Pozzi, C. Bendotti, S. Simeoni, F. Piccioni, V. Guerini, T. U. Marron, L. Martini, and A. Poletti. Androgen 5-alpha-reductase type 2 is highly expressed and active in rat spinal cord motor neurones. *J Neuroendocrinol*, 15(9):882–887, Sep 2003.

[388] A. O. Brinkmann, L. J. Blok, P. E. de Ruiter, P. Doesburg, K. Steketee, C. A. Berrevoets, and J. Trapman. Mechanisms of androgen receptor activation and function. *J Steroid Biochem Mol Biol*, 69(1-6):307–313, 1999.

[389] Lewis C Cantley. The phosphoinositide 3-kinase pathway. *Science*, 296(5573):1655–1657, May 2002.

[390] Juan Paez and William R Sellers. Pi3k/pten/akt pathway. a critical mediator of oncogenic signaling. *Cancer Treat Res*, 115:145–167, 2003.

[391] A Sekulic, C C Hudson, J L Homme, P Yin, D M Otterness, L M Karnitz, and R T Abraham. A direct linkage between the phosphoinositide 3-kinase-akt signaling pathway and the mammalian target of rapamycin in mitogen-stimulated and transformed cells. *Cancer Res*, 60(13):3504–3513, Jul 2000.

[392] T A Lin, X Kong, T A Haystead, A Pause, G Belsham, N Sonenberg, and J C Jr Lawrence. Phas-i as a link between mitogen-activated protein kinase and translation initiation. *Science*, 266(5185):653–656, Oct 1994.

[393] Lucy F Pemberton and Bryce M Paschal. Mechanisms of receptor-mediated nuclear import and nuclear export. *Traffic*, 6(3):187–198, Mar 2005.